



# Top, Higgs, SUSY and all those jets: analysing fully hadronic events at the LHC

Lorenzo Feligioni

## ► To cite this version:

Lorenzo Feligioni. Top, Higgs, SUSY and all those jets: analysing fully hadronic events at the LHC. High Energy Physics - Experiment [hep-ex]. Aix-Marseille Université (AMU), 2017. tel-01881686

**HAL Id: tel-01881686**

**<https://hal.science/tel-01881686>**

Submitted on 4 Oct 2018

**HAL** is a multi-disciplinary open access archive for the deposit and dissemination of scientific research documents, whether they are published or not. The documents may come from teaching and research institutions in France or abroad, or from public or private research centers.

L'archive ouverte pluridisciplinaire **HAL**, est destinée au dépôt et à la diffusion de documents scientifiques de niveau recherche, publiés ou non, émanant des établissements d'enseignement et de recherche français ou étrangers, des laboratoires publics ou privés.



# AIX-MARSEILLE UNIVERSITÉ

## ECOLE DOCTORALE 352

UMR 7346

CENTRE DE PHYSIQUE DES PARTICULES DE MARSEILLE

Habilitation à Diriger des Recherches

Discipline : Physique et sciences de la matière

Lorenzo FELIGIONI

Top, Higgs, SUSY and all those jets: analysing fully hadronic events  
at the LHC

Soutenue le 19/12/2017 devant le jury :

Cristinel DIACONU	CPPM	Examineur
Aurelio JUSTE	IFAE	Rapporteur
Aleandro NISATI	INFN/Rome	Rapporteur
Yves SIROIS	LLR	Rapporteur
Mossadek TALBY	CPPM	Tuteur
Isabelle WINGERTER	LAPP	Examineur



Cette oeuvre est mise à disposition selon les termes de la [Licence Creative Commons Attribution - Pas d'Utilisation Commerciale - Pas de Modification 3.0 France](#).

CONTACT  
INFORMATION

Address: Centre de Physique des Particules de Marseille  
163, avenue de Luminy Case 902  
13288 Marseille cedex 09  
Telephone: +33 4 91 82 76 21  
e-mail: lorenzo@in2p3.fr

## PERSONAL DATA

Date of Birth: 14 Mars 1973  
Place of Birth: Umbertide (PG), Italy  
Nationality: Italian

## EDUCATION

**Boston University**, Boston, MA USA  

- Ph.D, Graduate School of Arts and Science, January 2006
- Thesis Topic: *Search for Techniparticle at  $D\bar{0}$*
- Advisor: Professor Meenashi Narain

**Università degli Studi di Perugia**, Perugia (PG) Italy  
 Laurea, Physics Department of the University of Perugia, May 1999  

- Thesis Topic: *Calculation of the Electric Dipole Two-Time Correlation Functions for the Hydrogen Atom in Bohm Theory and Conventional Quantum Mechanics*
- Advisor: Professor Yogendra, N. Srivastava
- Area of Study: Quantum Mechanics

RESEARCH  
APPOINTMENTS

**CNRS Research Position (CR1)** October 2008 to present  
 Centre de Physique des Particules de Marseille UMR 6550, CNRS Institut national de physique nucléaire et de physique des particules (IN2P3) Aix-Marseille Université  

- Affiliated to the ATLAS Group

Phenomenological characterization of natural stop in R-parity violating SUSY models and experimental analysis aimed at the search for these class of models using Run 2 data collected at the LHC.

Search for the Standard Model Higgs boson decaying into  $b\bar{b}$  produced in association with top quarks decaying hadronically in  $p-p$  collisions at  $\sqrt{s} = 8$  TeV with the ATLAS detector.

Measurement of  $t\bar{t}$  production cross-section in the all-hadronic channel in  $p-p$  collisions at  $\sqrt{s} = 8$  TeV with the ATLAS detector.

Implementation, commissioning and maintenance of  $b$ -tagging algorithms at trigger level with the ATLAS detector.

**Postdoctoral Researcher**

January 2006 to October 2008

Centre de Physique des Particules de Marseille UMR 6550, CNRS Institut national de physique nucléaire et de physique des particules (IN2P3)



Aix-Marseille Université

- Affiliated to the ATLAS Group

---

Development of data-based methods for the evaluation of  $b$ -tagging efficiency with the ATLAS detector.

Sensitivity study for the Standard Model  $ttH(H \rightarrow b\bar{b})$  process with the ATLAS detector.

**Research Assistant**

January 2000 to December 2005

Physics Department, Boston University

- Affiliated to the DØ Group

---

Search for the Technicolor process  $\rho_T \rightarrow W\pi_T$  with the DØ experience using multivariate analysis techniques.

Analysis of DØ data in events with two calorimeter jets, one reconstructed electron and missing transverse energy as final state for Technicolor searches.

Optimisation and evaluation of DØ  $b$ -tagging capability. Study of Secondary Vertex Algorithm performances in data and Monte Carlo simulations.

Implementation of the online beam position measurement algorithm using DØ tracking detector.

Fermilab's Main Injector beam emittance monitoring studies.

SUPERVISING  
EXPERIENCE

**Master 2 diploma:** S. Aoun (2008), N. Tannoury (2009), D. Carabet (2012), Y. Duan (2016), N. Hoang Dai (2016), G. Bartolini (2017).

**Master 1 diploma:** D. Minenna (2014).

**PhD thesis:** C. Bertella (2013, actually at IHEP Bejing), Madaffari (2015, actually at IFIC Valencia), N. Hoang Dai (current).

CURRENT AND  
PAST GRANTS

*Search for new physics in top quark events with the ATLAS experiment, France-Stanford Center for Interdisciplinary Studies, September, 2011 – September, 2012.*

*Probing the Electroweak Symmetry Breaking with the ATLAS detector, Labex OCEVU, October 2013 –current.*

SCIENTIFIC  
RESPONSIBILITIES

*Co-direction of the Particle Physics working group of the LABEX OCEVU (2014-present).*

*Direction of ATLAS physics working group on fully hadronic  $ttH(H \rightarrow b\bar{b})$  analysis (2013-present).*

*Principal Investigator of the PESBLADe project funded by LABEX OCEVU (2013-present).*

*Co-convenership of the ATLAS  $b$ -jet trigger group (2012-2014).*

*Co-direction of the ATLAS physics working group on the  $t\bar{t}H(H \rightarrow b\bar{b})$  sensitivity study working group (2006-2008).*

MOST RELEVANT  
PUBLICATIONS

1. S. Diglio, L. Feligioni and G. Moulataka, *Stashing the stops in multijet events at the LHC*, Phys. Rev. D **96**, 55032 (2017) arXiv:1611.05850 [hep-ph].
2. ATLAS Collaboration, *Search for the Standard Model Higgs boson decaying into  $b\bar{b}$  produced in association with top quarks decaying hadronically in  $pp$  collisions at  $\sqrt{s} = 8$  TeV with the ATLAS detector*, JHEP **1605**, 160 (2016), arXiv:1604.03812 [hep-ex].
3. ATLAS Collaboration, *Performance of  $b$ -Jet Identification in the ATLAS Experiment*, JINST **11**, no. 04, P04008 (2016), arXiv:1512.01094 [hep-ex].
4. DØ Collaboration,  *$b$ -jet Identification in the DØ Experiment*, Nucl. Instrum. Methods in Phys. Res. Sect. A **620**, 490 (2010).
5. DØ Collaboration, *Search for Techniparticles Decaying into  $e$ -jets at DØ*, Phys. Rev. Lett. **98**, 221801 (2007); hep-ex/0612013; Fermilab-Pub-06/450-E.

CONTRIBUTIONS  
TO CONFERENCES

- L. Feligioni. *Searches for  $t\bar{t}$  resonances with the ATLAS detector at the LHC*, on behalf of ATLAS collaboration. SUSY 2015, 23<sup>rd</sup> International Conference on Supersymmetry and Unification of Fundamental Interactions, 23-29 August 2015, Lake Tahoe, California.
- L. Feligioni. *4<sup>th</sup> generation searches at ATLAS*, on behalf of ATLAS collaboration. 36<sup>th</sup> International Conference for High Energy Physics, 4-11 July 2012, Melbourne, Australia. *PoS(ICHEP2012) 560*.
- L. Feligioni. *Higgs at LHC*, on behalf of ATLAS and CMS collaborations. 21<sup>st</sup> International Workshop on Weak Interactions and Neutrinos, January 2007. Kolkata, India.
- L. Feligioni. *Searches for techniparticles at DØ*, on behalf of the DØ collaboration. Physics at LHC, July 2006. Cracow, Poland. *Acta Phys. Polon. B38*, 2007.
- L. Feligioni. *Search for technicolor particles at DØ*, on behalf of the DØ collaboration. Meeting of The Division of Particles and Fields of The American Physical Society, August 2004. Riverside, California. *Int. J. Mod. Phys. A20*, 2005.
- L. Feligioni, S. Bauceron.  *$Wb\bar{b}$  production at DØ*. Poster session. XXI International Symposium on Lepton and Photon Interaction at High Energies, August 2003. Fermilab, Batavia, Illinois.

L. Feligioni. *Search for Technicolor at DØ Run II*, on behalf of the DØ collaboration. A.P.S. Meeting, April 2002. Albuquerque, New Mexico.

TEACHING  
EXPERIENCE

**École Centrale Marseille,** December 2009 to March 2010.  
• Lecturer for the Option Generale, 30 hours module: *Introduction to Particle Physics*.

AWARDS

Boston University Physics Department: Goldhaber Prize for Achievements by a First Year Graduate Student, 2002.

# Contents

<b>List of figures</b>	<b>9</b>
<b>List of Tables</b>	<b>17</b>
<b>Introduction</b>	<b>27</b>
<b>1 Measurement of the <math>t\bar{t}</math> production cross section in the all-hadronic channel in <math>4.7 \text{ fb}^{-1}</math> of pp collisions at <math>\sqrt{s} = 7 \text{ TeV}</math> with the ATLAS detector</b>	<b>32</b>
1.1 Introduction	32
1.2 Data and simulated samples	33
1.2.1 Event selection	34
1.3 Kinematic fit analysis	35
1.3.1 Likelihood method	35
1.3.2 Top quark mass distribution	36
1.3.3 Modelling of the $m_t$ distribution for the multi-jet background	37
1.4 Cross section measurement	38
1.5 Systematic uncertainties	38
<b>2 Search for the Standard Model Higgs boson decaying into <math>b\bar{b}</math> produced in association with top quarks decaying hadronically in <math>pp</math> collisions at <math>\sqrt{s}=8 \text{ TeV}</math> with the ATLAS detector</b>	<b>43</b>
2.1 Introduction	43
2.2 Event selection	45
2.3 Signal and background modelling	45
2.3.1 Signal model	45
2.3.2 Simulated backgrounds	46
2.3.3 Common treatment of MC samples	47
2.3.4 Multijet background estimation using data: the $\text{TRF}_{\text{MJ}}$ method	48
2.3.5 Validation of the $\text{TRF}_{\text{MJ}}$ method in data and simulation	49
2.4 Multijet trigger efficiency	51
2.5 Event classification	52
2.6 Analysis method	58
2.7 Systematic uncertainties	62
2.8 Statistical methods	67
2.9 Results	67
2.10 Combination of $t\bar{t}H$ results at $\sqrt{s} = 7$ and $8 \text{ TeV}$	70
2.10.1 Individual $t\bar{t}H$ measurements and results	70
2.10.2 Correlations	72

2.10.3 Results of the combination	72
<b>3 Stashing the stops in multijet events at the LHC</b>	<b>88</b>
3.1 Introduction	88
3.2 Model assumptions	90
3.2.1 RPV-MSSM	90
3.2.2 LHC searches and new channels	92
3.2.3 mass spectrum	93
3.3 Stop production and decays	96
3.3.1 pair production	96
3.3.2 RPV final states	96
3.3.3 The $\lambda''_{33i}$ range	98
3.4 Narrow Width Approximation	101
3.5 Benchmark points and constraints	106
3.6 Cross-sections and uncertainties	111
3.6.1 Theoretical uncertainties	111
3.6.2 Final states sensitivity to $\lambda''_{33i}$	117
3.7 RPV Final States and SM background: a discussion	120
3.7.1 $2b2j$	121
3.7.2 $4b2j$ and $6b2j$	122
3.7.3 $1t5b2j$ and $2t4b2j$	123
<b>Conclusion</b>	<b>133</b>
<b>Bibliographie</b>	<b>134</b>
<b>ANNEXES</b>	<b>164</b>
A The ATLAS detector	164
A.1 Jets	164
A.2 Leptons and missing transverse momentum	165
A.3 Identification of $b$ -jets	166
A.4 $b$ -tagging at trigger level in Run 1	167
B Supervisory Experience	171
C Scientific Animation and Outreach	176
D Responsibilities	179

# List of figures

- 0.1 Expected region of exclusion (a) and excluded region (b) at the 95% C.L. in the  $M(\rho_T), M(\pi_T)$  plane for  $\rho_T \rightarrow W\pi_T \rightarrow e\nu b\bar{b}(\bar{c})$  production with  $M_V = 500$  GeV. Kinematic thresholds from  $W\pi_T$  and  $\pi_T\pi_T$  are shown on the figures [45, 46]. 28
- 0.2 Sensitivity for the discovery of a Standard Model Higgs boson. The statistical significances are plotted for individual channels as well as for the combination of all channels, assuming integrated luminosities of 30 fb<sup>-1</sup> (left) and 100 fb<sup>-1</sup> (right) of proton-proton collisions at center-of-mass energy  $\sqrt{s} = 14$  TeV. Depending on the numbers of signal and background events, the statistical significance has been computed as or using Poisson statistics. In the case of the  $H \rightarrow WW^* \rightarrow l\nu l\nu$  channel, a systematic uncertainty of  $\pm 5\%$  on the total number events has been included [63]. 29
- 0.3 One of the Feynman diagrams for  $t\bar{t}(H \rightarrow b\bar{b})$  production in the semi-leptonic final state [66]. 30
- 0.4 Example of Feynman diagrams for  $t\bar{t}b\bar{b}$  QCD production [66]. 30
- 0.5 Final data-to-Monte-Carlo  $b$ -tagging scale factors extracted from the System8 method and compared with results from the  $p_T^{rel}$  analysis, for the SV0 working point. [70] 31
- 1.1 Mass distributions obtained from the kinematic fit for simulated signal events with a top quark mass hypothesis of 172.5 GeV and passing the event selection. The distributions are normalized to unity. The distribution on the left is obtained from permutations that are fully matched to the  $t\bar{t}$  system. On the right hand side, permutations with at least one jet not correctly matched to the  $t\bar{t}$  system are shown. Filled circles (filled triangles) indicate that the fitted (reconstructed) jet energies are used to compute the mass of the top quark candidates. 37
- 1.2 Left hand side: Fit of the  $m_t$  distribution with an unbinned likelihood to the selected data sample (dots). The error bars associated to the data are statistical only. The two signal and background  $m_t$  templates are indicated as well. Right hand side:  $m_t$  distribution obtained after the kinematic fit to the untagged data sample (full line). The distributions after applying different corrections derived from Monte Carlo, as explained in Section 1.5, are overlaid (dashed and dotted lines). 39

- 2.1 Dependence of  $\varepsilon_{\text{MJ}}$  on the jet transverse momentum  $p_{\text{T}}$ , in regions of jet pseudorapidity  $\eta$  and average  $\Delta R$  between this jet and the two jets in the event with highest  $b$ -tagging weight,  $\langle \Delta R_{(j, \text{hMV1})} \rangle$ . The  $p_{\text{T}}$  bin boundaries are 25 (lowest), 40, 55, 70, 100, 200, 400, 600, 900 GeV (highest), chosen such as to have uniform number of events across bins of  $\langle \Delta R_{(j, \text{hMV1})} \rangle$ . 49
- 2.2 Comparison of the shapes predicted by the TRF<sub>MJ</sub> method (red histograms) and direct  $b$ -tagging (black circles) in data events with at least three jets and at least three  $b$ -tagged jets for (a) the third-leading  $b$ -tagged jet  $p_{\text{T}}$ , (b)  $H_{\text{T}}$ , and (c) Centrality<sub>Mass</sub>. The definitions of the variables are listed in Table 2.3. Events were selected with various single-jet triggers. The TRF<sub>MJ</sub> prediction is normalised to the same number of events as the data. The uncertainty band for the TRF<sub>MJ</sub> predictions shown in the ratio plot represents statistical uncertainties only. 50
- 2.3 Comparison of the shapes predicted for the TRF<sub>MJ</sub> method (red histograms) and direct  $b$ -tagging (black circles) in PYTHIA 8.1 multijet events with at least three jets and at least three  $b$ -tagged jets for (a) leading-jet  $p_{\text{T}}$ , (b)  $m_{jj}^{\text{min}}$  and (c) the third-leading  $b$ -tagged jet  $p_{\text{T}}$  in the event. The TRF<sub>MJ</sub> prediction is normalised to the same number of events as the data. The uncertainty band for the TRF<sub>MJ</sub> predictions shown in the ratio plot represents statistical uncertainties only. 51
- 2.4 Comparison of the shapes predicted by the TRF<sub>MJ</sub> method (red histograms) and direct  $b$ -tagging (black circles) in data events with at least three jets and at least three  $b$ -tagged jets for (a) the third-leading  $b$ -tagged jet  $p_{\text{T}}$ , (b)  $H_{\text{T}}$ , and (c) Centrality<sub>Mass</sub>. The definitions of the variables are listed in Table 2.3. Distributions are normalised to the same area. The uncertainty band for the TRF<sub>MJ</sub> predictions shown in the ratio plot represents statistical uncertainties only. 52
- 2.5 Comparison of the shapes predicted for the TRF<sub>MJ</sub> method (red histograms) and direct  $b$ -tagging (black circles) in PYTHIA 8.1 multijet events with at least three jets and at least three  $b$ -tagged jets for (a) leading-jet  $p_{\text{T}}$ , (b)  $m_{jj}^{\text{min}}$  and (c) the third-leading  $b$ -tagged jet  $p_{\text{T}}$  in the event. The definitions of the variables are listed in Table 2.3. Distributions are normalised to the same area. The uncertainty band for the TRF<sub>MJ</sub> predictions shown in the ratio plot represents statistical uncertainties only. 53
- 2.6 Single-jet trigger efficiencies,  $\epsilon_{\text{trig}}$ , (top) for data, simulated dijet events, and  $t\bar{t}H$  events, as a function of jet  $p_{\text{T}}$  for jets with  $|\eta| < 2.5$ ; (bottom)  $\text{SF}_{\text{trig}}(p_{\text{T}}, \eta) = \epsilon_{\text{trig}}^{\text{data}}(p_{\text{T}}, \eta) / \epsilon_{\text{trig}}^{\text{MC, dijet}}(p_{\text{T}}, \eta)$ . The uncertainty on  $\text{SF}_{\text{trig}}$ , shown as the green shaded area, is estimated from the difference between the efficiencies in dijet and  $t\bar{t}H$  simulated events in the denominator of  $\text{SF}_{\text{trig}}$ . 54

2.7	(a) $S/\sqrt{B}$ ratio for each of the regions assuming SM cross sections and branching fractions, and $m_H=125$ GeV. Each row shows the quantity for a specific jet multiplicity (6, 7, $\geq 8$ ), and the columns show the b-tag multiplicity (2, 3, $\geq 4$ ). Signal-rich regions are shaded in dark red, while the control regions are shown in light blue. The regions with two $b$ -tagged jets are not used in the fit and are presented in white. (b) The fractional contributions of the various backgrounds to the total background prediction in each considered region. The ordering of the rows and columns is the same as in (a). $t\bar{t}V$ and single top contributions are small and thus not visible in some of the analysis regions.	56
2.8	The distribution of the most discriminant variables entering the BDT in the 3 $b$ -tag regions (from (6j,3b) in (a)-(c), (7j,3b) in (d)-(f) to ( $\geq 8$ j,3b) in (g)-(i)). The plots show the separation power: the red histogram indicates the signal, the blue one the $t\bar{t}$ +jets background, and the green one the multijet background. The definitions of the variables are listed in Table 2.3.	60
2.9	The distribution of the most discriminant variables entering the BDT in the $\geq 4$ $b$ -tag regions (from (6j, $\geq 4$ b) in (a)-(c), (7j, $\geq 4$ b) in (d)-(f) to ( $\geq 8$ j, $\geq 4$ b) in (g)-(i)). The plots show the separation power: the red histogram indicates the signal, the blue one the $t\bar{t}$ +jets background, and the green one the multijet background. The definitions of the variables are listed in Table 2.3.	61
2.10	Response of the BDT algorithm for simulated signal (dashed red), $t\bar{t}$ +jets background (solid blue) and multijet background (dotted green) events in the (top) regions with 3 $b$ -tags ((a) 6, (b) 7 and (c) $\geq 8$ jets) and in the (bottom) regions with $\geq 4$ $b$ -tags ((d) 6, (e) 7 and (f) $\geq 8$ jets). The binning is the same as that used in the fit.	62
2.11	(a) Per event trigger scale factor $SF_{\text{trig}}$ (black dots) versus the BDT output of $t\bar{t}H$ events, shown with its corresponding systematic uncertainty (green band) for the ( $\geq 8$ j, $\geq 4$ b) region. (b) Comparison of the BDT output of the multijet background predicted with different sets of $TRF_{\text{MJ}}$ . The nominal $TRF_{\text{MJ}}$ is represented by the red points. The bottom panel shows the ratios of the alternative $TRF_{\text{MJ}}$ predictions to the nominal set.	64



- 2.12 Comparison between data and prediction for three top-ranked input variables in the (6j,3b) region before (left) and after (right) the fit. The fit is performed under the signal-plus-background hypothesis. Pre-fit plots show an overlay of the multijet distribution normalised to data for illustration purposes only. The plots include  $\text{Centrality}_{\text{Mass}}$ ,  $S_{\text{T}}$  and  $\Delta$ . The definitions of the variables are listed in Table 2.3. The first and last bins in all figures contain the underflow and overflow, respectively. The bottom panel displays the ratio of data to the total prediction, red arrows indicate the position of the point outside the ratio window. The hashed area represents the total uncertainty in the background predictions. The  $t\bar{t}H$  signal yield (solid red) is scaled by a fixed factor, shown in the figure, before the fit. 74
- 2.13 Comparison between data and prediction for three top-ranked input variables in the (6j, $\geq 4$ b) region before (left) and after (right) the fit. The fit is performed under the signal-plus-background hypothesis. Pre-fit plots show an overlay of the multijet distribution normalised to data for illustration purposes only. The plots include  $m_{2\text{jets}}$ ,  $\text{Centrality}_{\text{Mass}}$  and  $S_{\text{T}}$ . The definitions of the variables are listed in Table 2.3. The first and last bins in all figures contain the underflow and overflow, respectively. The bottom panel displays the ratio of data to the total prediction, red arrows indicate the position of the point outside the ratio window. The hashed area represents the total uncertainty in the background predictions. The  $t\bar{t}H$  signal yield (solid red) is scaled by a fixed factor, shown in the figure, before the fit. 75
- 2.14 Comparison between data and prediction for three top-ranked input variables in the (7j,3b) region before (left) and after (right) the fit. The fit is performed under the signal-plus-background hypothesis. Pre-fit plots show an overlay of the multijet distribution normalised to data for illustration purposes only. The plots include  $\frac{E_{\text{T}1} + E_{\text{T}2}}{\sum E_{\text{T}}^{\text{jets}}}$ ,  $\Delta R^{\text{min}}$  and  $\Delta$ . The definitions of the variables are listed in Table 2.3. The first and last bins in all figures contain the underflow and overflow, respectively. The bottom panel displays the ratio of data to the total prediction, red arrows indicate the position of the point outside the ratio window. The hashed area represents the total uncertainty in the background predictions. The  $t\bar{t}H$  signal yield (solid red) is scaled by a fixed factor, shown in the figure, before the fit. 76

- 2.15 Comparison between data and prediction for three top-ranked input variables in the  $(7j, \geq 4b)$  region before (left) and after (right) the fit. The fit is performed under the signal-plus-background hypothesis. Pre-fit plots show an overlay of the multijet distribution normalised to data for illustration purposes only. The plots include  $m_{2\text{jets}}$ ,  $\text{Centrality}_{\text{Mass}}$  and  $\frac{E_{T1}+E_{T2}}{\sum E_T^{\text{jets}}}$ . The definitions of the variables are listed in Table 2.3. The first and last bins in all figures contain the underflow and overflow, respectively. The bottom panel displays the ratio of data to the total prediction, red arrows indicate the position of the point outside the ratio window. The hashed area represents the total uncertainty in the background predictions. The  $t\bar{t}H$  signal yield (solid red) is scaled by a fixed factor, shown in the figure, before the fit. 77
- 2.16 Comparison between data and prediction for three top-ranked input variables in the  $(\geq 8j, 3b)$  region before (left) and after (right) the fit. The fit is performed under the signal-plus-background hypothesis. Pre-fit plots show an overlay of the multijet distribution normalised to data for illustration purposes only. The plots include  $S_T$ ,  $m_{\text{top},1}$  and  $\Lambda$ . The definitions of the variables are listed in Table 2.3. The first and last bins in all figures contain the underflow and overflow, respectively. The bottom panel displays the ratio of data to the total prediction, red arrows indicate the position of the point outside the ratio window. The hashed area represents the total uncertainty in the background predictions. The  $t\bar{t}H$  signal yield (solid red) is scaled by a fixed factor, shown in the figure, before the fit. 78
- 2.17 Comparison between data and prediction for three top-ranked input variables in the  $(\geq 8j, \geq 4b)$  region before (left) and after (right) the fit. The fit is performed under the signal-plus-background hypothesis. Pre-fit plots show an overlay of the multijet distribution normalised to data for illustration purposes only. The plots include  $m_{\text{top},1}$ ,  $\frac{E_{T1}+E_{T2}}{\sum E_T^{\text{jets}}}$  and  $\text{Centrality}_{\text{Mass}}$ . The definitions of the variables are listed in Table 2.3. The first and last bins in all figures contain the underflow and overflow, respectively. The bottom panel displays the ratio of data to the total prediction, red arrows indicate the position of the point outside the ratio window. The hashed area represents the total uncertainty in the background predictions. The  $t\bar{t}H$  signal yield (solid red) is scaled by a fixed factor, shown in the figure, before the fit. 79

- 2.18 Comparison between data and prediction for the BDT discriminant in the, from top to bottom, (6–8j, 3b) regions before (left) and after (right) the fit. The fit is performed under the signal-plus-background hypothesis. Pre-fit plots show an overlay of the multijet distribution normalised to data for illustration purposes only. The bottom panels display the ratios of data to the total prediction. The hashed areas represent the total uncertainty in the background predictions. The  $t\bar{t}H$  signal yield (solid red) is scaled by a fixed factor, shown in the figure, before the fit. 80
- 2.19 Comparison between data and prediction for the BDT discriminant in the, from top to bottom, (6–8j,  $\geq 4b$ ) regions before (left) and after (right) the fit. The fit is performed under the signal-plus-background hypothesis. Pre-fit plots show an overlay of the multijet distribution normalised to data for illustration purposes only. The bottom panels display the ratios of data to the total prediction. The hashed areas represent the total uncertainty in the background predictions. The  $t\bar{t}H$  signal yield (solid red) is scaled by a fixed factor, shown in the figure, before the fit. 81
- 2.20 Event yields as a function of  $\log_{10}(S/B)$ , where  $S$  (expected signal yield) and  $B$  (expected background yield) are taken from the corresponding BDT discriminant bin. Events from all fitted regions are included. The predicted background is obtained from the global signal-plus-background fit. The  $t\bar{t}H$  signal is shown both for the best-fit value ( $\mu = 1.6$ ) and for the upper limit at 95% CL ( $\mu = 6.4$ ). 82
- 2.21 The fitted values of the 20 nuisance parameters corresponding to the sources of systematic uncertainty with the largest impact on the fitted signal strength  $\mu$ . The points, which are drawn conforming to the scale of the bottom axis, show the deviation of each of the fitted nuisance parameters  $\hat{\theta}$  from  $\theta_0$ , which is the nominal value of that nuisance parameter, in units of the pre-fit standard deviation  $\Delta\theta$ . The plain yellow area represents the pre-fit impact on  $\mu$  and the hashed blue area its post-fit impact. The error bars show the post-fit uncertainties  $\sigma_\theta$ , which have size close to one if the data do not provide any further constraint on that uncertainty. Conversely, an error bar for  $\sigma_\theta$  smaller than one indicates a reduction with respect to the original uncertainty. The nuisance parameters are sorted according to their post-fit impact  $\Delta\theta$  (top horizontal scale). Multijet scale factors (SF) show the fitted values and uncertainties of the normalisation parameters that are freely floating in the fit. These normalisation parameters have a pre-fit value of unity. 83

2.22	Summary of the measurements of the signal strength $\mu$ for $t\bar{t}H(H \rightarrow b\bar{b})$ production for the individual $H \rightarrow b\bar{b}$ channels and for their combination, assuming $m_H = 125$ GeV. The total (tot) and statistical (stat) uncertainties of $\mu$ are shown. The SM $\mu = 1$ expectation is shown as the grey line.	84
2.23	Summary of the measurements of the signal strength $\mu$ for the individual channels and for their combination, assuming $m_H = 125$ GeV. The total (tot) and statistical (stat) uncertainties of $\mu$ are shown. The SM $\mu = 1$ expectation is shown as the grey line.	84
2.24	Upper limits on the signal strength $\mu$ for the individual channels as well as for their combination, at 95% CL. The observed limits (solid lines) are compared to the expected median limits under the background-only hypothesis (black dashed lines) and under the signal-plus-background hypothesis assuming the SM prediction for $\sigma(t\bar{t}H)$ (red dotted lines). The surrounding green and yellow bands correspond to the $\pm 1\sigma$ and $\pm 2\sigma$ ranges around the expected limits under the background-only hypothesis.	85
2.25	Log-likelihood for the combined $t\bar{t}H$ fit. The fit agrees with the SM expectation within the 68% CL contour. The physical boundary of $\kappa_V \geq 0$ is considered.	86
3.1	Leading RPV stop decays assuming Eqs. (3.11-3.13); (a): direct RPV stop decay ( $\tilde{t}$ -RPV), (b): shortest RPV cascade containing an (on-shell) chargino ( $\chi$ -RPV), (c): shortest RPV cascade containing an (on-shell) neutralino (RPC-like); $f, f', f_1, f'_1$ denote SM fermions and the oval encircles fermions too soft to be detected.	97
3.2	Benchmark 1: production cross-section for $\sigma(pp \rightarrow \tilde{t}\tilde{t} \rightarrow X)$ at $\sqrt{s} = 14$ TeV, where $X = 2b2j$ (red triangles), $4b2j$ (green squares), $6b2j$ (blue stars), $1t5b2j$ (black empty circles) and $2t4b2j$ (pink diamonds), as a function of $\lambda''_{33i}$ and for $m_{\tilde{t}} - m_{\chi^+} \simeq 0$ GeV(a), 50 GeV(b), 100 GeV(c) and 200 GeV(d). See Tabs. 3.2 and 3.3 for the low-energy values of the MSSM parameters.	112
3.3	Benchmark 2: production cross-section for $\sigma(pp \rightarrow \tilde{t}\tilde{t} \rightarrow X)$ at $\sqrt{s} = 14$ TeV, where $X = 2b2j$ (red triangles), $4b2j$ (green squares), $6b2j$ (blue stars), $1t5b2j$ (black empty circles) and $2t4b2j$ (pink diamonds), as a function of $\lambda''_{33i}$ and for $m_{\tilde{t}} - m_{\chi^+} \simeq 50$ GeV(a), 100 GeV(b), 150 GeV(c) and 200 GeV(d). See Tabs. 3.2 and 3.3 for the low-energy values of the MSSM parameters.	113

- 3.4 Benchmark 1: production cross-section for  $\sigma(pp \rightarrow \tilde{t}\tilde{t} \rightarrow X)$  at  $\sqrt{s} = 14$  TeV, where  $X = 2b2j$  (red triangles),  $4b2j$  (green squares),  $6b2j$  (blue stars),  $1t5b2j$  (black empty circles) and  $2t4b2j$  (pink diamonds), as a function of  $m_{\tilde{t}} - m_{\chi^+}$  and for  $\lambda''_{33i} = 10^{-1}$  (a),  $10^{-3}$  (b),  $10^{-5}$  (c) and  $10^{-7}$  (d). See Tabs. 3.2 and 3.3 for the low-energy values of the MSSM parameters. 114
- 3.5 Benchmark 2: production cross-section for  $\sigma(pp \rightarrow \tilde{t}\tilde{t} \rightarrow X)$  at  $\sqrt{s} = 14$  TeV, where  $X = 2b2j$  (red triangles),  $4b2j$  (green squares),  $6b2j$  (blue stars),  $1t5b2j$  (black empty circles) and  $2t4b2j$  (pink diamonds), as a function of  $m_{\tilde{t}} - m_{\chi^+}$  and for  $\lambda''_{33i} = 10^{-1}$  (a),  $10^{-3}$  (b),  $10^{-5}$  (c) and  $10^{-7}$  (d). See Tabs. 3.2 and 3.3 for the low-energy values of the MSSM parameters. 115
- 3.6 Schematic illustration of  $\lambda''_{33i}$  as a *signature generator*; different magnitudes of this coupling favor different final states. 120
- 3.7 Top-pair cross-section measurements at 7 TeV by the ATLAS and CMS collaborations. The band shows the NNLO QCD calculation complemented with NNLL resummation (top++2.0). The theory band represents uncertainties due to renormalisation and factorisation scale, parton density functions and the strong coupling. The measurements and the theory calculation is quoted at  $m_{\text{top}}=172.5$  GeV. The upper part of the figure shows early LHC measurements and their combination. The lower part summarizes measurements performed after the LHC cross-section combination. 127
- 3.8 The ATLAS  $b$ -jet trigger uses a BDT algorithm to separate  $b$ -jets from light and  $c$ -jet backgrounds. The BDT algorithm is re-optimized to improve  $b$ -tagging performance. Performance of  $b$ -tagging algorithms (measured using  $t\bar{t}$  Monte Carlo events) is shown in terms of light-jet rejection as a function of  $b$ -jet efficiency. Expected performance of  $b$ -tagging algorithm (MV2c10) for  $b$ -jet triggers in 2017 data-taking (green solid line) is compared to  $b$ -tagging algorithms used for  $b$ -jet triggers in 2016 (MV2c20) and 2015 (IP3D+SV1) data taking. Performance of  $b$ -tagging algorithm MV2c10 for offline jets is shown in purple dotted curve [303]. 130
- 3.9 Distribution of the classification BDT output for fully hadronic  $t\bar{t}H$  signal and  $t\bar{t}$ +jets background in events with at least eight jets and at least six  $b$ -tagged jets. 131
- 3.10  $H_T$  distribution for events with at least 8 jets at least 6  $b$ -tagged jets. The top signal from the  $6b2j$  final state (red full histogram) is stacked on top of the SM background composed by  $t\bar{t}b\bar{b}$  (blue full histogram),  $t\bar{t}H(H \rightarrow b\bar{b})$  (green full histogram),  $t\bar{t}Z(\rightarrow jj)$  (yellow full histogram),  $b\bar{b}b\bar{b} + X$  (purple full histogram). All histograms are normalized for an integrated luminosity of  $100 \text{ fb}^{-1}$  of  $pp$  collisions at  $\sqrt{s} = 14$  TeV. 132

A.I	Trigger rate for 2b/4j topology. LVL1, LVL2 and EF rate of a $b$ -jet trigger requiring at least four jets in the event and at least two $b$ -tagged jet. The jet thresholds correspond to 10, 25 and 30 GeV at LVL1, LVL2 and EF with energies measured at the electromagnetic scale. The $b$ -jet requirement is applied at LVL2 and EF is tuned to give 70% efficiency on a $b$ -tagged jet sample using top MC simulation.	167
A.II	Left hand side: Jet weight distribution for the tagger based on the combination of the impact parameter significance and the secondary vertex likelihood-based taggers, calculated from prescaled Level 2 tracks in Level 2 jets with $p_T > 50$ GeV and $ \eta  < 2.5$ . Only statistical errors are shown. Right hand side: Same for Event Filter jets with $p_T > 55$ GeV and $ \eta  < 2.5$ .	169
A.III	Histograms taken from the web display of Tier-0 offline monitoring of the XComb tagger weight. Left: for all the events passing the LVL2 trigger criteria for single jet triggers and for all the events passing the $\mu$ -jet trigger offline selection, without (Center) and with (Right) $p_T^{rel} \geq 2\text{GeV}$ requirement.	171

## List of Tables

1.1	Summary of the different systematic uncertainties associated with the kinematic fit analysis using the selected data events, $t\bar{t}$ MC simulated signal and data-driven background estimated events. Uncertainties are given in %. The asymmetric uncertainties are derived using [105].	42
2.1	Production cross sections for signal $t\bar{t}H$ , at $m_H = 125$ GeV, and various simulated background processes. The quoted errors arise from variations of the renormalisation and factorisation scales and uncertainties in the parton distribution functions.	48
2.2	Event yields from simulated backgrounds and the signal as well as data in each of the analysis regions prior to the fit (pre-fit). The quoted uncertainties are the sum in quadrature of the statistical and systematic uncertainties in the yields for all samples but the multijet background. The multijet normalisation and its systematic uncertainty are determined by the fit, so only its statistical uncertainty is quoted here. Since the numbers are rounded, the sum of all contributions may not equal the total value. The signal-to-background ratio, $S/B$ , and the significance, $S/\sqrt{B}$ , are also given. The $tH$ background is not shown as it amounts to fewer than 1.5 events in each region.	55

2.3	List of variables used in the BDT in the six analysis regions. The numbers indicate the ranking of the corresponding variables, ordered by decreasing discriminating power. Variables not used in the BDT of a specific region are marked by a dash.	57
2.4	Sources of systematic uncertainty considered in the analysis grouped in six categories. “N” denotes uncertainties affecting only the normalisation for the relevant processes and channels, whereas “S” denotes uncertainties which are considered to affect only the shape of normalised distributions. “SN” denotes uncertainties affecting both shape and normalisation. Some sources of systematic uncertainty are split into several components. The number of components is also reported.	63
2.5	Alternative predictions of the multijet background with the TRF <sub>MJ</sub> method. Multijet sets 1 to 5 correspond to variations of the nominal set of variables describing $\varepsilon_{\text{MJ}}$ . The next two sets specify the variation in the nominal set based on the two $b$ -tagged jets which are used to compute $\varepsilon_{\text{MJ}}$ . The last two refer to changes due to the residual mismodellings of $H_{\text{T}}$ and $S_{\text{T}}$ . Each of these variations of the multijet background shape is quantified by one nuisance parameter in the fit.	66
2.6	Event yields from simulated backgrounds and the signal as well as measured events in each of the analysis regions after the fit. The quoted uncertainties include statistical and systematical effects. The sum of all contributions may slightly differ from the total value due to rounding. The $tH$ background is not shown as fewer than 1.5 events in each region are predicted.	68
2.7	Observed and expected upper limits at 95% CL on $\sigma(t\bar{t}H)$ relative to the SM prediction assuming $m_H = 125$ GeV, for the background-only hypothesis. Confidence intervals around the expected limits under the background-only hypothesis are also provided, denoted by $\pm 1\sigma$ and $\pm 2\sigma$ , respectively. The expected (median) upper limit at 95% CL assuming the SM prediction for $\sigma(t\bar{t}H)$ is shown in the last column.	69
2.8	Effect of the different sources of systematic uncertainties on $\mu$ expressed in terms of percentage of the fitted value of $\mu$ sorted according to their post-fit effect.	70
2.9	Observed and expected (median, for the background-only hypothesis) upper limits at 95% CL on $\sigma(t\bar{t}H)$ relative to the SM prediction, for the individual channels as well as for their combination. The $\pm 1\sigma$ and $\pm 2\sigma$ ranges around the expected limit are also given. The expected median upper limits at 95% CL assuming the SM prediction for $\sigma(t\bar{t}H)$ are shown in the last column.	87

3.1	The various final states corresponding to different contents of heavy ( $b, t$ ) quarks, and light ( $d, s$ ) quarks denoted generically by $j$ , originating from the stop–anti-stop RPV decays; similar final states corresponding to interchanging the stop and anti-stop decays leading to the same particle content (irrespective of the electric charges) are listed only once.	98
3.2	Two lists of benchmark SUSY parameters defined at the low scale $Q_{EW\text{SB}}^2 = 1 \text{ TeV}^2$ taken as input for SPHENO. All other non-listed supersymmetric or soft SUSY breaking parameters are either computed from the input, such as $m_{H_{1,2}}^2$ , or irrelevant to the present study, such as $\lambda_{ijk}, \lambda'_{ijk}, \mu_i, T_{ijk}, T'_{ijk}, B_i, \tilde{m}_{1i}$ for all three generations, and $T''_{ijk}$ for $i, j = 1, 2$ . We also take $m_b(m_b)_{\overline{\text{MS}}} = 4.18\text{GeV}$ and $m_t(\text{pole}) = 173.5\text{GeV}$ . See [244] for the values of the other SM input parameters.	109
3.3	Two lists of benchmark observables generated with SPHENO corresponding to the input of Table 3.2 and taken as input for MADGRAPH5_AMC@NLO. Pole masses are evaluated at one-loop order except for the lightest CP-even Higgs which includes the 2-loop corrections.	110
3.4	Benchmark 1: production cross-section for $\sigma(pp \rightarrow \tilde{t}\tilde{t} \rightarrow X)$ at $\sqrt{s} = 14 \text{ TeV}$ , where $X = 2b2j, 4b2j, 6b2j, 1t5b2j$ and $2t4b2j$ , as a function of $\lambda''_{33i}$ and for different values of $m_{\tilde{t}} - m_{\chi^+}$ . See Tabs. 3.2 and 3.3 for the low-energy values of the MSSM parameters.	124
3.5	Benchmark 2: production cross-section for $\sigma(pp \rightarrow \tilde{t}\tilde{t} \rightarrow X)$ at $\sqrt{s} = 14 \text{ TeV}$ , where $X = 2b2j, 4b2j, 6b2j, 1t5b2j$ and $2t4b2j$ , as a function of $\lambda''_{33i}$ and for different values of $m_{\tilde{t}} - m_{\chi^+}$ . See Tabs. 3.2 and 3.3 for the low-energy values of the MSSM parameters.	125
3.6	Fit results for the parameterisation assuming the absence of BSM particles in the loops ( $B_{BSM} = 0$ ). The results with their measured uncertainties are reported for the combination of ATLAS and CMS, together with the individual results from each experiment.	128
A.I	ATLAS $b$ -tagging working points used for online xComb $b$ -tagging algorithm. These performance are evaluated on a sample of Monte Carlo $t\bar{t}$ events.	168



# Introduction

At the beginning there was the Standard Model (SM), well, it was not there from the start, but it was solidly standing when I first started working on experimental high energy physics, that was in January 2000.

If it were there it was thanks to the work of the theorists who formulated it and to the many teams of experimentalists who helped establishing it. We refer the reader to a first-hand testimony [1] for an historical review of how the work of Glashow, Weinberg and Salam [2, 3, 4] arose from the pioneering work of Heisenberg [5], Gell-Mann and Ne’emann [6] on flavor symmetries, from Yang-Mills first attempt to build a gauge theory for non-abelian groups [7], from the first formulation of weak interaction as mediated by a spin-1 massive particle [8, 9], from the work by Glashow itself on the introduction of the  $Z^0$  and finally from the work of Higgs and others [10, 11, 12, 13] on the mechanism of spontaneous symmetry breaking for gauge theories. To arrive at the SM as we know it now, we still had to wait for the work of Greenberg [14] and independently by Han and Nambu [15] on Quantum Chromodynamics (QCD) to be included on one side, and on the other for the discoveries of quarks [16, 17, 18, 19, 20, 21], gluons [22, 23] and all the leptons [24] and their neutrino partners [25, 26, 27] needed to complete the three families picture as we currently know it.

The great success of the SM as a predictive theory is still resonating today with the discovery in 2012 by the ATLAS and CMS experiments at the LHC [28, 29] of what was for a long time called “the elusive” Higgs boson. This is just the last of a series of experimental confirmations that, one after the other, contributed to the success of the SM, together with the first identification of neutral current in 1973 by the Gargamelle Neutrino Collaboration [30, 31], the discovery of the  $W$  [32, 33] and  $Z$  [34, 35] bosons by the UA1 and UA2 collaborations and all the precision measurements of the SM carried out at LEP [36].

From the rise of the SM era, until today, new theories have been formulated to address, even partly, the shortcomings of the SM. Probably the most established ones comes from the gravitational evidence for dark matter [37, 38], the discovery of the massive nature of neutrinos, as well as the observed baryon asymmetry [39] in the universe, which all suggest the existence of physics beyond the SM (BSM). On a mostly theoretical point of view it is worth to point that 18 free parameters are necessary to be measured for the SM to be defined, and therefore questions arise about the natures of these free parameters and why their value spans such a large range, i.e. 12 order of magnitude between the neutrino and the top-quark mass. The *flavor problem* enquires the flavour structure of the SM and the reason why there are exactly three families of leptons and quarks, with different mass hierarchy and mixing. In modern terms, the SM is seen as an effective field theory valid only up to certain energy scales. In this picture,

radiative corrections induce quadratic divergences to the Higgs mass, making it strongly dependent on the scale of the cut-off  $\Lambda$ . The higher the cut-off, namely the higher we can go in energy without encountering new physics, the more we need to fine tune the bare Higgs mass. No fine tuning is required if  $m_H \approx \Lambda$ , and given the measured value of the Higgs,  $\Lambda$  of order 1 TeV would still be quite natural, and require fine tuning within a factor of  $10^{-1} - 10^{-2}$ .

## Early work on Technicolor

I started my PhD by joining the Boston University DØ group lead by John Butler in January 2000. At the time DØ, a general purpose high energy detector was about to enter its Run II and getting ready to analyze the proton-anti-proton collisions at the unprecedented center-of-mass energy of 1.96 TeV produced by the Tevatron accelerator located at the Fermi National Laboratory (FNAL), in Batavia, IL. The two Fermilab experiments came out successfully from the first data taking, Run I, that took place from and that culminated with the discovery of the top-quark in 1995 [21, 40], one of the missing pieces that completed the list of fundamental fermions predicted by the SM. During Run II, FNAL experiments could exploit a time window, before the start of the LHC, when Tevatron was the most energetic collider running. Thanks in the improvement in the accelerator complex for Run II, Tevatron was the only place in the world where top-quark could be produced copiously and with a bit of luck either a hint of the presence of the Higgs boson or a sign of new physics beyond the Standard Model (BSM) could be found. In the first case the fact that LEP had an excess at 115 GeV [41] let the Tevatron people with the hope that the Higgs boson could be within the reach of Run II [42].

Technicolor (TC), first formulated by Weinberg and Susskind [43, 44], provides a dynamical explanation of electroweak symmetry breaking through a new strong  $SU(N_{TC})$  gauge interaction acting on new fermions, called “technifermions.” TC is a non-Abelian gauge theory modeled after Quantum Chromodynamics (QCD). In its low-energy limit, a spontaneous breaking of the global chiral symmetry in the technifermion sector leads to electroweak symmetry breaking. The Nambu-Goldstone bosons produced in this process are called technipions,  $\pi_T$ , in analogy with the pions of QCD. Three of these technipions become the longitudinal components of the  $W$  and  $Z$  bosons, making them massive.

An additional gauge interaction, called extended TC [47], couples standard model (SM) fermions and technifermions to provide a mechanism for generating quark and lepton masses. By slowing the running of the TC coupling constant, walking TC [48] can suppress flavor-changing neutral currents. To generate masses as large as the top quark mass, another interaction, topcolor, seems to be necessary, thereby giving rise to topcolor-assisted TC models [49].

Extensions of the basic TC model tend to require the number  $N_D$  of tech-

nifermion doublets to be large. In general, the TC scale  $\Lambda_{TC} \approx O(1) \times F_{TC}$ , where  $F_{TC}$  is the technipion decay constant, depends inversely on the number of technifermion doublets:  $F_{TC} \approx 246 \text{ GeV} / \sqrt{N_D}$ . For large  $N_D$ , the lowest lying technihadrons have masses on the order of few hundred GeV. This scenario is referred to as low-scale TC [50]. Low-scale TC models predict the existence of scalar technimesons,  $\pi_T^\pm$  and  $\pi_T^0$ , and vector technimesons,  $\rho_T$  and  $\omega_T$ .

General features of low-scale TC have been summarized in the TC straw-man model (TCSM) [51, 52]. Vector technimesons are expected to be produced with substantial rates at the proton-anti-proton collisions which were provided by the Fermilab Tevatron Collider via the Drell-Yan-like electroweak process  $p\bar{p} \rightarrow \rho_T + X$  or  $\omega_T + X$ . In walking TC, it is expected that vector technimesons decay to a gauge boson ( $\gamma, W, Z$ ) and a technipion or to fermion-antifermion pairs. The production cross sections and branching fractions depend on the masses of the vector technimesons,  $M(\rho_T)$  and  $M(\omega_T)$ , on the TC-charges of the technifermions, on the mass differences between the vector and scalar technimesons, which determine the spectrum of accessible decay channels, and on two mass parameters,  $M_A$  for axial-vector and  $M_V$  for vector couplings. The parameter  $M_V$  controls the rate for the decay  $\rho_T, \omega_T \rightarrow \gamma + \pi_T$  and is unknown *a priori*. Scaling from the QCD decay  $\rho, \omega \rightarrow \gamma + \pi^0$ , the authors of Ref. [52] suggest a value of several hundred GeV. We set  $M_A = M_V$ , and evaluate the production and decay rates at two different values: 100 and 500 GeV. For all other parameters, we use the default values quoted in Table III of Ref. [52]. The cross sections for  $\rho_T$  and  $\pi_T$  production at the Tevatron in the mass range of a few hundred GeV are expected to be in the range of 2 to 10 pb. Technipion coupling to the SM particles is proportional to their masses, therefore technipions in the mass range considered here predominantly decay into  $b\bar{b}$ ,  $b\bar{c}$ , or  $\bar{b}c$ , depending on their charge.

The analysis presented in my PhD thesis is based on Ref. [52]. I performed the search for the decay of vector technimesons to  $W\pi_T$ , followed by the decays  $W \rightarrow e\nu$  and  $\pi_T \rightarrow b\bar{b}, b\bar{c}, \text{ or } \bar{b}c$ . In the DØ detector, which is described in detail in Ref. [53], the signature of this process is an isolated electron and missing transverse momentum from the undetected neutrino from the decay of the  $W$  boson, and two jets of hadrons coming from the fragmentation of the quarks from the decay of the technipion. This search used events with this signature in the data collected with a single electron trigger until July 2004 and corresponding to an integrated luminosity of  $388 \pm 25 \text{ pb}^{-1}$ . After the event selection, two analysis strategies were used for discriminating signal and background, a cut-based one and a neural network (NN) one. The analysis ends with an estimation of the sources of systematic uncertainties and the final fit to extract the expected and observed 95% C.L. upper limit on the signal cross section. The expected sensitivity and the regions excluded at 95% C.L. by both analyses in the  $M(\rho_T), M(\pi_T)$  plane for  $M_V = 500 \text{ GeV}$  are shown in Fig. 0.1. For  $M_V = 100 \text{ GeV}$ , only a small region around  $M(\rho_T) = 190 \text{ GeV}$  and  $M(\pi_T) = 95 \text{ GeV}$  can be excluded.

Although differences in the employed TC models preclude a direct comparison with previous searches [54, 55], the sensitivity reached by this analysis supersedes previous searches for the same physics process.

Although Technicolor is an elegant way of describing a mechanism that dynamically produces the EWSB, its validity as viable alternative to the SM Higgs mechanism has been greatly undermined by experimental evidence both indirect, via EW precision measurements, and direct, the evidence of a scalar particle having a mass of 125 GeV behaving just like the SM Higgs [56] in association with the lack of evidence of the predicted QCD-like resonances at the EW scale at the LHC [57]. The idea of having an extended strong interacting sector is still considered viable in theories such as composite Higgs models [58, 59, 60, 61], where the Higgs boson can be the pseudo Nambu-Goldstone boson of an enlarged global symmetry of the strong dynamics. This is particularly interesting since such class of models predict also an extension of the fermionic content to reduce the UV sensitivity of the Higgs mass, in particular the presence of vector-like quarks that are looked for and could be seen at the LHC ([62] and references therein).

## Top-Higgs associated production at the LHC

I started working with the ATLAS group in 2006 when I joined the Centre de Physique de Particules de Marseille (CPPM). At that time both ATLAS and CMS collaborations were starting to re-evaluate their physics program with the help of both new Monte Carlo generators and more realistic detector simulations with respect to what was available just before. To put things in perspective, the ATLAS Higgs discovery potential was at the time still the one coming out of the Technical Design Report (TDR) [63], as represented in Figure 0.2, where the associated production of top quark pairs with a Higgs boson, subsequently decaying into  $b\bar{b}$   $t\bar{t}(H \rightarrow b\bar{b})$  was still considered a discovery channel for if the Higgs boson mass were sufficiently low.

The sensitivity study presented in the TDR made use of PYTHIA 5.7 [64] Monte Carlo generator to generate signal and the background events at leading order interfaced with a parametrized detector simulation. After that, there was an updated study by J. Cammin and M. Schumacher [65] which used a better MC generator (ACERMC), to simulate  $t\bar{t}$  + jets, the major source of physics background for  $t\bar{t}(H \rightarrow b\bar{b})$ . By making use of the matrix elements to generate the extra jets radiated from the  $t\bar{t}$  system, instead of using parton shower as in the case of PYTHIA 5.7, and by choosing  $Q_{QCD}^2 = (m_t + m_H/2)^2$  as the scale at which the  $t\bar{t}H$  cross section is calculated instead of the default PYTHIA value, which decreases the signal cross section by 20%, this analysis resulted on a reduction on the expected significance for a Higgs boson signal with a mass of 120 GeV and 30 fb<sup>-1</sup> of proton-proton collisions at  $\sqrt{s} = 14$  TeV from 3.6 to 1.9 $\sigma$ .

In 2007 the ATLAS collaboration reassessed its expected sensitivity for most physics analysis at the core of the LHC physics program. At that time the collaboration organized itself in small and effective working groups each one dedicated to the full assessment of different analyses using fully simulated events. On a side note, for some analyses such as many Higgs searches, this was the first time this could be done. I joined this effort and co-lead the working group responsible for the  $t\bar{t}H(H \rightarrow b\bar{b})$  analysis.

The semi-leptonic  $t\bar{t}H(H \rightarrow b\bar{b})$  final state, having a branching fraction, excluding tau leptons, of about 28%, is a good compromise between the all-hadronic channel, with the highest branching fraction and the largest background from QCD multijet, and the clean but statistically limited di-lepton final state. The analysis we performed analyzed signal from a Higgs boson mass of  $m_H = 120$  GeV generated with PYTHIA 6.403 [67]. The experimental signature consists of one energetic isolated lepton, high jet multiplicity with multiple  $b$ -tags, and missing transverse energy from the escaping neutrino, as shown in Figure 0.3. The production of  $t\bar{t}$  events is the main background. Given the high jet multiplicity in the signal process ( $\geq 6$  jets), only  $t\bar{t}$  events produced together with at least two extra jets contribute to the preselected data sample. Since most of these extra jets come from the hadronisation of light quarks, this contribution is greatly reduced by asking for four jets to be identified as  $b$ -jets. The irreducible background comes from  $t\bar{t}b\bar{b}$  production, see Figure 0.4. For this study state of the art cross section prediction and Monte Carlo generator were used for both signal and background. While no calculation was yet been performed for  $t\bar{t}b\bar{b}$  at next-to-leading order, (NLO), this study used a  $t\bar{t}b\bar{b}$  background simulated at LO.

The analysis consists of an initial preselection requirement, following which, two different techniques are implemented in order to reconstruct the top quark pairs and the Higgs boson through the identification of their decay products. At the preselection level we require exactly one isolated high- $p_T$  lepton (muon or electron), and at least six calorimeter jets, of which at least four must be identified as  $b$ -jets from the decay of the top quarks and the Higgs boson.

Two analyses were produced by the CPPM team, composed by a PhD student, Georges Aad and myself: a cut-based a likelihood-based one. In the first more simple one, top quarks are reconstructed by pairing two  $b$ -jets with the  $W$  boson candidates in the way which minimizes a  $\chi^2$ , based on the difference between the nominal and reconstructed masses. Only combinations which reconstruct reasonable well the top candidates are considered. The two remaining  $b$ -tagged jets are used to form the Higgs boson candidates. Only events in a mass window of 30 GeV from the nominal Higgs boson mass are used for the final estimation of the cut-based analysis significance. A straightforward improvement to the cut-based analysis is to use several discriminating topological distributions combined together in order to build a pairing likelihood. The only combination used is the one which maximizes the likelihood output. After this,  $b$ -jets are associated to reconstruct the Higgs boson.

The evaluation of systematic uncertainties, especially in the background level, is of vital importance in this analysis. Unfortunately at the time this analysis was performed it was not yet been brought to a satisfactory level and a robust method to infer background shapes and normalization from data, vital for this channel, still needed to be developed. The number of remaining events in the Higgs boson mass window (30 GeV around the nominal Higgs boson mass) has then been used to compute a crude estimate of the statistical significance for this channel with  $30 \text{ fb}^{-1}$ . For the cut-based analysis, a significance of 1.8 is achieved with signal to background ratio of approximately 0.11. With the pairing likelihood approach the significance is 1.95 for a signal to background ratio of 0.1. Finally the constrained fit likelihood, which was performed by other analyzers in the same working group, gives 2.2 (1.7) for a signal over background value of 0.12 (0.14), obtained with different cuts. The large systematic uncertainties estimated are an indication that a data driven background estimation is necessary.

This work lead to considerations on the necessity of measuring the background normalization from data. Further methods of extracting shape information from data had still to be developed, in particular, the extraction of the signal in the presence of a quasi-signal-like background as is exhibited in the invariant mass plots at the ends of the analyses. The result was finally published in what was known at the time as the *CSC book* [66].

## Performance studies with data: *b*-tagging efficiency calibration

Many analyses at the LHC rely on the identification of the presence of *b*-quarks in the final state. The class of algorithms which allows to recognize, with a different degree of certainty, the presence in the detector of a *b*-hadron within an hadronic jet of particles (*b*-jet) is known as *b*-tagging. The lifetime-based tagging algorithms take advantage of the relatively long lifetime of hadrons containing a *b*-quark, of the order of 1.5 ps ( $c\tau \approx 450 \text{ }\mu\text{m}$ ). A *b*-hadron with  $p_T = 50 \text{ GeV}$  will have a significant mean flight path length  $\langle l \rangle = \beta\gamma c\tau$ , travelling on average about 3 mm in the transverse direction before decaying and therefore leading to topologies with at least one vertex displaced (*secondary vertex*) from the point where the hard-scatter collision occurred, this displacement is referred to as the *decay length*  $L$ . Life-time alogorithms make use the impact parameters of the charged-particle tracks to discriminate calorimeter jets from the *b*-hadron decay products from the ones originating from *c* or light-quark hadronizations. Among the many lifetime algorithms developed in ATLAS, a simple one, *SV0*, require de presence of a secondary vertex with a large decay length significance, defined as  $L/\sigma(L)$  [68]. As a guidance principle the uncertainties on the efficiency of tagging a *b*-jet need to be known at percent level in order not to undermine the precision of measurements which use this class of algorithms.



In first approximation the knowledge of the  $b$ -tagging efficiency is correlated to the one of the  $b$ -jet content of the calibration data sample used. Calibration analyses either rely on topological properties of  $b$ -jets, such as the presence of a soft non-isolated muon within the jet ( $\mu$ -jet) with high  $p_T^{rel}$ , arising from the semileptonic decays of  $b$ -hadrons, or make use a highly pure sample from very tightly selected dileptonic top-quark pairs, where the only two jets in the events are  $b$ -jets.

At the beginning of the Run 1, top-quark-based calibration techniques were suffering from large statistical uncertainties. On the other hand the abundance of single jet events in data was sufficient for those techniques I helped to develop at DØ to calibrate the Secondary Vertex  $b$ -tagging algorithm, the so called *System8* method [69]. In 2008 a first feasibility studies using ATLAS simulated events was produced in collaboration with Prof. Gordon Watts and Orin Harris, PhD student, both from the University of Washington.

The *System8* method uses three uncorrelated selection criteria to construct a system of eight equations based on the number of events surviving any given subset of these criteria. The system, which is fully constrained, is used to solve for eight unknowns: the efficiencies for  $b$  and non- $b$ -jets to pass each of the three selection criteria, and the number of  $b$  and non- $b$ -jets originally present in the sample. As there are insufficient degrees of freedom to make a complete separation of the non- $b$  component into ( $c$ ,  $s$ ,  $d$ ,  $u$ ,  $g$ ) jet flavours, these are combined into one category and denoted  $cl$ . In simulated events, the flavour composition of the sample is relatively independent of jet  $p_T$  in the range studied, while the efficiencies to pass each of the selection criteria have a strong  $p_T$  dependence. The three selection criteria chosen are:

- The lifetime-based tagging criterion under study.
- The requirement of large  $p_T^{rel}$ .
- The requirement of at least another jet in the event, other than the one containing the muon, with a reconstructed secondary vertex with a signed decay length significance  $L/\sigma(L) > 1$ .

As a result of a collaboration between members of the CPPM group (Mossadek Talby, Nancy Tannoury and myself) and Prof. Joe Boudreau from the University of Pittsburgh who came as a visiting scientist at CPPM during the period 2009-2010. We were able to apply the *System8* method to a sample of  $\mu$ -jets from the full 2010 dataset, amounting to an integrated luminosity of  $35 \text{ pb}^{-1}$  collected at

---

<sup>a</sup>Because of their large mass compared to other quarks,  $b$ -hadron decays can be identified by the large transverse momentum of the muon with respect to the vectorial sum of the muon plus the hadronic jet momentums, this quantity is referred to as  $p_T^{rel}$ .

center of mass energy  $\sqrt{s} = 7$  TeV. The analysis is carried out for jets in four  $p_T$  bins and for several lifetime taggers and operating points resulting on  $b$ -tagging efficiencies and data-to-Monte-Carlo scale factor (see for example Figure 0.5). The method yielded results in good agreement with other ATLAS calibration techniques, these results were updated to use the full Run 1 data set and the System8 calibration used collaboratiowide by the Run 1 analyses [68].

## Top, Higgs, SUSY and all those jets

The work presented in this document mainly concerns physics analysis in final states with multiple hadronic jets. Chapter 1 describes the first data analysis I was involved with in Run 1: the measurement of the  $t\bar{t}$  production in the all-hadronic final state using the full 2011 dataset of proton-proton collisions at center of mass energy of 7 TeV [71]. The second chapter describes the evolution of the previous analysis into a search for the SM Higgs boson decaying into  $b\bar{b}$  produced in association with top quarks decaying hadronically, this time using 2012 ATLAS data at  $\sqrt{s} = 8$  TeV [72]. The third and final chapter describes a phenomenomenological work performed within the PESBLADe collaboration on the reinterpretation of the multi-jet SM analyses in terms of searches for new physics in Supersymmetric models where the R-parity is not conserved [73]. And finally, a set of conclusive remarks and outlook will be presented.



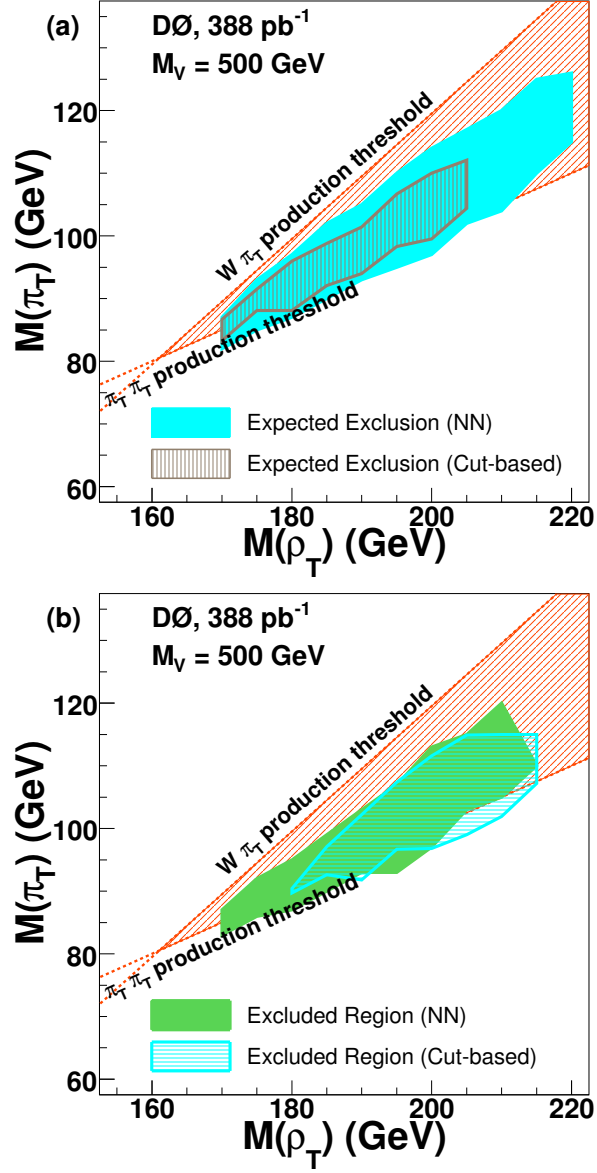


Figure 0.1.: Expected region of exclusion (a) and excluded region (b) at the 95% C.L. in the  $M(\rho_T)$ ,  $M(\pi_T)$  plane for  $\rho_T \rightarrow W\pi_T \rightarrow e\nu b\bar{b}(\bar{c})$  production with  $M_V = 500$  GeV. Kinematic thresholds from  $W\pi_T$  and  $\pi_T\pi_T$  are shown on the figures [45, 46].

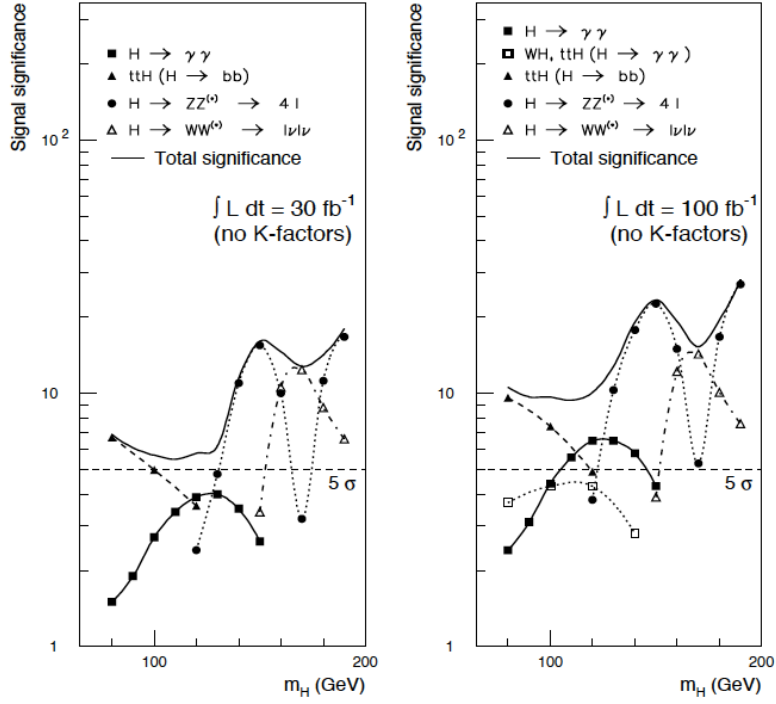


Figure 0.2.: Sensitivity for the discovery of a Standard Model Higgs boson. The statistical significances are plotted for individual channels as well as for the combination of all channels, assuming integrated luminosities of 30 fb<sup>-1</sup> (left) and 100 fb<sup>-1</sup> (right) of proton-proton collisions at center-of-mass energy  $\sqrt{s} = 14$  TeV. Depending on the numbers of signal and background events, the statistical significance has been computed as or using Poisson statistics. In the case of the  $H \rightarrow WW^* \rightarrow l\nu l\nu$  channel, a systematic uncertainty of  $\pm 5\%$  on the total number events has been included [63].

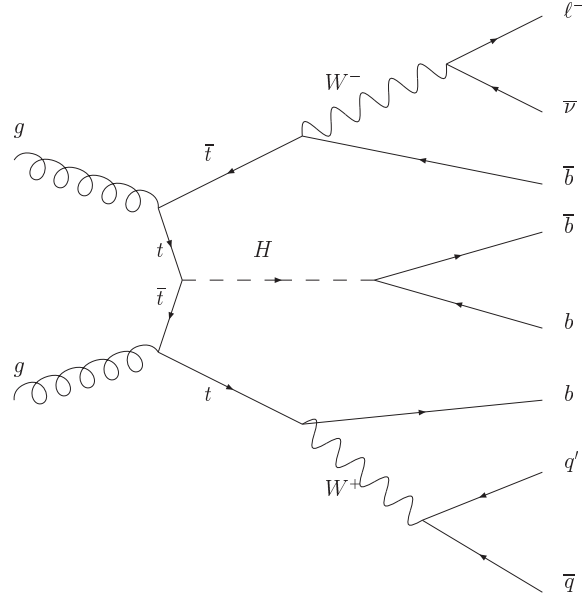


Figure 0.3.: One of the Feynman diagrams for  $t\bar{t}(H \rightarrow b\bar{b})$  production in the semi-leptonic final state [66].

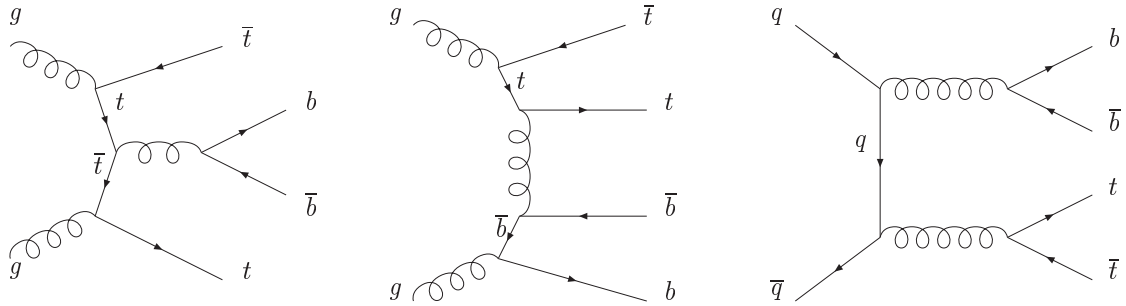


Figure 0.4.: Example of Feynman diagrams for  $t\bar{t}b\bar{b}$  QCD production [66].

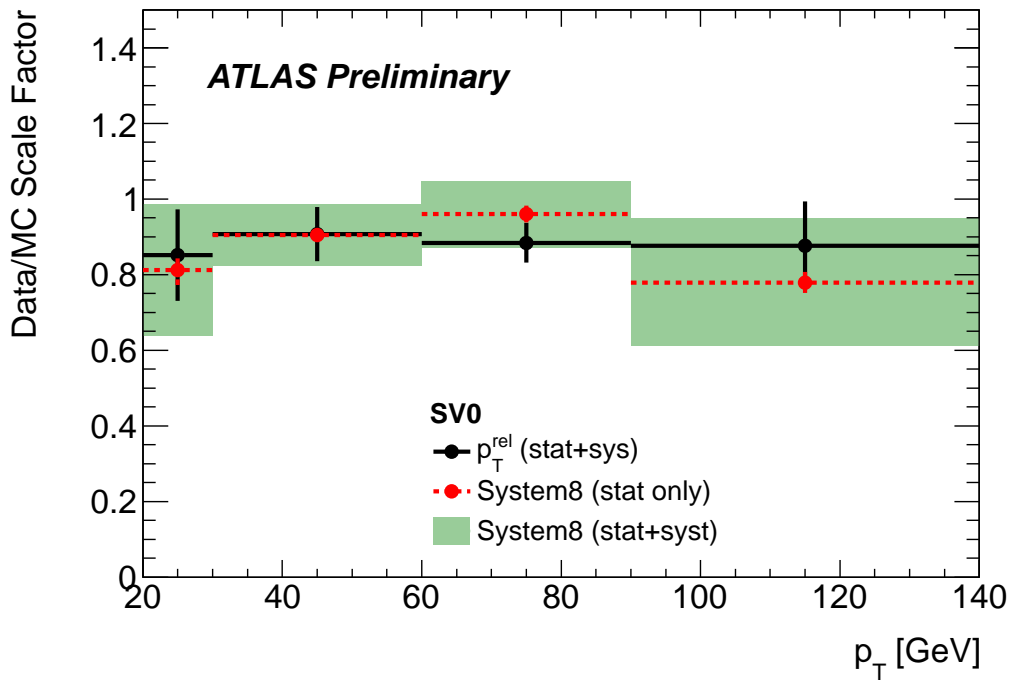


Figure 0.5.: Final data-to-Monte-Carlo  $b$ -tagging scale factors extracted from the System8 method and compared with results from the  $p_T^{\text{rel}}$  analysis, for the SV0 working point. [70]

# 1. Measurement of the $t\bar{t}$ production cross section in the all-hadronic channel in $4.7 \text{ fb}^{-1}$ of pp collisions at $\sqrt{s} = 7 \text{ TeV}$ with the ATLAS detector

From October 2011 through October 2014, together with Mossadek Talby, I co-directed the PhD thesis of Claudia Bertella. For her PhD she performed the measure of the top anti-top quark pair production cross section in the fully hadronic final state, using the data collected by ATLAS at the center-of-mass energy  $\sqrt{s} = 7 \text{ TeV}$ . At the time we started working on this analysis ATLAS had two results already published: one first search, using  $36 \text{ pb}^{-1}$  of  $p-p$  collisions produced at center-of-mass energy of  $\sqrt{s} = 7 \text{ TeV}$  and recorded in 2010, which could just set an observed (expected) upper limit at 261 (314) pb at 95% confidence level [74], and an actual measurement based on a data sample collected in 2011 with an integrated luminosity of  $1.02 \text{ fb}^{-1}$ , which resulted in a measured  $t\bar{t}$  total production cross section of  $\sigma_{t\bar{t}} = 167 \pm 18 \text{ (stat.)} \pm 78 \text{ (syst.)} \pm 6 \text{ (lum.) pb}$  [75]. The cross section measurement performed analyzing the full  $p-p$  collision at  $\sqrt{s} = 7 \text{ TeV}$  was at the beginning supposed to be just an update of the previous result, using the same analysis techniques. A team composed by Claudia Bertella, Ignacio Aracena (post-doc at SLAC National Accelerator Laboratory) and myself, came out with a different technique to reconstruct the  $t\bar{t}$  final state, based on a kinematic fit, which was instead retained for the final cross section extraction. The CPPM-SLAC team benefited from the support of the France-Stanford Center for Interdisciplinary Studies, which granted the necessary funds to cover the travel expenses US-Europe and allowed us to develop an analysis software infrastructure. This result was finally presented at the 2012 Rencontres de Moriond [71] by Ignacio Aracena.

## 1.1. Introduction

The measurement of the top quark pair production cross section in proton-proton collisions provides an important test of perturbative QCD calculations. Furthermore,  $t\bar{t}$  events constitute a major background to many new physics scenarios. The predicted  $t\bar{t}$  production cross section for proton-proton collisions at a centre-of-mass energy of  $\sqrt{s} = 7 \text{ TeV}$  is:  $\sigma_{\text{SM}}^{t\bar{t}} = 167_{-18}^{+17} \text{ pb}$ , for a top quark mass of

172.5 GeV. It has been calculated at approximate NNLO in QCD with HATHOR 1.2 [76] using the MSTW2008 90% NNLO PDF sets [77] incorporating PDF+ $\alpha_s$  uncertainties according to the MSTW prescription [78] and cross checked with the NLO+NNLL calculation [79] as implemented in TOP++ 1.0 [80]. In the SM, the top quark decays into a  $W$  boson and a  $b$ -quark with almost 100% probability. The  $W$  boson subsequently decays into either a quark-antiquark pair or a charged lepton and a neutrino. The analysis presented here is a measurement of  $t\bar{t}$  production in the all-hadronic final state where both  $W$  bosons decay hadronically, characterized by a six-jet topology. This channel has the advantage of a large branching ratio (46% [81]) but it suffers from a large multi-jet background.

The result presented in this document is based on  $pp$  collisions at a centre-of-mass energy of  $\sqrt{s} = 7$  TeV produced at the Large Hadron Collider (LHC) and recorded with the ATLAS detector [82] in 2011. The integrated luminosity is  $4.7 \text{ fb}^{-1}$ . This work is complementary to other ATLAS  $t\bar{t}$  cross section measurements performed in the single lepton and dilepton channels [83, 84, 85]. The chapter is structured as follows. A description of the ATLAS detector is given at the end of this document within the Appendix A. The description of the data and Monte Carlo (MC) simulation samples is given in Section 1.2. To isolate the  $t\bar{t}$  signal, several kinematic and topological characteristics can be exploited together with  $b$ -jet identification requirements ( $b$ -tagging). The reconstructed object definitions and event selections are described in Section 1.2. After the event selection, discussed in Section 1.2.1, a *Kinematic Fit* is performed to compute the reconstructed top quark mass ( $m_t$ ) of  $t\bar{t}$  candidate events, which is described in Section 1.3. This variable is used to perform an unbinned likelihood fit and extract the cross section. The resulting cross section is presented in Section 1.4. A review of the sources of systematic uncertainties is given in Section 1.5.

## 1.2. Data and simulated samples

The data used in this analysis were recorded during the 2011 data taking period with  $pp$  collisions at  $\sqrt{s} = 7$  TeV, with stable beam conditions and all subsystems operational. They represent a total integrated luminosity of  $4.7 \text{ fb}^{-1}$  with an uncertainty of 3.9% [86]. The analysed data sample was collected with a jet trigger requiring at least five jets in the pseudorapidity range  $|\eta| < 3.2$ , each having  $E_T > 30$  GeV at the Event Filter level [87]. In order to assure a high signal efficiency without introducing a large systematic uncertainty from the five-jet trigger threshold, an offline cut of  $E_T > 55$  GeV on the five leading jets is introduced. This value is derived from the five-jet trigger dependence on the fifth leading jet  $p_T$  and corresponds to a 90 % efficiency, with the efficiency plateau reached when all five jets have  $E_T > 60$  GeV.

The modelling of the  $t\bar{t}$  signal and its associated selection efficiency is derived from MC simulation. For the MC generation of the  $t\bar{t}$  signal, the MC@NLO

v3.41 [88] generator with PDF set CT10 [89, 90] is used. The signal is generated assuming a top quark mass of 172.5 GeV and is used to tune the selection criteria and build a signal template to fit the data. The generated events were processed through the full ATLAS detector [91] simulation based on GEANT4 [92] followed by the trigger simulation and the offline reconstruction software. Due to the large uncertainty in the multi-jet cross section prediction, a data-driven technique, described in Section 1.3.3, is employed to estimate the background. A MC sample of multi-jet events generated with ALPGEN [93] is used to assess the systematic uncertainty on the background modelling.

### 1.2.1. Event selection

Events are selected by first requiring that the trigger condition described in Section 1.2 is satisfied. Kinematic cuts are applied to the events to define the signal region. Events are required to have:

- at least one reconstructed primary vertex with five or more associated tracks;
- no isolated lepton with  $p_T > 20$  GeV;
- no jet produced by out-of-time or other fake energy deposits in the calorimeters. Such jets are produced by hardware problems in the calorimeter, LHC beam-gas interactions or cosmic-ray induced showers;
- all jets reconstructed with a jet vertex fraction<sup>a</sup>  $|JVF| \leq 0.75$  and  $p_T > 20$  GeV are vetoed;
- at least five jets with  $p_T > 55$  GeV and  $|\eta| < 2.5$ ;
- at least one more jet, a sixth one, having  $p_T > 30$  GeV and  $|\eta| < 2.5$ .
- at least two of the selected jets should be  $b$ -tagged by the MV1 algorithm and have  $p_T > 55$  GeV and  $|\eta| < 2.5$ ;
- the ratio  $S_t = E_T^{\text{miss}} / (0.5\sqrt{\text{GeV}} \times \sqrt{H_T}) < 6$ , where  $H_T$  is the scalar sum of the transverse momenta of all jets in the event. This ensures that the observed  $E_T^{\text{miss}}$  is not due to poorly reconstructed jets<sup>b</sup>;

---

<sup>a</sup>The jet vertex fraction (JVF) [94] allows for the identification and selection of jets originating from the hard scattering through the use of tracking and vertexing information. By combining information from tracks and their primary vertices with calorimeter jets into the JVF discriminant, it is possible to measure the probability that a jet originated from a particular vertex. Jets with no associated tracks are given a JVF of  $-1$ . Jet selection based on the JVF discriminant is shown to be insensitive to the contributions from simultaneous uncorrelated soft collisions that occur during pile-up.

<sup>b</sup>Units for  $H_T$  and  $E_T^{\text{miss}}$  are GeV.

- an angular distance between the two  $b$ -tagged jets  $\Delta R(b, \bar{b}) > 1.2$ , to reduce  $b\bar{b}$  pairs originating from gluon splittings which contribute to the multi-jet background at low  $\Delta R$ . In contrast, the  $t\bar{t}$  signal is characterised by two  $b$ -jets with a large  $\Delta R$ , around  $\pi$ ;
- an angular distance between any two reconstructed jets of  $\Delta R > 0.6$ . This separation between all identified jets removes the residual inefficiency of the trigger efficiency at large jet  $p_T$ .

The lepton veto and the  $S_t$  requirements are used to reject events from  $t\bar{t}$  processes which decay in the lepton+jets channel. After this selection, 16375 data events are left. According to the MC simulation, these selection requirements give an inclusive  $t\bar{t}$  signal efficiency of 0.73%.

## 1.3. Kinematic fit analysis

### 1.3.1. Likelihood method

To optimise the top quark mass reconstruction, a kinematic fit is performed on the selected events. The kinematic fit is based on a likelihood approach to find the correct association of jets with the final state partons of the fully hadronic  $t\bar{t}$  decays. The tools used in this method are implemented in KLFFitter [95, 96] which has been used in  $t\bar{t}$  analyses in the single lepton final state. The kinematic likelihood variable used in this analysis is defined as:

$$\begin{aligned}
\mathcal{L}_{\text{kin}} = & \text{BW}(m_{q_1 q_2} | m_W, \Gamma_W) \cdot \text{BW}(m_{q_3 q_4} | m_W, \Gamma_W) \cdot \\
& \text{BW}(m_{q_1 q_2 b_1} | m_{\text{top}}^{\text{reco}}, \Gamma_{\text{top}}) \cdot \text{BW}(m_{q_3 q_4 b_2} | m_{\text{top}}^{\text{reco}}, \Gamma_{\text{top}}) \cdot \\
& W(\hat{E}_{\text{jet}_1} | E_{b_1}) \cdot W(\hat{E}_{\text{jet}_2} | E_{b_2}) \cdot W(\hat{E}_{\text{jet}_3} | E_{q_1}) \cdot W(\hat{E}_{\text{jet}_4} | E_{q_2}) \cdot \\
& W(\hat{E}_{\text{jet}_5} | E_{q_3}) \cdot W(\hat{E}_{\text{jet}_6} | E_{q_4}) \cdot \\
& \prod_{i=1}^2 \left\{ \begin{array}{l} \epsilon; b_i \text{ } b\text{-tagged} \\ (1 - \epsilon); b_i \text{ not } b\text{-tagged} \end{array} \right\} \cdot \\
& \prod_{i=1}^4 \left\{ \begin{array}{l} \frac{1}{R}; q_i \text{ } b\text{-tagged} \\ (1 - \frac{1}{R}); q_i \text{ not } b\text{-tagged} \end{array} \right\}.
\end{aligned} \tag{1.1}$$

The labels  $q_i$  with  $i = 1, \dots, 4$  represent the four light quarks and  $b_i$  with  $i = 1, 2$  the  $b$ -quarks of the assumed final state. The labels  $\text{jet}_i$  represent the calorimeter jets that are assigned to one of the final state partons. The transfer functions  $W(\hat{E}_{\text{jet}_i} | E_{q_i})$  map the measured energy of a jet  $\hat{E}_{\text{jet}_i}$  to the energy of the final state parton  $E_{q_i}$ . These transfer functions are derived from MC@NLO  $t\bar{t}$  MC



events separately for light quarks and  $b$ -quarks in bins of  $p_T$  and in four different  $|\eta|$  regions in the range  $|\eta| < 2.5$ .

The Breit-Wigner functions (BW) are used to constrain the di-jet  $m_{jj}$  and the tri-jet  $m_{jjj}$  masses to the  $W$ -boson mass and to the top quark mass, respectively. For the  $W$ -boson both the mass and the width,  $m_W$  and  $\Gamma_W$ , are fixed to the known values. The top quark mass  $m_{\text{top}}^{\text{reco}}$  is treated as an additional free parameter of the fit but is constrained to be identical for the top and anti-top quark candidates on an event-by-event basis. The width  $\Gamma_{\text{top}}$  of the top-quark Breit-Wigner distribution is adjusted accordingly.

Since an *a priori* association of jets with quarks is not possible, the fit is performed for all distinguishable permutations. For each permutation the function  $-\ln \mathcal{L}_{\text{kin}}$  is minimized with respect to the seven parameters of the fit (six jet energies and  $m_{\text{top}}^{\text{reco}}$ ). In order to take advantage of the  $b$ -tagging algorithm a multiplicative term is introduced in Eq. 1.1. This term takes into account whether the jet assigned to a model parton has been  $b$ -tagged or not, with  $\epsilon$  denoting the  $b$ -tagging efficiency and  $\frac{1}{R}$  the rejection power for the chosen  $b$ -tagging working point. This term biases the likelihood to select permutations in which a  $b$ -tagged jet is placed in the  $b$ -quark position of the likelihood. The expression in Eq. 1.1 is computed for each permutation, the sum of  $\mathcal{L}_{\text{kin}}$  for all permutation is then normalized to unity and the relative weight of the best permutation is referred to as the *event probability*. The kinematic fit procedure is applied to all events passing the preselection with a jet multiplicity of  $6 \leq N_{\text{jet}} \leq 10$ . For the measurement, the permutation with the highest event probability is selected.

### 1.3.2. Top quark mass distribution

The method is applied to signal MC events passing the selection outlined in Section 1.2.1. Using the resulting four-momenta of the input jets after the fit the mass of the top and anti-top quark candidates,  $m_t$ , is reconstructed and shown in Figure 1.1 (referred to as “Fitted”). The mass obtained from permutations that are fully matched, using the original MC simulation truth information, to the  $t\bar{t}$  system is shown on the left-hand side of Figure 1.1. The top quark mass value obtained from the kinematic fit,  $m_t$ , is overlaid with that calculated using the measured “reconstructed” jet energies to demonstrate how the kinematic fit improves the mass resolution. After the event selection only 11% of signal events are fully matched. On the right-hand side of Figure 1.1 the mass distribution obtained from permutations where at least one jet has been wrongly matched to the  $t\bar{t}$  partons is shown. The lower tail falls rapidly at 100 GeV, which represents the lower limit of the fit parameter  $m_{\text{top}}^{\text{reco}}$ .

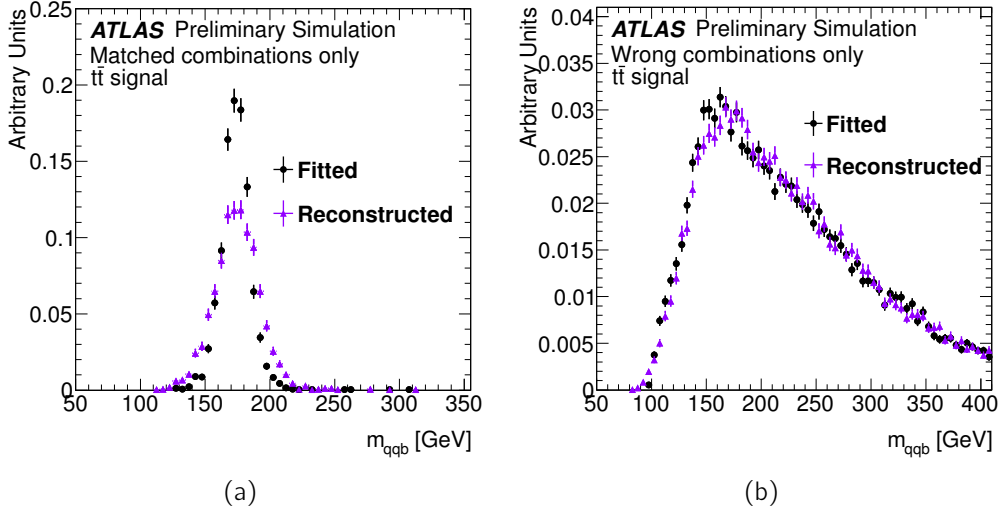


Figure 1.1.: Mass distributions obtained from the kinematic fit for simulated signal events with a top quark mass hypothesis of 172.5 GeV and passing the event selection. The distributions are normalized to unity. The distribution on the left is obtained from permutations that are fully matched to the  $t\bar{t}$  system. On the right hand side, permutations with at least one jet not correctly matched to the  $t\bar{t}$  system are shown. Filled circles (filled triangles) indicate that the fitted (reconstructed) jet energies are used to compute the mass of the top quark candidates.

### 1.3.3. Modelling of the $m_t$ distribution for the multi-jet background

The shape of the fitted top quark mass ( $m_t$ ) distribution for multi-jet events where no  $t\bar{t}$  production occurs is derived from events passing the cuts described in Section 1.2.1 without the requirement of the presence of  $b$ -tagged jets. In this sample, dominated by multi-jet events, the residual fraction of all hadronic  $t\bar{t}$  events is estimated to be 4.6%. In general, applying  $b$ -tagging impacts the shape of all kinematic variable distributions because of its strong dependence on the jet  $p_T$ . Applying  $b$ -tagging also has the effect of changing the sample flavour composition, i.e. enhancing the heavy flavor component, with a possible reshaping of the reconstructed  $m_t$  spectrum for background events, in case this reconstructed quantity shown a dependency on the kinematic properties of the different heavy flavour production mechanisms. For these reasons, the effect of applying  $b$ -tagging on the  $m_t$  shape is studied using MC events generated with ALPGEN [93], for both generic multi-jet production and exclusive  $b\bar{b}$ +jets events, generated using matrix elements with massive  $b$ -quarks. The procedure used to estimate the uncertainty on the background shape is discussed in Section 1.5.

## 1.4. Cross section measurement

The event yield and the background normalization are determined from an unbinned likelihood fit to the top quark mass distribution obtained from the kinematic fit. In addition to the event selection outlined in Section 1.2.1, events are required to have  $M_t > 125$  GeV with jet multiplicity  $6 \leq N_{\text{jet}} \leq 10$ . To further improve the signal to background ratio, cuts are introduced requiring the event probability to be greater than 0.8 and the minimal mass  $\chi^2$  to satisfy  $\chi^2 < 30$ . The  $\chi^2$  is defined as:

$$\chi^2 = \frac{(m_{j_1, j_2} - m_W)^2}{\sigma_W^2} + \frac{(m_{j_1, j_2, b_1} - m_t)^2}{\sigma_t^2} + \frac{(m_{j_3, j_4} - m_W)^2}{\sigma_W^2} + \frac{(m_{j_3, j_4, b_2} - m_t)^2}{\sigma_t^2}, \quad (1.2)$$

where the labels  $j_i$  with  $i=1, \dots, 4$  and  $b_1, b_2$  represent the reconstructed jets and  $b$ -tagged jets assigned to the two  $W$  bosons. The masses  $m_W$  and  $m_t$  as well as the widths  $\sigma_W$  and  $\sigma_t$  are given by the mean and the half-width Gauss parametrisation of the top-quark and  $W$  boson mass distributions derived from the  $t\bar{t}$  all-hadronic process MC simulation. To measure these quantities, only reconstructed jets matched to the original partons from the top-quark and  $W$  decay products are used. Since the width of the reconstructed  $W$  boson and top-quark masses are dominated by resolution effects, these were fitted iteratively assuming a Gaussian distribution. The minimum mass  $\chi^2$  is defined as the minimum  $\chi^2$  value obtained after computing the  $\chi^2$  for every permutation per event. With this final event selection, the fraction of correct permutations selected in signal  $t\bar{t}$  MC events rises to 36%.

The unbinned likelihood fit of the  $m_t$  distribution is performed on the final data sample, which contains 2118 events and is shown on the left-hand side of Figure 2.2. The signal parton distribution function (PDF) is derived from MC simulation and includes both  $t\bar{t}$  combinatorial background and correct combinations, whereas the background PDF is derived from data events in the same signal region, but without the  $b$ -tagging requirement, as described in Section 1.3.3. As a result the fit gives for the  $t\bar{t}$  signal fraction a value of  $31.4 \pm 2.3\%$ . Considering that after all requirements applied, the inclusive  $t\bar{t}$  selection efficiency derived from MC simulation is  $(0.086 \pm 0.003)\%$ , the measured value for the total  $t\bar{t}$  cross section is thus:

$$\sigma(pp \rightarrow t\bar{t}) = 168 \pm 12 \text{ (stat.) } {}^{+60}_{-57} \text{ (syst.) } \pm 7 \text{ (lum.) pb}$$

## 1.5. Systematic uncertainties

The background modelling is estimated by a data-driven method, so most of the systematic uncertainties are related to the signal modelling only. The only

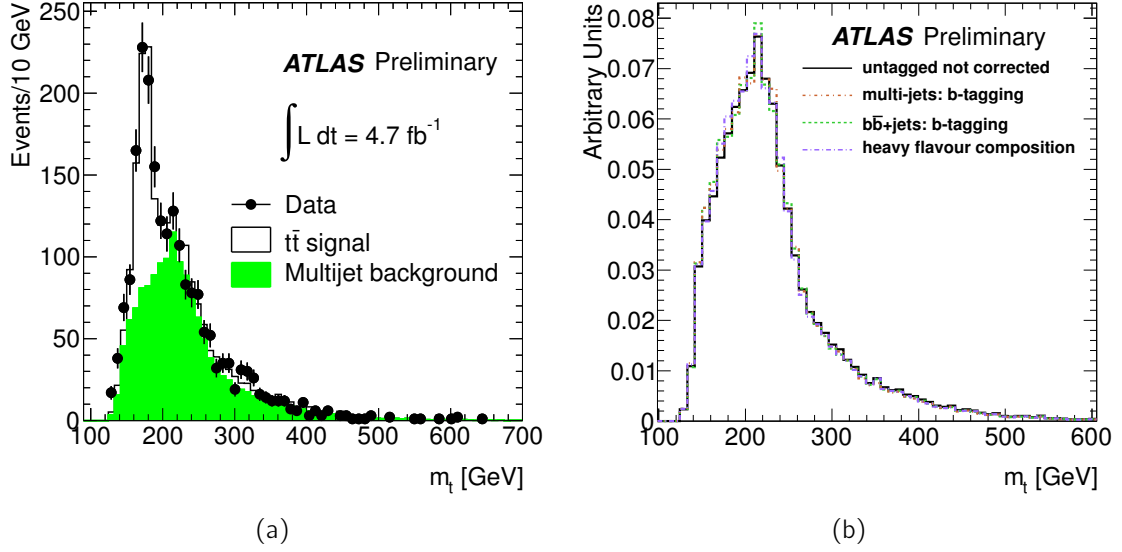


Figure 1.2.: Left hand side: Fit of the  $m_t$  distribution with an unbinned likelihood to the selected data sample (dots). The error bars associated to the data are statistical only. The two signal and background  $m_t$  templates are indicated as well. Right hand side:  $m_t$  distribution obtained after the kinematic fit to the untagged data sample (full line). The distributions after applying different corrections derived from Monte Carlo, as explained in Section 1.5, are overlaid (dashed and dotted lines).

systematic uncertainty assigned to the background is the background shape modelling. The systematic uncertainties associated with the signal  $t\bar{t}$  MC sample are divided into shape and acceptance effects. The systematic sources considered are described below together with an indication of whether they affect the shape or acceptance, or both:

- Jet energy scale (JES) and associated uncertainty [94] [shape and acceptance]:

The jet energy scale and its uncertainty have been derived by combining information from test-beam data, LHC collision data and MC simulation. Since the energy correction procedure involves a number of steps, the JES uncertainty has various components originating from the calibration method, the calorimeter response, the detector MC simulation, and the specific choice of parameters in the physics model employed in the MC event generator. The JES uncertainty varies between 2.5% and 8% in the central region, depending on the jet  $p_T$  and  $\eta$ . These values include uncertainties in the flavour composition of the sample and mis-measurements due to additional jets close by. Pileup gives an additional uncertainty of up to 2.5%

(5%) in the central (forward) region. The  $b$  JES uncertainty is uncorrelated with the JES uncertainty and accounts for the remaining differences between jets originating from light quarks and those from  $b$ -quarks after the global JES calibration factor has been determined. For this, an extra uncertainty ranging from 0.8% to 2.5% and depending on jet  $p_T$  and  $\eta$  is assigned to jets arising from the fragmentation of  $b$ -quarks;

- $b$ -tagging efficiency and mistag rate [shape and acceptance]:  
To take into account differences in the  $b$ -tagging efficiency between data and MC simulations, a set of scale factors derived from  $b$ -tagging calibration studies are applied to  $b$ -,  $c$ - and light-jets as a function of  $p_T$  and  $\eta$  [97]. These scale factors are varied individually within their maximal associated uncertainty and propagated through the analysis;
- Initial and Final State Radiation (ISR and FSR) [shape and acceptance]:  
The effects of variations in the amount of initial and final state QCD radiation (ISR/FSR) is studied using the ACERMC [98] generator interfaced to PYTHIA by varying the parameters controlling ISR and FSR in a range consistent with experimental data [99]. The systematic uncertainty is taken as half the maximum difference between the two samples, ISR and FSR;
- Generator and parton shower (PS) dependence [shape and acceptance]:  
The uncertainty due to the modelling of the  $t\bar{t}$  signal is quantified by replacing the MC@NLO Monte Carlo generator with POWHEG [100] for which the hadronisation is performed with either the PYTHIA [101] or HERWIG program and the difference of the two results is quoted as the systematic uncertainty;
- Trigger efficiency [acceptance only]:  
Events were selected with the five-jet trigger and by additionally requiring the fifth-jet  $p_T > 55$  GeV. The associated efficiency ranges from 90% to 100% [87], so a conservative 10% systematic uncertainty is assigned;
- Parton Distribution Function (PDF) [shape only]:  
The signal samples are generated using the CT10 [90] proton parton distribution functions (PDFs). These PDFs, obtained from experimental data, have an uncertainty that is reflected in pairs of additional PDF sets provided by the CTEQ group. To evaluate the impact of the PDF uncertainties on the signal templates, the events are reweighted with the corresponding ratios of PDFs, and 22 pairs of additional signal templates are constructed. The uncertainty is calculated as half the quadratic sum of the differences of the 22 pairs from the central result. Two other PDF sets, MSTW2008nlo68cl [77] and NNPDF20 [102] are considered as well. Half of the difference between the maximum variation up and down of the derived cross section is taken as the final systematic uncertainty;

- Background modelling [shape only]:  
As described in Section 1.3, the background modelling for  $m_t$  is taken from the shape of the untagged data sample. To estimate the associated uncertainty, the  $m_t$  distributions obtained from inclusive multi-jet and exclusive  $b\bar{b}$  + jets ALPGEN MC samples were produced with and without the  $b$ -tag requirement. The ratio between the tagged and un-tagged  $m_t$  distributions for each sample as well as the ratio between the distribution of the multi-jet and  $b\bar{b}$  + jets samples, are computed and applied to the un-tagged data sample. The effect of these corrections on the data-driven background is shown on the right-hand side of Figure 2.2. The maximum variation between the nominal cross section and the corrected one gives the systematic uncertainty on the background modelling of 4%;
- Luminosity [acceptance]:  
The uncertainty on the luminosity propagates directly to the cross section measurement, leading to a systematic uncertainty of 3.9% [103, 86];
- Jet energy resolution (JER) [104] [shape and acceptance]:  
To assess the impact of the JER uncertainty, the energy of each reconstructed jet in the MC simulation is additionally smeared by a Gaussian function before performing the event selection. The width of the resulting Gaussian distribution corresponds to that including the uncertainty on the jet energy resolution;
- Jet reconstruction efficiency (JRE) [shape and acceptance]:  
The difference between the jet reconstruction efficiency determined from MC simulation and data is propagated as a systematic uncertainty. The jet reconstruction efficiency for data and the MC simulation are found to be in agreement to better than 2% [94]. To evaluate this, 2% of jets are randomly removed from the MC events.

The systematic uncertainties are summarized in Table 1.1.

Source of uncertainty	Contribution (%)
Jet energy scale (JES)	+20/−11
<i>b</i> -tagging	± 17
ISR, FSR	± 17
Parton shower and Hadronisation	± 13
Multi-jet trigger	± 10
Generator	± 7
PDF	+7/−4
Pile-up	+5/−7
Background model	± 4
Luminosity	± 4
Jet energy resolution	± 3
Jet reconstruction efficiency	< 1
Total	+36/−34

Table 1.1.: Summary of the different systematic uncertainties associated with the kinematic fit analysis using the selected data events,  $t\bar{t}$  MC simulated signal and data-driven background estimated events. Uncertainties are given in %. The asymmetric uncertainties are derived using [105].

## 2. Search for the Standard Model Higgs boson decaying into $b\bar{b}$ produced in association with top quarks decaying hadronically in $pp$ collisions at $\sqrt{s}=8$ TeV with the ATLAS detector

The analysis presented in this chapter has been the subject of the PhD thesis of Daniele Madaffari, co-directed by Mossadek Talby and myself. This work was initiated by Claudia Bertella, who, at the end of her PhD, moved from the fully hadronic  $t\bar{t}$  cross section measurement at  $\sqrt{s} = 7$  TeV to the fully hadronic  $t\bar{t}H$  searches with the same dataset. At the beginning the CPPM team also included Nancy Tannoury, newly graduate ATLAS-CPPM student, at the time holding a one year mixed teaching and research position obtained after the end of her thesis. Nancy left CPPM to join the Bonn University ATLAS group where she continued to contribute to the analysis. At about the time when we start analyzing the 2012  $p - p$  collisions at  $\sqrt{s} = 8$  TeV, Elemer Nagy, also from CPPM, joined the team; since then Elemer has been continuously working on the analysis, he is now actively involved in the Run 2 activities. It is worth mentioning that by the end of Run 1, a consistent group of physicists from different institutes (Glasgow, Barcelona, Bonn, Freiburg) had joined the fully hadronic  $t\bar{t}H$  group, which finally became part of the ATLAS management structure as one of the Higgs working group activities. Diane Cinca, postdoc with the University of Glasgow and myself co-lead the Run 1 publication.

### 2.1. Introduction

After the discovery of a new boson with a mass of around 125 GeV in July 2012 by the ATLAS [28] and CMS [29] collaborations, the focus has now shifted to confirming whether this particle is the Standard Model (SM) Higgs boson [10, 11, 12, 13] or another boson. While any deviation from SM predictions would indicate the presence of new physics, all measurements of the properties of this new boson thus far performed at the Large Hadron Collider (LHC), including spin, parity, total width, and coupling to SM particles, are consistent with the SM prediction [106, 107, 108, 109, 110, 111].



Because of its large mass, the top quark is the fermion with the largest Yukawa coupling ( $y_t$ ) to the Higgs field in the SM, with a value close to unity. The coupling  $y_t$  is experimentally accessible by measuring the gluon fusion (ggF) production process or the  $H \rightarrow \gamma\gamma$  decay, where a sizeable contribution derives from a top-quark loop. This case requires the assumption that no new physics contributes with additional induced loops in order to measure  $y_t$ . Currently, the only process where  $y_t$  can be accessed directly is the production of a top-quark pair in association with a Higgs boson ( $t\bar{t}H$ ).

The results of searches for the Higgs boson are usually expressed in terms of the signal-strength parameter  $\mu$ , which is defined as the ratio of the observed to the expected number of signal events. The latter is calculated using the SM cross section times branching ratio [112]. The combined  $t\bar{t}H$  signal strength measured by the CMS Collaboration [113] in Run 1, obtained by merging searches in several final states, is  $\mu = 2.8 \pm 1.0$ . Before the analysis described in this chapter, the ATLAS Collaboration has been searching for a  $t\bar{t}H$  signal in events enriched in Higgs boson decays to two massive vector bosons or  $\tau$  leptons in the multilepton channel [114], finding  $\mu = 2.1^{+1.4}_{-1.2}$ , for  $t\bar{t}H(H \rightarrow b\bar{b})$  [115] in final states with at least one lepton obtaining  $\mu = 1.5 \pm 1.1$ , and for  $t\bar{t}H(H \rightarrow \gamma\gamma)$  [116] measuring  $\mu = 1.3^{+2.6}_{-1.7}$ .

Among all  $t\bar{t}H$  final states, the one where both  $W$  bosons from  $t \rightarrow Wb$  decay hadronically and the Higgs boson decays into a  $b\bar{b}$  pair has the largest branching ratio, but also the least signal purity. This paper describes a search for this all-hadronic  $t\bar{t}H(H \rightarrow b\bar{b})$  decay mode. The analysis uses proton–proton collision data corresponding to an integrated luminosity of  $20.3 \text{ fb}^{-1}$  at center-of-mass energy  $\sqrt{s} = 8 \text{ TeV}$  recorded with the ATLAS detector at the LHC.

At Born level, the signal signature is eight jets, four of which are  $b$ -quark jets. The dominant background is the non-resonant production of multijet events. For this analysis, a data-driven method is applied to estimate the multijet background by extrapolating its contribution from a control region with the same jet multiplicity, but a lower multiplicity of jets containing  $b$ -hadrons than the signal process. The parameters used for the extrapolation are measured from a control region and checked using Monte Carlo (MC) simulations. Other subdominant background processes are estimated using MC simulations. To maximise the signal sensitivity, the events are categorised according to their number of jets and jets identified as containing  $b$ -hadrons ( $b$ -tagged). A boosted decision tree (BDT) algorithm, based on event shape and kinematic variables, is used to discriminate the signal from the background. The extraction of  $\mu$  is performed through a fit to the BDT discriminant distribution. After the fit the dominant uncertainty is the  $t\bar{t} + b\bar{b}$  production cross section. The sensitivity is also limited by systematic uncertainties from the data-driven method used for the modelling of the large non-resonant multijet production.

## 2.2. Event selection

This search for  $t\bar{t}H(H \rightarrow b\bar{b})$  is based on data collected in 2012 using a multijet trigger<sup>a</sup>, which requires at least five jets passing the EF stage, each having  $p_T > 55$  GeV and  $|\eta| < 2.5$ . Events are discarded if any jet with  $p_T > 20$  GeV is identified as out-of-time activity from a previous  $pp$  collision or as calorimeter noise [117].

The five leading jets in  $p_T$  are required to have  $p_T > 55$  GeV with  $|\eta| < 2.5$  and all other jets are required to have  $p_T > 25$  GeV and  $|\eta| < 2.5$ . Events are required to have at least six jets, of which at least two must be  $b$ -tagged. Events with well-identified isolated muons or electrons with  $p_T > 25$  GeV are discarded in order to avoid overlap with other  $t\bar{t}H$  analyses.

To enhance the sensitivity, the selected events are categorised into various distinct regions, according to their jet and  $b$ -tag multiplicities: the region with  $m$  jets, of which  $n$  are  $b$ -jets, is referred to as “( $m_j, n_b$ )”.

## 2.3. Signal and background modelling

### 2.3.1. Signal model

The  $t\bar{t}H$  signal process is modelled using matrix elements calculations obtained from the HELAC-Oneloop package [118]<sup>b</sup> with next-to-leading order (NLO) accuracy in  $\alpha_s$ . POWHEG-BOX [119, 120, 121] serves as an interface to the MC programs used to simulate the parton shower and hadronisation. The samples created using this approach are referred to as POWHEL samples [122]. They include all SM Higgs boson and top-quark decays and use the CT10NLO [123] parton distribution function (PDF) sets with the factorisation ( $\mu_F$ ) and renormalisation ( $\mu_R$ ) scales set to  $\mu_F = \mu_R = m_t + m_H/2$ . The POWHEL  $t\bar{t}H$  samples use PYTHIA 8.1 [124] to simulate the parton shower with the CTEQ6L1 [125] PDF and the AU2 underlying-event set of generator parameters (tune) [126], while HERWIG [127] is used to estimate systematic uncertainties due to the fragmentation modelling.

For these  $t\bar{t}H$  samples the cross-section normalisations and the Higgs boson decay branching fractions are taken from the NLO QCD and from the NLO QCD + EW theoretical calculations [112] respectively. The masses of the Higgs boson and the top quark are set to 125 GeV and to 172.5 GeV respectively.

---

<sup>a</sup>A description of the ATLAS detector is given at the end of this document in Appendix A.

<sup>b</sup>The MC and the PDFs used represent the status of the art choices used by the whole collaborations at the time the analysis was developed.

### 2.3.2. Simulated backgrounds

The dominant background to the all-hadronic  $t\bar{t}H$  signal is multijet production, followed by  $t\bar{t} + \text{jets}$  production. Small background contributions come from the production of a single top quark and from the associated production of a vector boson and a  $t\bar{t}$  pair,  $t\bar{t}V$  ( $V = W, Z$ ). The multijet background is determined from data using a dedicated method described in Section 2.3.4. The other background contributions are estimated using MC simulations.

The multijet events, which are used for jet trigger studies and for the validation of the data-driven multijet background estimation, are simulated with PYTHIA 8.1 using the NNPDF2.3 LO [128] PDFs.

The main  $t\bar{t}$  sample is generated using the POWHEG NLO generator with the CT10NLO PDF set, assuming a value of the top-quark mass of 172.5 GeV. It is interfaced to PYTHIA 6.425 [129] with the CTEQ6L1 PDF set and the Perugia2011C [130] underlying-event tune; this combination of generator and showering programs is hereafter referred to as POWHEG+PYTHIA. The sample is normalised to the top++2.0 theoretical calculation performed at next-to-next-to leading order (NNLO) in QCD and includes resummation of next-to-next-to leading logarithmic (NNLL) soft gluon terms [131, 132, 133, 134, 135, 136]. A second  $t\bar{t}$  sample is generated using fully matched NLO predictions with massive  $b$ -quarks [137] within the SHERPA with OPENLOOPS framework [138, 139] henceforth referred to as SHERPA+OPENLOOPS. The SHERPA+OPENLOOPS NLO sample is generated following the four-flavour scheme using the SHERPA2.0 pre-release and the CT10NLO PDF set. The renormalisation scale is set to  $\mu_R = \prod_{i=t,\bar{t},b,\bar{b}} E_{T,i}^{1/4}$ , where  $E_{T,i}$  is the transverse energy of parton  $i$ , and the factorisation and resummation scales are both set to  $(E_{T,t} + E_{T,\bar{t}})/2$ .

The prediction from SHERPA+OPENLOOPS is expected to model the  $t\bar{t} + b\bar{b}$  contribution more accurately than POWHEG+PYTHIA, since the latter MC produces  $t\bar{t} + b\bar{b}$  exclusively via the parton shower. The SHERPA+OPENLOOPS sample is not passed through full detector simulation. Thus,  $t\bar{t} + \text{jets}$  events from POWHEG+PYTHIA are categorised into three non-overlapping samples,  $t\bar{t} + b\bar{b}$ ,  $t\bar{t} + c\bar{c}$ , and  $t\bar{t} + \text{light-jets}$ , hereafter called  $t\bar{t} + \text{light}$ , using a labelling based on an algorithm that matches hadrons to particle jets. Then,  $t\bar{t} + b\bar{b}$  events from POWHEG+PYTHIA are reweighted to reproduce the SHERPA+OPENLOOPS NLO  $t\bar{t} + b\bar{b}$  prediction. The reweighting is done at generator level using a finer categorisation to distinguish events where one particle jet is matched to two  $b$ -hadrons, or where only one  $b$ -hadron is matched. The reweighting is applied using several kinematic variables such as the top-quark  $p_T$ , the  $t\bar{t}$  system  $p_T$ , and, where this can be defined,  $\Delta R$  and  $p_T$  of the dijet system not originating from the top-quark decay [115].

Unlike  $t\bar{t} + b\bar{b}$ , no fully matched NLO predictions exist for  $t\bar{t} + c\bar{c}$  and  $t\bar{t} + \text{light}$  events. A dedicated reweighting is therefore applied to the top-quark  $p_T$  spectra as well as to the  $p_T$  spectra of the  $t\bar{t}$  system of  $t\bar{t} + \text{light}$  and  $t\bar{t} + c\bar{c}$  events in

POWHEG+PYTHIA, based on the ratio of data to simulation of the measured differential cross sections at  $\sqrt{s} = 7$  TeV [140]. No such reweighting is applied to the  $t\bar{t} + b\bar{b}$  sample, which is already corrected to match the best available theory calculation.

Samples of single-top-quark events produced in the  $s$ - and  $Wt$ -channels are generated with POWHEG-BOX 2.0 using the CT10NLO PDF set. The samples are interfaced to PYTHIA 6.425 with the CTEQ6L1 set of parton distribution functions and Perugia2011C underlying-event tune. The  $t$ -channel production mode is generated with ACERMC [141] interfaced to PYTHIA 6.425 with the CTEQ6L1 PDF set and the Perugia2011C underlying-event tune. Overlaps between the  $t\bar{t}$  and  $Wt$  final states are removed [142]. The single-top-quark samples are normalised to the approximate NNLO theoretical cross sections [143, 144] using the MSTW2008 NNLO PDF set [145, 146].

The samples of  $t\bar{t}V$  ( $V = W, Z$ ) events are generated with the MADGRAPH v5 LO generator [147] and the CTEQ6L1 PDF set. PYTHIA 6.425 with the AUET2B tune is used to generate the parton shower. The  $t\bar{t}V$  samples are normalised to NLO cross-sections [148, 149].

Finally, event samples for single top quark plus Higgs boson production,  $tHqb$  and  $tHW$ , are generated. Their cross sections are computed using the generator MG5\_aMC@NLO [150] at NLO in QCD. For  $tHqb$ , samples are generated with MADGRAPH in the four-flavour scheme and  $\mu_F = \mu_R = 75$  GeV then showered with PYTHIA 8.1 with the CTEQ6L1 PDF and the AU2 underlying-event tune. For  $tHW$ , computed with the five-flavour scheme, dynamic  $\mu_F$  and  $\mu_R$  scales are used and events are generated at NLO with MG5\_aMC@NLO+HERWIG++ [151, 152]. These two processes together are referred to as  $tH$ .

A summary of the cross-section values and their uncertainties for the signal as well as for the MC simulated background processes is given in Table 2.1.

### 2.3.3. Common treatment of MC samples

All samples using HERWIG are also interfaced to JIMMY v4.31 [153] to simulate the underlying event. With the exception of SHERPA, all MC samples use PHOTOS 2.15 [154] to simulate photon radiation and TAUOLA 1.20 [155] to simulate  $\tau$  decays. The samples are then processed through a simulation [156] of the detector geometry and response using GEANT4 [157]. The single-top-quark sample produced in the  $t$ -channel is simulated with a parameterised calorimeter response [158].

All simulated events are processed through the same reconstruction software as the data. Simulated events are corrected so that the lepton and jet identification efficiencies, energy scales and energy resolutions match those in data.

When selecting based on the output value of the  $b$ -tagging algorithm, the number of selected simulated events is significantly reduced, leading to large statistical fluctuations in the resulting distributions for samples with a high  $b$ -tag mul-

Table 2.1.: Production cross sections for signal  $t\bar{t}H$ , at  $m_H = 125$  GeV, and various simulated background processes. The quoted errors arise from variations of the renormalisation and factorisation scales and uncertainties in the parton distribution functions.

Process	$\sigma$ [pb]
$t\bar{t}H$	$0.129^{+0.012}_{-0.016}$
$t\bar{t}$	$253^{+13}_{-15}$
Single top $Wt$ -channel	$22.4 \pm 1.5$
Single top $t$ -channel	$87.7^{+3.4}_{-1.9}$
Single top $s$ -channel	$5.61 \pm 0.22$
$t\bar{t} + W$	$0.232 \pm 0.070$
$t\bar{t} + Z$	$0.205 \pm 0.061$
$tHqb$	$0.0172^{+0.0012}_{-0.0011}$
$WtH$	$0.0047^{+0.0010}_{-0.0009}$

tiplicity. Therefore, rather than tagging the jets individually, the normalisation and the shape of these distributions are predicted by calculating the probability that a jet with a given flavour,  $p_T$ , and  $\eta$  is  $b$ -tagged [159]. The method is validated by verifying that the predictions reproduce the normalisation and shape obtained for a given working point of the  $b$ -tagging algorithm. The method is applied to all simulated signal and background samples.

#### 2.3.4. Multijet background estimation using data: the TRF<sub>MJ</sub> method

A data-driven technique, the tag rate function for multijet events (TRF<sub>MJ</sub>) method, is used to estimate the multijet background. After measuring  $\varepsilon_{MJ}$ , the probability of  $b$ -tagging a third jet in a sample of events with at least two  $b$ -tagged jets, the TRF<sub>MJ</sub> method uses  $\varepsilon_{MJ}$  to extrapolate the multijet background from the regions with lower  $b$ -tag multiplicity to the search regions with higher  $b$ -tag multiplicity but otherwise identical event selection.

In the first step, the  $b$ -tagging rate is measured in data samples selected with various single-jet triggers, which are enriched in multijet events and have limited ( $\approx 10\%$ ) overlap with the search region. The events in this TRF<sub>MJ</sub> extraction region are required to have at least three jets with  $p_T > 25$  GeV and  $|\eta| < 2.5$ , with at least two  $b$ -tagged jets. Excluding the two jets with the highest  $b$ -tagging weight in the event,  $\varepsilon_{MJ}$  is defined as the rate of  $b$ -tagging any other jet in the

event. It is parameterised as a function of the jet  $p_T$  and  $\eta$ , and also of the average  $\Delta R$  between this jet and the two jets in the event with highest  $b$ -tagging weight,  $\langle \Delta R_{(j,hMV1)} \rangle$ . The  $p_T$  and  $\eta$  dependence of  $\varepsilon_{MJ}$  reflects the corresponding sensitivity of the  $b$ -tagging efficiency to these variables. In multijet events, the  $\Delta R$  dependence of  $\varepsilon_{MJ}$  is correlated with the multi- $b$ -jet production mechanism. This affects  $\varepsilon_{MJ}$ , shown in Figure 2.1, which decreases by up to a factor two as  $\Delta R$  increases for fixed  $p_T$  and  $\eta$ .

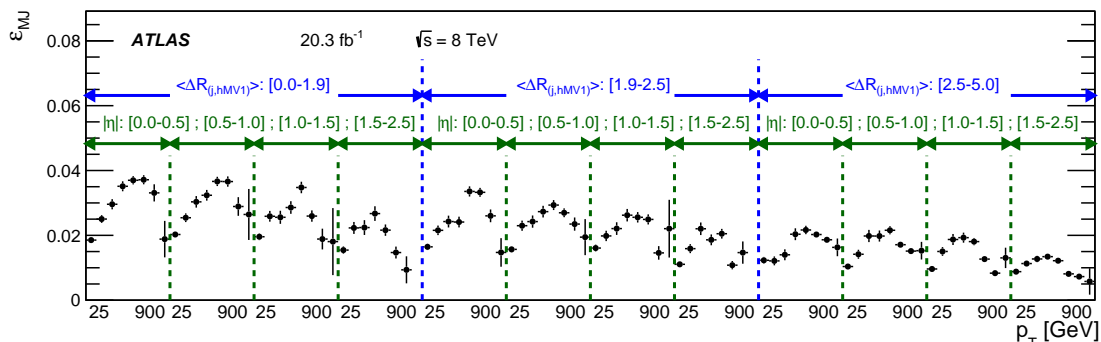


Figure 2.1.: Dependence of  $\varepsilon_{MJ}$  on the jet transverse momentum  $p_T$ , in regions of jet pseudorapidity  $\eta$  and average  $\Delta R$  between this jet and the two jets in the event with highest  $b$ -tagging weight,  $\langle \Delta R_{(j,hMV1)} \rangle$ . The  $p_T$  bin boundaries are 25 (lowest), 40, 55, 70, 100, 200, 400, 600, 900 GeV (highest), chosen such as to have uniform number of events across bins of  $\langle \Delta R_{(j,hMV1)} \rangle$ .

In the search region the  $\text{TRF}_{MJ}$  method starts from the data sample with exactly two  $b$ -tagged jets subtracting the contributions from all other backgrounds obtained from MC simulation. Multijet background samples containing  $m$  jets ( $m \geq 6$ ), out of which  $n$  are  $b$ -tagged ( $n \geq 3$ ) are then constructed, using an event weight  $w(mj, nb)$ , which is calculated from  $\varepsilon_{MJ}$  analogously to the method described in Ref. [159], accounting for the fact that the starting sample contains two  $b$ -tagged jets. In each multijet event emulated using  $\text{TRF}_{MJ}$  by means of  $\varepsilon_{MJ}$ ,  $(m - 2)$  jets not originally  $b$ -tagged can be used for the emulation of the properties of additional  $b$ -tagged jets. This procedure allows to emulate observables that depend on the number of  $b$ -tagged jets.

### 2.3.5. Validation of the $\text{TRF}_{MJ}$ method in data and simulation

Validation of the  $\text{TRF}_{MJ}$  method is performed by a ‘closure test’, separately in data and simulation. This is performed using the same data samples that were employed to estimate  $\varepsilon_{MJ}$ . In these low jet multiplicity samples, the  $\text{TRF}_{MJ}$  method, which is applied to the events with exactly two  $b$ -tagged jets, is used to predict distributions in events with at least three  $b$ -tagged jets. Using  $\varepsilon_{MJ}$  derived inde-

pendently in data and simulation, the predicted distributions are compared to those resulting when directly applying  $b$ -tagging. This is done for a number of variables, such as  $b$ -tagged jet  $p_T$ , angular distance between  $b$ -tagged jets, and event shapes. As an example, for events with at least three jets and at least three  $b$ -tagged jets ( $\geq 3j, \geq 3b$ ), Figures 2.2 and 2.4 show the closure test in data and simulated multijet events for the third-leading-jet  $p_T$ ,  $H_T$  (the scalar sum of the  $p_T$  of all jets), and  $\text{Centrality}_{\text{Mass}}$  (defined as  $H_T$  divided by the invariant mass of the jets). Figures 2.3 and 2.5 show the results of the closure test in data and simulated multijet events for distributions of the leading-jet  $p_T$ , the minimum mass of all jet pairs in the event ( $m_{jj}^{\text{min}}$ ), and the third-leading  $b$ -tagged jet  $p_T$ . The definitions of these variables can be found in Table 2.3. In both data and simulated multijet events with at least three  $b$ -tagged jets, the predicted and observed number of events agree within 5%. In events with a higher  $b$ -tagged jet multiplicity the numbers agree within the large statistical uncertainty. For this reason the systematic uncertainties related to the  $\text{TRF}_{\text{MJ}}$  method are not estimated in the validation regions.

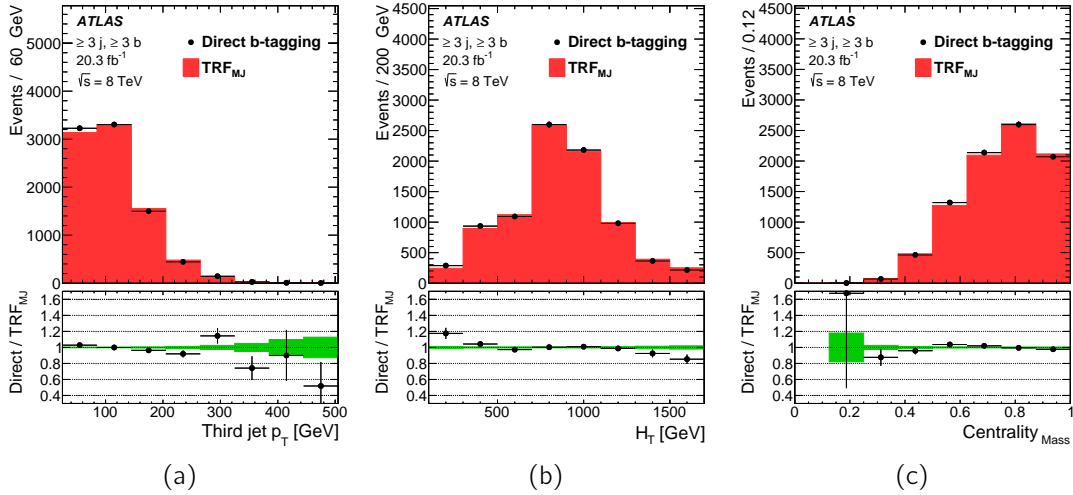


Figure 2.2.: Comparison of the shapes predicted by the  $\text{TRF}_{\text{MJ}}$  method (red histograms) and direct  $b$ -tagging (black circles) in data events with at least three jets and at least three  $b$ -tagged jets for (a) the third-leading  $b$ -tagged jet  $p_T$ , (b)  $H_T$ , and (c)  $\text{Centrality}_{\text{Mass}}$ . The definitions of the variables are listed in Table 2.3. Events were selected with various single-jet triggers. The  $\text{TRF}_{\text{MJ}}$  prediction is normalised to the same number of events as the data. The uncertainty band for the  $\text{TRF}_{\text{MJ}}$  predictions shown in the ratio plot represents statistical uncertainties only.



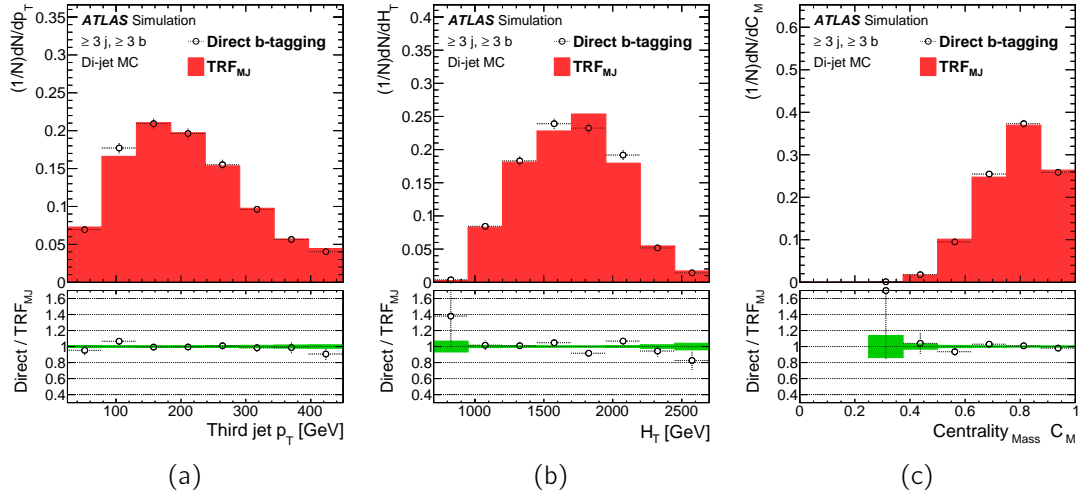


Figure 2.3.: Comparison of the shapes predicted for the  $\text{TRF}_{\text{MJ}}$  method (red histograms) and direct  $b$ -tagging (black circles) in PYTHIA 8.1 multijet events with at least three jets and at least three  $b$ -tagged jets for (a) leading-jet  $p_T$ , (b)  $m_{jj}^{\min}$  and (c) the third-leading  $b$ -tagged jet  $p_T$  in the event. The  $\text{TRF}_{\text{MJ}}$  prediction is normalised to the same number of events as the data. The uncertainty band for the  $\text{TRF}_{\text{MJ}}$  predictions shown in the ratio plot represents statistical uncertainties only.

## 2.4. Multijet trigger efficiency

Not all jets are reconstructed at the trigger level, mainly due to the Level-1 sliding window algorithm and the Level-1 resolution [160]. The multijet trigger efficiency with respect to the offline selection is derived in terms of the efficiency for a single jet to be associated with a complete jet trigger chain, i.e., a complete sequence of jets reconstructed at Level-1, Level-2 and EF satisfying the requirements described in Section 2.2. This single-jet trigger efficiency,  $\epsilon_{\text{trig}}$ , is evaluated in intervals of offline reconstructed  $p_T$  and  $\eta$ :

$$\epsilon_{\text{trig}}(p_T, \eta) = \frac{N_{\text{trig}}(p_T, \eta)}{N(p_T, \eta)}, \quad (2.1)$$

where  $N_{\text{trig}}(p_T, \eta)$  is the number of jets matched with a trigger chain and  $N(p_T, \eta)$  is the total number of jets within a given offline reconstructed  $p_T$  and  $\eta$  interval. Figure 2.6 shows that for large jet  $p_T$ ,  $\epsilon_{\text{trig}}$  reaches a plateau close to unity.

For both data and simulation,  $\epsilon_{\text{trig}}(p_T, \eta)$  is derived using events triggered by a single-jet trigger with a  $p_T$  threshold of 110 GeV, and only the offline jets which are in the hemisphere opposite to the trigger jet are used. To avoid additional trigger bias, events are discarded if more than one jet with  $p_T \geq 110$  GeV is



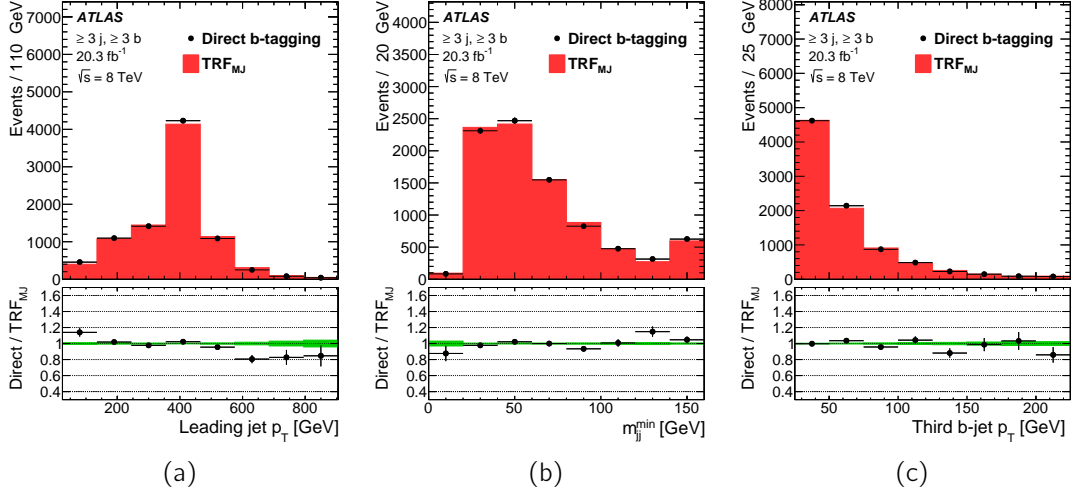


Figure 2.4.: Comparison of the shapes predicted by the TRF<sub>MJ</sub> method (red histograms) and direct  $b$ -tagging (black circles) in data events with at least three jets and at least three  $b$ -tagged jets for (a) the third-leading  $b$ -tagged jet  $p_T$ , (b)  $H_T$ , and (c) Centrality<sub>Mass</sub>. The definitions of the variables are listed in Table 2.3. Distributions are normalised to the same area. The uncertainty band for the TRF<sub>MJ</sub> predictions shown in the ratio plot represents statistical uncertainties only.

reconstructed. The ratio of  $\epsilon_{\text{trig}}^{\text{data}}(p_T, \eta)$  to  $\epsilon_{\text{trig}}^{\text{MC,dijet}}$ , where the latter is estimated in simulated dijet events, is referred to as  $\text{SF}_{\text{trig}}(p_T, \eta)$ . In the analysis, for each MC sample  $\alpha$  considered, the final number of events passing the multijet trigger is estimated by weighting each jet by the product of  $\epsilon_{\text{trig}}^{\text{MC},\alpha}(p_T, \eta)$  and  $\text{SF}_{\text{trig}}(p_T, \eta)$ . The parameters  $\epsilon_{\text{trig}}(p_T, \eta)$  and  $\text{SF}_{\text{trig}}(p_T, \eta)$  are estimated for jet  $p_T$  up to 100 GeV. Figure 2.6 shows the  $p_T$  dependence of  $\epsilon_{\text{trig}}^{\text{data}}(p_T, \eta)$ ,  $\epsilon_{\text{trig}}^{\text{MC},t\bar{t}H}(p_T, \eta)$ ,  $\epsilon_{\text{trig}}^{\text{MC,dijet}}(p_T, \eta)$  and  $\text{SF}_{\text{trig}}(p_T, \eta)$  for jets within  $|\eta| < 2.5$ , together with the uncertainties from the difference between  $\epsilon_{\text{trig}}^{\text{MC},t\bar{t}H}(p_T, \eta)$  and  $\epsilon_{\text{trig}}^{\text{MC,dijet}}(p_T, \eta)$ , which is taken as the systematic uncertainty of the method.

## 2.5. Event classification

Six independent analysis regions are considered for the fit used in the analysis: two control regions (6j, 3b), (6j,  $\geq 4b$ ) and four signal regions (7j, 3b), (7j,  $\geq 4b$ ), ( $\geq 8j$ , 3b) and ( $\geq 8j$ ,  $\geq 4b$ ). In addition, the three regions with exactly two  $b$ -tagged jets, (6j, 2b), (7j, 2b) and ( $\geq 8j$ , 2b), are used to predict the multijet contribution to higher  $b$ -tagging multiplicity regions, using the TRF<sub>MJ</sub> method, as described above. The event yields in the different analysis regions prior to the

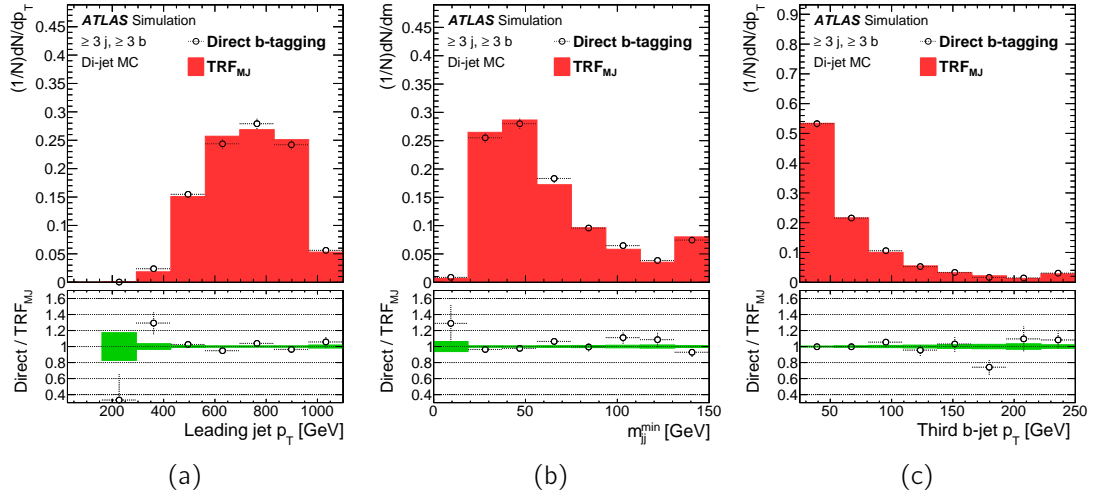


Figure 2.5.: Comparison of the shapes predicted for the  $\text{TRF}_{\text{MJ}}$  method (red histograms) and direct  $b$ -tagging (black circles) in PYTHIA 8.1 multijet events with at least three jets and at least three  $b$ -tagged jets for (a) leading-jet  $p_T$ , (b)  $m_{jj}^{\text{min}}$  and (c) the third-leading  $b$ -tagged jet  $p_T$  in the event. The definitions of the variables are listed in Table 2.3. Distributions are normalised to the same area. The uncertainty band for the  $\text{TRF}_{\text{MJ}}$  predictions shown in the ratio plot represents statistical uncertainties only.

fit are summarised in Table 2.2.

The regions are analysed separately and combined statistically to maximise the overall sensitivity. The most sensitive regions,  $(\geq 8j, \geq 3b)$  and  $(\geq 8j, \geq 4b)$ , are expected to contribute more than 50% of the total significance.

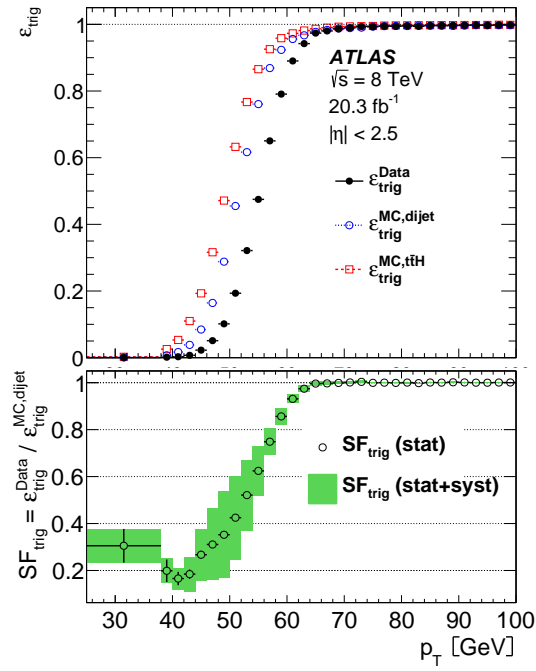


Figure 2.6.: Single-jet trigger efficiencies,  $\epsilon_{\text{trig}}$ , (top) for data, simulated dijet events, and  $t\bar{t}H$  events, as a function of jet  $p_T$  for jets with  $|\eta| < 2.5$ ; (bottom)  $\text{SF}_{\text{trig}}(p_T, \eta) = \epsilon_{\text{trig}}^{\text{data}}(p_T, \eta) / \epsilon_{\text{trig}}^{\text{MC,dijet}}(p_T, \eta)$ . The uncertainty on  $\text{SF}_{\text{trig}}$ , shown as the green shaded area, is estimated from the difference between the efficiencies in dijet and  $t\bar{t}H$  simulated events in the denominator of  $\text{SF}_{\text{trig}}$ .

Table 2.2.: Event yields from simulated backgrounds and the signal as well as data in each of the analysis regions prior to the fit (pre-fit). The quoted uncertainties are the sum in quadrature of the statistical and systematic uncertainties in the yields for all samples but the multijet background. The multijet normalisation and its systematic uncertainty are determined by the fit, so only its statistical uncertainty is quoted here. Since the numbers are rounded, the sum of all contributions may not equal the total value. The signal-to-background ratio,  $S/B$ , and the significance,  $S/\sqrt{B}$ , are also given. The  $tH$  background is not shown as it amounts to fewer than 1.5 events in each region.

	6j, 3b	6j, $\geq 4b$	7j, 3b	7j, $\geq 4b$	$\geq 8j$ , 3b	$\geq 8j$ , $\geq 4b$
Multijet	16380 $\pm$ 130	1112 $\pm$ 33	12530 $\pm$ 110	1123 $\pm$ 34	10670 $\pm$ 100	1324 $\pm$ 36
$t\bar{t}$ +light	1530 $\pm$ 390	48 $\pm$ 18	1370 $\pm$ 430	45 $\pm$ 18	1200 $\pm$ 520	40 $\pm$ 23
$t\bar{t}$ + $c\bar{c}$	280 $\pm$ 180	17 $\pm$ 12	390 $\pm$ 240	21 $\pm$ 15	560 $\pm$ 350	48 $\pm$ 33
$t\bar{t}$ + $b\bar{b}$	330 $\pm$ 180	44 $\pm$ 26	490 $\pm$ 270	87 $\pm$ 51	760 $\pm$ 450	190 $\pm$ 110
$t\bar{t}$ + $V$	14.2 $\pm$ 6.3	1.8 $\pm$ 1.5	22.0 $\pm$ 9.0	3.5 $\pm$ 2.3	40 $\pm$ 15	8.0 $\pm$ 4.2
Single top	168 $\pm$ 63	6.0 $\pm$ 3.7	139 $\pm$ 55	8.3 $\pm$ 4.6	110 $\pm$ 49	10.6 $\pm$ 5.9
Total background	18700 $\pm$ 480	1229 $\pm$ 48	14940 $\pm$ 580	1288 $\pm$ 66	13330 $\pm$ 780	1620 $\pm$ 130
$t\bar{t}H$ ( $m_H=125$ GeV)	14.3 $\pm$ 4.6	3.3 $\pm$ 2.1	23.7 $\pm$ 6.4	7.2 $\pm$ 3.3	48 $\pm$ 11	16.8 $\pm$ 6.1
Data events	18508	1545	14741	1402	13131	1587
$S/B$	< 0.001	0.003	0.002	0.006	0.004	0.010
$S/\sqrt{B}$	0.10	0.095	0.194	0.20	0.415	0.417

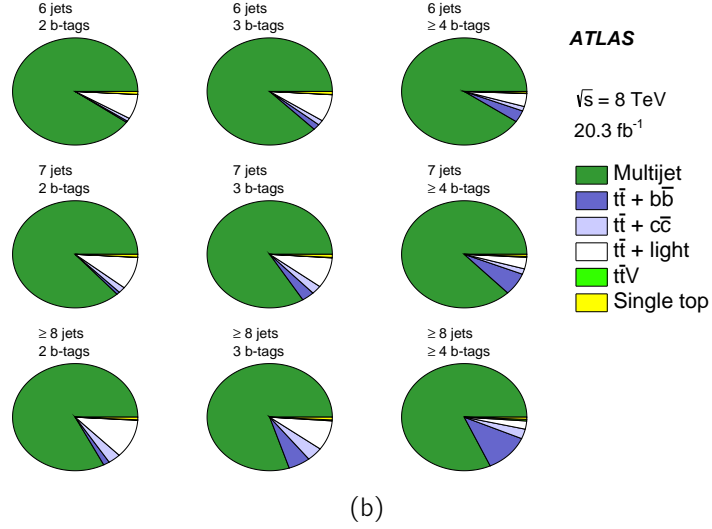
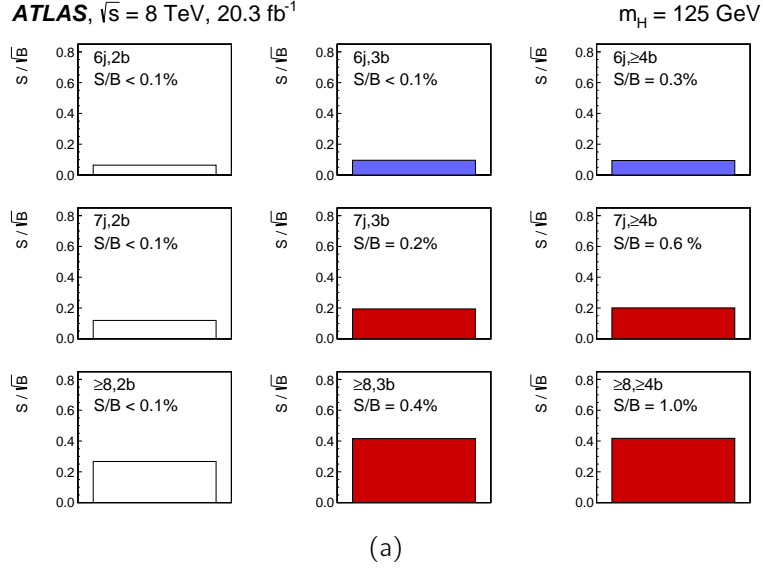


Figure 2.7.: (a)  $S/\sqrt{B}$  ratio for each of the regions assuming SM cross sections and branching fractions, and  $m_H=125$  GeV. Each row shows the quantity for a specific jet multiplicity (6, 7,  $\geq 8$ ), and the columns show the b-tag multiplicity (2, 3,  $\geq 4$ ). Signal-rich regions are shaded in dark red, while the control regions are shown in light blue. The regions with two  $b$ -tagged jets are not used in the fit and are presented in white. (b) The fractional contributions of the various backgrounds to the total background prediction in each considered region. The ordering of the rows and columns is the same as in (a).  $t\bar{t}V$  and single top contributions are small and thus not visible in some of the analysis regions.

Table 2.3.: List of variables used in the BDT in the six analysis regions. The numbers indicate the ranking of the corresponding variables, ordered by decreasing discriminating power. Variables not used in the BDT of a specific region are marked by a dash.

Variable	Definition	BDT rank					
		6j, 3b	6j, $\geq 4b$	7j, 3b	7j, $\geq 4b$	$\geq 8j$ , 3b	$\geq 8j$ , $\geq 4b$
Centrality <sub>Mass</sub>	Scalar sum of the jet $p_T$ divided by the invariant mass of the jets	1	1	1	1	9	6
Aplanarity	$1.5\lambda_2$ , where $\lambda_2$ is the second eigenvalue of the momentum tensor built with all jets	-	11	-	-	6	-
$S_T$	The modulus of the vector sum of jet $p_T$	2	2	2	4	2	2
$H_{T5}$	Scalar sum of jet $p_T$ starting from the fifth jet	8	-	-	7	-	-
$m_{jj}^{\min}$	Smallest invariant mass of any combination of two jets	9	-	6	10	11	12
$\Delta R^{\min}$	Minimum $\Delta R$ between two jets	6	5	9	-	8	4
$p_T^{\text{softest, jet}}$	$p_T$ of the softest jet	-	6	10	-	-	10
$\Delta R(b, b)p_T^{\max}$	$\Delta R$ between two $b$ -tagged jets with the largest vector sum $p_T$	11	-	7	5	5	3
$m_{bb}^{\Delta R(b,b)^{\min}}$	Invariant mass of the combination of two $b$ -tagged jets with the smallest $\Delta R$	3	3	8	9	3	9
$\frac{E_{\text{jet}} + E_{T2}}{\sum E_T^{\text{jets}}}$	Sum of the $E_T$ of the two jets with leading $E_T$ divided by the sum of the $E_T$ of all jets	5	8	4	2	7	5
$m_{2\text{ jets}}$	The mass of the dijet pair, which, when combined with any $b$ -tagged jet, maximises the magnitude of the vector sum of the $p_T$ of the three-jet system	10	-	-	8	-	-
$m_{2\text{ b-jets}}$	The invariant mass of the two $b$ -tagged jets which are selected by requiring that the invariant mass of all the remaining jets is maximal	12	7	-	6	-	8
$m_{\text{top},1}$	Mass of the reconstructed top quark	13	10	-	-	4	11
$m_{\text{top},2}$	Mass of the reconstructed top quark calculated from the jets not entering $m_{\text{top},1}$	7	9	5	-	10	7
$\Lambda$	The logarithm of the ratio of event probabilities under the signal and background hypotheses	4	4	3	3	1	1

## 2.6. Analysis method

The Toolkit for Multivariate Data Analysis (TMVA) [161] is used to train a BDT to separate the  $t\bar{t}H$  signal from the background. A dedicated BDT is defined and optimised in each of the six analysis regions. The variables entering the BDT and their definitions are listed in Table 2.3.

The input variables include event-shape variables such as Centrality<sub>Mass</sub> and aplanarity, global event variables, such as  $S_T$  (the modulus of the vector sum of the jet  $p_T$ ),  $H_{T5}$  (the scalar sum of the jet  $p_T$  starting from the fifth jet in  $p_T$  order),  $m_{jj}^{\min}$  (the smallest invariant mass of all dijet combinations), and the minimum  $\Delta R$  between jets. The  $p_T$  of the softest jet in the event is the only individual kinematic variable that enters the BDT directly. Other variables are calculated from pairs of objects:  $\Delta R(b, b)^{p_T^{\max}}$  (the  $\Delta R$  between the two  $b$ -tagged jets with highest vector sum  $p_T$ ),  $m_{bb}^{\Delta R(b, b)^{\min}}$  (the invariant mass of the two  $b$ -tagged jets with the smallest  $\Delta R$ ),  $(E_{T1} + E_{T2}) / \sum E_T^{\text{jets}}$  (the sum of the transverse energies of the two leading jets divided by the sum of the transverse energies of all jets),  $m_{2\text{jets}}$  (the mass of the dijet pair, which, when combined with any  $b$ -tagged jet, maximises the magnitude of the vector sum of the  $p_T$  of the three-jet system) and  $m_{2b\text{-jets}}$  (the invariant mass of the two  $b$ -tagged jets which are selected by requiring that the invariant mass of all the remaining jets is maximal). Two variables are calculated as the invariant mass of three jets:  $m_{\text{top},1}$  is computed from the three jets whose invariant mass is nearest to the top quark mass, taking into account the jet energy resolutions; the  $m_{\text{top},2}$  calculation uses the same algorithm but excludes the jets which enter  $m_{\text{top},1}$ . Finally, a log-likelihood ratio variable,  $\Lambda$ , is used; it is related to the probability of an event to be a signal candidate, compared to the probability of being a background candidate.

The  $\Lambda$  variable is the sum of the logarithms of ratios of relative probability densities for  $W$  boson, top quark and Higgs boson resonances to be reconstructed in the event. For a given resonance  $X$  decaying to two jets, the  $\Lambda$  component is built as  $\Lambda_X(m_{jj}) = \ln \frac{P_{\text{sig}}(m_{jj})}{P_{\text{bkg}}(m_{jj})}$  within a mass window  $w_X = \pm 30$  GeV around the given particle mass:

$$P_{\text{sig}}(m_{jj}) = \begin{cases} s \cdot G(m_{jj}|m_X, \sigma_X), & \text{for } |m_{jj} - m_X| \leq w_X, \\ 1 - s, & \text{for } |m_{jj} - m_X| > w_X. \end{cases} \quad (2.2)$$

$$P_{\text{bkg}}(m_{jj}) = \begin{cases} b \cdot \text{Rect}(m_X, w_X), & \text{for } |m_{jj} - m_X| \leq w_X, \\ 1 - b, & \text{for } |m_{jj} - m_X| > w_X. \end{cases} \quad (2.3)$$

Here  $s$  and  $b$  are the probabilities to find a jet pair with an invariant mass within  $\pm w_X$  of  $m_X$ . They are calculated from the signal simulation and from the multi-jet background respectively. The signal mass distribution is modelled with a Gaussian  $G(m_{jj}|m_X, \sigma_X)$ , while the background is modelled with a uniform dis-

tribution  $\text{Rect}(m_X, w_X)$  between  $m_X - w_X$  and  $m_X + w_X$ . Both functions  $P_{\text{sig}}(m_{jj})$  and  $P_{\text{bkg}}(m_{jj})$  are normalised to unity. For the top quark resonance the three-particle mass,  $m_{jjb}$ , is used. The width of the Gaussian is set to  $\sigma_X = 18$  GeV for all resonances; this value corresponds to the expected experimental width of a Higgs boson with no combinatoric background.

The expression for the complete event  $\Lambda$  is:

$$\Lambda(m_{jj}, m_{jjb}, m_{bb}) = \Lambda_W(m_{jj}|m_W, \sigma_X) + \Lambda_{\text{top}}(p_{T,jjb}, m_{jjb}|m_{\text{top}}, \sigma_X) + \Lambda_H(p_{T,bb}, m_{bb}|m_H, \sigma_X). \quad (2.4)$$

The three terms refer to  $W$ , top, and Higgs resonances respectively. For the top quark and Higgs boson resonances the masses,  $m_{jjb}$  and  $m_{bb}$ , as well as the  $p_T$ , defined as the magnitude of the vector sum of the  $p_T$  of the jets used to reconstruct the top quark,  $p_{T,jjb}$ , and to reconstruct the Higgs boson,  $p_{T,bb}$ , are used. The value of  $\Lambda$  is calculated for all possible jet combinations and the maximum  $\Lambda$  of the event is chosen.

The variables entering the BDT are selected and ranked according to their separation power with an iterative procedure, which stops when adding more variables does not significantly improve the separation between signal and background. The cut-off corresponds to the point when adding a variable increases the significance, defined as  $\sqrt{\sum_i S_i^2 / B_i^2}$  where  $S_i$  and  $B_i$  are the expected signal and background yields in the  $i^{\text{th}}$  bin of the BDT discriminant, by less than 1%. Signal and background samples are classified as described in Section 2.5, and then each subsample is further subdivided randomly into two subsamples of equal size for training and for testing.

The ranking of the input variables in terms of separation power for each analysis region is shown in Table 2.3. Figures 2.8 and 2.9 show the distribution of the most discriminant variables entering the BDT in the 3  $b$ -tag and  $\geq 4$   $b$ -tagged jets regions. The distributions of the BDT outputs for simulated signal and background events are shown in Figure 2.10 for each analysis region. The Figure shows a better separation between signal and background for low jet multiplicities than for high jet multiplicities. This is explained by the number of possible jet permutations. The number of jet permutations increases giving the background more configurations to mimic the signal.



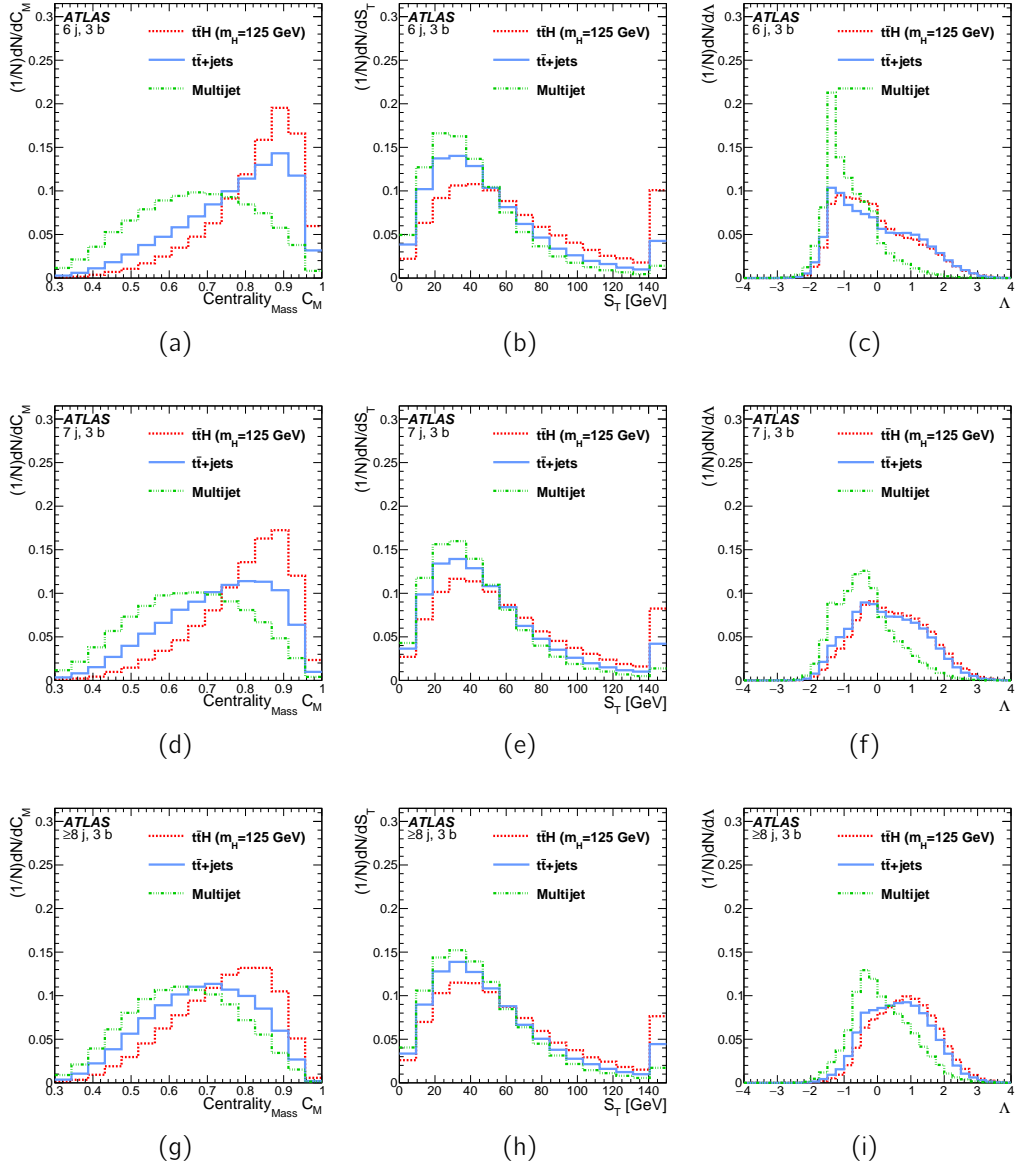


Figure 2.8.: The distribution of the most discriminant variables entering the BDT in the 3  $b$ -tag regions (from  $(6j, 3b)$  in (a)-(c),  $(7j, 3b)$  in (d)-(f) to  $(\geq 8j, 3b)$  in (g)-(i)). The plots show the separation power: the red histogram indicates the signal, the blue one the  $t\bar{t}$ +jets background, and the green one the multijet background. The definitions of the variables are listed in Table 2.3.

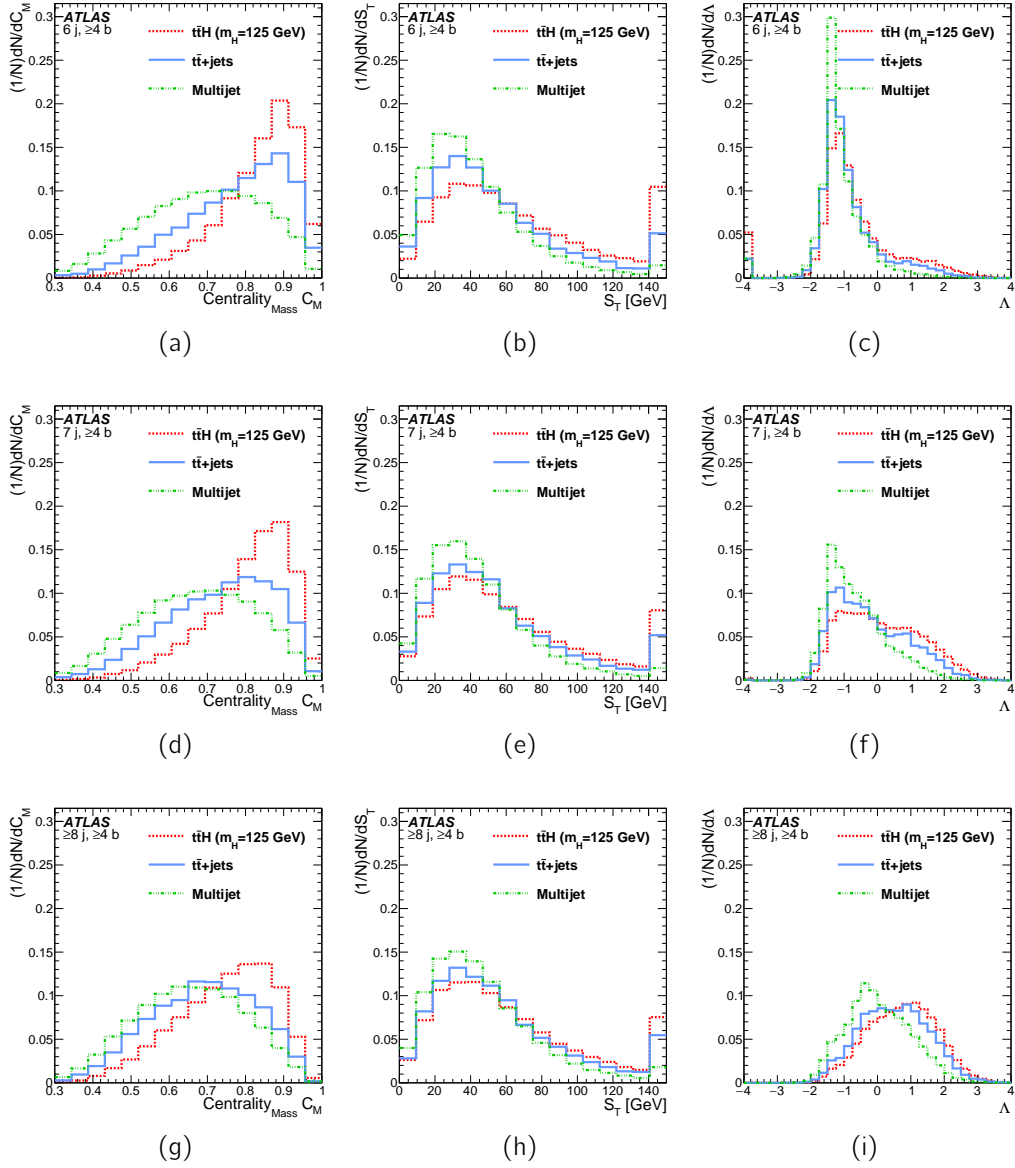


Figure 2.9.: The distribution of the most discriminant variables entering the BDT in the  $\geq 4$   $b$ -tag regions (from  $(6j, \geq 4b)$  in (a)-(c),  $(7j, \geq 4b)$  in (d)-(f) to  $(\geq 8j, \geq 4b)$  in (g)-(i)). The plots show the separation power: the red histogram indicates the signal, the blue one the  $t\bar{t}$ +jets background, and the green one the multijet background. The definitions of the variables are listed in Table 2.3.

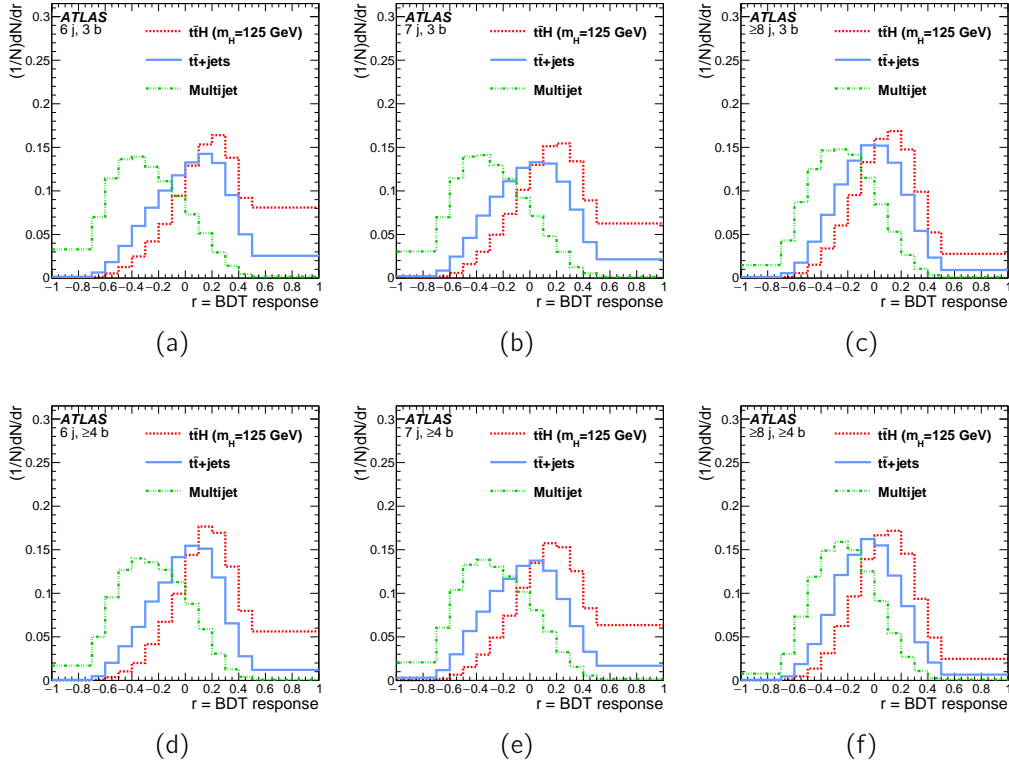


Figure 2.10.: Response of the BDT algorithm for simulated signal (dashed red),  $t\bar{t}$ +jets background (solid blue) and multijet background (dotted green) events in the (top) regions with 3  $b$ -tags ((a) 6, (b) 7 and (c)  $\geq 8$  jets) and in the (bottom) regions with  $\geq 4$   $b$ -tags ((d) 6, (e) 7 and (f)  $\geq 8$  jets). The binning is the same as that used in the fit.

## 2.7. Systematic uncertainties

The sources of systematic uncertainty considered in this analysis can be grouped into six main categories as summarised in Table 2.4. Each systematic uncertainty is represented by an independent parameter, referred to as a nuisance parameter, and is parameterised with a Gaussian function for the shape uncertainties and a log-normal distribution for the normalisations [162]. They are centred around zero and one, respectively, with a width that corresponds to the given uncertainty. The uncertainties in the integrated luminosity, reconstruction of the physics objects, and the signal and background MC models are treated as in Ref. [115]. The uncertainties related to the jet trigger as well as those related to the data-driven method to estimate the multijet background are discussed below. In total, 99 fit parameters are considered. The determination and treatment of the systematic uncertainties are detailed in this section. Their impact on the

fitted signal strength is summarised in Table 2.8 in Section 3.6.

Table 2.4.: Sources of systematic uncertainty considered in the analysis grouped in six categories. “N” denotes uncertainties affecting only the normalisation for the relevant processes and channels, whereas “S” denotes uncertainties which are considered to affect only the shape of normalised distributions. “SN” denotes uncertainties affecting both shape and normalisation. Some sources of systematic uncertainty are split into several components. The number of components is also reported.

Systematic uncertainty source	Type	Number of components
Luminosity	N	1
Trigger	SN	1
<i>Physics Objects</i>		
Jet energy scale	SN	21
Jet vertex fraction	SN	1
Jet energy resolution	SN	1
$b$ -tagging efficiency	SN	7
$c$ -tagging efficiency	SN	4
Light-jet tagging efficiency	SN	12
<i>Background MC Model</i>		
$t\bar{t}$ cross section	N	1
$t\bar{t}$ modelling: $p_T$ reweighting	SN	9
$t\bar{t}$ modelling: parton shower	SN	3
$t\bar{t}$ +heavy-flavour: normalisation	N	2
$t\bar{t}+c\bar{c}$ : heavy-flavour reweighting	SN	2
$t\bar{t}+c\bar{c}$ : generator	SN	4
$t\bar{t}+b\bar{b}$ : NLO Shape	SN	8
$t\bar{t}V$ cross section	N	1
$t\bar{t}V$ modelling	SN	1
Single top cross section	N	1
<i>Data driven background</i>		
Multijet normalisation	N	6
Multijet TRF <sub>MJ</sub> parameterisation	S	6
Multijet $H_T$ correction	S	1
Multijet $S_T$ correction	S	1
<i>Signal Model</i>		
$t\bar{t}H$ scale	SN	2
$t\bar{t}H$ generator	SN	1
$t\bar{t}H$ hadronisation	SN	1
$t\bar{t}H$ parton shower	SN	1

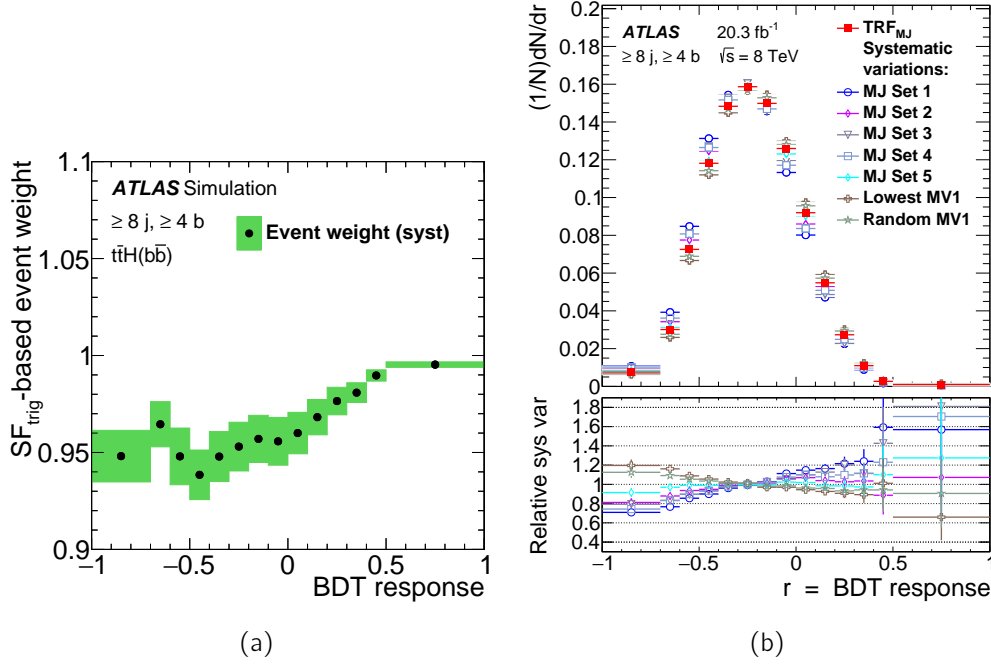


Figure 2.11.: (a) Per event trigger scale factor  $SF_{\text{trig}}$  (black dots) versus the BDT output of  $t\bar{t}H$  events, shown with its corresponding systematic uncertainty (green band) for the ( $\geq 8j, \geq 4b$ ) region. (b) Comparison of the BDT output of the multijet background predicted with different sets of  $TRF_{\text{MJ}}$ . The nominal  $TRF_{\text{MJ}}$  is represented by the red points. The bottom panel shows the ratios of the alternative  $TRF_{\text{MJ}}$  predictions to the nominal set.

The systematic uncertainty in the luminosity for the data sample is 2.8%. It is derived following the same methodology as that detailed in Ref. [163]. The trigger uncertainty is determined from the difference between  $\epsilon_{\text{trig}}$ , estimated using  $t\bar{t}H$  and dijet MC events. Each jet in the event is weighted according to  $SF_{\text{trig}}(p_T, \eta)$ , the uncertainty of which is propagated to the shape and normalisation of the BDT output distribution, as shown in Figure 2.11(a).

The uncertainties in physics objects are related to the reconstruction and  $b$ -tagging of jets. The jet energy resolution (JER) and the jet energy scale (JES) uncertainties are derived combining the information from test-beam data and simulation [164]. The JES uncertainties are split into 21 uncorrelated components. The largest of these uncertainties is due to the jet flavour composition. The JVF uncertainty is derived from  $Z(\rightarrow \ell^+\ell^-) + 1$ -jet events in data and simulation by varying the nominal cut value by 0.1 up and down.

The uncertainty related to the  $b$ -tagging is modelled with six independent parameters, while four parameters model the  $c$ -tagging uncertainty [btagpaper].

These are eigenvalues obtained by diagonalising the matrix which parameterises the tagging efficiency as a function of  $p_T$ , taking into account bin-to-bin correlations. Twelve parameters, which depend on  $p_T$  and  $\eta$ , are used to parameterise the light-jet-tagging systematic uncertainties [165]. The per-jet  $b$ -tagging uncertainties are 3%–5%, about 10% for  $c$ -tagging and 20% for light jet tagging. An additional uncertainty is assigned to the  $b$ -tagging efficiency for jets with  $p_T > 300$  GeV, which lacks statistics for an accurate calibration from data.

A combined uncertainty of  $\pm 6.0\%$  is assigned to the  $t\bar{t}$ +jets production cross section, including modelling components due to the value of  $\alpha_s$ , the PDF used, the process energy scale, and the top quark mass. Other systematic uncertainties related to  $t\bar{t}$ +jets production are due to the modelling of parton showers and hadronisation.

The systematic uncertainties arising from the reweighting procedure to improve  $t\bar{t}$  background description by simulation (Section 2.3.2), have been extensively studied in Ref. [115] and adopted in this analysis. The largest uncertainties in the  $t\bar{t}$  background description arise from radiation modelling, the choice of generator to simulate  $t\bar{t}$  production, the JES, JER, and flavour modelling. These systematic uncertainties are applied to the  $t\bar{t}$ +light and  $t\bar{t} + c\bar{c}$  components. Two additional systematic uncertainties, the full difference between applying and not applying the reweightings of the  $t\bar{t}$  system  $p_T$  and top quark  $p_T$ , are assigned to the  $t\bar{t} + c\bar{c}$  component.

Four additional systematic uncertainties in the  $t\bar{t} + c\bar{c}$  estimate are derived from the simultaneous variation of factorisation and renormalisation scales in MADGRAPH+PYTHIA. For the  $t\bar{t} + b\bar{b}$  background, three scale uncertainties are evaluated by varying the renormalisation and resummation scales. The shower recoil model uncertainty and two uncertainties due to the PDF choice in the SHERPA+OPENLOOPS NLO calculation are also taken into account.

The  $t\bar{t}$ +jets background is parameterised to allow a varying percentage of heavy flavours  $c$  and  $b$  in the additional jets not originating from the top quark decay products. An uncertainty of  $\pm 50\%$  is assigned to the  $t\bar{t} + b\bar{b}$  and  $t\bar{t} + c\bar{c}$  components of the  $t\bar{t}$ +jets cross section, which are treated as uncorrelated and are derived by comparing POWHEG+PYTHIA with a NLO result based on SHERPA+OPENLOOPS. The uncertainty in the  $t\bar{t} + b\bar{b}$  contribution represents the dominant systematic effect in this analysis. An uncertainty of  $\pm 30\%$  in the total cross section is assumed for  $t\bar{t} + V$  [148, 149].

The multijet background is estimated using data in regions with exactly two  $b$ -tagged jets after subtraction of contributions from other events using MC simulation. All systematic uncertainties mentioned above are fully propagated to the data-driven multijet background estimation and treated in a correlated manner.

To estimate the uncertainties associated with the multijet background, the values of  $\varepsilon_{\text{MJ}}$  are determined as a function of different sets of variables, listed in the first part of Table 2.5, which are sensitive to the amount and the mechanism of heavy-flavour production. Alternative variables used are  $\Delta R_{(j,j)}^{\text{min}}$ , the minimum

Table 2.5.: Alternative predictions of the multijet background with the  $\text{TRF}_{\text{MJ}}$  method. Multijet sets 1 to 5 correspond to variations of the nominal set of variables describing  $\varepsilon_{\text{MJ}}$ . The next two sets specify the variation in the nominal set based on the two  $b$ -tagged jets which are used to compute  $\varepsilon_{\text{MJ}}$ . The last two refer to changes due to the residual mismodellings of  $H_{\text{T}}$  and  $S_{\text{T}}$ . Each of these variations of the multijet background shape is quantified by one nuisance parameter in the fit.

TRF <sub>MJ</sub> predictions	Parameterisation variables in the TRF <sub>MJ</sub> method
Nominal set	$p_{\text{T}},  \eta , \langle \Delta R_{(j,\text{hMV1})} \rangle$
Multijet set 1	$p_{\text{T}}, \Delta R_{\text{MV1}}, \Delta R_{(j,\text{hMV1})}^{\text{min}}$
Multijet set 2	$p_{\text{T}}, \Delta R_{\text{MV1}}, \Delta R_{(j,j)}^{\text{min}}$
Multijet set 3	$p_{\text{T}},  \eta , \Delta R_{(j,\text{hMV1})}^{\text{min}}$
Multijet set 4	$p_{\text{T}},  \eta , \Delta R_{\text{MV1}}, \Delta R_{(j,\text{hMV1})}^{\text{min}}$
Multijet set 5	$p_{\text{T}}, \Delta R_{\text{MV1}}, \langle \Delta R_{(j,\text{hMV1})} \rangle$
Multijet lowest MV1	Nominal set removing the two lowest MV1 jets from computation
Multijet random MV1	Nominal set removing randomly two MV1 jets from computation
Multijet HT RW	Nominal set with $H_{\text{T}}$ reweighting
Multijet ST RW	Nominal set with $S_{\text{T}}$ reweighting

$\Delta R$  between the probed jet and any other jet in the event,  $\Delta R_{(j,\text{hMV1})}^{\text{min}}$ , the minimum  $\Delta R$  between the probed jet and the two jets with highest  $b$ -tag probability or  $\langle \Delta R_{(j,\text{hMV1})} \rangle$ , its average value, and  $\Delta R_{\text{MV1}}$ , the  $\Delta R$  between the two jets with the highest  $b$ -tag probability. In addition, different choices of methods to exclude  $b$ -tagged jets when determining  $\varepsilon_{\text{MJ}}$  in the  $\text{TRF}_{\text{MJ}}$  method are considered: the two  $b$ -tagged jets with the lowest MV1 weight or a random choice of two jets among all  $b$ -tagged jets in the event are chosen. The different sets of variables used to define  $\varepsilon_{\text{MJ}}$  affect the shape of the BDT distribution for the multijet background, as shown in Figure 2.11(b). Each of these shape variations is taken into account by a nuisance parameter in the fit. These parameterisations also affect the overall normalisation, with a maximum variation of 18% in the 3- $b$ -tag regions and 38% in the  $\geq 4$ - $b$ -tag regions. Residual mismodelling of  $H_{\text{T}}$  and  $S_{\text{T}}$  from the extraction region are also taken into account as systematic uncertainties. The normalisation of the multijet background is evaluated independently in each of the six analysis regions.

For the signal MC modelling, the POWHEL factorisation and renormalisation scales are varied independently by a factor two and 0.5. The kinematics of the MC simulated samples are then reweighted to reproduce the effects of these variations. The uncertainties related to the choice of PDFs are evaluated using the recommendations of PDF4LHC [166]. The systematic uncertainties from the parton shower and fragmentation models are evaluated using POWHEL+HERWIG

samples. The uncertainty due to the choice of generator is evaluated by comparing POWHEL+PYTHIA8 with MADGRAPH5\_AMC@NLO+HERWIG++.

## 2.8. Statistical methods

The binned distributions of the BDT output discriminants for each of the six analysis regions are combined as inputs to a test statistic to search for the presence of a signal. The analysis uses a maximum-likelihood fit [162] to measure the compatibility of the observed data with the background-only hypothesis, i.e.,  $\mu = 0$ , and to make statistical inferences about  $\mu$ , such as upper limits, using the CL<sub>s</sub> method [167, 168] as implemented in the ROOFIT package [169].

A fit is performed under the signal-plus-background hypothesis to obtain the value of the signal strength, assuming a SM Higgs boson mass of  $m_H = 125$  GeV. The value of  $\mu$  is a free parameter in the fit. The normalisation of each component of the background and  $\mu$  are determined simultaneously from the fit. Contributions from  $t\bar{t}$ +jets,  $t\bar{t} + V$  and single-top-quark backgrounds are constrained by the uncertainties of the respective theoretical calculations, the uncertainty in the luminosity, and experimental data. The multijet background normalisations are free parameters in the fit and are independent in each region. The performance of the fit is validated using simulated events by injecting a signal with variable strength and comparing the known strength to the fitted value.

## 2.9. Results

The yields in the different analysis regions considered in the analysis after the fit (post-fit) are summarised in Table 2.6. In each region, the variations of background and signal events with respect to the pre-fit values (cf. Table 2.2) are modest and, in particular, the fitted multijet background component is well constrained by the fit within an uncertainty of 8%.

Figures 2.12, 2.13, 2.14, 2.15, 2.16, 2.17, 2.18 and 2.19 show the the distribution of the most discriminant variables entering the BDT and the BDT output distributions for data and the predictions in each analysis region, both before (left panels) and after (right panels) the fit to data. The relative uncertainties decrease significantly in all regions due to the constraints provided by the data, exploiting the correlations between the uncertainties in the different analysis regions.



Table 2.6.: Event yields from simulated backgrounds and the signal as well as measured events in each of the analysis regions after the fit. The quoted uncertainties include statistical and systematical effects. The sum of all contributions may slightly differ from the total value due to rounding. The  $tH$  background is not shown as fewer than 1.5 events in each region are predicted.

	6j, 3b	6j, $\geq 4b$	7j, 3b	7j, $\geq 4b$	$\geq 8j$ , 3b	$\geq 8j$ , $\geq 4b$
Multijet	15940 $\pm$ 320	1423 $\pm$ 66	12060 $\pm$ 350	1233 $\pm$ 78	10020 $\pm$ 490	1280 $\pm$ 100
$t\bar{t}$ +light	1750 $\pm$ 270	55 $\pm$ 13	1650 $\pm$ 340	54 $\pm$ 15	1550 $\pm$ 450	54 $\pm$ 21
$t\bar{t} + c\bar{c}$	350 $\pm$ 170	22 $\pm$ 11	490 $\pm$ 240	28 $\pm$ 14	750 $\pm$ 360	66 $\pm$ 33
$t\bar{t} + b\bar{b}$	230 $\pm$ 120	31 $\pm$ 17	350 $\pm$ 190	63 $\pm$ 34	560 $\pm$ 320	139 $\pm$ 75
$t\bar{t} + V$	15.0 $\pm$ 6.2	1.9 $\pm$ 1.5	23.3 $\pm$ 8.9	3.6 $\pm$ 2.2	43 $\pm$ 15	8.7 $\pm$ 4.2
Single top	184 $\pm$ 59	6.7 $\pm$ 3.6	153 $\pm$ 52	9.4 $\pm$ 4.4	123 $\pm$ 48	11.8 $\pm$ 5.8
Total background	18470 $\pm$ 320	1539 $\pm$ 58	14720 $\pm$ 320	1391 $\pm$ 69	13030 $\pm$ 340	1561 $\pm$ 63
$t\bar{t}H$ ( $m_H=125$ GeV)	23.4 $\pm$ 6.3	5.6 $\pm$ 2.8	39.1 $\pm$ 8.9	11.9 $\pm$ 4.5	71 $\pm$ 15	28.8 $\pm$ 8.5
Data events	18508	1545	14741	1402	13131	1587

The signal strength in the all-hadronic  $t\bar{t}H$  decay mode, for  $m_H = 125$  GeV, is measured to be:

$$\mu(m_H = 125 \text{ GeV}) = 1.6 \pm 2.6. \quad (2.5)$$

The expected uncertainty in the signal strength ( $\mu = 1$ ) is  $\pm 2.8$ . The observed (expected) significance of the signal is 0.6 (0.4) standard deviations, corresponding to an observed (expected)  $p$ -value of 27% (34%), where the  $p$ -value is the probability to obtain a result at least as signal-like as observed if no signal were present.

The observed and expected limits are summarised in Table 2.7. A  $t\bar{t}H$  signal 6.4 times larger than predicted by the SM is excluded at 95% CL. A signal 5.4 times larger than the signal of a SM Higgs boson is expected to be excluded for the background-only hypothesis.

Table 2.7.: Observed and expected upper limits at 95% CL on  $\sigma(t\bar{t}H)$  relative to the SM prediction assuming  $m_H = 125$  GeV, for the background-only hypothesis. Confidence intervals around the expected limits under the background-only hypothesis are also provided, denoted by  $\pm 1\sigma$  and  $\pm 2\sigma$ , respectively. The expected (median) upper limit at 95% CL assuming the SM prediction for  $\sigma(t\bar{t}H)$  is shown in the last column.

	Observed	Expected if $\mu = 0$					Expected if $\mu = 1$
		$-2\sigma$	$-1\sigma$	Median	$+1\sigma$	$+2\sigma$	Median
Upper limit on $\mu$ at 95%	6.4	2.9	3.9	5.4	7.5	10.1	6.4

Figure 2.20 summarises the post-fit event yields for data, total background and signal expectations as a function of  $\log_{10}(S/B)$ . The signal is normalised to the fitted value of the signal strength ( $\mu = 1.6$ ). A signal strength 6.4 times larger than predicted by the SM is also shown in Figure 2.20.

Figure 2.21 shows the effect of the major systematic uncertainties on the fitted value of  $\mu$  and the constraints provided by the data. The ranking, from top to bottom, is determined by the post-fit impact on  $\mu$ . This effect is calculated by fixing the corresponding nuisance parameter at  $\hat{\theta} \pm \sigma_\theta$  and performing the fit again. Here  $\hat{\theta}$  is the fitted value of the nuisance parameter and  $\sigma_\theta$  is its post-fit uncertainty. The difference between the default and the modified  $\mu$ ,  $\Delta\mu$ , represents the effect on  $\mu$  of this particular systematic uncertainty. This is also shown in Table 2.8.

The largest effect arises from the uncertainty in the normalisation of the irreducible  $t\bar{t} + b\bar{b}$  background. The  $t\bar{t} + b\bar{b}$  background normalisation is smaller by 30% in the fit than the prediction, resulting in a decrease of the observed  $t\bar{t} + b\bar{b}$  yield with respect to the POWHEG+PYTHIA prediction. The second largest effect comes from the multijet background normalisation. The data-driven method

Table 2.8.: Effect of the different sources of systematic uncertainties on  $\mu$  expressed in terms of percentage of the fitted value of  $\mu$  sorted according to their post-fit effect.

Sources of systematic uncertainty	$\pm 1\sigma$ post-fit impact on $\mu$
$t\bar{t}$ normalisation	108%
Multijet normalisation	71%
Multijet shape	60%
Main contributions from $t\bar{t}$ modelling	34%–41%
Flavour tagging	31%
Jet energy scale	27%
Signal modelling	22%
Luminosity+trigger+JVF+JER	18%

focuses on modelling the shape of the multijet background while the normalisation is constrained by the regions dominated by multijet background. The uncertainty in the normalisation parameters amounts to few percent and the values from each region are consistent with the variations applied to these parameters to account for systematic uncertainties. Two of the multijet background shape uncertainties are ranked fourth and fifth, and their pulls are slightly positive.

Other important uncertainties include  $b$ -tagging and JES. Uncertainties arising from jet energy resolution, jet vertex fraction, jet reconstruction and JES that affect primarily low- $p_T$  jets, as well as the  $t\bar{t}$ +light-jet background modelling uncertainties, do not have a significant impact on the result.

## 2.10. Combination of $t\bar{t}H$ results at $\sqrt{s} = 7$ and 8 TeV

The sensitivity of the search for  $t\bar{t}H$  production can be increased by statistically combining different Higgs boson decay channels. This combination is described in the following.

### 2.10.1. Individual $t\bar{t}H$ measurements and results

The  $t\bar{t}H$  searches that are combined are:

- $t\bar{t}H(H \rightarrow b\bar{b})$  in the single-lepton and opposite-charge dilepton  $t\bar{t}$  decay channels using data at  $\sqrt{s} = 8$  TeV [115],
- $t\bar{t}H(H \rightarrow b\bar{b})$  in the all-hadronic  $t\bar{t}$  decay channel using data at  $\sqrt{s} = 8$  TeV as presented in this paper,

- $t\bar{t}H(H \rightarrow (WW^{(*)}, \tau\tau, ZZ^{(*)}) \rightarrow \text{leptons})$  with two same-charge leptons ( $e$  or  $\mu$ ), three leptons, four leptons, two hadronically decaying  $\tau$  leptons plus one lepton and one hadronically decaying  $\tau$  lepton plus two leptons in the final state using data at  $\sqrt{s} = 8$  TeV [114],
- $t\bar{t}H(H \rightarrow \gamma\gamma)$  at  $\sqrt{s} = 7$  and 8 TeV in both the hadronic and leptonic ( $e$  or  $\mu$ )  $t\bar{t}$  pair decay channels [116].

First all  $H \rightarrow b\bar{b}$  final states are combined, obtaining a signal strength for the  $t\bar{t}H(H \rightarrow b\bar{b})$  combination, and then the outcome is combined with the remaining (non- $H \rightarrow b\bar{b}$ ) channels.

#### 2.10.1.1. $H \rightarrow b\bar{b}$ (single lepton and dilepton $t\bar{t}$ decays)

The search for  $t\bar{t}H$  production with  $H \rightarrow b\bar{b}$  is performed in both the single-lepton and dilepton  $t\bar{t}$  decay modes [115]. The single-lepton analysis requires one charged lepton with at least four jets, of which at least two need to be  $b$ -tagged, while the dilepton analysis requires two opposite-charge leptons with at least two jets, of which at least two must be  $b$ -tagged. The events are then categorised according to the jet and  $b$ -tagged jet multiplicity. The dominant background in the signal-enriched regions is from  $t\bar{t} + b\bar{b}$  events. In these regions, neural networks [170] are built using kinematic information in order to separate the  $t\bar{t}H$  signal from  $t\bar{t}$  background. Furthermore, in the single-lepton channel, a matrix-element discriminant is built in the most signal-enriched regions and is used as an input to the neural network.

#### 2.10.1.2. $H \rightarrow (WW^{(*)}, \tau\tau, ZZ^{(*)}) \rightarrow \text{leptons}$

The  $t\bar{t}H$  search with  $H \rightarrow (WW^{(*)}, \tau\tau, ZZ^{(*)}) \rightarrow \text{leptons}$  [114] exploits several multilepton signatures resulting from Higgs boson decays to vector bosons and/or  $\tau$  leptons. Events are categorised based on the number of charged leptons and/or hadronically decaying  $\tau$  leptons in the final state. The categorisation includes events with two same-charge leptons, three leptons, four leptons, one lepton and two hadronic  $\tau$  leptons, as well as two same-charge leptons with one hadronically decaying  $\tau$  lepton. Backgrounds include events with electron charge misidentification, which are estimated using data-driven techniques, non-prompt leptons arising from semileptonic  $b$ -hadron decays, mostly from  $t\bar{t}$  events, again estimated from data-driven techniques, and production of  $t\bar{t}+W$  and  $t\bar{t}+Z$ , which are estimated using MC simulations. Signal and background event yields are obtained from a simultaneous fit to all channels.

#### 2.10.1.3. $H \rightarrow \gamma\gamma$

The  $t\bar{t}H$  search in the  $H \rightarrow \gamma\gamma$  channel [116] exploits the sharp peak in the diphoton mass distribution from the  $H \rightarrow \gamma\gamma$  decay over the continuum back-

ground. The analysis is split according to the decay mode of the  $t\bar{t}$  pair. A leptonic selection requires at least one lepton and at least one  $b$ -tagged jet, and missing transverse momentum if there is only one  $b$ -tagged jet, whereas a hadronic selection requires a combination of jets and  $b$ -tagged jets. Contributions from peaking non- $t\bar{t}H$  Higgs boson production modes are estimated from MC simulations. The signal is extracted with a fit using the diphoton mass distribution as a discriminant.

## 2.10.2. Correlations

Nuisance parameters corresponding to the same source of uncertainty in different analyses are generally considered to be correlated with each other, except for the following sets:

- Nuisance parameters related to  $b$ -tagging (also  $c$ -tagging and light mistagging) are considered to be independent among the analyses as different  $b$ -tagging working points are employed.
- The electron identification uncertainty is considered to be uncorrelated between analyses due to different selections used.

## 2.10.3. Results of the combination

### 2.10.3.1. Signal strength

The result of the  $t\bar{t}H(H \rightarrow b\bar{b})$  combination for the signal strength is  $\mu = 1.4 \pm 1.0$ . The observed signal strengths for the individual  $t\bar{t}H(H \rightarrow b\bar{b})$  channels and for their combination are summarised in Figure 2.22. The  $t\bar{t} + b\bar{b}$  normalisation nuisance parameters obtained in the all-hadronic analysis ( $-0.6 \pm 0.8$ ) and the leptonic analysis ( $+0.8 \pm 0.4$ ). The expected significance increases from  $1.0\sigma$  for the leptonic final state of  $t\bar{t}H(H \rightarrow b\bar{b})$  to  $1.1\sigma$  for the combined  $t\bar{t}H(H \rightarrow b\bar{b})$ . Because the combined  $t\bar{t}H(H \rightarrow b\bar{b})$  best-fit value of  $\mu$  is lower than the leptonic-only value, the observed significance for the  $t\bar{t}H(H \rightarrow b\bar{b})$  combination is reduced from  $1.4\sigma$  (leptonic [115]) to  $1.35\sigma$  (combined).

Figure 2.23 summarises the observed signal strength  $\mu$  of the individual  $t\bar{t}H$  channels ( $H \rightarrow b\bar{b}$ ,  $H \rightarrow \gamma\gamma$  and  $H \rightarrow (WW^{(*)}, \tau\tau, ZZ^{(*)}) \rightarrow \text{leptons}$ ) and the  $t\bar{t}H$  combination. The observed (expected) significance of the combined  $t\bar{t}H$  result is  $2.33\sigma$  ( $1.53\sigma$ ).

The combination of all  $t\bar{t}H$  analyses yields an observed (expected) 95% CL upper limit of 3.1 (1.4) times the SM cross section. The observed 95% CL limits for the individual  $t\bar{t}H$  channels and for the combination are shown in Figure 2.24 and in Table 2.9.

The result for the best-fit value is  $\mu = 1.7 \pm 0.8$ .

### 2.10.3.2. Couplings

Sensitivity to  $t - H$  and  $W - H$  couplings stems from several sources: from the  $t\bar{t}H$  production itself, from the Higgs boson decay branching fractions, from associated single top and Higgs boson production processes ( $tHjb$  and  $WtH$ ), where interference terms include both the  $t\bar{t}H$  and  $WWH$  vertices, and from the  $H \rightarrow \gamma\gamma$  branching fraction, where again interferences between loop contributions from the top quark and the  $W$  boson are present. Different channels differ in their sensitivity to these components. A two-parameter fit is performed, assuming that all boson couplings scale with the same modifier  $\kappa_V$ , while all fermion couplings scale with the same modifier  $\kappa_F$ <sup>c</sup>.

The parameterisation of the couplings for the  $t\bar{t}H$  and  $tH$  production modes and for the different Higgs boson decay modes is taken from Refs. [106, 172]. Figure 2.25 shows the log-likelihood contours of  $\kappa_F$  versus  $\kappa_V$  for the combined  $t\bar{t}H$  fit. The combination of all analysis channels slightly prefers positive  $\kappa_F$ . Additional studies, performed to determine the contribution of the individual analyses to the combined coupling measurement, indicate that the  $t\bar{t}H$ ,  $H \rightarrow (WW^{(*)}, \tau\tau, ZZ^{(*)}) \rightarrow \text{leptons}$  analysis prefers somewhat enhanced  $W - H$  coupling, which can only be compatible with the  $t\bar{t}H(H \rightarrow \gamma\gamma)$  rate if the interference between  $t\bar{t}H$  and  $WWH$  amplitudes is destructive, as expected in the SM.

---

<sup>c</sup>Based on a leading-order motivated framework ( $\kappa$ -framework), coupling modifiers have been proposed to interpret the LHC data using specific modifications of the Higgs boson couplings related to new physics beyond the SM [56, 171].

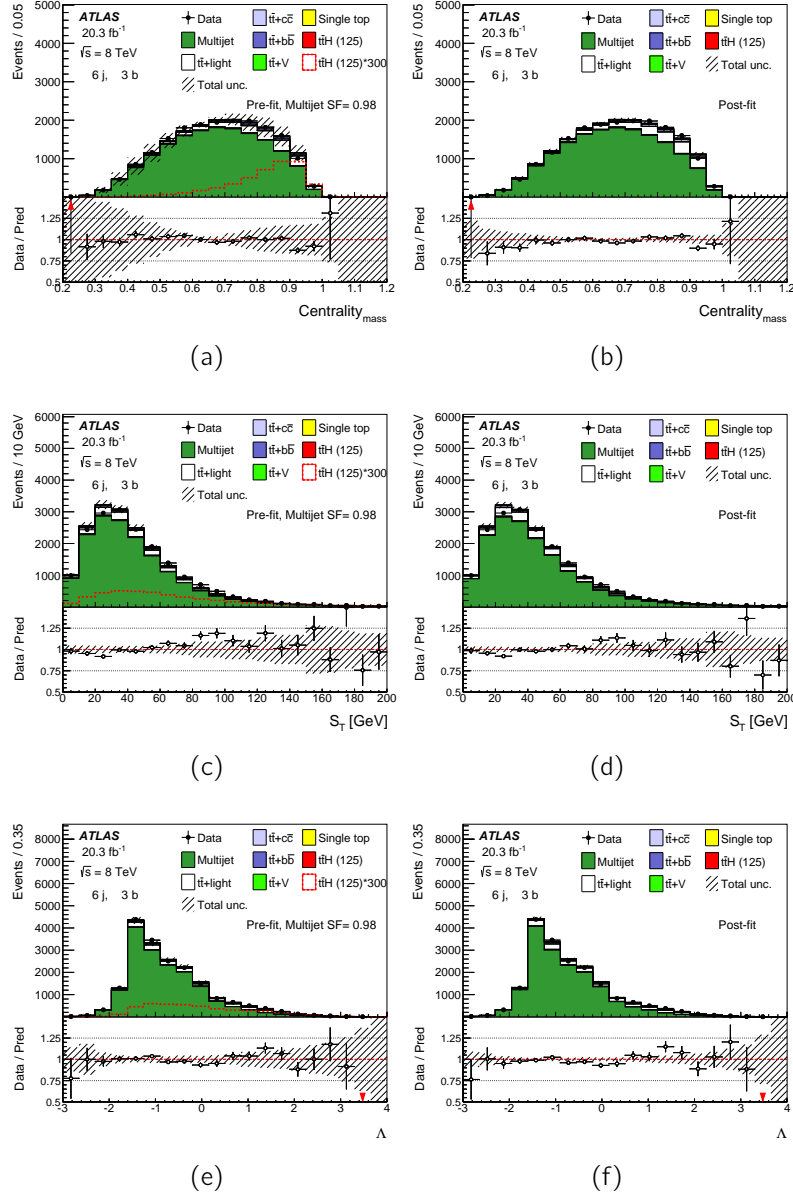


Figure 2.12.: Comparison between data and prediction for three top-ranked input variables in the (6j,3b) region before (left) and after (right) the fit. The fit is performed under the signal-plus-background hypothesis. Pre-fit plots show an overlay of the multijet distribution normalised to data for illustration purposes only. The plots include  $\text{Centrality}_{\text{Mass}}$ ,  $S_T$  and  $\Lambda$ . The definitions of the variables are listed in Table 2.3. The first and last bins in all figures contain the underflow and overflow, respectively. The bottom panel displays the ratio of data to the total prediction, red arrows indicate the position of the point outside the ratio window. The hashed area represents the total uncertainty in the background predictions. The  $t\bar{t}H$  signal yield (solid red) is scaled by a fixed factor, shown in the figure, before the fit.

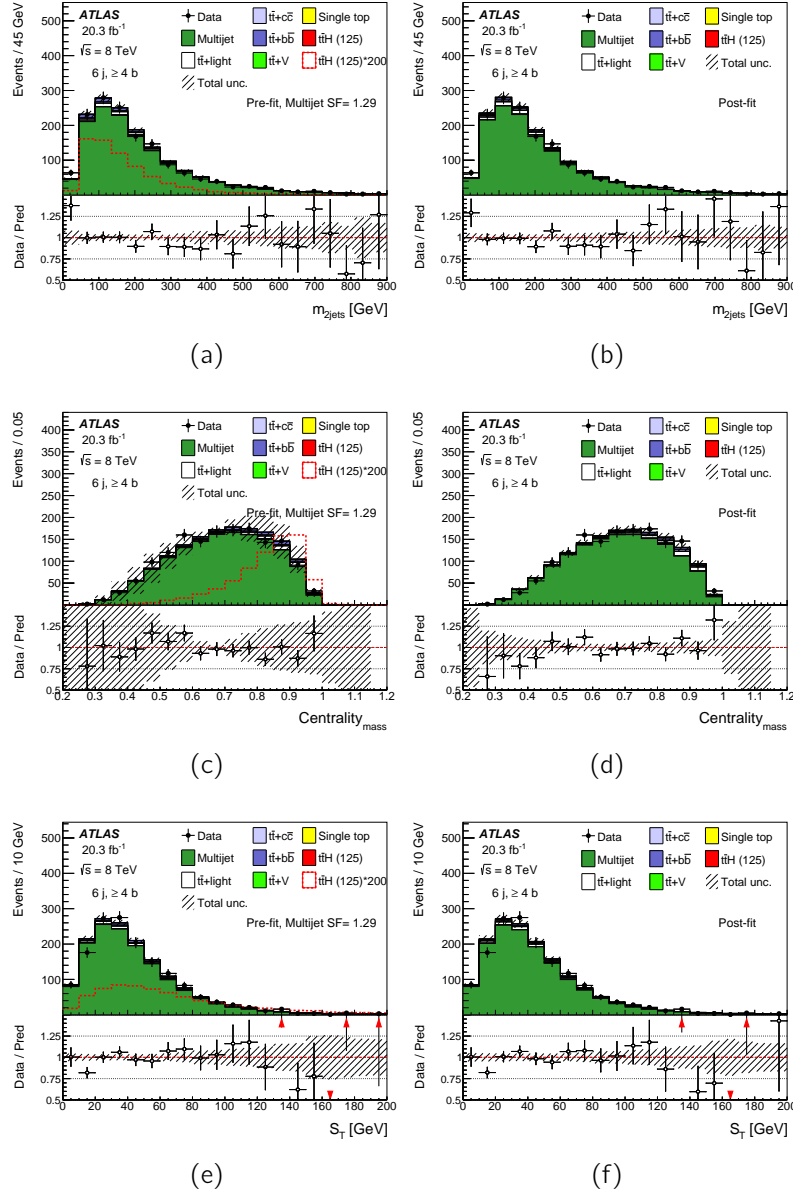


Figure 2.13.: Comparison between data and prediction for three top-ranked input variables in the  $(6j, \geq 4b)$  region before (left) and after (right) the fit. The fit is performed under the signal-plus-background hypothesis. Pre-fit plots show an overlay of the multijet distribution normalised to data for illustration purposes only. The plots include  $m_{2\text{jets}}$ ,  $\text{Centrality}_{\text{Mass}}$  and  $S_T$ . The definitions of the variables are listed in Table 2.3. The first and last bins in all figures contain the underflow and overflow, respectively. The bottom panel displays the ratio of data to the total prediction, red arrows indicate the position of the point outside the ratio window. The hashed area represents the total uncertainty in the background predictions. The  $t\bar{t}H$  signal yield (solid red) is scaled by a fixed factor, shown in the figure, before the fit.



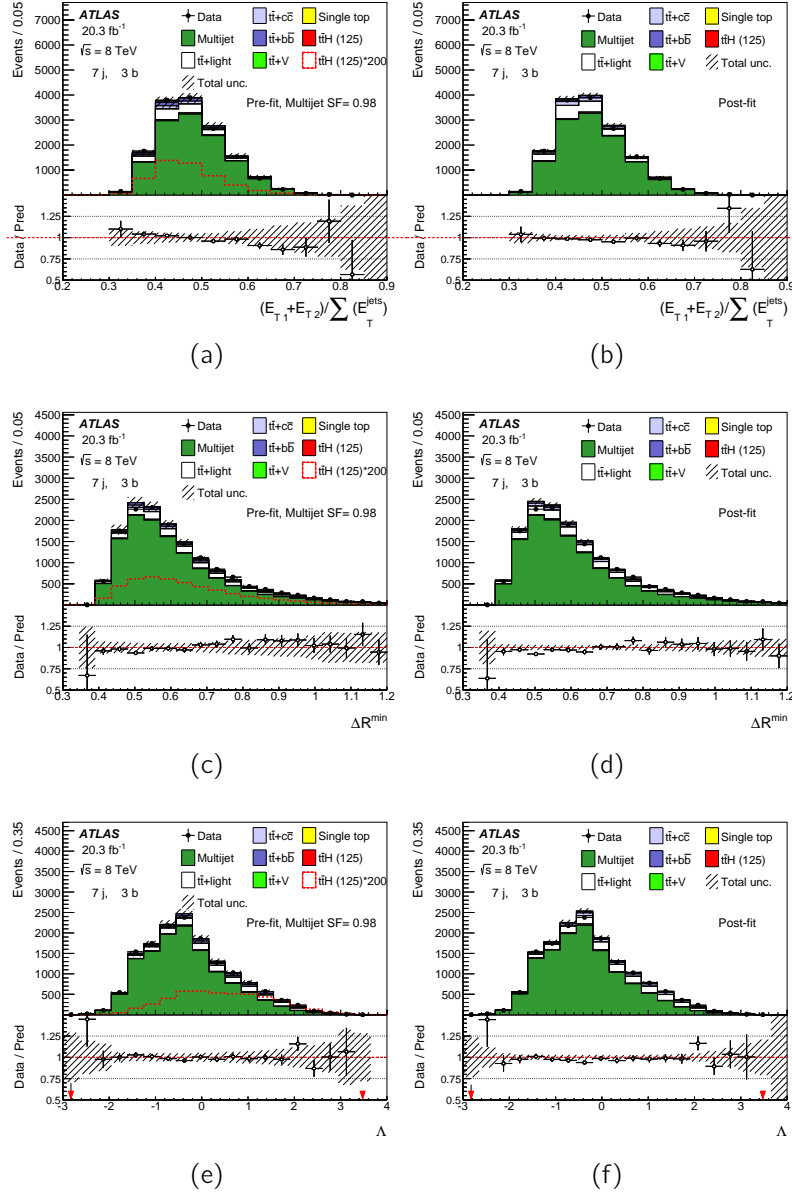


Figure 2.14.: Comparison between data and prediction for three top-ranked input variables in the (7j,3b) region before (left) and after (right) the fit. The fit is performed under the signal-plus-background hypothesis. Pre-fit plots show an overlay of the multijet distribution normalised to data for illustration purposes only. The plots include  $\frac{E_{T1}+E_{T2}}{\sum E_T^{\text{jets}}}$ ,  $\Delta R^{\min}$  and  $\Lambda$ . The definitions of the variables are listed in Table 2.3. The first and last bins in all figures contain the underflow and overflow, respectively. The bottom panel displays the ratio of data to the total prediction, red arrows indicate the position of the point outside the ratio window. The hashed area represents the total uncertainty in the background predictions. The  $t\bar{t}H$  signal yield (solid red) is scaled by a fixed factor, shown in the figure, before the fit.

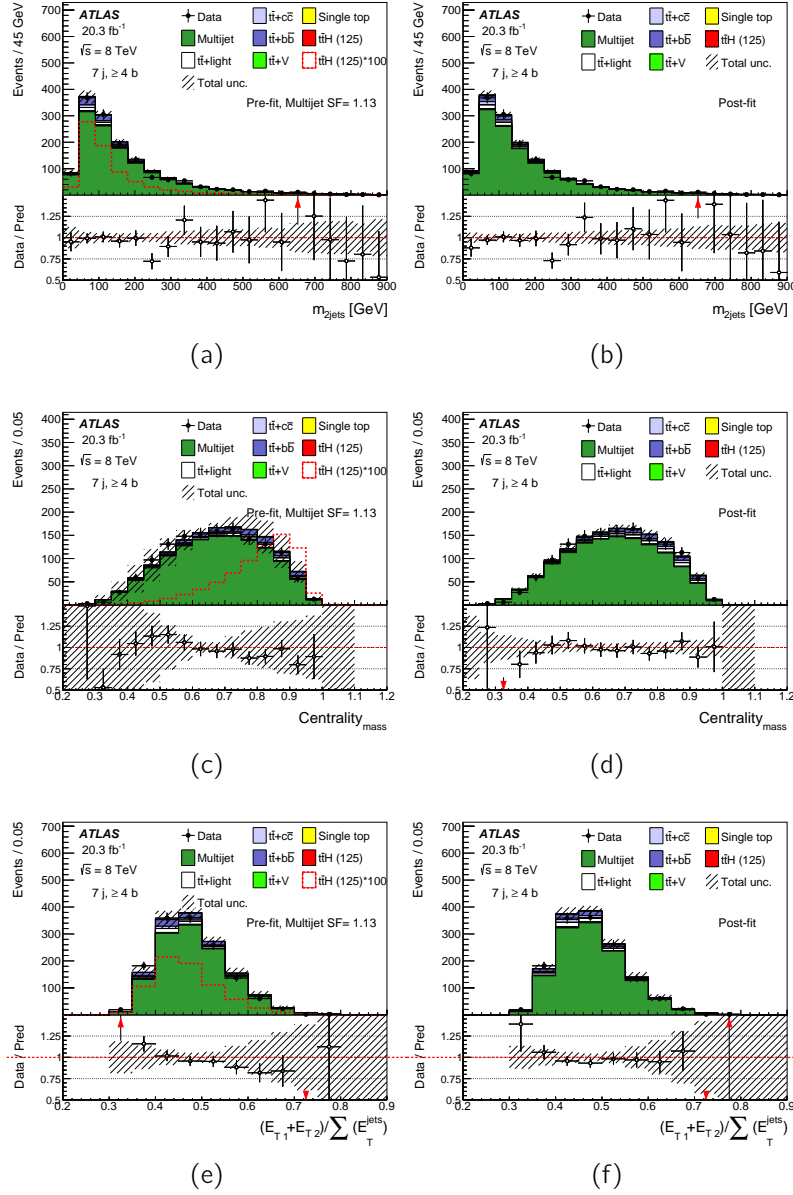


Figure 2.15.: Comparison between data and prediction for three top-ranked input variables in the  $(7j, \geq 4b)$  region before (left) and after (right) the fit. The fit is performed under the signal-plus-background hypothesis. Pre-fit plots show an overlay of the multijet distribution normalised to data for illustration purposes only. The plots include  $m_{2\text{jets}}$ ,  $\text{Centrality}_{\text{Mass}}$  and  $\frac{E_{T1} + E_{T2}}{\sum E_T^{\text{jets}}}$ . The definitions of the variables are listed in Table 2.3. The first and last bins in all figures contain the underflow and overflow, respectively. The bottom panel displays the ratio of data to the total prediction, red arrows indicate the position of the point outside the ratio window. The hashed area represents the total uncertainty in the background predictions. The  $t\bar{t}H$  signal yield (solid red) is scaled by a fixed factor, shown in the figure, before the fit.

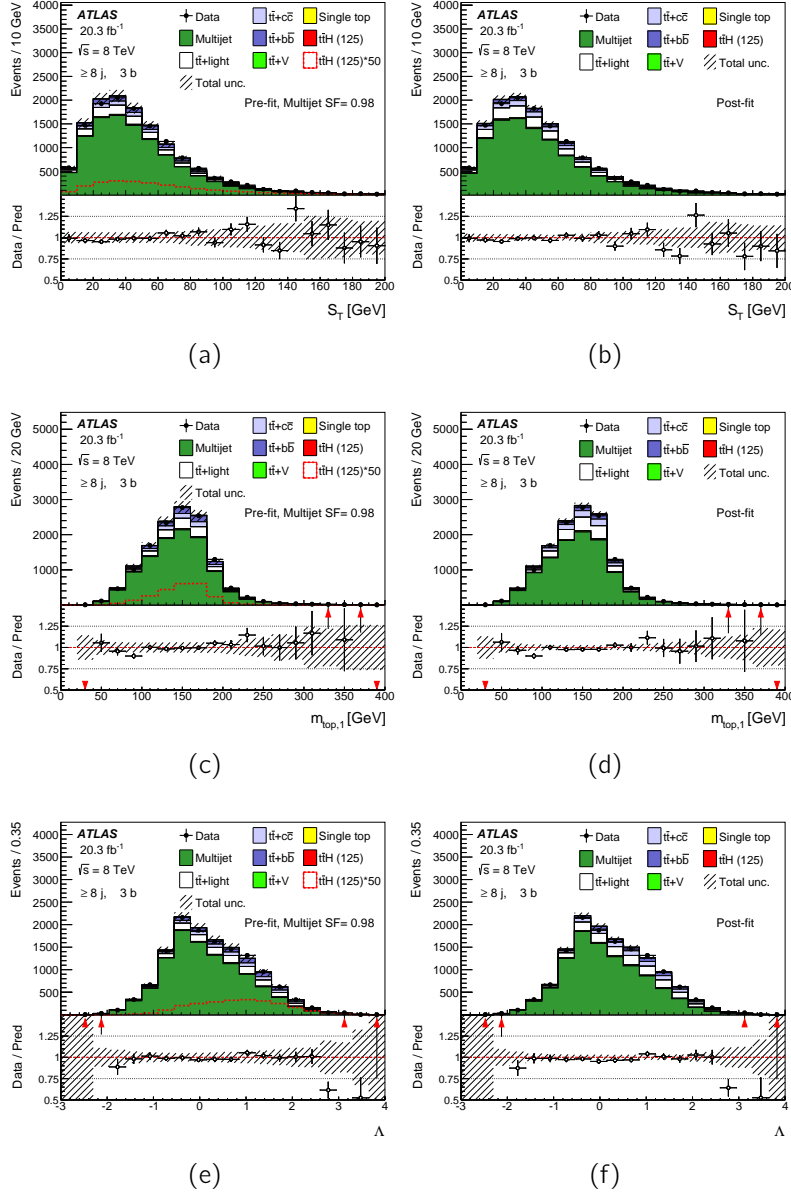


Figure 2.16.: Comparison between data and prediction for three top-ranked input variables in the  $(\geq 8j, 3b)$  region before (left) and after (right) the fit. The fit is performed under the signal-plus-background hypothesis. Pre-fit plots show an overlay of the multijet distribution normalised to data for illustration purposes only. The plots include  $S_T$ ,  $m_{top,1}$  and  $\Lambda$ . The definitions of the variables are listed in Table 2.3. The first and last bins in all figures contain the underflow and overflow, respectively. The bottom panel displays the ratio of data to the total prediction, red arrows indicate the position of the point outside the ratio window. The hashed area represents the total uncertainty in the ratio window. The  $t\bar{t}H$  signal yield (solid red) is scaled by a fixed factor, shown in the figure, before the fit.

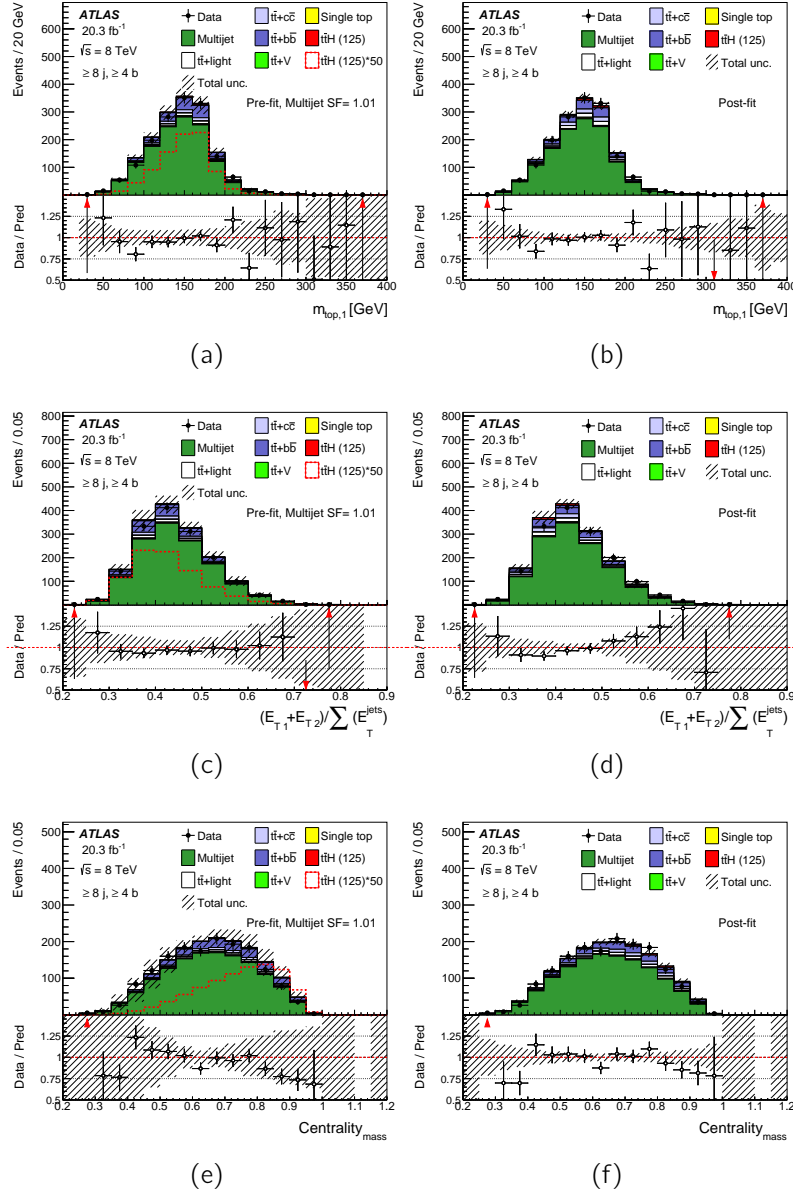


Figure 2.17.: Comparison between data and prediction for three top-ranked input variables in the  $(\geq 8j, \geq 4b)$  region before (left) and after (right) the fit. The fit is performed under the signal-plus-background hypothesis. Pre-fit plots show an overlay of the multijet distribution normalised to data for illustration purposes only. The plots include  $m_{\text{top},1}$ ,  $\frac{E_{T1} + E_{T2}}{\sum E_T^{\text{jets}}}$  and  $\text{Centrality}_{\text{Mass}}$ . The definitions of the variables are listed in Table 2.3. The first and last bins in all figures contain the underflow and overflow, respectively. The bottom panel displays the ratio of data to the total prediction, red arrows indicate the position of the point outside the ratio window. The hashed area represents the total uncertainty in the background predictions. The  $t\bar{t}H$  signal yield (solid red) is scaled by a fixed factor, shown in the figure, before the fit.

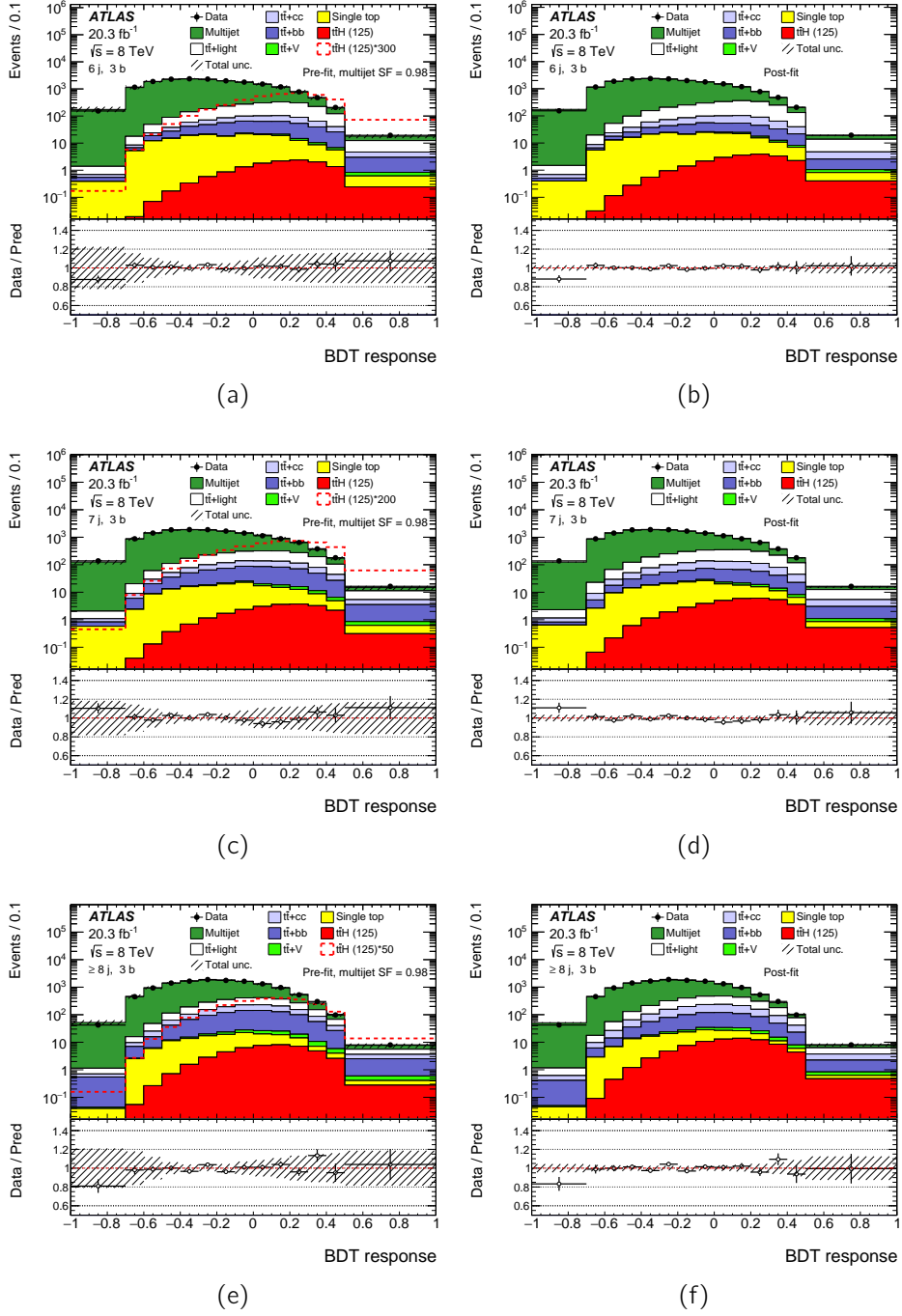


Figure 2.18.: Comparison between data and prediction for the BDT discriminant in the, from top to bottom, (6–8j, 3b) regions before (left) and after (right) the fit. The fit is performed under the signal-plus-background hypothesis. Pre-fit plots show an overlay of the multijet distribution normalised to data for illustration purposes only. The bottom panels display the ratios of data to the total prediction. The hashed areas represent the total uncertainty in the background predictions. The  $t\bar{t}H$  signal yield (solid red) is scaled by a fixed factor, shown in the figure, before the fit.

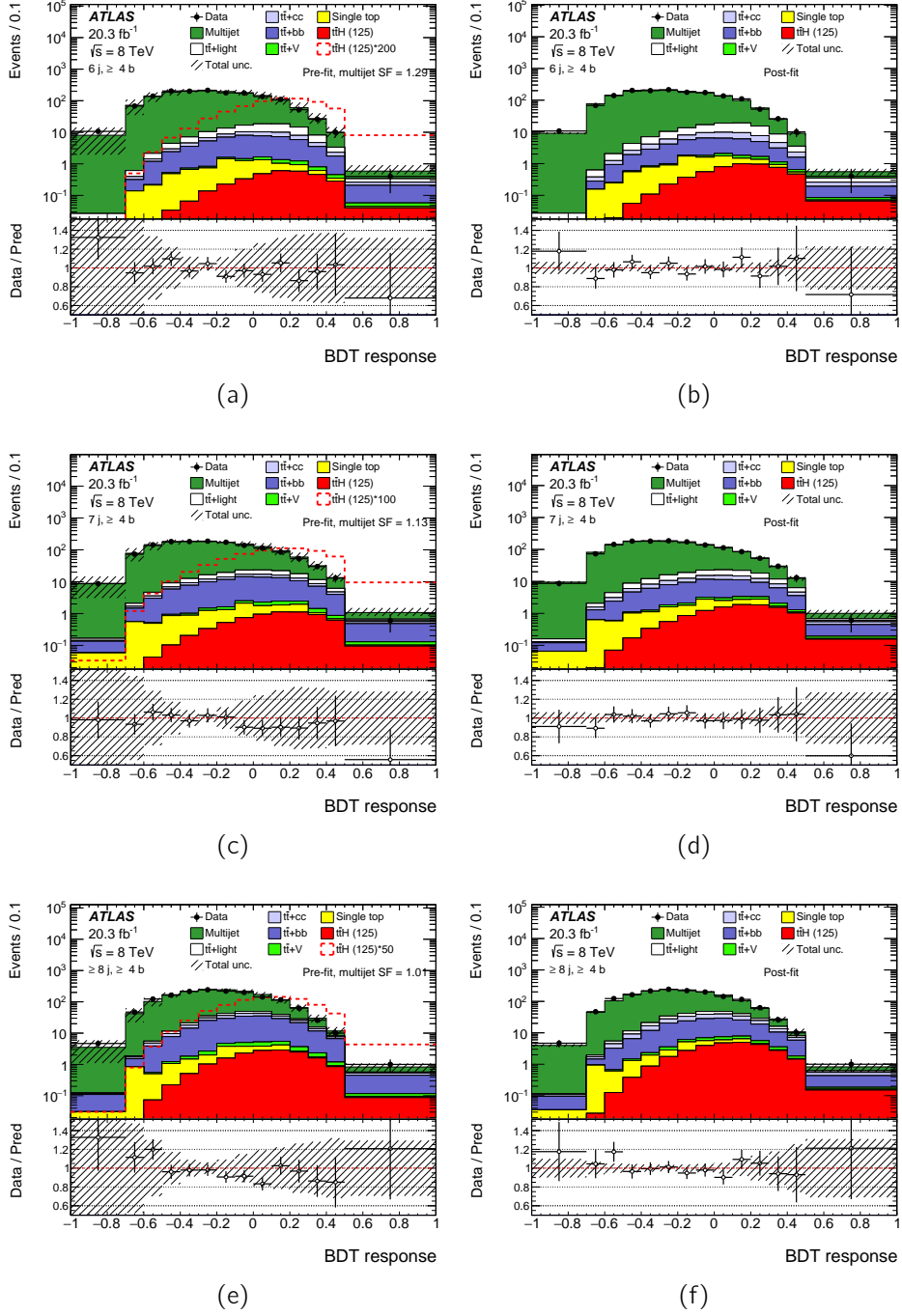


Figure 2.19.: Comparison between data and prediction for the BDT discriminant in the, from top to bottom,  $(6-8j, \geq 4b)$  regions before (left) and after (right) the fit. The fit is performed under the signal-plus-background hypothesis. Pre-fit plots show an overlay of the multijet distribution normalised to data for illustration purposes only. The bottom panels display the ratios of data to the total prediction. The hashed areas represent the total uncertainty in the background predictions. The  $t\bar{t}H$  signal yield (solid red) is scaled by a fixed factor, shown in the figure, before the fit.

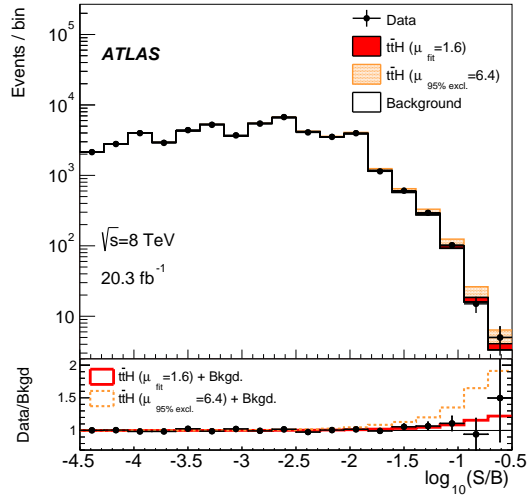


Figure 2.20.: Event yields as a function of  $\log_{10}(S/B)$ , where  $S$  (expected signal yield) and  $B$  (expected background yield) are taken from the corresponding BDT discriminant bin. Events from all fitted regions are included. The predicted background is obtained from the global signal-plus-background fit. The  $t\bar{t}H$  signal is shown both for the best-fit value ( $\mu = 1.6$ ) and for the upper limit at 95% CL ( $\mu = 6.4$ ).

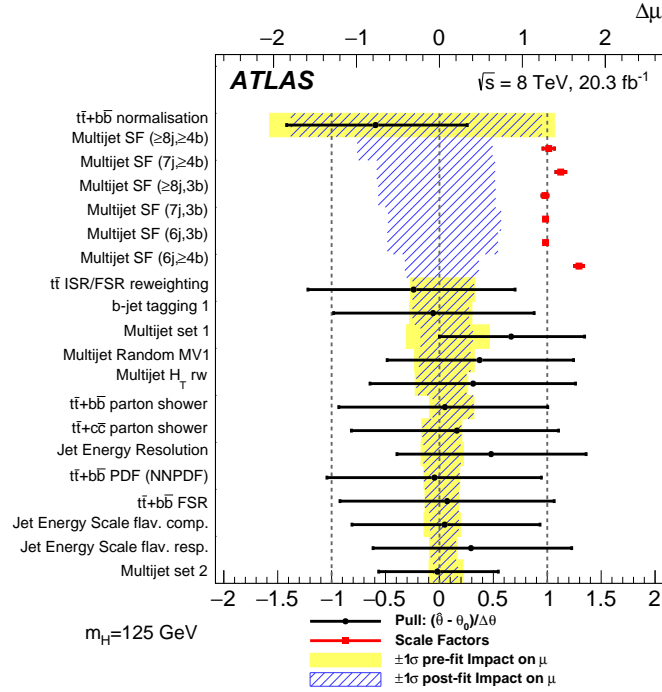


Figure 2.21.: The fitted values of the 20 nuisance parameters corresponding to the sources of systematic uncertainty with the largest impact on the fitted signal strength  $\mu$ . The points, which are drawn conforming to the scale of the bottom axis, show the deviation of each of the fitted nuisance parameters  $\hat{\theta}$  from  $\theta_0$ , which is the nominal value of that nuisance parameter, in units of the pre-fit standard deviation  $\Delta\theta$ . The plain yellow area represents the pre-fit impact on  $\mu$  and the hashed blue area its post-fit impact. The error bars show the post-fit uncertainties  $\sigma_\theta$ , which have size close to one if the data do not provide any further constraint on that uncertainty. Conversely, an error bar for  $\sigma_\theta$  smaller than one indicates a reduction with respect to the original uncertainty. The nuisance parameters are sorted according to their post-fit impact  $\Delta\theta$  (top horizontal scale). Multijet scale factors (SF) show the fitted values and uncertainties of the normalisation parameters that are freely floating in the fit. These normalisation parameters have a pre-fit value of unity.



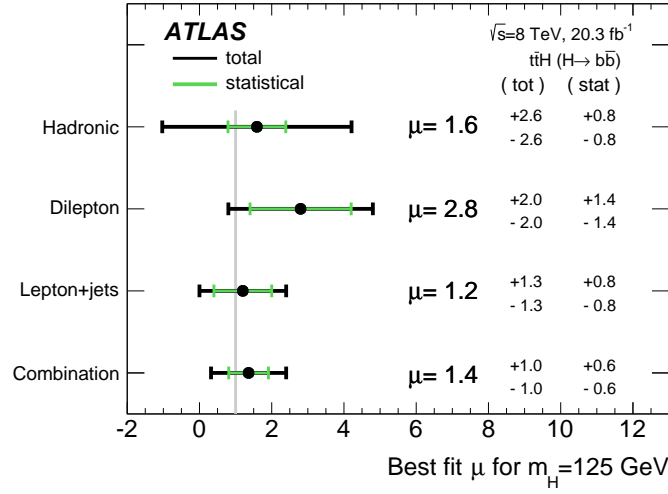


Figure 2.22.: Summary of the measurements of the signal strength  $\mu$  for  $t\bar{t}H(H \rightarrow b\bar{b})$  production for the individual  $H \rightarrow b\bar{b}$  channels and for their combination, assuming  $m_H = 125$  GeV. The total (tot) and statistical (stat) uncertainties of  $\mu$  are shown. The SM  $\mu = 1$  expectation is shown as the grey line.

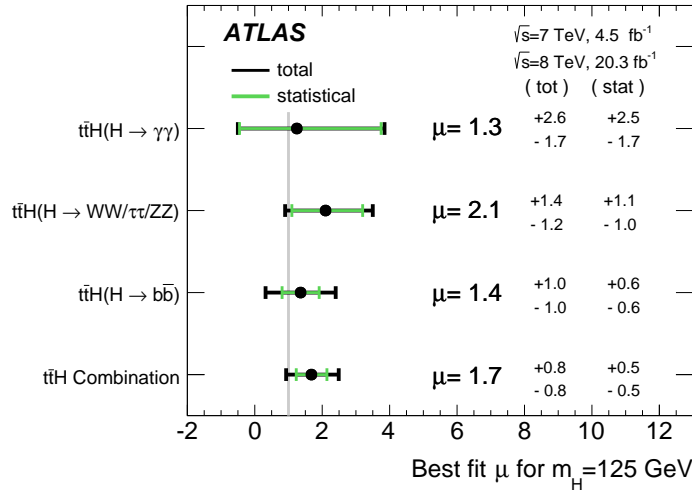


Figure 2.23.: Summary of the measurements of the signal strength  $\mu$  for the individual channels and for their combination, assuming  $m_H = 125$  GeV. The total (tot) and statistical (stat) uncertainties of  $\mu$  are shown. The SM  $\mu = 1$  expectation is shown as the grey line.

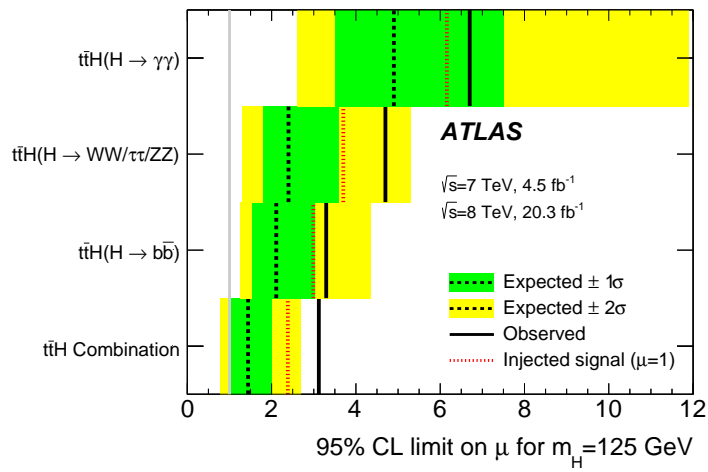


Figure 2.24.: Upper limits on the signal strength  $\mu$  for the individual channels as well as for their combination, at 95% CL. The observed limits (solid lines) are compared to the expected median limits under the background-only hypothesis (black dashed lines) and under the signal-plus-background hypothesis assuming the SM prediction for  $\sigma(tt\bar{t}H)$  (red dotted lines). The surrounding green and yellow bands correspond to the  $\pm 1\sigma$  and  $\pm 2\sigma$  ranges around the expected limits under the background-only hypothesis.

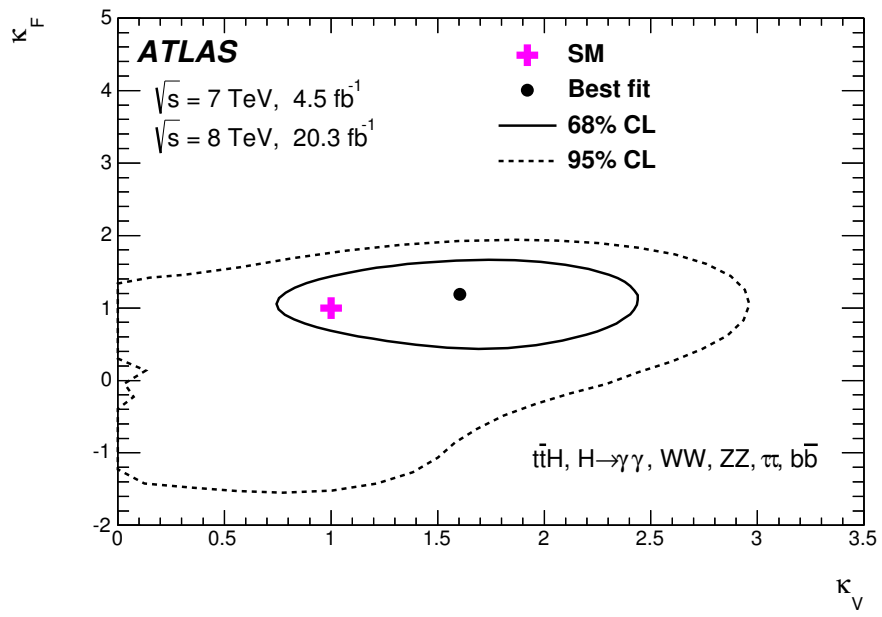


Figure 2.25.: Log-likelihood for the combined  $t\bar{t}H$  fit. The fit agrees with the SM expectation within the 68% CL contour. The physical boundary of  $\kappa_V \geq 0$  is considered.

Table 2.9.: Observed and expected (median, for the background-only hypothesis) upper limits at 95% CL on  $\sigma(t\bar{t}H)$  relative to the SM prediction, for the individual channels as well as for their combination. The  $\pm 1\sigma$  and  $\pm 2\sigma$  ranges around the expected limit are also given. The expected median upper limits at 95% CL assuming the SM prediction for  $\sigma(t\bar{t}H)$  are shown in the last column.

Analysis	95% CL upper limit						Signal strength
	Observed	Expected					
		$-2\sigma$	$-1\sigma$	median	$+1\sigma$	$+2\sigma$	
$t\bar{t}H(H \rightarrow \gamma\gamma)$	6.7	2.6	3.5	4.9	7.5	11.9	$1.2^{+2.6}_{-1.8}$
$t\bar{t}H(H \rightarrow \text{leptons})$	4.7	1.3	1.8	2.4	3.6	5.3	$2.1^{+1.4}_{-1.2}$
$t\bar{t}H(H \rightarrow b\bar{b})$	3.3	1.3	1.5	2.1	3.0	4.4	$1.4 \pm 1.0$
$t\bar{t}H$ Combination	3.1	0.8	1.0	1.4	2.0	2.7	$1.7 \pm 0.8$

# 3. Stashing the stops in multijet events at the LHC

The work presented in this chapter was performed in the framework of the PES-BLADe collaboration (Probing the nature of Electroweak Symmetry Breaking at the LHC with the ATLAS Detector), a project involving particle physicists experimentalists from the ATLAS CPPM group, and theorists from L2C and LUPM, funded by the labex OCEVU <sup>a</sup>. This chapter describes the work carried out by Gilbert Moulta (Laboratoire Charles Coulomb, Université de Montpellier), myself and Sara Diglio, CPPM post-doc with a background on phenomenology, hired by OCEVU. The project aimed at re-interpreting  $t\bar{t}H$ -like analyses, at the core of the CPPM-ATLAS group activities, in terms of searches for signatures of BSM physics, and finally it focused on investigating signatures of stop squark pair production for R-parity violating supersymmetric models. This work was just recently published [73].

## 3.1. Introduction

The discovery at the Large Hadron Collider (LHC) of a weakly-coupled, spin-0 particle compatible with the Higgs boson [10, 11, 12, 13], by both ATLAS [173] and CMS [174] collaborations, with a mass of approximately 125 GeV [175], constrains all theoretical extensions to the Standard Model (SM) that aim at a mechanism for spontaneous Electroweak Symmetry Breaking (EWSB) relieved of the *naturalness problem*. In the coming years the measurements of the properties of this new particle will shed further light on the possibility of new physics at the TeV scale. While the presence of a new class of phenomena at the TeV scale is predicted by a large variety of models which address the various theoretical shortcomings of the SM, the LHC Run 1 and first Run 2 data sets analysed so far gave no evidence for new physics Beyond the Standard Model (BSM). Indirect manifestations might be hiding in heavy flavor rare decays anomalies reported by LHCb [176, 177] with moderate to sizable statistical significance [178], and the well established neutrino oscillation phenomena [46] can be viewed as clear indications for the need for BSM physics [179].

Supersymmetry (SUSY) [180, 181, 182, 183, 184, 185] has long been considered to be an elegant way of triggering the EWSB, relating it radiatively through perturbative quantum effects to possible new physics at much higher scales, such as Grand Unification, while stabilizing the various scales without unnatural fine-tunings. It can also provide in its R-parity conserving (RPC) version several dark

---

<sup>a</sup><https://www.labex-ocevu.univ-amu.fr/>

matter candidates, the most popular being a neutralino when the lightest supersymmetric particle (LSP). Nonetheless, the naturalness of the Higgs potential favors light third-generation squarks whose RPC striking signatures have yet to be observed at hadron colliders, pushing the limits on the mass of such particles at the boundary of what is accepted to be natural. This could be a hint that the role of SUSY as a panacea for all SM standing problems should be revised. In particular if R-parity violating (RPV) operators [186, 187] in the superpotential are not artificially suppressed to allow for instance for a neutralino dark matter, RPV SUSY could be welcome for a natural EWSB since most of LHC constraints based on searches for missing energy signatures would not be valid anymore. One thus expects the interest in RPV SUSY searches at the LHC to build up significantly in the coming years [188].

From the theoretical point of view, it is attractive to view R-parity breaking as a dynamical issue. The magnitude of the RPV couplings could then be related to residual low-energy effects of some ultraviolet completions of the minimal SUSY extension of the Standard Model, see e.g. [189, 190] for recent reviews. On a more fundamental level, whether R-parity is conserved or not as a residual discrete symmetry of continuous R-symmetries, could also depend on the breaking mechanisms of the latter, which is an open question intimately related to the origin of SUSY breaking itself [191]. The presence of RPV operators with small couplings, but still sufficiently large to trigger prompt decays within the detector, is thus not unlikely. It can also preserve some of the appealing features of the RPC scenarios; e.g. a very light metastable gravitino can provide a viable dark matter candidate, and the stability of the proton can be protected by other discrete symmetries [192].

Limits on RPV scenarios have been given by ATLAS [193, 194, 195, 196, 197, 198, 199] and CMS [200, 201, 202, 203, 204, 205, 206, 207, 208]. These limits rely on simplifying model assumptions. In particular, the mass limits on the lighter stop assume in the case of hadronic stop RPV decays 100% branching ratio into two body final states [208, 198, 199]. It follows that, apart from the qualitative requirement of prompt decays, the derived limits are independent of the size of the RPV couplings themselves, and thus insensitive to the experimental limits on the latter [209]. While this assumption is clearly valid if the stop were the LSP, it calls for more model-dependence in the opposite case.

It has been pointed out in Ref. [210] that busier final states with high  $b$ -quark multiplicities, not looked for by the LHC experiments so far, can become the dominant stop decay channels in regions of the parameter space where part of the neutralino/chargino sector is lighter than the lightest stop, thus mitigating the present LHC limits. Furthermore, as shown in Refs. [211, 212, 213], existing experimental searches performed at the LHC, such as di-jet resonant production, top-quark pairs, four-tops and displaced decays, can be re-interpreted as limits for a class of RPV couplings involving the stop and SM quarks.

In the present work we go a step further by considering extensively the sensi-

tivity to the magnitudes of the RPV couplings for stop-pairs production. This pinpoints the critical role of the size of these couplings in unveiling the final states that are dominant among all the different combinations of stop decay chains. It also unfolds the experimental strategy to be sensitive to stop pair production and decays, spanning several orders of magnitude for the value of the RPV couplings.

The rest of the chapter is organized as follows: in Section 3.2 we recall the main theoretical ingredients of the RPV sector of the Minimal Supersymmetric Standard Model (RPV-MSSM), as well as the present LHC limits on RPV stop searches, discussing possible new search channels, and give the simplifying model assumptions we make. In Section 3.3 we describe the general features of the stop pair production and decays, classify all the possible decay channels triggered by R-parity violation and motivate the allowed range of the corresponding couplings. In Section 3.4 we give an analytical discussion of the sensitivity to the considered RPV coupling, while in Section 3.5 we identify two classes of benchmark points of the model. The stop pair production total cross-section and decay channels for these two benchmark points are evaluated in Section 3.6 illustrating quantitatively the phenomenological sensitivities to the RPV coupling and to the stop-chargino mass splitting. Section 3.7 is devoted to a discussion of the signal and background issues for each of the promising final states.

## 3.2. Model assumptions

### 3.2.1. RPV-MSSM

The superpotential of the RPV-MSSM (see for instance [209]) has three distinct parts:

$$W_{\text{RPV}} = W_{\text{RPC}} + W_{\mathbb{L}} + W_{\mathbb{B}} . \quad (3.1)$$

The R-parity conserving part,

$$W_{\text{RPC}} = (Y^L)_{ij} \hat{L}_i \cdot \hat{H}_1 \hat{E}_j^c + (Y^D)_{ij} \hat{Q}_i \cdot \hat{H}_1 \hat{D}_j^c + (Y^U)_{ij} \hat{Q}_i \cdot \hat{H}_2 \hat{U}_j^c + \mu \hat{H}_2 \cdot \hat{H}_1 , \quad (3.2)$$

involves the Yukawa coupling matrices  $Y^L, Y^D, Y^U$  and the Higgs mixing parameter  $\mu$ . The R-parity violating part,  $W_{\mathbb{L}} + W_{\mathbb{B}}$ , splits into a lepton number violating sector involving bilinear and trilinear couplings,

$$W_{\mathbb{L}} = \frac{1}{2} \lambda_{ijk} \hat{L}_i \cdot \hat{L}_j \hat{E}_k^c + \lambda'_{ijk} \hat{L}_i \cdot \hat{Q}_j \hat{D}_k^c + \mu_i \hat{L}_i \cdot \hat{H}_2, \quad (3.3)$$

and a baryon number violating sector involving trilinear couplings,

$$W_{\mathbb{B}} = \frac{1}{2} \lambda''_{ijk} \hat{U}_i^{\alpha c} \hat{D}_j^{\beta c} \hat{D}_k^{\gamma c} \epsilon_{\alpha\beta\gamma}. \quad (3.4)$$

The chiral superfields  $\hat{L}$  and  $\hat{Q}$  denote respectively the lepton and quark  $SU(2)$

doublets,  $\hat{E}, \hat{D}$  and  $\hat{U}$  the corresponding singlets, and  $\hat{H}_1$  and  $\hat{H}_2$  are the two Higgs doublets, together with their conventional  $U(1)_Y$  hypercharges. Summation over repeated indices is understood in all the above expressions where  $\alpha, \beta, \gamma = 1, 2, 3$  denote the  $SU(3)$  color indices, the dots ( $A \cdot B \equiv \epsilon_{ab} A^a B^b$ ) define  $SU(2)$  invariants, the  $i, j, k = 1, 2, 3$  are generation indices, and  $c$  indicates charge conjugation. Also the trilinear RPV couplings should satisfy the relation:

$$\lambda_{ijk} = -\lambda_{jik} \text{ and } \lambda''_{ijk} = -\lambda''_{ikj}, \quad (3.5)$$

as an immediate consequence of the antisymmetry of the  $\epsilon_{ab}$  and  $\epsilon_{\alpha\beta\gamma}$  symbols respectively.

Recall that to account for SUSY breaking, assumed to be soft in the visible sector, the low energy MSSM is expected to have additional RPC and RPV terms in the Lagrangian density with the following general structure,

$$\mathcal{L}_{\text{RPC}}^{\text{soft}} = -V_{\text{RPC}}^{\text{soft}} - \frac{1}{2}(M_1 \tilde{B} \tilde{B} + M_2 \tilde{W} \tilde{W} + M_3 \tilde{g} \tilde{g}), \quad (3.6)$$

where

$$\begin{aligned} V_{\text{RPC}}^{\text{soft}} = & (m_{\tilde{Q}}^2)_{ij} \tilde{Q}_i^\dagger \tilde{Q}_j + (m_{\tilde{U}}^2)_{ij} \tilde{U}_i^\dagger \tilde{U}_j + (m_{\tilde{D}}^2)_{ij} \tilde{D}_i^\dagger \tilde{D}_j + (m_{\tilde{L}}^2)_{ij} \tilde{L}_i^\dagger \tilde{L}_j \\ & + (m_{\tilde{E}}^2)_{ij} \tilde{E}_i^\dagger \tilde{E}_j + m_{H_1}^2 |\tilde{H}_1|^2 + m_{H_2}^2 |\tilde{H}_2|^2 + ((T^l)_{ij} \tilde{L}_i \cdot \tilde{H}_1 \tilde{E}_j^c \\ & + (T^d)_{ij} \tilde{Q}_i \cdot \tilde{H}_1 \tilde{D}_j^c + (T^u)_{ij} \tilde{Q}_i \cdot \tilde{H}_2 \tilde{U}_j^c + B_\mu \tilde{H}_2 \cdot \tilde{H}_1 + \text{h.c.}) \end{aligned} \quad (3.7)$$

involves the RPC soft SUSY breaking scalar masses, trilinear couplings and Higgs mixing, and

$$\mathcal{L}_{\text{RPV}}^{\text{soft}} = -V_{\not{L}}^{\text{soft}} - V_{\not{B}}^{\text{soft}}, \quad (3.8)$$

where

$$V_{\not{L}}^{\text{soft}} = \frac{1}{2} T_{ijk} \tilde{L}_i \cdot \tilde{L}_j \tilde{E}_k^c + T'_{ijk} \tilde{L}_i \cdot \tilde{Q}_j \tilde{D}_k^c + B_i \tilde{L}_i \cdot \tilde{H}_2 + \tilde{m}_{1i}^2 \tilde{H}_1^\dagger \tilde{L}_i + \text{h.c.}, \quad (3.9)$$

and

$$V_{\not{B}}^{\text{soft}} = \frac{1}{2} T''_{ijk} \tilde{U}_i^{\alpha c} \tilde{D}_j^{\beta c} \tilde{D}_k^{\gamma c} \epsilon_{\alpha\beta\gamma} + \text{h.c.} \quad (3.10)$$

involve respectively the lepton and baryon number violating soft SUSY breaking bilinear and trilinear couplings. In Eq. (3.6) the twiddled fields denote the  $U(1)_Y$ ,  $SU(2)_L$ , and  $SU(3)$  gauginos in the Weyl representation where we have suppressed the gauge indices, and  $M_1, M_2, M_3$  denote their soft masses. The fields in Eqs. (3.7, 3.9, 3.10) are the scalar components of the chiral superfields entering the superpotentials (3.2–3.4) and the  $m^2$ 's,  $B_\mu, B_i, T^{l,d,u}, T, T' T''$  are the bilinear and trilinear soft-susy breaking parameters. We define also  $\tan \beta \equiv \frac{v_2}{v_1}$ , the ratio of the vacuum expectation values developed by  $H_2$  and  $H_1$  after EWSB.



In the sequel we do not rely on specific high scale model assumptions which can trigger the EWSB and correlate the various low-energy SUSY preserving and soft breaking parameters, or possibly provide a dynamical origin to the RPV couplings [189, 190]. Given the low-energy phenomenological assumptions we rely on, the process of stop production and decays under consideration depends only on a reduced set of MSSM parameters insensitive to such correlations. Furthermore, we assume conservatively minimal flavor violation (MFV) [214], since the heavy versus light quark content of the final states is instrumental to our study.

### 3.2.2. LHC searches and new channels

The likeliness of a relatively light stop, motivated by natural SUSY and a large mass splitting between the two stop states that could account for the observed Higgs boson mass (at least within the MSSM), together with the more general expectation that the third (s)quark generation plays a central role in triggering the electroweak symmetry breaking, makes the search for light stops particularly compelling. This is true both in RPC and RPV scenarios. The present LHC mass limits from direct production in the RPC scenarios are of order 800 GeV [215, 216, 217, 218] and the exploitable range is expected to cross the TeV scale towards the end of Run 2. Moreover, some of the all-leptonic RPV searches have already increased this limit in some cases up to 1020 GeV [200]. Lighter stops could however still be hiding in the all-hadronic channels final states with very low missing energy, as would be typically the case in RPV scenarios if dominated by baryon number violating couplings  $\lambda''_{33i}$ , cf. Eq. (3.4). Searches for directly produced stop pairs each decaying into one jet originating from a  $b$  and one jet from a light quark with the data collected in 2012 at  $\sqrt{s} = 8$  TeV and in 2015 at  $\sqrt{s} = 13$  TeV lead to exclusion mass limits in the range 100-380 GeV by the CMS [208] and ATLAS [198, 199] collaborations.

Both ATLAS [193, 194, 195, 196, 197] and CMS [200, 201, 202, 203, 204, 205, 206, 207] have also looked for signatures of RPV scenarios through either gluino decays assuming baryon number violating couplings, or squark decays assuming lepton number violating bilinear and trilinear couplings. The ensuing mass limits for the gluino and first and second generation squarks range from 800 GeV up to 1.9 TeV depending on the model assumptions.

It is important to keep in mind that the limits quoted above assume the RPV decays to proceed through the shortest decay chains. In particular the ones on direct production of stops decaying through baryon number violating couplings, are derived under the assumption of 100% decay into a bottom and a light quark. These limits carry thus some model-dependence irrespective of whether lepton number violating decays are ignored or not. As observed in Ref. [210], if the stop is not the LSP in parts of the parameter space motivated by natural SUSY, then its decays may become dominated by channels with higher  $b$ -quark multiplicities. In this case, a different experimental strategy is called for when looking for a sig-

nal or setting limits, thus putting into more perspective the meaning and reach of the present experimental limits on light stops. However, it is to be stressed that even in Ref. [210] a 100% decay in the final states under consideration is assumed, this time not for the decaying mother stop itself but for the subsequent decay of the intermediate on-shell chargino present in the decay chain. As noted in the introduction, such an assumption makes the processes and the experimental limits insensitive to the magnitude of the relevant RPV couplings. Not only is it desirable to be able to set limits on these couplings as well, but in fact, in the configurations where *the LSP is neither a squark nor a slepton*, the branching fractions of the various RPV decays of the latter depend necessarily on the magnitudes of the RPV couplings. That this is to be expected on general grounds can be seen from the simple fact that in the limit of vanishing RPV couplings the RPC theory should be recovered smoothly. Indeed, in this limit, of all the RPV signal processes only the ones that tend to the RPC signals, i.e. containing an on-shell long-lived LSP in the decay chain, will survive. This implies that when decreasing the RPV couplings a crossover in favor of the decays containing the LSP must occur at some point. Moreover, in the regions where they become sizable, the latter channels tend to be less sensitive to the RPV couplings since the LSP decays only through RPV channels, thus with branching ratio 1 to the relevant final states. The only limitation is that the RPV couplings should remain sufficiently large for the LSP to decay within the detector, otherwise the RPC search limits become effective.

Put differently, assuming a branching ratio of 1 for a given decay channel implicitly entails a given range of the RPV couplings, that would further depend on the mass spectrum and RPC couplings of the particles involved in the decay. This observation has two consequences:

- while all the quoted present experimental limits on RPV scenarios have obviously some model-dependence, the sensitivity to the RPV couplings exacerbates this model-dependence;
- higher jet and/or lepton multiplicity decays probe smaller (even tiny) RPV couplings benefiting in the same time from a reduced SM background.

The aim of the subsequent sections is to demonstrate the above general features quantitatively in the case of baryon number violating RPV couplings  $\lambda''_{331}$  or  $\lambda''_{332}$  that trigger the decay of stops leading to  $b$ -quarks, light quarks and possibly leptons in the final states.

### 3.2.3. mass spectrum

In this section we describe the simplified working assumptions made in the paper:

- (i)  $\lambda''_{33i}$ , with  $i = 1$  or  $2$ , is the only non-vanishing RPV coupling,

- (ii) the light part of the SUSY spectrum is composed of one stop, one chargino, two neutralinos and the lightest CP-even Higgs (referred to respectively as  $\tilde{t}, \chi^+, \chi^0/\chi_2^0$  the lighter/heavier neutralino and  $h^0$  the SM-like Higgs throughout the paper). All other SUSY and Higgs particles, except possibly for the gluino, are assumed to be too heavy to be produced at the LHC,
- (iii) the RPV-MSSM-LSP is the lightest neutralino  $\chi^0$ .

A few comments are in order here. Assumptions (i), (ii), (iii) are not mandatory for the validity of the general message we convey in this paper regarding the final-state-dependent sensitivity to the RPV couplings. They serve as a concrete illustration in one possible physically interesting configuration. Assumption (i) can be seen as an idealization of some generic assumptions such as MFV where baryon number violating RPV couplings containing 1st and 2nd generation indices are suppressed with respect to  $\lambda''_{332}$  (or  $\lambda''_{331}$ ) [219, 220]. Alternatively, it could result from a dynamical collective effect due to the running of several RPV couplings from a common value at some very high scale down to the electroweak scale where  $\lambda''_{332}$  becomes much larger than the other couplings [221, 222]. In fact, our analysis does not depend crucially on the single RPV coupling dominance assumption: indeed, combined with assumption (ii), assumption (i) is not particularly restrictive given the hadronic final states and parameter space under consideration. For one thing,  $\lambda''_{33i}$  can be viewed as accounting for the combination  $\sqrt{(\lambda''_{332})^2 + (\lambda''_{331})^2}$  since at present hadron colliders light  $d$ - and  $s$ -quark productions are indistinguishable.<sup>b</sup> For another, most of the lepton number violating couplings in Eq. (3.3) do not contribute to the final states under consideration, or else are irrelevant due to the assumed heaviness of the squarks and sleptons. The only possible exception is the set of  $\lambda'_{ij3}$  couplings that induce  $\tilde{t}$  decays into bottom quark and a lepton. This channel would however be suppressed for a small left-handed component of the lightest stop, and in any case can be vetoed as it leads to final states with leptons and no light quarks, different from the ones we study. Finally the baryon number violating couplings  $\lambda''_{132}, \lambda''_{232}$  can in principle contribute to final states containing  $b$ - and light quarks through the flavor mixing of the 3rd generation with the 1st and 2nd generation squarks (current states). However this mixing is very small for the SUSY spectrum we consider which suppresses the sensitivity to these couplings altogether. Thus most of the RPV couplings could still be non-vanishing without affecting our analysis. Assumption (ii) can be motivated on one hand by simplicity, with only a small part of the MSSM spectrum to deal with phenomenologically, and on the other by the need to account for the light CP-even Higgs mass while keeping at a relatively moderate level the fine-tuning required to get the electroweak scale from the

---

<sup>b</sup>This correspondence is valid up to indirect effects originating from RPV induced loop corrections to the  $\tilde{t}$  mass [223]. These effects remain, however, negligibly small in the  $\lambda''_{33i}$  range we consider.

radiative electroweak symmetry breaking, see e.g. [224]. It should be stressed however that the latter naturalness criterion being more a practical guide than a physics principle, the actual realisation of the low lying states of supersymmetry could well be through quite different configurations than the ones motivated by naturalness.

As concerns assumption (iii), obviously not motivated by dark matter issues since the RPV-MSSM-LSP is unstable and assumed to decay promptly, its aim is to remain as close as possible to the conventional spectrum configurations for which most of the present experimental bounds for RPC scenarios have been established. In particular this allows to relate in a well defined way to the latter bounds whenever  $\lambda''_{33i}$  becomes too small for the  $\chi^0$  to decay within the detector. Still it is important from a more general perspective to assess the dark matter candidates in the RPV context. We only note here that among the possible scenarios a light gravitino, being for that matter the true LSP (leaving the  $\chi^0$  as the RPV-MSSM-LSP), can indeed provide a good metastable candidate even for moderately large RPV couplings of order  $10^{-2}$  or larger, for sufficiently heavy sfermions [225, 226, 227]. In fact, with assumption (i), a gravitino lighter than twice the  $b$ -quark mass would be even totally stable.

Besides assumptions (i), (ii), (iii), we focus mainly, though not exclusively, on the MSSM parameter regions that are consistent with the following mass configuration:

$$m_{\tilde{t}} \gtrsim m_{\chi_2^0} \gtrsim m_{\chi^+} \gtrsim m_{\chi^0} > m_t , \quad (3.11)$$

$$m_{\tilde{t}} - m_{\chi^0} < m_t , \quad (3.12)$$

$$m_{\tilde{t}} - m_{\chi^+} > m_b . \quad (3.13)$$

Such a configuration has been already considered in Ref. [210] to illustrate the relevance of multi  $b$ -quark final states when an on-shell chargino is present in the stop decay chain. In the present work we stress the relevance of the longer decay chain not considered previously, containing on-shell chargino and neutralino, and in particular the importance of the magnitude of  $\lambda''_{33i}$  in selecting the stop decay channels that actually dominate. Note also the presence of two neutralinos in the low energy spectrum. This is unavoidable when the chargino/neutralino light sector is assumed to be Higgsino-like as we do: in the limit  $M_1 \simeq M_2 \gg \mu \gg m_W$  and  $\tan \beta \gg 1$  one finds  $m_{\chi_2^0} - m_{\chi^+} \sim m_{\chi^+} - m_{\chi^0} \simeq \frac{5}{8} \frac{m_W^2}{M_1}$  up to loop corrections, which corresponds to a compressed spectrum satisfying the mass hierarchy in the chargino/neutralino sector as given in Eq. (3.11). However, as long as the configuration in Eq. (3.12) is satisfied the second neutralino,  $\chi_2^0$ , does not contribute significantly to the stop decay since it enters the decay chain only off shell, and is neglected throughout the study.

### 3.3. Stop production and decays

#### 3.3.1. pair production

The stop pair production at the LHC,  $pp \rightarrow \tilde{t}\tilde{t}^* + X$ , proceeds mainly through gluon-gluon fusion QCD processes, see [228, 229, 230] and references therein. While quark-anti-quark partonic contributions are subdominant at LHC energies, there could also be interesting single, or same-sign pair, stop (associated) productions respectively through RPV quark-quark processes or QCD gluon-gluon processes [231], [213]. Some of these channels are suppressed in our case, either because  $\lambda''_{3ki}$  with  $k \neq 3$  are assumed to be vanishing or due to the assumed heaviness of the gluino and first and second squark generations. The single stop production and decays can already constrain parts of the parameter space for a light LSP as shown in [213]. Note however that the corresponding production cross-section becomes subdominant as compared to the pair production when  $\lambda''_{33i}$  is taken  $\lesssim O(10^{-2})$  and  $m_{\tilde{t}} \gtrsim 500$  GeV, and even totally suppressed for the much smaller values of  $\lambda''_{33i}$  that we consider in this paper.

#### 3.3.2. RPV final states

Given the mass configurations described in Eqs. (3.11–3.13), the leading RPV and RPC  $\tilde{t}$  decays are respectively  $\tilde{t} \rightarrow \bar{b}\bar{d}_i$  and  $\tilde{t} \rightarrow \chi^+ b$ , where  $d_i$  with  $i = 1, 2$ , denotes respectively the  $d$ - and  $s$ -quark. Other decay channels such as  $\tilde{t} \rightarrow \chi^0 t^* \rightarrow \chi^0 b f_1 \bar{f}'_1$  or  $\tilde{t} \rightarrow h^0 \tilde{t}^* \rightarrow h^0 \bar{b} \bar{d}_i$  (where  $f_1$  and  $\bar{f}'_1$  indicate SM fermions and the star off-shell states), are suppressed by the off-shellness of the (s)top quark. Note also that a potential enhancement of the Higgs channel by large soft-susy breaking trilinear coupling is suppressed when the  $\tilde{t}$  is essentially right-handed. The subsequent leading RPV induced  $\chi^+$  decays are  $\chi^+ \rightarrow \tilde{t}^* \bar{b} \rightarrow \bar{b} \bar{d}_i$  and the much longer chain  $\chi^+ \rightarrow \chi^0 W^{+*} \rightarrow \tilde{t}^* \bar{t} (\tilde{t}^* t) W^{+*} \rightarrow \bar{b} \bar{d}_i \bar{t} (b d_i t) f \bar{f}'$  with the top decaying ultimately to  $b f_1 \bar{f}'_1$  and where we assumed  $\chi^0$  decays through the shortest possible chain. The latter decay,  $\chi^0 \rightarrow \tilde{t}^* \bar{t} (\tilde{t}^* t) \rightarrow \bar{b} \bar{d}_i \bar{t} (b d_i t) f_1 \bar{f}'_1$ , is indeed dominant as a consequence of assumption (ii) of Section 3.2.3. The other equally short chain  $\chi^0 \rightarrow \tilde{b}^* \bar{b} (\tilde{b}^* \bar{b}) \rightarrow \bar{t}^{(*)} \bar{d}_i b (t^{(*)} d_i \bar{b})$  is suppressed for sufficiently heavy  $\tilde{b}$ . The longer chains  $\chi^0 \rightarrow \chi^{+*} W^{-(*)} (\chi^{-*} W^{+*}) \rightarrow \tilde{t}^* \bar{b} W^{-(*)} (\tilde{t}^* b W^{+*}) \rightarrow \bar{b} \bar{d}_i \bar{b} (b d_i b) f \bar{f}'$  or  $\chi^0 \rightarrow \chi^{+*} W^{-(*)} (\chi^{-*} W^{+*}) \rightarrow \tilde{b}^* t W^{-(*)} (\tilde{b}^* \bar{t} W^{+*}) \rightarrow t d_i t (\bar{t} \bar{d}_i \bar{t}) f \bar{f}'$  are obviously even further suppressed.

We have thus at hand the three different decay channels depicted in Figs. 3.1 (a), (b) and (c). We refer to these respectively as  $\tilde{t}$ -RPV,  $\chi$ -RPV and RPC-like, to stress the fact that channel (a) is the direct RPV stop decay, channel (b) the shortest RPV cascade containing an (on-shell) chargino, and channel (c), defined as having an *on-shell*  $\chi^0$  intermediate state, corresponds to the only

surviving channel in the RPC limit  $\lambda''_{33i} \rightarrow 0$ . It is to be noted that the latter channel has not been considered in [210].

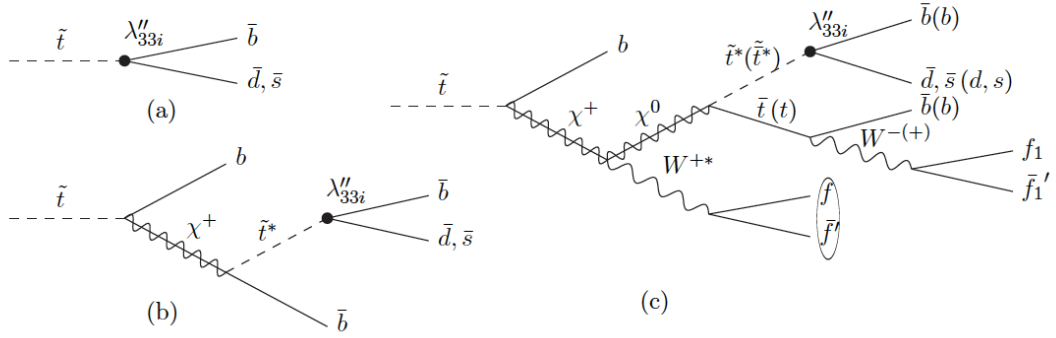


Figure 3.1.: Leading RPV stop decays assuming Eqs. (3.11-3.13); (a): direct RPV stop decay ( $\tilde{t}$ -RPV), (b): shortest RPV cascade containing an (on-shell) chargino ( $\chi$ -RPV), (c): shortest RPV cascade containing an (on-shell) neutralino (**RPC-like**);  $f, f', f_1, f'_1$  denote SM fermions and the oval encircles fermions too soft to be detected.

Note that because of the nearly mass degenerate chargino and neutralino in our scenario, off-shell  $W$  bosons from the **RPC-like** stop decay chain are produced with a too small transverse momentum for their decay products to be reconstructed in High Energy Physics detectors. These are thus ignored in the following.

Since jets electric charges cannot be discriminated experimentally, we tag the various final states by their flavor content as follows:

- $\tilde{t}$ -RPV  $\equiv 1b1j$ ,
- $\chi$ -RPV  $\equiv 3b1j$ ,
- **RPC-like**  $\equiv 1t2b1j$ ,

where  $b$  ( $t$ ) stands for the presence of a bottom-quark jet (top-quark) and  $j$  indicates the presence of a light-quark jet. Since the **RPC-like** channels are characterized by the presence of a top quark in the decay chain followed by SM top decays, we have indicated only the presence of the top quark. We are thus left effectively with six different categories of final states corresponding to the decays of the produced stop and anti-stop as summarized in Table 3.1. Final states with the same particle content (but opposite charges) are not duplicated in the table. We however continue to indicate explicitly the charges for definiteness when discussing the analytical structure of the cross-sections in Section 3.4.

$\begin{array}{c} \tilde{t} \\ \hline \tilde{\bar{t}} \end{array}$	$\tilde{t}$ -RPV	$\chi$ -RPV	RPC-like
$\tilde{t}$ -RPV	$2b2j$	$4b2j$	$1t3b2j$
$\chi$ -RPV		$6b2j$	$1t5b2j$
RPC-like			$2t4b2j$

Table 3.1.: The various final states corresponding to different contents of heavy ( $b, t$ ) quarks, and light ( $d, s$ ) quarks denoted generically by  $j$ , originating from the stop–anti-stop RPV decays; similar final states corresponding to interchanging the stop and anti-stop decays leading to the same particle content (irrespective of the electric charges) are listed only once.

### 3.3.3. The $\lambda''_{33i}$ range

There exists a large set of upper bounds on the RPV couplings (see [209] for a detailed discussion), some of which involve  $\lambda''_{33i}$ . Together with assumption (i) of Sec. 3.2.3, we allow in the sequel  $\lambda''_{33i}$  to vary in the range

$$10^{-7} \lesssim |\lambda''_{33i}| \lesssim 10^{-1} . \quad (3.14)$$

Experimental upper bounds on  $\lambda''_{331}$  and  $\lambda''_{332}$  are typically weaker than the ones involving only first and second generation, let alone the bounds on the lepton number violating couplings. Moreover, most of these bounds are on products of  $\lambda''_{33i}$  with other RPV couplings. Such bounds can thus be easily satisfied through assumption (i) of Sec. 3.2.3. There are also upper bounds set directly on  $\lambda''_{332}$  and/or  $\lambda''_{331}$ , coming from constraints on the  $Z$ -boson hadronic width, neutron–anti-neutron oscillations and single nucleon decays: the first is  $\mathcal{O}(1)$ , the second and the third are model-dependent and are made easily compatible with the



upper bound in Eq. (3.14) for squark masses  $\gtrsim 500$  GeV (even more so for single nucleon decays assuming a gravitino mass  $\gg 1$  eV or an axion scale  $\gtrsim 10^{10}$  GeV). Likewise, the upper bound in Eq. (3.14) can be easily made compatible with bounds on the product  $|\lambda''_{331}(\lambda''_{332})^*|$  obtained from  $K^0 - \bar{K}^0$  mixing for squark masses in the few hundred GeV range. All in all, the upper bound of Eq. (3.14) is only taken as a working assumption and could in principle be somewhat larger. Note however that values of  $\lambda''_{33i}$  much larger than  $10^{-1}$  would lead to too large and negative loop corrections to the squared stop mass [223].

The lower bound in Eq. (3.14) is an estimate of the magnitude of  $\lambda''_{33i}$  that guarantees decays within the detector. Since in the configuration under study the lightest stop is not the lightest MSSM particle, one should consider not only the lifetime due to direct RPV two-body decay of the stop, Fig. 3.1(a), but also that of the daughter chargino due to its decay as given in Fig. 3.1(b), or the neutralino due to its decay as given in Fig. 3.1(c). In the absence of any prior about which channel among the  $\tilde{t}$ -RPV,  $\chi$ -RPV or RPC-like is dominant one should consider the most conservative bound, i.e. the longest decay length. The various  $c\tau$ 's are (approximately) given by

$$c\tau_{\tilde{t} \rightarrow bd_i}[\text{meter}] \simeq \frac{8.3 \times 10^{-18}}{|\lambda''_{33i}|^2} \left( \frac{600 \text{ GeV}}{m_{\tilde{t}}} \right), \quad (3.15)$$

for the direct RPV stop decay, where  $d_{1,2}$  denote the first and second generation down quarks, and

$$\begin{aligned} c\tau_{\chi^0 \rightarrow tbd_i}[\text{meter}] &\simeq \frac{2.6 \times 10^{-16}}{\alpha_{\chi^0} |\lambda''_{33i}|^2} \left( \frac{m_{\tilde{t}}}{600 \text{ GeV}} \right)^4 \left( \frac{500 \text{ GeV}}{m_{\chi^0}} \right)^5 \cdot \\ &\cdot \left( (1 - r^4)(1 - 8r^2 + r^4) - 24r^4 \log r \right)^{-1}, \end{aligned} \quad (3.16)$$

for the Higgsino component of the neutralino RPV decay where we defined  $\alpha_{\chi^0} \equiv \frac{g_{\chi^0}^2}{4\pi}$ ,  $g_{\chi^0}$  denoting the  $\chi^0 - \tilde{t} - t$  coupling, and  $r \equiv \frac{m_t}{m_{\chi^0}}$  where  $m_t$  is the top mass, and neglected  $b$ - and light quark masses.<sup>c</sup> In Eq. (3.16) we approximate the stop propagator by a point interaction which leads to an overestimate of the decay

---

<sup>c</sup>In deriving these expressions we included consistently the color factors, averaged over the spin of the decaying particle and assumed the lightest stop to be essentially right-handed. (Note that some simple formulae for the neutralino decay length in the literature, e.g. Eq.(7.6) of Ref. [209], assume a pure photino content and do not apply in our case.) We also rely on the simplifying assumption of instantaneous decay at the mean lifetime, and travel of the decaying particle close to (70% of) the speed of light in the laboratory frame. A more accurate evaluation of the decay lengths should take into account boost factors from the actual mass and energy distributions of the decaying particles produced at various energies at the partonic level, as well as their lifetimes distribution.



length and thus to a safe conservative bound, but we provide the exact integral over the three-body phase space taking into account the matrix element spinorial structure of the final state. The  $c\tau$  corresponding to the chargino decay  $\chi^+ \rightarrow bbd_i$  is given by  $2 \times c\tau_{\chi^0 \rightarrow tbd_i}$  in the limit  $m_t \rightarrow 0$  and with the proper substitution of chargino mass and coupling, where the global factor two difference between the two  $c\tau$ 's is due to the majorana nature of  $\chi^0$ . From Eqs. (3.15, 3.16) one has generically the hierarchy

$$c\tau_{\tilde{t} \rightarrow b d_i} \ll c\tau_{\chi^+ \rightarrow b b d_i} \lesssim c\tau_{\chi^0 \rightarrow t b d_i} , \quad (3.17)$$

if  $m_{\tilde{t}} > m_{\chi^0} \simeq m_{\chi^+} \lesssim 550$  GeV and  $\alpha_{\chi^0}, \alpha_{\chi^+} < 1$ . The lower bound for  $|\lambda''_{33i}|$  is thus determined by the decay length of the neutralino provided that it corresponds to values of  $|\lambda''_{33i}|$  for which the stop decays containing a neutralino indeed dominate.

With a fiducial region of  $c\tau \lesssim 3$  meters and taking  $m_{\tilde{t}} = 600$  GeV, one has from Eq. (3.15) the lower bound  $|\lambda''_{33i}| \gtrsim 1.6 \times 10^{-9}$ , while varying  $m_{\chi^0} \simeq m_{\chi^+}$  in the range  $(600 \text{ GeV} - m_t)$  to 600 GeV, one obtains from Eq. (3.16) with a typical  $\alpha_{\chi^0} \simeq 10^{-2}$  the stronger bound  $|\lambda''_{33i}| \gtrsim (0.8 - 2.4) \times 10^{-7}$ . Of course, lighter stop and neutralino lead to more stringent lower bounds, e.g.  $m_{\tilde{t}} = 400$  GeV and  $m_{\chi^0} = m_{\tilde{t}} - m_t$  would require  $|\lambda''_{33i}| \gtrsim 3.4 \times 10^{-6}$ . However, a stop that light becomes barely compatible with our assumption that it is heavier than a chargino, since such a low mass configuration would start conflicting with limits on rare  $B$ -decays (see also the discussion in Section 3.5.0.1).

When  $m_{\chi^0} \simeq m_{\chi^+} \gtrsim 560$  GeV but still smaller than the stop mass, the 3-body phase space reduction in the  $\chi^0$  decay width as compared to that in the  $\chi^+$  decay width, does not compensate anymore for the factor two difference between the two widths. As a result, the hierarchy of the chargino and neutralino  $c\tau$ 's is reversed with respect to Eq. (3.17). However, the relevant lower bound for  $|\lambda''_{33i}|$  is still determined by the decay length of the neutralino. Indeed the chargino becomes detector-stable typically also for  $|\lambda''_{33i}| = \mathcal{O}(10^{-7})$ , where, as shown in the following Sections, the stop decay channels not containing a neutralino become highly suppressed.

Finally, note that we neglect altogether the gravitationally induced direct stop decay into a top-quark and a gravitino. This channel could lead to large missing energy in the final state. However, it is Planck scale suppressed unless the gravitino mass is in the deep sub-eV range [232]. As noted previously in this section, a gravitino much lighter than 1eV is disfavored by proton decay bounds, otherwise  $\lambda''_{331}$  and  $\lambda''_{332}$  would have to be typically much smaller than  $\mathcal{O}(10^{-7})$  where the LHC exclusion limits on RPC signatures apply. This suggests a rather heavy gravitino, for which stop decays with missing energy are not significant, and which is moreover welcome in scenarios of gravitino dark matter. One should however keep in mind that such stringent individual upper bounds on  $\lambda''_{331}$  and  $\lambda''_{332}$  from proton decay [233], can be relaxed through possible destruc-

tive interference if the two RPV couplings are allowed to be simultaneously non-vanishing, thus bringing them again within the lower part of the range given in Eq. (3.14).<sup>d</sup>

More generally, recasting experimental LHC limits on long-lived particle searches [234, 235] as done in [212, 213], constrains the various  $c\tau$ 's to be in the millimeter range. Although the latter studies do not compare directly to ours, as they scan different mass spectra configurations, a  $c\tau \simeq 3\text{mm}$  for a decaying chargino LSP of 600GeV [212] would increase the lower bound in Eq. (3.14) to  $\simeq 2.5 \times 10^{-6}$ .

### 3.4. Narrow Width Approximation

A key point is the relative magnitudes of the various cross-sections and their sensitivities to  $\lambda''_{33i}$ . By looking at Fig. 3.1, one could naively expect the six channels listed in Table 3.1 to all scale similarly with  $(\lambda''_{33i})^4$ . If this were the case, then the relative magnitudes of the corresponding cross-sections would not be affected by  $\lambda''_{33i}$ , and the longer chains would yield smaller cross-sections due to phase space effects as well as to matrix elements suppression by other couplings and intermediate propagators. There is in fact much more to it if one takes into account total widths and branching ratios of the unstable intermediate particles. This section is devoted to an analytical study of these features. To help understand the sensitivity to the RPV coupling we derive the expressions for the cross-sections of the various stop decay channels relying on the narrow width approximation (NWA), see e.g. [236]. It is well-known that the NWA is not always quantitatively reliable. In particular it can fail not only when couplings are large leading to large widths, but also for mass configurations similar to the ones we are considering in this paper, even for small couplings, that is when daughter and parent particles are very close in mass and the effective center of mass energy at the partonic level is of the same order as (twice) the parent particle mass [237, 238, 239, 240]. The quantitative analysis in the subsequent Sections will thus not rely on this approximation. Nonetheless, the NWA renders reasonably well the qualitative behavior, providing a physical understanding of the effects. Moreover in the configurations where the NWA is expected to be valid, a very good quantitative agreement with the numerical simulation based on exact matrix element calculation gives a significant cross-check of the results.

Following the discussion in Section 3.3.2, the predominant decay chain for the RPV-MSSM-LSP is  $\chi^0 \rightarrow \tilde{t}^* \bar{t} (\tilde{t}^* t) \rightarrow \bar{b} \bar{d}_i \bar{b} (b d_i b) f_1 \bar{f}'_1$ . We can thus take, irrespective

---

<sup>d</sup>In such configurations where the decay into gravitinos can be comparable to the RPV decays, one could make use of the very different scaling in  $m_{\tilde{t}}$  in the  $c\tau$ 's, namely  $m_{\tilde{t}}^4$  for the **RPC-like** decay, as compared to  $m_{\tilde{t}}^{-5}$  or  $m_{\chi^0}^{-5}$  for the stop or the neutralino decaying into gravitinos, to extract information from limits on both prompt decays and displaced vertices, see e.g. [211].

of the mass hierarchy involving  $\tilde{t}$  and  $\chi^+$ :

$$BR(\chi^0 \rightarrow \tilde{t}^* \bar{t}(\tilde{t}^* t) \rightarrow \bar{b} \bar{d}_i \bar{b}(b d_i b) f_1 \bar{f}'_1) \approx 1. \quad (3.18)$$

To be specific we first derive the various expressions under the assumptions  $\lambda''_{332} \neq 0$ ,  $\lambda''_{331} = 0$ , and  $d_i = s$  (i.e.  $i = 2$ ). Defining

$$\Gamma_{\tilde{t}\text{-RPV}} \equiv \Gamma(\tilde{t} \rightarrow \bar{b} \bar{s}) \quad (3.19)$$

$$\Gamma_{\chi\text{-RPV}} \equiv \Gamma(\tilde{t} \rightarrow \bar{b} \bar{s} \bar{b} b) \quad (3.20)$$

$$\Gamma_{\text{RPC-like}} \equiv \Gamma(\tilde{t} \rightarrow \bar{b} \bar{s} \bar{b}(b s b) f_1 \bar{f}'_1 b f \bar{f}'), \quad (3.21)$$

the NWA allows to write,

$$\Gamma_{\chi\text{-RPV}} \simeq \Gamma(\tilde{t} \rightarrow \chi^+ b) \times BR(\chi^+ \rightarrow \bar{b} \bar{s} \bar{b}) \quad (3.22)$$

$$\Gamma_{\text{RPC-like}} \simeq \Gamma(\tilde{t} \rightarrow \chi^+ b) \times BR(\chi^+ \rightarrow \bar{b} \bar{s} \bar{b}(b s b) f_1 \bar{f}'_1 f \bar{f}') \quad (3.23)$$

$$\begin{aligned} &\simeq \Gamma(\tilde{t} \rightarrow \chi^0 f \bar{f}' b) \times BR(\chi^0 \rightarrow \bar{b} \bar{s} \bar{b}(b s b) f_1 \bar{f}'_1) \\ &\simeq \Gamma(\tilde{t} \rightarrow \chi^0 f \bar{f}' b) \end{aligned} \quad (3.24)$$

where we made use of Eq. (3.18) when writing Eq. (3.24). Moreover, the fact that  $\chi^+$  decays with branching ratio  $\simeq 1$  into  $\bar{b} \bar{s} \bar{b}$  and  $\bar{b} \bar{s} \bar{b}(b s b) f_1 \bar{f}'_1 f \bar{f}'$  leads through Eqs. (3.22, 3.23) to

$$\Gamma_{\chi\text{-RPV}} + \Gamma_{\text{RPC-like}} \simeq \Gamma(\tilde{t} \rightarrow \chi^+ b) \simeq \text{“}\lambda''_{332}\text{-independent”}. \quad (3.25)$$

A residual sensitivity to  $\lambda''_{332}$  in  $\Gamma_{\chi\text{-RPV}} + \Gamma_{\text{RPC-like}}$  would still come from loop contributions to the stop mass itself that enters  $\Gamma(\tilde{t} \rightarrow \chi^+ b)$ . However this higher order effect is essentially screened for the range  $\lambda''_{332} \lesssim 0.1$  under consideration. Therefore, the only significant dependence on the RPV coupling in the stop total width<sup>e</sup>,  $\Gamma_{\tilde{t}\text{-RPV}} + \Gamma_{\chi\text{-RPV}} + \Gamma_{\text{RPC-like}}$ , originates from the two body stop decay which can be parametrized as follows,

$$\Gamma_{\tilde{t}\text{-RPV}} = (\lambda''_{332})^2 \times \Gamma_1(\tilde{t} \rightarrow \bar{b} \bar{s}), \quad (3.26)$$

with the notation

$$\Gamma_1 \equiv \Gamma_{|\lambda''_{332}=1}. \quad (3.27)$$

We now show that the longest decay chain width  $\Gamma_{\text{RPC-like}}$  is not always negligible with respect to  $\Gamma_{\chi\text{-RPV}}$  or  $\Gamma_{\tilde{t}\text{-RPV}}$  and can even overpower these. The relative magnitude of  $\Gamma_{\text{RPC-like}}$  and  $\Gamma_{\chi\text{-RPV}}$  is controlled by that of  $BR(\chi^+ \rightarrow \bar{b} \bar{s} \bar{b})$  and  $BR(\chi^+ \rightarrow \bar{b} \bar{s} \bar{b}(b s b) f_1 \bar{f}'_1 f \bar{f}')$  through Eqs. (3.22, 3.23), where the relative magnitude of the latter branching ratios depends on the value of  $\lambda''_{332}$ . Indeed, on the

---

<sup>e</sup> neglecting flavor violating transitions such as  $\tilde{t} \rightarrow \chi^+ s$  and the decay channels  $\tilde{t} \rightarrow \chi^0 t^* \rightarrow \chi^0 b f_1 \bar{f}'_1$  or  $\tilde{t} \rightarrow h^0 \tilde{t}^* \rightarrow h^0 \bar{b} \bar{s}$  as noted in Section 3.3.2.

one hand the NWA and Eq. (3.18) imply that

$$\begin{aligned}\Gamma(\chi^+ \rightarrow \bar{b}\bar{s}\bar{b}(bsb)f_1\bar{f}'_1f\bar{f}') &= \Gamma(\chi^+ \rightarrow \chi^0 f\bar{f}') \times BR(\chi^0 \rightarrow \bar{b}\bar{s}\bar{b}(bsb)f_1\bar{f}'_1) \\ &\simeq \Gamma(\chi^+ \rightarrow \chi^0 f\bar{f}'),\end{aligned}\quad (3.28)$$

showing that  $\Gamma(\chi^+ \rightarrow \bar{b}\bar{s}\bar{b}(bsb)f_1\bar{f}'_1f\bar{f}')$  is essentially  $\lambda''_{332}$  independent and is *identical* to the  $\chi^+$  width of the RPC case  $\Gamma(\chi^+ \rightarrow \chi^0 f\bar{f}')$ . On the other hand, since the stop is *off-shell* in the decay  $\chi^+ \rightarrow \bar{b}\bar{s}\bar{b}$ , obviously the corresponding width scales with  $(\lambda''_{332})^2$ ,

$$\Gamma(\chi^+ \rightarrow \bar{b}\bar{s}\bar{b}) = (\lambda''_{332})^2 \times \Gamma_1(\chi^+ \rightarrow \bar{b}\bar{s}\bar{b}). \quad (3.29)$$

Let us now define the following two ratios,

$$r_1 \equiv \frac{\Gamma_1(\tilde{t} \rightarrow \bar{b}\bar{s})}{\Gamma(\tilde{t} \rightarrow \chi^+ b)}, \quad (3.30)$$

$$r_2 \equiv \frac{\Gamma_1(\chi^+ \rightarrow \bar{b}\bar{s}\bar{b})}{\Gamma(\chi^+ \rightarrow \bar{b}\bar{s}\bar{b}(bsb)f_1\bar{f}'_1f\bar{f}')} = \frac{\Gamma_1(\chi^+ \rightarrow \bar{b}\bar{s}\bar{b})}{\Gamma(\chi^+ \rightarrow \chi^0 f\bar{f}')}, \quad (3.31)$$

that are essentially  $\lambda''_{33i}$  independent (apart from a very small sensitivity in the loop correction to the stop mass, as noted previously), and determined mainly by the RPC parameters of the MSSM. The dependence of the chargino decay branching ratios on  $\lambda''_{332}$  follows then easily from Eqs. (3.28, 3.29, 3.31),

$$BR(\chi^+ \rightarrow \bar{b}\bar{s}\bar{b}) = \frac{r_2 \times (\lambda''_{332})^2}{1 + r_2 \times (\lambda''_{332})^2}, \quad (3.32)$$

$$BR(\chi^+ \rightarrow \bar{b}\bar{s}\bar{b}(bsb)f_1\bar{f}'_1f\bar{f}') = \frac{1}{1 + r_2 \times (\lambda''_{332})^2}. \quad (3.33)$$

It is clear from these expressions that for sufficiently small  $\lambda''_{332}$  the RPC-like decay  $\chi^+ \rightarrow \bar{b}\bar{s}\bar{b}(bsb)f_1\bar{f}'_1f\bar{f}'$  becomes comparable or even dominates the RPV decay  $\chi^+ \rightarrow \bar{b}\bar{s}\bar{b}$ . Upon use of Eqs. (3.22, 3.23, 3.26) the same conclusion holds for the stop widths: the size of  $\lambda''_{332}$  controls the relative magnitudes of  $\Gamma_{\tilde{t}\text{-RPV}}$ ,  $\Gamma_{\chi\text{-RPV}}$  and  $\Gamma_{\text{RPC-like}}$ , the latter becoming largely dominant for a very small RPV coupling!

We note in passing that the form of Eq. (3.24) might wrongly suggest that  $\Gamma_{\text{RPC-like}}$  is  $\lambda''_{332}$  independent. In fact the  $\lambda''_{332}$  dependence in  $\Gamma(\tilde{t} \rightarrow \chi^0 f\bar{f}'b)$  is encoded in the total width of  $\chi^+$ , or equivalently in  $BR(\chi^+ \rightarrow \bar{b}\bar{s}\bar{b}(bsb)f_1\bar{f}'_1f\bar{f}')$ . This should be contrasted with  $\Gamma(\chi^+ \rightarrow \bar{b}\bar{s}\bar{b}(bsb)f_1\bar{f}'_1f\bar{f}')$  which is independent of  $\lambda''_{332}$ .

Using the above results, it is now straightforward to express the stop decay branching ratios, and the stop pair production and decay cross-sections, in terms of  $\lambda''_{332}$ ,  $r_1$  and  $r_2$ . Before doing so, we note first that all the above steps remain valid if  $\lambda''_{332}$  is replaced by  $\lambda''_{331}$  and the  $s$ - replaced by the  $d$ -quark, but also when both couplings  $\lambda''_{331}$  and  $\lambda''_{332}$  are simultaneously non-vanishing. Since the

difference between the  $d$ - and  $s$ -quark masses is irrelevant, the ratios  $r_1$  and  $r_2$  are essentially unchanged when replacing the  $s$ - by a  $d$ -quark. The general case, summing up the  $s$  and  $d$  contributions, is thus obtained by simply replacing  $\lambda''_{332}$  by  $\lambda''_{33i}$  with

$$\lambda''_{33i} \equiv \sqrt{(\lambda''_{332})^2 + (\lambda''_{331})^2}, \quad (3.34)$$

in the above formulae. Putting everything together one finds the following general form for the stop pair production and decay cross-sections:

- $\tilde{t}$ -RPV –  $\tilde{t}$ -RPV  $\equiv 2b2j$ ,

$$\begin{aligned} \sigma(2b2j) &\simeq \sigma(pp \rightarrow \tilde{t}\tilde{t}) \times BR(\tilde{t} \rightarrow \bar{b}\bar{d}_i) \times BR(\tilde{t} \rightarrow bd_i) \\ &\simeq \sigma(pp \rightarrow \tilde{t}\tilde{t}) \times \frac{r_1^2 \times (\lambda''_{33i})^4}{\left(1 + r_1 \times (\lambda''_{33i})^2\right)^2}, \end{aligned} \quad (3.35)$$

with

$$BR(\tilde{t} \rightarrow \bar{b}\bar{d}_i) = \frac{\Gamma_{\tilde{t}\text{-RPV}}}{\Gamma_{\tilde{t}\text{-RPV}} + \Gamma_{\chi\text{-RPV}} + \Gamma_{\text{RPC-like}}}.$$

- $\tilde{t}$ -RPV –  $\chi$ -RPV  $\equiv 4b2j$ ,

$$\begin{aligned} \sigma(4b2j) &\simeq \sigma(pp \rightarrow \tilde{t}\tilde{t}) \times \left( BR(\tilde{t} \rightarrow \bar{b}\bar{d}_i\bar{b}b) \times BR(\tilde{t} \rightarrow bd_i) \right. \\ &\quad \left. + BR(\tilde{t} \rightarrow bd_i\bar{b}b) \times BR(\tilde{t} \rightarrow \bar{b}\bar{d}_i) \right) \\ &\simeq 2 \times \sigma(pp \rightarrow \tilde{t}\tilde{t}) \times BR(\tilde{t} \rightarrow \bar{b}\bar{d}_i\bar{b}b) \times BR(\tilde{t} \rightarrow bd_i) \\ &\simeq \sigma(pp \rightarrow \tilde{t}\tilde{t}) \times \frac{2r_1r_2 \times (\lambda''_{33i})^4}{\left(1 + r_1 \times (\lambda''_{33i})^2\right)^2 \left(1 + r_2 \times (\lambda''_{33i})^2\right)}, \end{aligned} \quad (3.36)$$

with

$$BR(\tilde{t} \rightarrow \bar{b}\bar{d}_i\bar{b}b) = \frac{\Gamma_{\chi\text{-RPV}}}{\Gamma_{\tilde{t}\text{-RPV}} + \Gamma_{\chi\text{-RPV}} + \Gamma_{\text{RPC-like}}}.$$

- $\chi$ -RPV –  $\chi$ -RPV  $\equiv 6b2j$ ,

$$\begin{aligned} \sigma(6b2j) &\simeq \sigma(pp \rightarrow \tilde{t}\tilde{t}) \times BR(\tilde{t} \rightarrow \bar{b}\bar{d}_i\bar{b}b) \times BR(\tilde{t} \rightarrow bd_i\bar{b}b) \\ &\simeq \sigma(pp \rightarrow \tilde{t}\tilde{t}) \times \frac{r_2^2 \times (\lambda''_{33i})^4}{\left(1 + r_1 \times (\lambda''_{33i})^2\right)^2 \left(1 + r_2 \times (\lambda''_{33i})^2\right)^2} \end{aligned} \quad (3.37)$$

- **RPC-like- $\tilde{t}$ -RPV**  $\equiv 1t3b2j$ ,

$$\begin{aligned}
\sigma(1t3b2j) &\simeq \sigma(pp \rightarrow \tilde{t}\tilde{t}) \times \left( BR(\tilde{t} \rightarrow \bar{b}\bar{d}_i\bar{b}(bd_i b) f_1 \bar{f}'_1 b f \bar{f}') \times BR(\tilde{t} \rightarrow bd_i) \right. \\
&\quad \left. + BR(\tilde{t} \rightarrow j\bar{b}) \times BR(\tilde{t} \rightarrow bd_i b(\bar{b}\bar{d}_i\bar{b}) \bar{f}_1 \bar{f}'_1 \bar{b} \bar{f} \bar{f}') \right) \\
&\simeq 2 \times \sigma(pp \rightarrow \tilde{t}\tilde{t}) \times BR(\tilde{t} \rightarrow \bar{b}\bar{d}_i\bar{b}(bd_i b) f_1 \bar{f}'_1 b f \bar{f}') \times BR(\tilde{t} \rightarrow bd_i) \\
&\simeq \sigma(pp \rightarrow \tilde{t}\tilde{t}) \times \frac{2r_1 \times (\lambda''_{33i})^2}{\left(1 + r_1 \times (\lambda''_{33i})^2\right)^2 \left(1 + r_2 \times (\lambda''_{33i})^2\right)}, \quad (3.38)
\end{aligned}$$

with

$$BR(\tilde{t} \rightarrow \bar{b}\bar{d}_i\bar{b}(bd_i b) f_1 \bar{f}'_1 b f \bar{f}') = \frac{\Gamma_{\text{RPC-like}}}{\Gamma_{\tilde{t}\text{-RPV}} + \Gamma_{\chi\text{-RPV}} + \Gamma_{\text{RPC-like}}}.$$

- **RPC-like- $\chi$ -RPV**  $\equiv 1t5b2j$ ,

$$\begin{aligned}
\sigma(1t5b2j) &\simeq \sigma(pp \rightarrow \tilde{t}\tilde{t}) \times \left( BR(\tilde{t} \rightarrow \bar{b}\bar{d}_i\bar{b}(bd_i b) f_1 \bar{f}'_1 b f \bar{f}') \times BR(\tilde{t} \rightarrow bd_i b\bar{b}) \right. \\
&\quad \left. + BR(\tilde{t} \rightarrow \bar{b}\bar{d}_i\bar{b}b) \times BR(\tilde{t} \rightarrow bd_i b(\bar{b}\bar{d}_i\bar{b}) \bar{f}_1 \bar{f}'_1 \bar{b} \bar{f} \bar{f}') \right) \\
&\simeq 2 \times \sigma(pp \rightarrow \tilde{t}\tilde{t}) \times BR(\tilde{t} \rightarrow \bar{b}\bar{d}_i\bar{b}(bd_i b) f_1 \bar{f}'_1 b f \bar{f}') \times BR(\tilde{t} \rightarrow bd_i b\bar{b}) \\
&\simeq \sigma(pp \rightarrow \tilde{t}\tilde{t}) \times \frac{2r_2 \times (\lambda''_{33i})^2}{\left(1 + r_1 \times (\lambda''_{33i})^2\right)^2 \left(1 + r_2 \times (\lambda''_{33i})^2\right)^2}. \quad (3.39)
\end{aligned}$$

- **RPC-like-RPC-like**  $\equiv 2t4b2j$ ,

$$\begin{aligned}
\sigma(2t4b2j) &\simeq \sigma(pp \rightarrow \tilde{t}\tilde{t}) \times BR(\tilde{t} \rightarrow \bar{b}\bar{d}_i\bar{b}(bd_i b) f_1 \bar{f}'_1 b f \bar{f}') \times BR(\tilde{t} \rightarrow bd_i b(\bar{b}\bar{d}_i\bar{b}) \bar{f}_1 \bar{f}'_1 \bar{b} \bar{f} \bar{f}') \\
&\simeq \sigma(pp \rightarrow \tilde{t}\tilde{t}) \times \frac{1}{\left(1 + r_1 \times (\lambda''_{33i})^2\right)^2 \left(1 + r_2 \times (\lambda''_{33i})^2\right)^2}. \quad (3.40)
\end{aligned}$$

We have replaced  $s$  by  $d_i$  in the above expressions to stress the fact that these are valid either for the case of  $s$  alone, or for the case of  $d$  alone, or else for the sum of the two, depending on the values of  $\lambda''_{331}, \lambda''_{332}$  in Eq. (3.34).

The analytical form of Eqs. (3.35 – 3.40) illustrate clearly the deviation from the naive expectation that all cross-sections would scale with  $(\lambda''_{33i})^4$ . One sees that such scaling is generically modified by the **RPC-like** component. Moreover, even for the  $\tilde{t}$ -RPV and  $\chi$ -RPV contributions different final state cross-sections can have various sensitivities to  $\lambda''_{332}$  depending on the following possible regimes:

$$r_a \ll (\lambda''_{33i})^{-2}, \quad r_a \sim (\lambda''_{33i})^{-2}, \quad r_a \gg (\lambda''_{33i})^{-2}, \quad (a = 1, 2). \quad (3.41)$$

These regimes are triggered by the interplay between the RPV and RPC sectors. For instance the magnitude of  $r_1$  is controlled by the degree of mass degen-

eracy between the stop and the chargino. Similarly, the degeneracy between the chargino and neutralino masses implies typically a large  $r_2$ . Perhaps the most striking feature that comes out of the NWA expressions is that the variation of  $\lambda''_{33i}$  over several orders of magnitude, within the range given in Eq. (3.14), triggers the dominance of very different final states without reducing the total cross-sections. In particular, while the  $\tilde{t}$ -RPV– $\tilde{t}$ -RPV clearly dominates for relatively large values of  $\lambda''_{33i}$ , the RPC-like–RPC-like becomes dominant for very small values of this coupling. Furthermore, one can easily determine from Eqs. (3.35, 3.36, 3.37, 3.39, 3.40) the scaling relations

$$\frac{\sigma(2b2j) \cdot \sigma(6b2j)}{[\sigma(4b2j)]^2} = \frac{1}{4}, \quad (3.42)$$

$$\frac{\sigma(6b2j) \cdot \sigma(2t4b2j)}{[\sigma(1t5b2j)]^2} = \frac{1}{4}. \quad (3.43)$$

We refer to these two scaling relations respectively as b-SR and t-SR, where the first one involves shorter decay chains with no top-quark final states and the second longer decay chains with top-quark final states. These scaling relations lead also to

$$\frac{\sigma(2t4b2j)}{\sigma(2b2j)} = \left( \frac{\sigma(1t5b2j)}{\sigma(4b2j)} \right)^2. \quad (3.44)$$

To summarize, we derived in this Section analytical expressions for the cross-sections with all possible stop decay final states, in a form that untangles the dependence on the RPV  $\lambda''_{33i}$  coupling from that on the MSSM mass spectrum and RPC couplings encoded in the  $r_a$  ratios Eqs. (3.30, 3.31). Moreover these expressions imply scaling relations among the cross-sections independently of the couplings and masses. Given the complexity of the long chain decays, these analytical results will prove very useful, even though established within the approximation of narrow width, when interpreting the results and assessing the validity of the exact matrix element numerical computation in Section 3.6.

### 3.5. Benchmark points and constraints

In order to estimate the cross-sections for the processes of interest, we interfaced several software packages as discussed in the following. Firstly we used the SARAH [241, 242] MATHEMATICA [243] package to generate model files in UFO format compatible with the MADGRAPH5\_AMC@NLO [150] Monte Carlo generator. Then we used SARAH to implement the MSSM trilinear RPV model in SPHENO [244] so as to calculate the entire SUSY mass spectrum and couplings. We adopted a bottom-bottom approach, where the values of the supersymmetric and soft SUSY breaking parameters are provided directly at the electroweak

scale. This approach has the benefit of being simple without sacrificing the typical supersymmetric correlations among various low energy states masses and couplings, and of being model-independent in view of our present ignorance of how supersymmetry is realized at high scales.

Using the low scale MSSM option of the SPHENO code, we performed a scan over the SUSY input parameters to determine benchmark points that are consistent with our spectrum assumptions discussed in Sections 3.2.3 and 3.3, as well as with constraints from the available physical observables. We generated several mass spectra in different regions of the relevant MSSM parameter space, fixing the EWSB scale to  $Q_{EWSB} = 1$  TeV and including 1-loop corrections to all SUSY particle masses and 2-loop corrections to the lightest CP-even Higgs mass. For each given parameter point we used HIGGSBOUNDS [245, 246] and HIGGSIGNALS [247] to confront the Higgs sector computed by SPHENO with existing measurements and exclusion limits. Moreover we accounted for the low energy flavor constraints coming from the recent measurements of  $B^0$  decaying into a pair of muons [248, 249, 250]. For given values of the soft SUSY breaking parameters in the stop and gaugino sectors satisfying these constraints, a further scan over the  $\mu$  parameter was performed such that the lighter chargino and neutralinos remain Higgsino-like and the resulting masses reproduce the hierarchy given by Eqs. (3.11 – 3.13). For the remainder of this paper we choose two benchmark sets of input parameters as given in Table 3.2, corresponding to two stop mass values  $m_{\tilde{t}} = 600$  GeV and 1 TeV. The values we take in Table 3.2 should be understood as given at the EWSB scale. Note that we have put to zero several of these parameters (see last line of Table 3.2), in particular the off-diagonal components in flavor space of soft masses keeping up with our MFV assumption, and the soft SUSY breaking trilinear couplings  $T''_{33i}$  associated with  $\lambda''_{33i}$  as they involve only scalar states and thus would not contribute to our study at leading order.

The large mass splitting between the two stop states in accordance with assumption (ii) of Sec. 3.2.3 is achieved through the large numerical difference between  $(m_{\tilde{Q}})_{33}$  and  $(m_{\tilde{U}})_{33}$  rather than through a large off-diagonal component of the mass matrix. The mixing between the light and heavy stops is thus very small, therefore the lighter stop, essentially right-handed, has its baryon number violating RPV decay controlled mainly by the magnitude of  $\lambda''_{33i}$ . Note also that the values of  $m_{\tilde{t}}$ , respectively 600 GeV and 1 TeV in the two benchmark scenarios still vary slightly by about  $-0.5\% + 1.5\%$  around the central value due on one hand to the sensitivity to  $\mu$  through the mixing in the stop sector, though suppressed by the moderately large value of  $\tan \beta$ , and on the other hand to the sensitivity to  $\lambda''_{33i}$  through loop corrections [223].

Including 1- and 2-loop corrections from the RPC sector, the lighter CP-even Higgs mass remains essentially at 125 GeV, as extra 1-loop corrections from the RPV sector [251] which have also been included, are negligible in the scanned  $\lambda''_{33i}$  range given in Eq. (3.14). The small variation in the mass splitting among



the light chargino and neutralinos is a residual effect of the small  $\mu/M_1$  and  $\mu/M_2$  ratios as already noted in Sec. 3.3. All other states are very heavy (between 1.5 and 3 TeV) and do not affect our study. Since we rely on the low scale MSSM option the renormalization group running of couplings and masses involves only the range between  $m_Z$  and the EWSB scale. This allows to treat consistently the gauge and Yukawa couplings extracted at the  $m_Z$  scale and the input SUSY parameters  $\mu, \tan \beta$  and the (tree-level) CP-odd neutral Higgs mass  $m_A$  defined at the EWSB scale. In particular we make no theoretical assumptions relating the RPV-MSSM parameters at very high scales that would have induced correlations at low scales through the renormalization group evolution. In this context assumption (i) of Sec. 3.2.3 with values in the range defined in Eq. (3.14) should be viewed as defined at the EWSB scale. The running of  $\lambda''_{33i}$  from the EWSB to the  $m_{\tilde{t}}$  or  $m_{\chi^+}$  scales where the various stop decay channels are evaluated, remains very small and it is neglected in our study. Note however, that  $\lambda''_{332}$  affects the running of the top-quark Yukawa coupling between the EWSB scale and  $m_Z$ . Similarly, there are no high scale assumptions about the soft SUSY breaking masses and trilinear couplings.

### 3.5.0.1. Low energy constraints

A large number of low energy and precision observables can be very sensitive to BSM physics. Among these, the LEP/SLC electroweak precision observables, the leptons anomalous magnetic moments and electric dipole moments as well as low energy quark or lepton number violating processes. In Table 3.3 we give the values in our two benchmark points of only a few of them.<sup>f</sup>

The anomalous magnetic moment of the muon is a very important test bed for virtual effects from BSM physics as it is one of the most accurately measured quantities in particle physics; for a review see e.g. Ref. [252]. At the one-loop level  $(g-2)_\mu$  receives contributions from the purely SUSY neutralino/smuon and chargino/muonic-sneutrino RPC sectors. In our benchmark points the smuon sector is very heavy and the chargino/neutralino relatively heavy as well, leading to the small contribution reported in Table 3.3 given the chosen moderate value of  $\tan \beta$ . Other possible one-loop effects from nonzero  $\lambda, \lambda'$  RPV couplings, or from CP-violating phases [253], are absent in our scenario. Moreover, two-loop RPC SUSY corrections [254], are not expected to be significant in our case even for a relatively light stop, due to the moderate values of the  $\mu$  parameter and  $\tan \beta$ . The  $3.6\sigma$  discrepancy  $\Delta\left(\frac{1}{2}(g-2)_\mu\right) = 288(63)(49) \times 10^{-11}$ , [46], between the experimental measurement and the theoretical SM predictions is thus too large to be accounted for by our benchmark points, leaving open the issue of the uncertainties on the theoretical estimates of the SM hadronic contributions.

Virtual corrections to the  $\rho$  parameter originate from the squark and slepton

---

<sup>f</sup>For more details on the level of accuracy used see [244] and references therein.

Benchmark points	1	2
$\tan \beta$	10	
$M_1$	2.5 TeV	
$M_2$	1.5 TeV	
$M_3$	1.7 TeV	
$(m_{\tilde{Q}})_{33}$	2 TeV	
$(m_{\tilde{U}})_{33}$	570 GeV	964 GeV
$(m_{\tilde{D}})_{33} = (m_{\tilde{U}})_{ii} = (m_{\tilde{D}})_{ii} =$ $(m_{\tilde{E}})_{ii} = (m_{\tilde{Q}})_{ii} = (m_{\tilde{L}})_{ii}, i = 1, 2$	3 TeV	
$(T^u)_{33}$	-2100 GeV	-2150 GeV
$m_A$	2.5 TeV	
$\mu$	400-650 GeV	750-1000 GeV
$\lambda''_{33i} \equiv \sqrt{(\lambda''_{332})^2 + (\lambda''_{331})^2}$	$10^{-7} - 10^{-1}$	
$T^l, T^d, (T^u)_{ij}, (m_{\tilde{Q}, \tilde{U}, \tilde{D}, \tilde{L}, \tilde{E}})_{ij}, T''_{33i},$ $i \neq j = 1, 2, 3, (T^u)_{ii}, i = 1, 2$	0	

Table 3.2.: Two lists of benchmark SUSY parameters defined at the low scale  $Q_{EW\text{SB}}^2 = 1 \text{ TeV}^2$  taken as input for SPHENO. All other non-listed supersymmetric or soft SUSY breaking parameters are either computed from the input, such as  $m_{H_{1,2}}^2$ , or irrelevant to the present study, such as  $\lambda_{ijk}, \lambda'_{ijk}, \mu_i, T_{ijk}, T'_{ijk}, \tilde{B}_i, \tilde{m}_{1i}$  for all three generations, and  $T''_{ijk}$  for  $i, j = 1, 2$ . We also take  $m_b(m_b)_{\overline{\text{MS}}} = 4.18 \text{ GeV}$  and  $m_t(\text{pole}) = 173.5 \text{ GeV}$ . See [244] for the values of the other SM input parameters.

left-handed states. They tend to be suppressed for heavy states as a result of decoupling but can be enhanced by mass splitting between up and down flavors as a result of custodial symmetry breaking [255]. In our benchmark scenario where the lighter stop is mainly right-handed and all other squark and slepton states heavy and almost degenerate, no sizable effects on  $\delta\rho$  are expected from these sectors even for a relatively light  $\tilde{t}$ . The resulting range for  $\rho \simeq 1 + \delta\rho^{\text{SUSY}}$  obtained in our scan remains consistent within  $2\sigma$  with the experimental value [46].

The  $B$ -meson radiative inclusive decay  $B \rightarrow X_s \gamma$  is sensitive to virtual ef-

Benchmark points	1	2
$m_{\tilde{t}}$	$\sim 600$ GeV	$\sim 1$ TeV
$m_{\chi^+}$	$\sim 400\text{-}650$ GeV	$\sim 750\text{-}1000$ GeV
$m_{\chi^+} - m_{\chi^0}$	$\sim 1.5\text{-}2.5$ GeV	
$m_{\tilde{t}} - m_{\chi^+}$	$\sim -45 - 200$ GeV	$\sim 1 - 245$ GeV
$m_{\chi_2^0} - m_{\chi^+}$	$\sim 4\text{-}5$ GeV	
$m_{\chi_3^0} \sim m_{\chi_2^+}, m_{\chi_4^0}$	$\sim 1.5$ TeV, $\sim 2.5$ TeV	
$m_{h^0}$	$\sim 125$ GeV	
$m_A \approx m_{H^0} \approx m_{H^\pm}$	$\sim 2.5$ TeV	
$M_{\tilde{g}}$	$\sim 1.87$ TeV	
$M_{\tilde{t}_2} \approx M_{\tilde{b}_1}$	$\sim 2$ TeV	
$M_{\tilde{b}_2} \approx M_{\tilde{u}_{1,2}} \approx M_{\tilde{d}_{1,2}}$	$\sim 3$ TeV	
$M_{\tilde{l}_{1,2}}, M_{\tilde{\nu}_{1,2}}$	$\sim 3$ TeV	
$(g - 2)_\mu^{\text{SUSY}}$	$3 - 3.3 \times 10^{-11}$	$3.2 - 3.3 \times 10^{-11}$
$\delta\rho^{\text{SUSY}}$	$5.7 - 5.9 \times 10^{-5}$	$\sim 5.5 \times 10^{-5}$
$BR(B \rightarrow X_s \gamma) / BR(B \rightarrow X_s \gamma)^{SM}$	$0.89 - 0.92$	$0.95 - 0.96$
$BR(B_s^0 \rightarrow \mu\mu)$	$3.36 - 3.39 \times 10^{-9}$	$3.38 - 3.40 \times 10^{-9}$
$BR(B_d^0 \rightarrow \mu\mu)$	$1.08 - 1.09 \times 10^{-10}$	$\sim 1.09 \times 10^{-10}$

Table 3.3.: Two lists of benchmark observables generated with SPHENO corresponding to the input of Table 3.2 and taken as input for MADGRAPH5\_AMC@NLO. Pole masses are evaluated at one-loop order except for the lightest CP-even Higgs which includes the 2-loop corrections.

fects from various sectors of the MSSM associating the charged Higgs to the top quark, the up squarks to the charginos and the down squarks to the neutralinos or to the gluino [256]. Only the  $\chi^+ - \tilde{t}$  loops are sizable in our case as the stop is much lighter than all other squarks and the gluino. Moreover it is mainly right-handed and the chargino higgsino-like, thus further leading to a  $\mathcal{O}(m_t/M_W)$  enhancement in the amplitude. The charged Higgs yields like-wise suppressed contributions due to its very heavy mass. Taking into account the recent up-

date for the SM theoretical prediction  $BR(B \rightarrow X_s \gamma) = (3.36 \pm 0.23) \times 10^{-4}$  [257], our scan remains within  $1.2\sigma$  from the combined experimental value  $BR(B \rightarrow X_s \gamma) = (3.43 \pm 0.21 \pm 0.07) \times 10^{-4}$  [258]. It is however interesting to note that keeping only the right-handed stop and Higgsino-like contributions, the mass ratio dependence in the loop functions favor, for lighter stops, heavier charginos in order to cope with the  $BR(B \rightarrow X_s \gamma)$  constraints. As a consequence a sufficiently light stop would require a reduced mass splitting with respect to the lighter chargino, eventually even forbidding the hierarchy given in Eq. (3.11) and favoring a stop MSSM-LSP. The latter would imply a stop decaying 100% into  $b$ +jet final states, giving support to the model-independence of the present exclusion limits based on this assumption, as long as the ensuing bounds remain low enough. For instance we find that a lower bound of 0.89 on  $BR(B \rightarrow X_s \gamma)/BR(B \rightarrow X_s \gamma)^{SM}$  as adopted e.g. in [259] would typically require  $m_{\tilde{t}} \gtrsim 400$  GeV. Still, a more quantitative study is needed as mass degeneracy between the stop and chargino could still be allowed favoring the third regime of Eq. (3.41) and thus final states with  $\chi$ -RPV or RPC-like components. For instance relaxing the lower bound to  $\sim 0.84$  would allow lighter non-LSP stops, e.g.  $m_{\tilde{t}} \lesssim 385$  GeV, with  $m_{\chi^+} \gtrsim 198$  GeV.

Finally, regarding the  $B^0$  decay into a pair of muons, LHCb [248, 249] and CMS [250] have recently reported observation of such decays, with the combined fits leading to  $BR(B_s^0 \rightarrow \mu\mu) = (2.8_{-0.6}^{+0.7}) \times 10^{-9}$  and  $BR(B_d^0 \rightarrow \mu\mu) = (3.9_{-1.4}^{+1.6}) \times 10^{-10}$  that are compatible with the SM at  $2\sigma$ -level [260]. Our benchmark numbers are consistent with the updated SM theoretical predictions  $BR(B_s^0 \rightarrow \mu\mu) = (3.65 \pm 0.23) \times 10^{-9}$  and  $BR(B_d^0 \rightarrow \mu\mu) = (1.06 \pm 0.09) \times 10^{-10}$  [261].

## 3.6. Cross-sections and uncertainties

Using the spectrum calculator and event generator tools as described in the previous Sections we have computed the total cross-section and decays of a pair of stops in  $pp$  collisions at  $\sqrt{s} = 14$  TeV for the two benchmark points given in Table 3.2 and the various combinations of final states given in Table 3.1, except for the  $1t3b2j$  final state since it remains subdominant everywhere in the considered  $\lambda''_{33i}$  range. In Figs. 3.2 and 3.3 we illustrate the sensitivity to the magnitude of  $\lambda''_{33i}$ , and in Figs. 3.4 and 3.5 the sensitivity to the stop-chargino mass splitting for the two benchmark points. Before commenting these results, we discuss first the various theoretical uncertainties.

### 3.6.1. Theoretical uncertainties

Besides the BSM uncertainties which cannot be really quantified and are somewhat fixed through the choice of the MSSM parameters, there are other the-

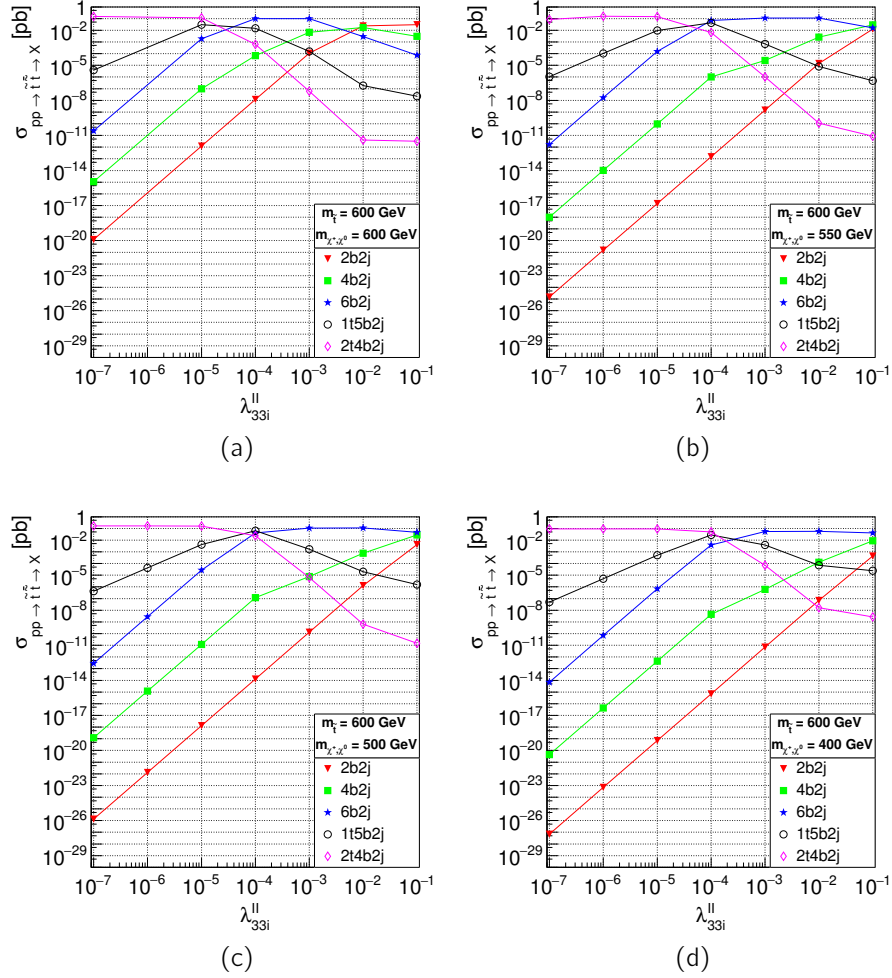


Figure 3.2.: Benchmark 1: production cross-section for  $\sigma(pp \rightarrow t\bar{t} \rightarrow X)$  at  $\sqrt{s} = 14$  TeV, where  $X = 2b2j$  (red triangles),  $4b2j$  (green squares),  $6b2j$  (blue stars),  $1t5b2j$  (black empty circles) and  $2t4b2j$  (pink diamonds), as a function of  $\lambda''_{33i}$  and for  $m_{\tilde{t}} - m_{\chi^+} \simeq 0$  GeV(a), 50 GeV(b), 100 GeV(c) and 200 GeV(d). See Tabs. 3.2 and 3.3 for the low-energy values of the MSSM parameters.

oretical inputs, whose uncertainties must be taken into account when quoting the expected cross sections for a given process. Since we are interested in the evaluation of the total cross-sections involving the SUSY-QCD process of stop pair production followed by SUSY-EW decays through various short and long chains, we choose to generate the  $pp \rightarrow t\bar{t}$  processes at the leading order (LO) accuracy level. SUSY-QCD calculations up to next-to-leading-order (NLO) as well as resummed soft gluons at next-to-leading-logarithmic (NLL) level for the

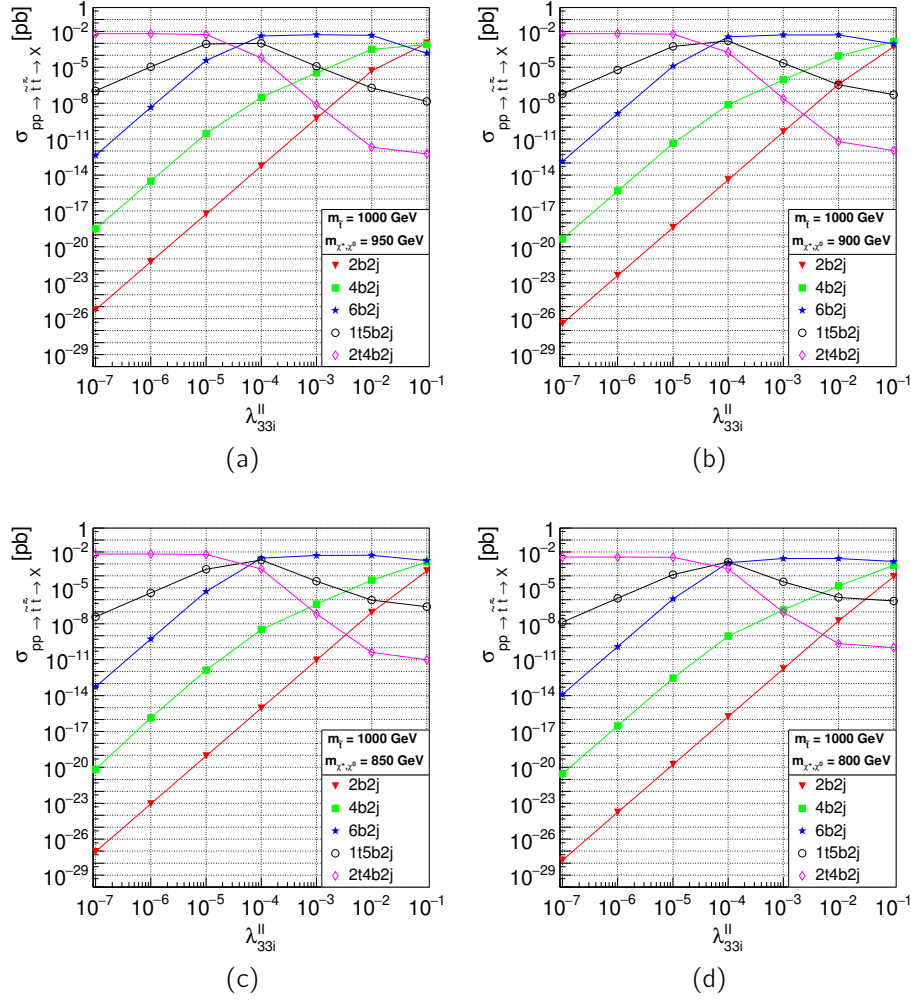


Figure 3.3.: Benchmark 2: production cross-section for  $\sigma(pp \rightarrow t\bar{t} \rightarrow X)$  at  $\sqrt{s} = 14$  TeV, where  $X = 2b2j$  (red triangles),  $4b2j$  (green squares),  $6b2j$  (blue stars),  $1t5b2j$  (black empty circles) and  $2t4b2j$  (pink diamonds), as a function of  $\lambda''_{33i}$  and for  $m_{\tilde{t}} - m_{\chi^+} \simeq 50$  GeV(a), 100 GeV(b), 150 GeV(c) and 200 GeV(d). See Tabs. 3.2 and 3.3 for the low-energy values of the MSSM parameters.

partonic stop pair production cross-section in proton-(anti)proton collisions are well-known, see [262] for a recent appraisal. These calculations contribute to reducing scale uncertainties and typically lead to an increase of the cross-section above LO results [263, 264, 265], especially near the partonic stop pair production threshold. On the other hand, Parton Distribution Functions (PDFs) have been recently supplemented by soft gluon threshold resummation at the NLO accuracy [266]. Using these PDFs consistently in conjunction with the resummed

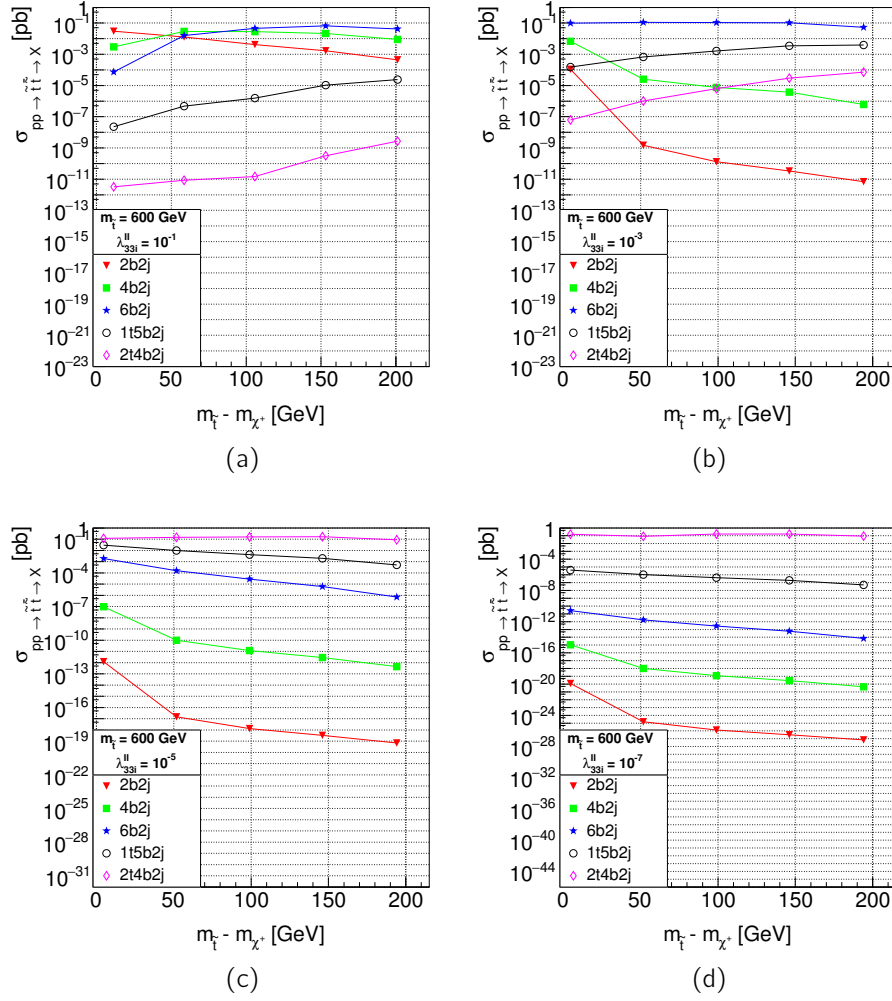


Figure 3.4.: Benchmark 1: production cross-section for  $\sigma(pp \rightarrow t\bar{t} \rightarrow X)$  at  $\sqrt{s} = 14$  TeV, where  $X = 2b2j$  (red triangles),  $4b2j$  (green squares),  $6b2j$  (blue stars),  $1t5b2j$  (black empty circles) and  $2t4b2j$  (pink diamonds), as a function of  $m_{\tilde{t}} - m_{\chi^+}$  and for  $\lambda''_{33i} = 10^{-1}$  (a),  $10^{-3}$  (b),  $10^{-5}$  (c) and  $10^{-7}$  (d). See Tabs. 3.2 and 3.3 for the low-energy values of the MSSM parameters.

partonic matrix element calculations, showed a partial cancellation of the above mentioned threshold effects bringing them closer to the fixed order results. One thus expects the cross-section for heavy stop pair production to be well approximated by fixed order NLO results. Moreover, the latter corrections are in turn expected to be moderate for our benchmark points with very heavy colored SUSY states. In fact comparing for instance the NLO-NLL results in the decoupled gluon/squarks limits given in [262] to the LO results we find an increase of the



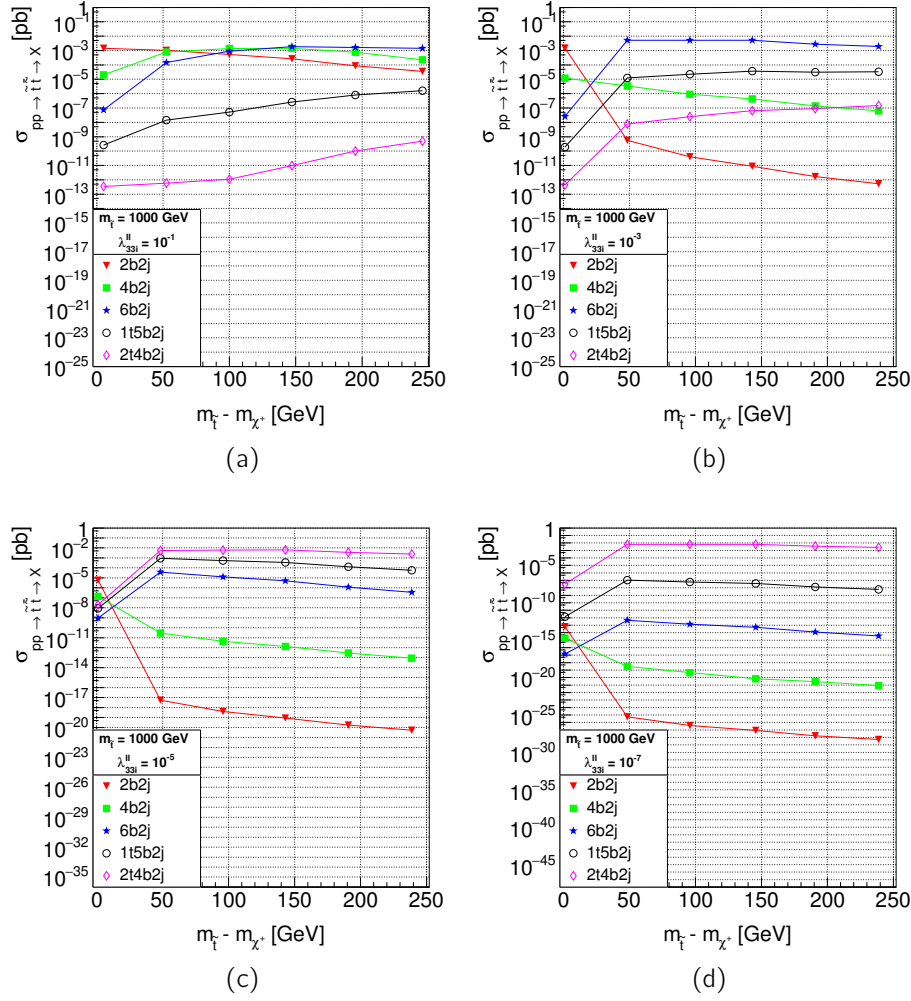


Figure 3.5.: Benchmark 2: production cross-section for  $\sigma(pp \rightarrow t\bar{t} \rightarrow X)$  at  $\sqrt{s} = 14$  TeV, where  $X = 2b2j$  (red triangles),  $4b2j$  (green squares),  $6b2j$  (blue stars),  $1t5b2j$  (black empty circles) and  $2t4b2j$  (pink diamonds), as a function of  $m_{\tilde{t}} - m_{\chi^+}$  and for  $\lambda''_{33i} = 10^{-1}$  (a),  $10^{-3}$  (b),  $10^{-5}$  (c) and  $10^{-7}$  (d). See Tabs. 3.2 and 3.3 for the low-energy values of the MSSM parameters.

former in excess of 30% for  $m_{\tilde{t}} = 600$  GeV at  $\sqrt{s} = 14$  TeV. However, due to the above mentioned partial cancellation the effect would be smaller for production cross-sections dominated by stops almost at rest when NLL contributions are consistently included also in the PDFs. The difference between NLO and LO production cross-sections would thus be within the uncertainties related to scale variation or to the choice of PDF sets (discussed below). Another reason to stick consistently to LO accuracy for the production cross-section in the present



study, is that the dominant virtual QCD corrections to the stop decay chains are not readily available at the level of matrix element calculations for the considered channels. Moreover, even though some of these corrections could partly cancel in branching ratios, the latter entail the NWA which, as pointed out in Section 3.4 and discussed quantitatively in Section 3.6.2, is not always a good approximation to the full matrix element calculations.

We now turn to the uncertainties from the PDFs and from the factorization and renormalization scales, evaluated for the  $2b2j$  and  $6b2j$  final state processes at the center of mass energy of 14 TeV using MADGRAPH5\_AMC@NLO.

### 3.6.1.1. Systematic uncertainty from scale variation

In order to evaluate the scale uncertainty, we vary the renormalization and factorization scales independently with respect to the fixed scales central values  $\mu_R = \mu_F = m_{\tilde{t}}$ . We choose values within the range  $m_{\tilde{t}}/2 < \mu_R, \mu_F < 2m_{\tilde{t}}$ . The computation is performed using the NNPDF23LO1 set [267] for three different stop mass points corresponding to  $m_{\tilde{t}} = 600, 800$  and  $1000$  GeV, three different stop-chargino mass splitting equal to 50, 100 and 150 GeV and three different values of the coupling  $\lambda''_{33i} = 10^{-1}, 10^{-3}$  and  $10^{-6}$ . At a given  $m_{\tilde{t}}$ , we take the scale uncertainty to be the largest difference in cross section relative to the central value. We note that the fractional scale uncertainty for both  $2b2j$  and  $6b2j$  processes is approximately  ${}^{+40\%}_{-25\%}$ , independently from the stop mass, the stop-chargino mass splitting and the  $\lambda''_{33i}$  value.

### 3.6.1.2. Systematic uncertainty from PDF

Systematic uncertainties due to PDFs are evaluated by computing the cross sections of the two processes  $2b2j$  and  $6b2j$  at the center of mass energy of 14 TeV with MADGRAPH5\_AMC@NLO using two different PDF sets: NNPDF23LO1 [267], CTEQ6L [268]. The estimation of these uncertainties is performed similarly to the evaluation of the scale uncertainty, for three values of the stop mass,  $m_{\tilde{t}} = 600, 800$  and  $1000$  GeV, three stop-chargino mass splitting equal to 50, 100 and 150 GeV and three RPV  $\lambda''_{33i}$  couplings corresponding to  $10^{-1}, 10^{-3}$  and  $10^{-6}$ . The result appears to be slightly dependent on  $m_{\tilde{t}}$ . The resulting relative variation in cross sections is found to be around 24% for  $m_{\tilde{t}} = 600$  GeV, 28% for  $m_{\tilde{t}} = 800$  GeV and 32% for  $m_{\tilde{t}} = 1$  TeV.

Finally, we note that both PDF and scale uncertainties associated with the  $2b2j$  final state process are consistent within 2% with the ones found for the  $6b2j$  final state: this result allows us to assume the same order of magnitude for the uncertainty associated with the other RPV-processes listed in Sec. 3.3.2.

### 3.6.2. Final states sensitivity to $\lambda''_{33i}$

As can be seen from Figs. 3.2 and 3.3, the various cross-sections vary over several orders of magnitude due to a very high sensitivity to  $\lambda''_{33i}$ . The extreme values of  $\lambda''_{33i}$  feature a reversed hierarchy of the contributions of the different final states. The most striking aspect is that the busiest  $2t4b2j$  final state dominates for extremely small values  $\mathcal{O}(10^{-7} - 10^{-5})$  of  $\lambda''_{33i}$  while the  $2b2j$ ,  $4b2j$  and  $6b2j$  final states dominate for  $\lambda''_{33i}$  of  $\mathcal{O}(10^{-3} - 10^{-1})$ , yet with comparable cross-sections of order a few tens to a hundred femtobarns. Moreover, as shown on Figs. 3.4(a) and 3.5(a), the relative contributions of the dominant  $2b2j$ ,  $4b2j$  and  $6b2j$  final states for large  $\lambda''_{33i}$  depend also on the stop chargino mass splitting, typically with a (reversed) hierarchy given by the  $b$ -quark multiplicity. The  $4b2j$  channel can be comparable to the two other channels but is rarely dominant. The  $2b2j$  will always eventually dominate for sufficiently large  $\lambda''_{33i} \gtrsim 10^{-2}$  (e.g. for  $\lambda''_{33i} \gtrsim 10^{-1}$  not shown on the figures, its dominance prevails for small to moderate ranges of mass splitting). In contrast, the  $6b2j$  channel dominates in a range of intermediate values of  $\lambda''_{33i} \gtrsim 10^{-3}$  when the mass splitting is moderate to large.

These features illustrate clearly the complementarity of the different final states in view of extracting information in the RPV-coupling/mass-splitting parameter space. The general trend of the sensitivity to  $\lambda''_{33i}$  can be understood qualitatively from the NWA expressions, Eqs. (3.35) through (3.40). From the asymptotic behavior of these NWA expressions at small  $\lambda''_{33i}$ , in the regime  $r_1 \times (\lambda''_{33i})^2 \ll 1$  and  $r_2 \times (\lambda''_{33i})^2 \ll 1$ , one sees that all the topless final state channels scale with  $(\lambda''_{33i})^4$ , the channels with one top scale with  $(\lambda''_{33i})^2$  and the channel with two top-quarks tends to be constant in  $\lambda''_{33i}$ , which explains the tremendous orders of magnitude difference in the cross-sections and the dominance of the RPC-like channel. If the other extreme of asymptotically large  $\lambda''_{33i}$  were allowed, i.e.  $\lambda''_{33i} \gtrsim 1$ ,  $r_1 \times (\lambda''_{33i})^2 \gg 1$  and  $r_2 \times (\lambda''_{33i})^2 \gg 1$ , then only the  $2b2j$  would survive, becoming almost  $\lambda''_{33i}$ -independent, the other channels scaling with increasing inverse powers of  $\lambda''_{33i}$  for increasing multiplicity of  $b$ - and  $t$ -quarks in the final state. In fact, if one remains in the domain of moderate values of  $\lambda''_{33i}$  the behavior becomes more sensitive to  $r_1, r_2$ . In our scenario  $r_2$  is always very large, typically several orders of magnitude larger than  $r_1$ , due to the smallness of the decay width of  $\Gamma(\chi^+ \rightarrow \chi^0 f'_2 \bar{f}_2)$  and to the fact that  $\chi^+$  and  $\chi^0$  are almost degenerate. For the considered range of  $\lambda''_{33i}$  we are always in the regime  $r_2 \times (\lambda''_{33i})^2 \gg 1$ . Similarly,  $r_1$  can become equally large but only in corners of the parameter space where the stop is almost degenerate with the chargino as seen from Eq. (3.30). This allows to understand the relative magnitudes of the various cross-sections shown on the figures. For instance the ratio  $\sigma(6b2j)/\sigma(2b2j)$  scales with  $r_1^{-2}(\lambda''_{33i})^{-4}$  and is indeed (much) larger than 1 even at the upper edge of the domain of Eq. (3.14), except when  $r_1$  becomes large due to small stop-chargino mass splitting, eventually reversing the hierarchy between the two cross-sections consistently with the numerical behavior shown on

Figs. 3.4(a) and 3.5(a). One can understand similarly the behavior of  $\sigma(4b2j)$  that is bounded essentially between the  $2b2j$  and  $6b2j$  cross-sections irrespective of the mass splitting. Note however that  $\sigma(4b2j)/\sigma(6b2j)$  scales with  $2r_1(\lambda''_{33i})^2$ , so that the  $4b2j$  channel can come to dominate over all the other channels for moderate mass splitting and a  $\lambda''_{33i}$  somewhat larger than the range we consider for the analysis. Turning to the final states containing one or two top-quarks, their tiny contribution in the upper part of the  $\lambda''_{33i}$  range, cf. Figs. 3.2 and 3.3, is due to the size of  $r_2$ . For instance  $\sigma(2b2j)/\sigma(2t4b2j)$  scales with  $r_1^2 r_2^2 (\lambda''_{33i})^8$ , but the large suppression for  $\lambda''_{33i} \lesssim 0.1$  is compensated for by a very large value of  $r_2 \approx \mathcal{O}(10^7)$  as a consequence of the compressed light chargino/neutralino sector.

We turn now to a quantitative discussion of the comparison between the full matrix element calculation and the NWA. Given the huge difference in the scaling of the various cross-sections and the variations over several orders of magnitudes, this comparison is an important cross-check of the results. We indeed find that the NWA works reasonably well in configurations where it is expected to do so [237, 238, 239, 240]. We check first the scaling relations t-SR and b-SR given in Eqs. (3.42, 3.43), as these provide global tests that do not require the knowledge of the stop production cross-section nor the  $r_1, r_2$  ratios. A systematic test of t-SR and b-SR using all the cross-sections in Table 3.4 and in Table 3.5 gave a relative deviation of 10% or more from these scaling relations only in  $\lesssim 9\%$  of the cases, while a deviation of  $\lesssim 5\%$  obtains in  $\sim 80\%$  of the cases and a deviation of  $\lesssim 1\%$  in  $\sim 66\%$  of the cases. It is also instructive to identify the configurations where the NWA fails badly. We find that deviations of more than 30%, reaching up to 135%, occur in less than 5% of the cases and only for t-SR that involves long chain decays. These correspond to points of benchmark 1 having large values of  $\lambda''_{33i}$  and very small stop-chargino mass splitting, such as for  $\lambda''_{33i} = 10^{-1}$  and  $m_{\tilde{t}} - m_{\chi^+} = 59$  and 11 GeV and for  $\lambda''_{33i} = 10^{-2}$  and  $m_{\tilde{t}} - m_{\chi^+} = 5$  GeV, shown in Table 3.4. Such large deviations are in accord with the general expectations [237]. We have also checked the NWA for individual cross-sections. This allowed to disentangle the reasons for the differences from the results of the full matrix element calculations. Very good quantitative agreement is observed for the shortest decay chains, and for small values of  $\lambda''_{33i}$  and/or large mass splitting for longer decay chains. The cross-sections given by Eqs. (3.35–3.40) reproduce globally the behavior shown in Figs. 3.2 and 3.3.

We discuss now three spectrum configurations that are outside one or the other of the assumptions given in Eqs. (3.11 – 3.13). The values of  $m_{\tilde{t}} - m_{\chi^+} = -36$  or  $-43$  GeV, shown in Table 3.4, correspond to points violating Eq. (3.11) with an MSSM-LSP stop. As expected, in this case the  $2b2j$  channel largely dominates independently of the magnitude of  $\lambda''_{33i}$ , the next-to-leading channel,  $4b2j$ , being two to three orders of magnitude smaller. It is however noteworthy that the  $2b2j$  channel can be dominant even when Eq. (3.11) is satisfied, provided that the positive mass splitting  $m_{\tilde{t}} - m_{\chi^+}$  remains sufficiently small and  $\lambda''_{33i}$  sufficiently

large. One sees this tendency from the  $m_{\tilde{t}} - m_{\chi^+} = 5$  and 11 GeV points in Table 3.4 for benchmark 1. For instance, the  $2b2j$  channel can still be an order of magnitude greater than the total of the remaining channels for a stop/chargino mass splitting in excess of 10 GeV, as illustrated for  $m_{\tilde{t}} - m_{\chi^+} = 11$  GeV and  $\lambda''_{33i} = 10^{-1}$ . A smaller mass splitting, at the edge of the validity of Eq. (3.13), leads to even larger effects, as one can see in Table 3.5 by looking at the point  $m_{\tilde{t}} - m_{\chi^+} = 5$  GeV and  $\lambda''_{33i} = 10^{-1}$ . In this case the  $2b2j$  channel dominates the other channels by almost two orders of magnitude. A larger mass splitting would require larger values of  $\lambda''_{33i}$  to ensure the dominance of the  $2b2j$  channel. In fact there is a correlation between the mass splitting and the size of the RPV coupling that can be understood in terms of the NWA cross-section of Eq. (3.35): the  $2b2j$  channel becomes dominant, with a branching ratio close to one, when  $r_1 \times (\lambda''_{33i})^2 \gg 1$ , say  $\mathcal{O}(10)$  or larger. Indeed, the ratio  $r_1$  becomes large for small stop/chargino mass splitting due to phase-space suppression of the width  $\Gamma(\tilde{t} \rightarrow \chi^+ b)$ , see Eq. (3.30), implying that  $2b2j$  can dominate for moderately small  $\lambda''_{33i}$ . More generally the regime where  $2b2j$  dominates is characterized roughly by  $|\lambda''_{33i}| \gtrsim 3 \times r_1^{-1/2}$ . The present LHC limits [198, 199, 208] where the  $2b2j$  dominance is assumed, can thus be interpreted as excluding either scenarios where the stop is the MSSM-LSP, or the domain delineated by the above relation in scenarios where a chargino and a neutralino are lighter than the stop.

If Eq. (3.13) is not satisfied but the mass splitting still larger than the  $s$ -quark or  $d$ -quark masses then the  $\chi$ -RPV and RPC-like decays occur dominantly through the LFV channel  $\tilde{t} \rightarrow s(d)\chi^+$  (recall that we assume MFV). The effect is thus noticeable for the small values of  $\lambda''_{33i}$  where the  $\chi$ -RPV or RPC-like decays are expected to dominate. This is illustrated for all values of  $\lambda''_{33i}$  with mass splitting of 1 GeV in Table 3.5. There are two effects: for  $\lambda''_{33i}$  in the intermediate range  $10^{-4}$ – $10^{-2}$ , the  $2b2j$  channel becomes largely dominant over the  $6b2j$  and  $1t5b2j$  channels contrary to the typical cases with larger stop/chargino mass splitting. In this intermediate  $\lambda''_{33i}$  range the LFV channels with smaller  $b$ -quark multiplicity and larger light jet multiplicity such as  $4b4j$  and  $1t3b4j$  final states have cross-sections comparable to that of the  $2b2j$  channel given the size of the corresponding CKM mixing angles. In contrast, in the range  $10^{-7} \lesssim \lambda''_{33i} \lesssim 10^{-5}$  the cross-sections for all the final states listed in Table 3.1 become suppressed as can be seen in the corresponding blocks of Table 3.5 and mass splitting of 1 GeV indicating that the dominant channel corresponds now to the LFV RPC-like–RPC-like final state  $2t2b4j$ . The study of final states with more light quarks and less  $b$ -quark multiplicity can thus be motivated in the context of an inclusive search comprising the very narrow part of the parameter space having an extremely compressed  $\tilde{t}/\chi^+$  spectrum.

Last but not least, we consider the case where Eq. (3.12) is not satisfied. The decay channel  $\tilde{t} \rightarrow t\chi^0(\chi_2^0)$  is now open leading to  $4t2b2j$  final states. A detailed study of this channel is outside the scope of the present paper and we do not give here the corresponding cross-section. It is however interesting to note the

indirect effect of this channel on the cross-sections given in Tables 3.4 and 3.5. Indeed, the expected drop of the latter when the top-neutralino channel sets in is found to remain relatively moderate. For instance, comparing the points  $m_{\tilde{t}} - m_{\chi^+} = 146$  GeV and 194 GeV of Table 3.4 one sees that the drop in the leading cross-sections  $6b2j$ ,  $1t5b2j$  and  $2t4b2j$  is by a factor of order 2–2.5 or less, depending on the magnitude of  $\lambda''_{33i}$ . Similar effects are found for benchmark 2, as seen from a comparison of the points  $m_{\tilde{t}} - m_{\chi^+} = 143$  GeV and 239 GeV of Table 3.5. This suggests that the final states considered in the present study can still contribute to signatures outside the specific mass configurations that we relied on.

To conclude this section, we stress the main point of the analysis: if part of the chargino/neutralino sector is lighter than the lightest stop, channels with different jet multiplicities probe dominantly different ranges of the RPV coupling. This is due to a distinct dependence on  $\lambda''_{33i}$  of the various decay widths and branching ratios, thus triggering the dominance of different channels for different values of this coupling. We depict this general feature schematically in Fig. 3.6 for a typical configuration, keeping in mind that the actual dominance ranges can change depending on the masses and RPC couplings. The analytical expressions for the cross-sections in terms of the RPV coupling and decay widths in the RPC sector given in Sec. 3.4 allow a clear qualitative understanding of these features. The

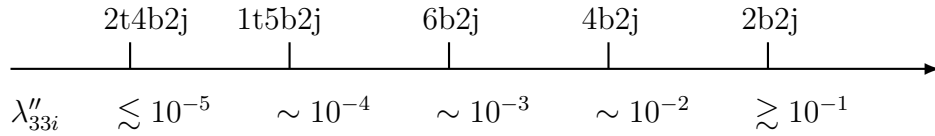


Figure 3.6.: Schematic illustration of  $\lambda''_{33i}$  as a *signature generator*; different magnitudes of this coupling favor different final states.

RPV coupling thus plays the role of a *signature generator*.

### 3.7. RPV Final States and SM background: a discussion

The LHC is currently in its Run 2 data taking period, which started in 2015 and it is now providing proton-proton collisions at  $\sqrt{s} = 13$  TeV to both ATLAS and CMS, continuously improving in the delivered peak luminosity. With the current schedule,  $100 \text{ fb}^{-1}$  of data and a possible further push in the center-of-mass energy to  $\sqrt{s} = 14$  TeV, both ATLAS and CMS will be able to carry the BSM searches which are the core of the LHC Run 2 physics program. In what follows we give a brief overview of how the different RPV signatures, which are the focus of this paper, are, or can be looked for at the LHC. For the different final states treated,

$2b2j$ ,  $4b2j$ ,  $6b2j$ ,  $1t5b2j$  and  $2t4b2j$ , we either review the current experimental analyses, or, for those channels where no experimental analyses have been performed yet, we propose, based on similar existing analyses, a search strategy with a list of SM backgrounds which could impact their sensitivities.

### 3.7.1. $2b2j$

Direct production of stop quarks with a subsequent RPV decay into two jets has been searched for at LEP and Tevatron, where a 95% upper limit on the mass of such particles was set to respectively 82.5 GeV [269] and 100 GeV [270]. As pointed out by Ref. [271] first searches for stop production at the LHC did not succeed on being sensitive to any stop mass until the trigger strategy changed from using high transverse momentum ( $p_T$ ) multi-jet triggers, which had the effect of shaping the background towards high masses, to triggering on the totality of the hadronic energy deposited in the calorimeter (ATLAS [272]), a variable less correlated to the two masses of the di-jet resonances, or lower  $p_T$  jets (CMS [208]). Both ATLAS and CMS have looked for stop production pairs final state where the two stops decay into  $\bar{b}\bar{s} + bs$ . The two stop-quark resonances are identified as wide hadronic calorimeter “fat” jets with a cone size,  $R$ , of the order of 1, 1.5 [273]. Given that the characteristic distance between the two particles stemmed from a resonance,  $\Delta R$ , is of the order  $2m/p_T$ , where  $m$  is the stop-quark mass and  $p_T$  its transverse momentum, this kind of signature allows to access a relatively low mass spectra, where most of the center of mass energy goes to the boost of the produced resonance pair.

The main challenge for hadronic jet based searches is to understand the normalizations and shapes of the multijet background, this has been shown to be possible using data-driven techniques [72]. The discrimination between signal and background is done by exploiting kinematic quantities such as the value of the reconstructed fat jet masses, which is the same for the two fat jets from stop pair production, and other jet substructure properties such as the difference in  $p_T$  between the two subjets identified by un-doing the last step of the fat jet clustering, more pronounced in multijet events (see Ref. [199] and reference therein). Also fundamental to reduce multi-jet background,  $b$ -tagging algorithms are used to identify the presence of jets issued from the hadronization of  $b$ -quarks [274, 275]. After bump hunting, the two LHC experiments could exclude at 95% Confidence Level stop quark production for masses up to 345 GeV(ATLAS) [199] and 385 GeV(CMS) [208]. This final state is sensitive not only to the value of the stop mass in the case the stop is the LSP, but if the lightest neutralino and the lightest chargino are lighter than the stop quark, then this class of analyses could be sensitive to the hardest part of the  $\lambda''_{332}$  spectrum considered, as shown in Fig. 3.2, see also Section 3.6.2.



### 3.7.2. $4b2j$ and $6b2j$

As discussed in section 3.6.2 the topless multi- $b$ -jet signatures saturate the stop quark branching ratio for intermediate values of  $\lambda''_{33i} \gtrsim 10^{-3}$ . The  $4b2j$  and  $6b2j$  signatures have the highest cross sections at large  $\lambda''_{33i}$  value when the differences between the stop and the chargino/neutralino masses are maximal, see Figs 3.2 and 3.4. In this scenario, for low stop masses, such that  $2m/p_T$  is  $O(1)$ , the same strategy as the searches in the  $2b2j$  final state can be used, where two structured large sized hadronic jets of particles are produced back to back. This facilitates the task of eliminating the combinatorial background that arises when the presence of multiple reconstructed objects in the final state does not allow to assign them to one of the particle originating the decay. This results in a poor reconstruction of the resonant peaks. Moreover the presence of resonances within the fat jets helps discriminating against the background when using the value of the reconstructed invariant mass of the stop and chargino candidates and of more specific jet substructure related quantities such as the  $k_t$  splitting scale and  $n$ -subjettiness (see Ref. [276] and references therein). It has also been recently suggested [277] that jet reconstruction techniques based on a mass-jump clustering algorithm with variable size can be used to reconstruct multi-jet resonance in very busy environment as the one produced by boosted stop squarks decay into  $4b2j$  or  $6b2j$  final states.

In the case of resolved regime, where most jets from the stop and chargino decay are reconstructed, the signal is characterized by events with high jet and  $b$ -jet multiplicity. If no  $b$ -tagging is required at the analysis level, the signal, even for stop masses of about one TeV, although it would present very high jet multiplicity, would be still swamped by the presence of a large multi-jet background [278].

When the  $b$ -jet identification is used, the physics processes that could mimic RPV stop signal, include any resonant multi- $b$ -jet production such as  $t\bar{t} + X$ , abundantly produced in the  $\sqrt{s} = 14$  TeV proton-proton collisions at the LHC. Background processes to this final state include  $t\bar{t}$  plus light and heavy flavored jets,  $t\bar{t}$  plus vector boson, and  $t\bar{t}H(\rightarrow b\bar{b})$  production, where both top quarks decay fully hadronically. The inclusive  $t\bar{t}$  cross section is known at NNLO in QCD including resummation of soft gluon terms at next-to-leading-logarithmic (NNLL) [135]; at  $\sqrt{s} = 14$  TeV,  $\sigma_{t\bar{t}} = 954^{+23}_{-34}(\text{scale})^{+16}_{-18}(\text{pdf})$  pb, 45.7% of which decays fully hadronically [46]. At the analysis level when asking for more than 2  $b$ -tagged jets it is more likely to select events from processes where extra heavy flavors are produced. For  $\sqrt{s} = 14$  TeV,  $\sigma_{t\bar{t}+b\bar{b}}$  is known at NLO to be  $2.63^{+86}_{-70}(\text{scale})$  pb [279],  $\sigma_{t\bar{t}\rightarrow Z}$  is also known at NLO with a value of  $1057^{+110}_{-104}(\text{scale})^{+20}_{-25}(\text{pdf})$  fb [280] while  $\sigma_{t\bar{t}\rightarrow W} = 769^{+228}_{-170}(\text{scale})^{+54}_{-61}(\text{pdf})$  fb [281]. As for the associated top and Higgs production,  $t\bar{t}H$  cross section is known at NNLO in QCD and EW plus resummation of soft gluon at NNLL; at  $\sqrt{s} = 14$  TeV,  $\sigma_{t\bar{t}H(H\rightarrow b\bar{b})} = 625^{+29}_{-42}(\text{scale})^{+14}_{-14}(\text{pdf})$  fb [282]. Recent LHC analyses at

$\sqrt{s} = 8$  TeV [72] show how by just selecting a high multi-jet ( $\approx 8$ ) and  $b$ -jet multiplicity ( $\approx 4$ ) the background composition is made at about 80% of multi-jets. This background has little resemblance with multi-resonant production and can be discriminated using multi-variate analysis which exploits different energy regime, event shape, using quantities such as centrality, aplanarity and the mass of the reconstructed top quark candidates. Such kind of analysis needs to control the uncertainties on the main top-like background and at the same time removing as much as possible multi-jet background.

Despite the large background from multi-jet events, given the large energy deposit in the hadronic calorimeter from the decay products of the pair of massive resonances, and the large presence of jets coming from  $b$ -quark, as also stated in Ref. [210], this channel is very promising. Searches at hadron colliders for gluino pair production and subsequent RPV decay into  $tbs$ , where similar final states are investigated, could already show sensitivity to this channel [205].

### 3.7.3. $1t5b2j$ and $2t4b2j$

Signatures with decays into top quarks saturate the branching ratio for  $\lambda''_{33i} < 10^{-5}$ , as already discussed in Section 3.6.2. These signatures are interesting since the presence of a lepton from the top quark decay can be easily identified at trigger level and used to eliminate the otherwise overwhelming multi-jet background, such as in the fully hadronic signatures. After selecting at least six  $b$ -tagged jets in addition to at least two light-jets and one lepton, for the case of  $1t5b2j$ , or two leptons, for the case of  $2t4b2j$ , the main irreducible background arises from  $t\bar{t} + jets$  and  $t\bar{t}H(\rightarrow b\bar{b}) + jets$ . For simplicity in this discussion we limit ourself to analyzing the dileptonic top quark decay for the  $2t4b2j$  final state to allow discussing the backgrounds composition to both final states. In this case, the main background for both final states comes from  $t\bar{t} + b\bar{b}b\bar{b} + jets$ . The LO cross section for  $t\bar{t} + b\bar{b}b\bar{b}$  at  $\sqrt{s} = 14$  TeV, estimated with MADGRAPH5\_AMC@NLO using LHAPDF 6.1.6 [283], is  $290^{+400}_{-160}(\text{scale})^{+90}_{-50}(\text{pdf})$  fb, comparable with the signal cross section in the low  $\lambda''_{33i}$  regime, see for example  $\lambda''_{33i} < 10^{-5}$  in Table 3.4. The presence of neutrinos and the large jet multiplicity present in this final state makes it difficult to reconstruct completely the final state, i.e. to assign unambiguously reconstructed leptons and jets to the stop and anti-stop decays. This effect weakens the power of distributions such as the invariant mass of the reconstructed stop and chargino candidates, to discriminate signal and background events. The large energy deposited in the detectors, equal approximately to twice the stop mass, could have the role of the missing transverse energy for RPC searches, to discriminate signal against the softer top quark pair production, using for example the transverse energy of the event ( $H_T$ ). On the other hand the softer part of the  $H_T$  distribution can be useful to control the effect of major systematic uncertainties, especially the large theoretical uncertainties on  $t\bar{t} + b\bar{b}b\bar{b}$  cross section, on the LHC sensitivity for this



channel. This class of final states can use the analysis techniques developed for  $ttH(H \rightarrow b\bar{b})$  searches and that need to be extended to higher jet multiplicity.

As for the case of  $4b2j$  and  $6b2j$ , both ATLAS and CMS searches for gluino pair production and subsequent RPV decay to a pair of top quarks and jets through the R-parity violating decay of either the neutralino into three quarks or the top squark into SM quarks [205, 197], could already be reinterpreted as limits on  $\lambda''_{33i}$  using this channel.

$\lambda''_{33i}$	$\mu$ [GeV]	$m_{\tilde{t}} - m_{\chi^+}$ [GeV]	$\sigma(2b2j)$ [pb]	$\sigma(4b2j)$ [pb]	$\sigma(6b2j)$ [pb]	$\sigma(1t5b2j)$ [pb]	$\sigma(2t4b2j)$ [pb]
$10^{-1}$	400	201	$4.38 \cdot 10^{-4}$	$8.80 \cdot 10^{-3}$	$4.19 \cdot 10^{-2}$	$2.42 \cdot 10^{-5}$	$2.70 \cdot 10^{-9}$
	450	153	$1.67 \cdot 10^{-3}$	$2.16 \cdot 10^{-2}$	$6.66 \cdot 10^{-2}$	$1.05 \cdot 10^{-5}$	$3.21 \cdot 10^{-10}$
	500	106	$4.17 \cdot 10^{-3}$	$2.83 \cdot 10^{-2}$	$4.63 \cdot 10^{-2}$	$1.56 \cdot 10^{-6}$	$1.47 \cdot 10^{-11}$
	550	59	$1.26 \cdot 10^{-2}$	$2.87 \cdot 10^{-2}$	$1.60 \cdot 10^{-2}$	$4.79 \cdot 10^{-7}$	$8.45 \cdot 10^{-12}$
	600	11	$3.01 \cdot 10^{-2}$	$2.98 \cdot 10^{-3}$	$7.29 \cdot 10^{-5}$	$2.30 \cdot 10^{-8}$	$3.23 \cdot 10^{-12}$
	650	-36	$3.08 \cdot 10^{-2}$	$7.02 \cdot 10^{-5}$	$5.19 \cdot 10^{-8}$	$6.36 \cdot 10^{-10}$	$2.65 \cdot 10^{-12}$
$10^{-2}$	400	194	$6.92 \cdot 10^{-8}$	$1.28 \cdot 10^{-4}$	$5.72 \cdot 10^{-2}$	$6.99 \cdot 10^{-5}$	$1.67 \cdot 10^{-8}$
	450	146	$3.30 \cdot 10^{-7}$	$3.88 \cdot 10^{-4}$	$1.09 \cdot 10^{-1}$	$4.93 \cdot 10^{-5}$	$4.35 \cdot 10^{-9}$
	500	100	$1.30 \cdot 10^{-6}$	$7.68 \cdot 10^{-4}$	$1.09 \cdot 10^{-1}$	$1.97 \cdot 10^{-5}$	$6.37 \cdot 10^{-10}$
	550	52	$1.44 \cdot 10^{-5}$	$2.57 \cdot 10^{-3}$	$1.12 \cdot 10^{-1}$	$7.86 \cdot 10^{-6}$	$1.14 \cdot 10^{-10}$
	600	5	$2.40 \cdot 10^{-2}$	$1.71 \cdot 10^{-2}$	$2.96 \cdot 10^{-3}$	$1.82 \cdot 10^{-7}$	$4.10 \cdot 10^{-12}$
	650	-43	$3.29 \cdot 10^{-2}$	$6.68 \cdot 10^{-5}$	$4.51 \cdot 10^{-8}$	$5.88 \cdot 10^{-10}$	$2.62 \cdot 10^{-12}$
$10^{-3}$	400	194	$6.96 \cdot 10^{-12}$	$1.23 \cdot 10^{-6}$	$5.40 \cdot 10^{-2}$	$3.90 \cdot 10^{-3}$	$7.06 \cdot 10^{-5}$
	450	146	$3.33 \cdot 10^{-11}$	$3.77 \cdot 10^{-6}$	$1.06 \cdot 10^{-1}$	$3.53 \cdot 10^{-3}$	$2.93 \cdot 10^{-5}$
	500	99	$1.32 \cdot 10^{-10}$	$7.56 \cdot 10^{-6}$	$1.09 \cdot 10^{-1}$	$1.64 \cdot 10^{-3}$	$6.28 \cdot 10^{-6}$
	550	52	$1.50 \cdot 10^{-9}$	$2.58 \cdot 10^{-5}$	$1.09 \cdot 10^{-1}$	$6.71 \cdot 10^{-4}$	$1.03 \cdot 10^{-6}$
	600	5	$1.08 \cdot 10^{-4}$	$6.81 \cdot 10^{-3}$	$9.82 \cdot 10^{-2}$	$1.55 \cdot 10^{-4}$	$6.16 \cdot 10^{-8}$
	650	-43	$3.29 \cdot 10^{-2}$	$6.51 \cdot 10^{-5}$	$4.35 \cdot 10^{-8}$	$5.85 \cdot 10^{-10}$	$2.62 \cdot 10^{-12}$
$10^{-4}$	400	194	$6.96 \cdot 10^{-16}$	$3.27 \cdot 10^{-9}$	$3.85 \cdot 10^{-3}$	$2.76 \cdot 10^{-2}$	$4.96 \cdot 10^{-2}$
	450	146	$3.33 \cdot 10^{-15}$	$1.62 \cdot 10^{-8}$	$1.97 \cdot 10^{-2}$	$6.57 \cdot 10^{-2}$	$5.46 \cdot 10^{-2}$
	500	99	$1.32 \cdot 10^{-14}$	$4.68 \cdot 10^{-8}$	$4.13 \cdot 10^{-2}$	$6.30 \cdot 10^{-2}$	$2.40 \cdot 10^{-2}$
	550	52	$1.51 \cdot 10^{-13}$	$2.05 \cdot 10^{-7}$	$6.98 \cdot 10^{-2}$	$4.28 \cdot 10^{-2}$	$6.55 \cdot 10^{-3}$
	600	5	$1.22 \cdot 10^{-8}$	$6.87 \cdot 10^{-5}$	$9.68 \cdot 10^{-2}$	$1.50 \cdot 10^{-2}$	$6.22 \cdot 10^{-4}$
	650	-43	$3.29 \cdot 10^{-2}$	$6.30 \cdot 10^{-5}$	$4.14 \cdot 10^{-8}$	$5.75 \cdot 10^{-10}$	$2.62 \cdot 10^{-12}$
$10^{-5}$	400	194	$6.96 \cdot 10^{-20}$	$4.40 \cdot 10^{-13}$	$6.97 \cdot 10^{-7}$	$5.01 \cdot 10^{-4}$	$8.98 \cdot 10^{-2}$
	450	146	$3.33 \cdot 10^{-19}$	$2.81 \cdot 10^{-12}$	$5.93 \cdot 10^{-6}$	$1.97 \cdot 10^{-3}$	$1.64 \cdot 10^{-1}$
	500	99	$1.32 \cdot 10^{-18}$	$1.20 \cdot 10^{-11}$	$2.71 \cdot 10^{-5}$	$4.13 \cdot 10^{-3}$	$1.57 \cdot 10^{-1}$
	550	52	$1.51 \cdot 10^{-17}$	$9.73 \cdot 10^{-11}$	$1.57 \cdot 10^{-4}$	$9.63 \cdot 10^{-3}$	$1.48 \cdot 10^{-1}$
	600	5	$1.22 \cdot 10^{-12}$	$9.65 \cdot 10^{-8}$	$1.91 \cdot 10^{-3}$	$2.98 \cdot 10^{-2}$	$1.16 \cdot 10^{-1}$
	650	-43	$3.29 \cdot 10^{-2}$	$6.26 \cdot 10^{-5}$	$3.97 \cdot 10^{-8}$	$5.54 \cdot 10^{-10}$	$2.62 \cdot 10^{-12}$
$10^{-6}$	400	194	$6.96 \cdot 10^{-24}$	$4.42 \cdot 10^{-17}$	$7.03 \cdot 10^{-11}$	$5.04 \cdot 10^{-6}$	$9.04 \cdot 10^{-2}$
	450	146	$3.33 \cdot 10^{-23}$	$2.83 \cdot 10^{-16}$	$6.01 \cdot 10^{-10}$	$2.00 \cdot 10^{-5}$	$1.66 \cdot 10^{-1}$
	500	99	$1.32 \cdot 10^{-22}$	$1.22 \cdot 10^{-15}$	$2.80 \cdot 10^{-9}$	$4.26 \cdot 10^{-5}$	$1.63 \cdot 10^{-1}$
	550	52	$1.51 \cdot 10^{-21}$	$1.01 \cdot 10^{-14}$	$1.70 \cdot 10^{-8}$	$1.04 \cdot 10^{-4}$	$1.59 \cdot 10^{-1}$
	600	5	$1.22 \cdot 10^{-16}$	$1.11 \cdot 10^{-11}$	$2.53 \cdot 10^{-7}$	$3.96 \cdot 10^{-4}$	$1.54 \cdot 10^{-1}$
	650	-43	$3.29 \cdot 10^{-2}$	$6.26 \cdot 10^{-5}$	$3.97 \cdot 10^{-8}$	$5.53 \cdot 10^{-10}$	$2.62 \cdot 10^{-12}$
$10^{-7}$	400	194	$6.96 \cdot 10^{-28}$	$4.43 \cdot 10^{-21}$	$7.01 \cdot 10^{-15}$	$5.04 \cdot 10^{-8}$	$9.05 \cdot 10^{-2}$
	450	146	$3.33 \cdot 10^{-27}$	$2.83 \cdot 10^{-20}$	$6.01 \cdot 10^{-14}$	$2.00 \cdot 10^{-7}$	$1.66 \cdot 10^{-1}$
	500	99	$1.32 \cdot 10^{-26}$	$1.21 \cdot 10^{-19}$	$2.80 \cdot 10^{-13}$	$4.26 \cdot 10^{-7}$	$1.63 \cdot 10^{-1}$
	550	52	$1.51 \cdot 10^{-25}$	$1.01 \cdot 10^{-18}$	$1.70 \cdot 10^{-12}$	$1.04 \cdot 10^{-6}$	$1.59 \cdot 10^{-1}$
	600	5	$1.22 \cdot 10^{-20}$	$1.11 \cdot 10^{-15}$	$2.54 \cdot 10^{-11}$	$3.96 \cdot 10^{-6}$	$1.54 \cdot 10^{-1}$
	650	-43	$3.37 \cdot 10^{-2}$	$6.31 \cdot 10^{-5}$	$3.99 \cdot 10^{-8}$	$5.54 \cdot 10^{-10}$	$2.61 \cdot 10^{-12}$

Table 3.4.: Benchmark 1: production cross-section for  $\sigma(pp \rightarrow \tilde{t}\tilde{t} \rightarrow X)$  at  $\sqrt{s} = 14$  TeV, where  $X = 2b2j, 4b2j, 6b2j, 1t5b2j$  and  $2t4b2j$ , as a function of  $\lambda''_{33i}$  and for different values of  $m_{\tilde{t}} - m_{\chi^+}$ . See Tabs. 3.2 and 3.3 for the low-energy values of the MSSM parameters.

$\lambda''_{33i}$	$\mu$ [GeV]	$m_{\tilde{t}} - m_{\chi^+}$ [GeV]	$\sigma(2b2j)$ [pb]	$\sigma(4b2j)$ [pb]	$\sigma(6b2j)$ [pb]	$\sigma(1t5b2j)$ [pb]	$\sigma(2t4b2j)$ [pb]
$10^{-1}$	750	243	$3.52 \cdot 10^{-5}$	$4.57 \cdot 10^{-4}$	$1.45 \cdot 10^{-3}$	$1.62 \cdot 10^{-6}$	$4.88 \cdot 10^{-10}$
	800	195	$8.53 \cdot 10^{-5}$	$7.56 \cdot 10^{-4}$	$1.64 \cdot 10^{-3}$	$8.09 \cdot 10^{-7}$	$1.00 \cdot 10^{-10}$
	850	147	$2.63 \cdot 10^{-4}$	$1.42 \cdot 10^{-3}$	$1.87 \cdot 10^{-3}$	$2.63 \cdot 10^{-7}$	$9.83 \cdot 10^{-12}$
	900	100	$5.30 \cdot 10^{-4}$	$1.38 \cdot 10^{-3}$	$8.93 \cdot 10^{-4}$	$5.12 \cdot 10^{-8}$	$1.09 \cdot 10^{-12}$
	950	52	$1.02 \cdot 10^{-3}$	$7.80 \cdot 10^{-4}$	$1.48 \cdot 10^{-4}$	$1.42 \cdot 10^{-8}$	$5.78 \cdot 10^{-13}$
	1000	5	$1.43 \cdot 10^{-3}$	$2.02 \cdot 10^{-5}$	$7.30 \cdot 10^{-8}$	$2.66 \cdot 10^{-10}$	$3.51 \cdot 10^{-13}$
$10^{-2}$	750	239	$5.34 \cdot 10^{-9}$	$6.72 \cdot 10^{-6}$	$1.89 \cdot 10^{-3}$	$2.53 \cdot 10^{-6}$	$7.96 \cdot 10^{-10}$
	800	191	$1.70 \cdot 10^{-8}$	$1.45 \cdot 10^{-5}$	$2.79 \cdot 10^{-3}$	$1.57 \cdot 10^{-6}$	$2.19 \cdot 10^{-10}$
	850	143	$8.74 \cdot 10^{-8}$	$4.39 \cdot 10^{-5}$	$5.35 \cdot 10^{-3}$	$9.25 \cdot 10^{-7}$	$4.05 \cdot 10^{-11}$
	900	96	$3.85 \cdot 10^{-7}$	$9.09 \cdot 10^{-5}$	$5.08 \cdot 10^{-3}$	$3.46 \cdot 10^{-7}$	$6.14 \cdot 10^{-12}$
	950	48	$4.94 \cdot 10^{-6}$	$3.13 \cdot 10^{-4}$	$4.64 \cdot 10^{-3}$	$1.95 \cdot 10^{-7}$	$2.18 \cdot 10^{-12}$
	1000	1	$1.47 \cdot 10^{-3}$	$1.22 \cdot 10^{-5}$	$2.63 \cdot 10^{-8}$	$1.67 \cdot 10^{-10}$	$3.47 \cdot 10^{-13}$
$10^{-3}$	750	239	$5.37 \cdot 10^{-13}$	$6.38 \cdot 10^{-8}$	$1.90 \cdot 10^{-3}$	$3.35 \cdot 10^{-5}$	$1.50 \cdot 10^{-7}$
	800	191	$1.71 \cdot 10^{-12}$	$1.38 \cdot 10^{-7}$	$2.77 \cdot 10^{-3}$	$3.15 \cdot 10^{-5}$	$8.94 \cdot 10^{-8}$
	850	143	$8.88 \cdot 10^{-12}$	$4.26 \cdot 10^{-7}$	$5.11 \cdot 10^{-3}$	$3.65 \cdot 10^{-5}$	$6.51 \cdot 10^{-8}$
	900	96	$3.98 \cdot 10^{-11}$	$9.04 \cdot 10^{-7}$	$5.16 \cdot 10^{-3}$	$2.27 \cdot 10^{-5}$	$2.49 \cdot 10^{-8}$
	950	48	$5.57 \cdot 10^{-10}$	$3.41 \cdot 10^{-6}$	$5.17 \cdot 10^{-3}$	$1.25 \cdot 10^{-5}$	$7.57 \cdot 10^{-9}$
	1000	1	$1.47 \cdot 10^{-3}$	$1.18 \cdot 10^{-5}$	$2.57 \cdot 10^{-8}$	$1.90 \cdot 10^{-10}$	$4.29 \cdot 10^{-13}$
$10^{-4}$	750	239	$5.37 \cdot 10^{-17}$	$3.70 \cdot 10^{-10}$	$6.38 \cdot 10^{-4}$	$1.07 \cdot 10^{-3}$	$4.49 \cdot 10^{-4}$
	800	191	$1.71 \cdot 10^{-16}$	$9.37 \cdot 10^{-10}$	$1.28 \cdot 10^{-3}$	$1.40 \cdot 10^{-3}$	$3.82 \cdot 10^{-4}$
	850	143	$8.89 \cdot 10^{-16}$	$3.26 \cdot 10^{-9}$	$2.99 \cdot 10^{-3}$	$2.11 \cdot 10^{-3}$	$3.71 \cdot 10^{-4}$
	900	96	$3.98 \cdot 10^{-15}$	$7.58 \cdot 10^{-9}$	$3.61 \cdot 10^{-3}$	$1.58 \cdot 10^{-3}$	$1.73 \cdot 10^{-4}$
	950	48	$5.58 \cdot 10^{-14}$	$3.06 \cdot 10^{-8}$	$4.21 \cdot 10^{-3}$	$1.02 \cdot 10^{-3}$	$6.12 \cdot 10^{-5}$
	1000	1	$1.11 \cdot 10^{-3}$	$9.79 \cdot 10^{-6}$	$2.36 \cdot 10^{-8}$	$2.38 \cdot 10^{-9}$	$6.02 \cdot 10^{-11}$
$10^{-5}$	750	239	$5.37 \cdot 10^{-21}$	$8.67 \cdot 10^{-14}$	$3.50 \cdot 10^{-7}$	$5.88 \cdot 10^{-5}$	$2.47 \cdot 10^{-3}$
	800	191	$1.71 \cdot 10^{-20}$	$2.84 \cdot 10^{-13}$	$1.18 \cdot 10^{-6}$	$1.29 \cdot 10^{-4}$	$3.51 \cdot 10^{-3}$
	850	143	$8.89 \cdot 10^{-20}$	$1.34 \cdot 10^{-12}$	$5.02 \cdot 10^{-6}$	$3.54 \cdot 10^{-4}$	$6.22 \cdot 10^{-3}$
	900	96	$3.98 \cdot 10^{-19}$	$4.44 \cdot 10^{-12}$	$1.24 \cdot 10^{-5}$	$5.41 \cdot 10^{-4}$	$5.92 \cdot 10^{-3}$
	950	48	$5.58 \cdot 10^{-18}$	$2.89 \cdot 10^{-11}$	$3.75 \cdot 10^{-5}$	$9.01 \cdot 10^{-4}$	$5.43 \cdot 10^{-3}$
	1000	1	$5.75 \cdot 10^{-6}$	$1.40 \cdot 10^{-7}$	$9.36 \cdot 10^{-10}$	$8.84 \cdot 10^{-9}$	$2.09 \cdot 10^{-8}$
$10^{-6}$	750	239	$5.37 \cdot 10^{-25}$	$8.79 \cdot 10^{-18}$	$3.60 \cdot 10^{-11}$	$6.04 \cdot 10^{-7}$	$2.54 \cdot 10^{-3}$
	800	191	$1.71 \cdot 10^{-24}$	$2.90 \cdot 10^{-17}$	$1.23 \cdot 10^{-10}$	$1.34 \cdot 10^{-6}$	$3.67 \cdot 10^{-3}$
	850	143	$8.89 \cdot 10^{-24}$	$1.38 \cdot 10^{-16}$	$5.34 \cdot 10^{-10}$	$3.77 \cdot 10^{-6}$	$6.62 \cdot 10^{-3}$
	900	96	$3.98 \cdot 10^{-23}$	$4.66 \cdot 10^{-16}$	$1.36 \cdot 10^{-9}$	$5.98 \cdot 10^{-6}$	$6.55 \cdot 10^{-3}$
	950	48	$5.58 \cdot 10^{-22}$	$3.15 \cdot 10^{-15}$	$4.46 \cdot 10^{-9}$	$1.07 \cdot 10^{-5}$	$6.47 \cdot 10^{-3}$
	1000	1	$6.53 \cdot 10^{-10}$	$1.84 \cdot 10^{-11}$	$1.42 \cdot 10^{-13}$	$1.34 \cdot 10^{-10}$	$3.17 \cdot 10^{-8}$
$10^{-7}$	750	239	$5.37 \cdot 10^{-29}$	$8.80 \cdot 10^{-22}$	$3.60 \cdot 10^{-15}$	$6.04 \cdot 10^{-9}$	$2.54 \cdot 10^{-3}$
	800	191	$1.71 \cdot 10^{-28}$	$2.90 \cdot 10^{-21}$	$1.23 \cdot 10^{-14}$	$1.34 \cdot 10^{-8}$	$3.67 \cdot 10^{-3}$
	850	143	$8.89 \cdot 10^{-28}$	$1.38 \cdot 10^{-20}$	$5.35 \cdot 10^{-14}$	$3.78 \cdot 10^{-8}$	$6.59 \cdot 10^{-3}$
	900	96	$3.98 \cdot 10^{-27}$	$4.66 \cdot 10^{-20}$	$1.37 \cdot 10^{-13}$	$5.98 \cdot 10^{-8}$	$6.54 \cdot 10^{-3}$
	950	48	$5.58 \cdot 10^{-26}$	$3.16 \cdot 10^{-19}$	$4.47 \cdot 10^{-13}$	$1.08 \cdot 10^{-7}$	$6.49 \cdot 10^{-3}$
	1000	1	$6.54 \cdot 10^{-14}$	$1.85 \cdot 10^{-15}$	$1.43 \cdot 10^{-17}$	$1.35 \cdot 10^{-12}$	$3.19 \cdot 10^{-8}$

Table 3.5.: Benchmark 2: production cross-section for  $\sigma(pp \rightarrow t\bar{t} \rightarrow X)$  at  $\sqrt{s} = 14$  TeV, where  $X = 2b2j, 4b2j, 6b2j, 1t5b2j$  and  $2t4b2j$ , as a function of  $\lambda''_{33i}$  and for different values of  $m_{\tilde{t}} - m_{\chi^+}$ . See Tabs. 3.2 and 3.3 for the low-energy values of the MSSM parameters.

# Conclusions

The series of success of the Standard Model of particle physics coronated with the discovery in 2012 of the Higgs boson at the LHC. During Run 1 and the beginning of the Run 2 data taking both ATLAS and CMS have been starting the era of precision measurement in the Higgs sector. So far, not only all most precise measurements have confirmed that the particle discovered behaves as the fundamental scalar of the SM [284, 285, 286, 287, 288, 289, 290], but also all direct searches for new physics BSM have given negative answers. On the other hand the naturalness principle [291] tells us that new physics, if any should lie at the TeV scale. If Supersymmetry or Dynamical Electroweak Symmetry Breaking are realised close to the TeV scale, then the electroweak scale is protected against large radiative corrections from new physics at higher scales. Therefore, the hierarchy between the electroweak scale and higher scales, such as the Planck scale, does not require fine-tuning any longer. A byproduct of this could be TeV-scale dark matter candidates.

Supersymmetry has long been considered to be an elegant way of triggering the EWSB, relating it radiatively through perturbative quantum effects to possible new physics at much higher scales, such as Grand Unification, while stabilizing the various scales without unnatural fine-tunings. Though, the ever stronger exclusion limits on SUSY particle masses from negative searches at the LHC seem to disfavor, if not to rule out, low energy supersymmetry as the correct theory beyond the SM. However, one should not lose sight of the distinction between SUSY as a general framework and its various possible model realizations. Only a class of the latter, leading to RPC signatures with striking missing energy, is being heavily excluded by the LHC. If RPV violating couplings are allowed, a class of signatures, generally with high jet and lepton multiplicity and no missing energy is expected at the LHC.

I have been investigating those final states since my involvement in the ATLAS measure of the production cross section of top-antitop quark pairs in the all-hadronic decay channel at the LHC with a centre-of-mass energy of  $\sqrt{s} = 7$  TeV and an integrated luminosity of  $4.7 \text{ fb}^{-1}$ . One of the challenge of this class of analysis is the modeling of the shapes of the dominant multi-jet background, which is estimated with a data driven technique. This particular analysis considered a *Kinematic Fit* to derive the top mass distribution  $m_t$  from which the  $t\bar{t}$  signal is then extracted from data with an unbinned likelihood fit:

$$\sigma(pp \rightarrow t\bar{t}) = 168 \pm 12 \text{ (stat.) } {}^{+60}_{-57} \text{ (syst.) } \pm 7 \text{ (lum.) pb.}$$

This measured cross-section is compatible with the Standard Model expectation of  $\sigma_{\text{SM}} = 167^{+17}_{-18} \text{ pb}$ . As it can be seen in Figure 3.7, the fully hadronic measurement for the top pair production is the one with the highest uncertainty, mostly

due the uncertainties on the energy of the many jets present in the event, as shown in Table 1.1. After releasing our fully hadronic  $t\bar{t}$  cross section measure-

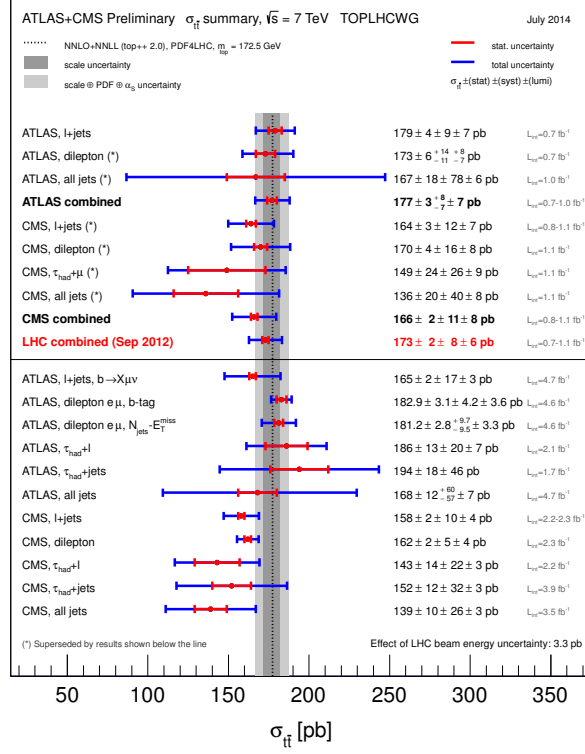


Figure 3.7.: Top-pair cross-section measurements at 7 TeV by the ATLAS and CMS collaborations. The band shows the NNLO QCD calculation complemented with NNLL resummation (top++2.0). The theory band represents uncertainties due to renormalisation and factorisation scale, parton density functions and the strong coupling. The measurements and the theory calculation is quoted at  $m_{\text{top}} = 172.5$  GeV. The upper part of the figure shows early LHC measurements and their combination. The lower part summarizes measurements performed after the LHC cross-section combination.

ment at  $\sqrt{s} = 7$  TeV, we investigated the possibility of reducing the large systematic uncertainties affecting this measure. The findings of this process brought us to consider moving to the search for  $t\bar{t}H$  in the fully hadronic final state.

Ultimately, if no presence of new particles arise from the SM background in both ATLAS and CMS experiments, the different measurements of the Higgs coupling performed at the LHC can be used to bound the scale of the new physics. Lately model independent formalisms have been developed [292] in order to put limits on effective field theory (EFT) parametrization used to detect defor-

mations for example of the Higgs couplings. LHC can even be sensitive to constrain the Higgs cubic self-coupling, a way to check whether the EWSB follows from a simple Ginzburg–Landau  $\phi^4$  potential [293]. At the EW scale the top quark Yukawa coupling has a value close to unity, which could be an indication of a special role [294] in the EWSB for the most massive SM fermion. With the assumption that no new particles in the loops entering gluon gluon fusion production and  $H \rightarrow \gamma\gamma$  decay, assumption supported by the measurements of the effective coupling modifiers  $\kappa_g$  and  $\kappa_\gamma$ , which are consistent with the SM predictions, the top-Yukawa coupling modifier could be established already in Run 1, see Table 3.6 [56].

Table 3.6.: Fit results for the parameterisation assuming the absence of BSM particles in the loops ( $B_{BSM} = 0$ ). The results with their measured uncertainties are reported for the combination of ATLAS and CMS, together with the individual results from each experiment.

Parameter	ATLAS + CMS Measured	ATLAS Measured	CMS Measured
$\kappa_t$	$0.87^{+0.15}_{-0.15}$	$0.98^{+0.21}_{-0.20}$	$0.77^{+0.20}_{-0.18}$

The direct measurement of  $y_t$  is extremely challenging and it benefits from combining all possible final states in order to control the large systematics which currently limit its precision. Among the plethora of decay modes of the Higgs boson and the two top quarks involved, the most abundant, the fully hadronic signatures, is also the most challenging because of the large presence of the multi-jet background.

Contrary to the fully hadronic  $t\bar{t}$  cross section measurement, the  $t\bar{t}H$  analysis uses MC simulations to estimate part of the physics background. This allows to define background dominated control regions and to use a maximum-likelihood fit procedure to determine simultaneously the normalisation of each component of the background and the signal strength. This procedure reduces the impact of the background uncertainties in the final result. The limited impact of the large systematics present in the top cross section measurement are then limited. This combined with the large potential in terms of separating  $t\bar{t}$ -like events from the multi-jet background, as shown by Figure 1.2a are the key ingredients for this analysis.

The data used for the Run 1 fully hadronic  $t\bar{t}H$  analysis corresponds to an integrated luminosity of  $20.3 \text{ fb}^{-1}$  of  $pp$  collisions at  $\sqrt{s} = 8 \text{ TeV}$  collected with the ATLAS detector. The search selects events with at least six energetic jets and used a boosted decision tree algorithm to discriminate between signal and Standard

Model background. The dominant multijet background has been estimated using a dedicated data-driven technique, different and more precise than the one used for the previous  $t\bar{t}$  production measurement, which was completely For a Higgs boson mass of 125 GeV, an upper limit of 6.4 (5.4) times the Standard Model cross section was observed (expected) at 95% confidence level. The best-fit value for the signal strength is  $\mu = 1.6 \pm 2.6$  times the Standard Model expectation for  $m_H = 125$  GeV. Combining all  $t\bar{t}H$  searches carried out by ATLAS at  $\sqrt{s} = 8$  and 7 TeV, an observed (expected) upper limit of 3.1 (1.4) times the Standard Model expectation is obtained at 95% confidence level, with a signal strength  $\mu = 1.7 \pm 0.8$ . For completeness, the final Run 1 ATLAS + CMS combination gives as a result for the signal strength  $\mu = 2.3^{+0.7}_{-0.6}$ .

In Run 2, taking advantage of the highest center-of-mass  $p - p$  collisions at  $\sqrt{s} = 13$  TeV both ATLAS and CMS have been searching for a  $t\bar{t}H$  signal in events enriched in Higgs boson decay into  $b\bar{b}$ , finding respectively  $\mu = 0.84^{+0.64}_{-0.61}$  [295] (ATLAS) and  $\mu = -0.19 \pm 0.8$  [296] (CMS), for events enriched in Higgs boson decays to leptons via two massive vector bosons, obtaining  $\mu = 1.6^{+0.5}_{-0.4}$  [297] (ATLAS) and  $\mu = 1.5 \pm 0.5$  [298], considering exclusively leptonic final states, and  $\mu = 0.72^{+0.62}_{-0.53}$  [299], considering hadronically decaying  $\tau$ -leptons, (CMS) and finally for  $t\bar{t}H(H \rightarrow \gamma\gamma)$ , measuring  $\mu = 0.5 \pm 0.6$  [300] (ATLAS) and  $\mu = 2.2^{+0.9}_{-0.8}$  [301]. Finally, the combined  $t\bar{t}H$  signal strength measured by the ATLAS Collaboration [297] in Run 2 using only 2015 and 2016 data, obtained by merging searches in several final states, is  $\mu = 1.2 \pm 0.3$ , with an observed (expected) significance of  $4.2\sigma$  ( $3.8\sigma$ ), confirming the evidence for  $t\bar{t}H$  production already seen by CMS with  $3.3\sigma$  ( $2.5\sigma$ ) expected significance [298], and indicating that both experiments are on the edge of finally *discovering*  $t\bar{t}H$ .

Two series of considerations can be made about the worthiness of pursuing the fully hadronic  $t\bar{t}H$  analysis with Run 2 data. First, despite the lower sensitivity showed in Run 1 compared to more powerful signautres, the fully hadronic  $t\bar{t}H$  benefits in Run 2 from the improvement of ATLAS online  $b$ -tagging, on one hand with the development of  $b$ -tagging algorithms which are now close to the offline ones (see Figure 3.8), on the other hand with the foreseen integration of the FTK [302], allowing this final state to progressively increase in terms of trigger acceptance. Second, surprisingly enough one of the outcome of the Run 1 analysis is that the large multi-jet background is not responsible for the largest systematic uncertainty affecting the result but it is the modeling of the  $t\bar{t}b\bar{b}$  background the largest culprit, same as all other  $t\bar{t}H(H \rightarrow b\bar{b})$  analyses. For this reason, Giovanni Bartolini, master student from the University of Perugia, and myself performed the development of a multi-variate strategy aimed at the separation of the fully hadronic  $t\bar{t}H$  signal from the  $t\bar{t}$ +jets background with the use of a BDT. This is divided in two levels: a reconstruction level and a classification level. In the reconstruction level, simulated  $t\bar{t}H$  events are used to train two different BDTs to perform a full event reconstruction thanks to kinematic and Higgs related variables. In the classification level informations from the two reconstruc-

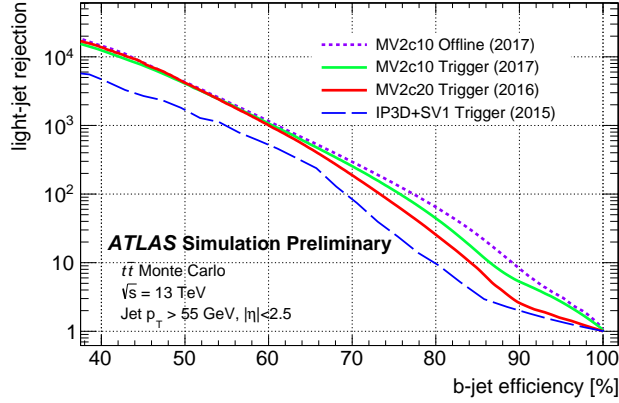


Figure 3.8.: The ATLAS  $b$ -jet trigger uses a BDT algorithm to separate  $b$ -jets from light and  $c$ -jet backgrounds. The BDT algorithm is re-optimized to improve  $b$ -tagging performance. Performance of  $b$ -tagging algorithms (measured using  $t\bar{t}$  Monte Carlo events) is shown in terms of light-jet rejection as a function of  $b$ -jet efficiency. Expected performance of  $b$ -tagging algorithm (MV2c10) for  $b$ -jet triggers in 2017 data-taking (green solid line) is compared to  $b$ -tagging algorithms used for  $b$ -jet triggers in 2016 (MV2c20) and 2015 (IP3D+SV1) data taking. Performance of  $b$ -tagging algorithm MV2c10 for offline jets is shown in purple dotted curve [303].

tion BDTs are combined together with other global event shape informations are used to train  $t\bar{t}H$  signal versus  $t\bar{t}$ +jets. The final classification BDT output can be seen in Figure 3.9 and can be compared with the discriminating power of the one used in Run 1 in Figure 2.10 for the same region with at least eight jets and at least four  $b$ -tagged jets.

Another way of looking at the relevance of the most massive top quark is connected to the importance of *top partners* in most BSM theories that address the EWSB free of the naturalness problem: in the presence of new physics close to the TeV scale, the only SM contribution to the Higgs mass that must be compensated at sub-TeV scales is the one-loop correction from the top sector. Thus, the TeV particles that soften the divergence in the top loop provide a uniquely well-motivated target for searches at the LHC [304].

As we already motivated through this document, Run 2 analyses are probing supersymmetry at a mass scale of over a TeV suggesting that if supersymmetry is still a natural theory, it is hiding in experimentally hard-to-reach locations, i.e. if non-null R-parity violating couplings were to exist, the stop quark limits would relax substantially. Moreover those signatures with multi-jets and  $b$ -jets are at the center of my interest as experimental signatures. Within the PESBLADE collaboration we have been investigating how different stop-pair final states arise when different values of the RPV coupling and different supersymmetric particle



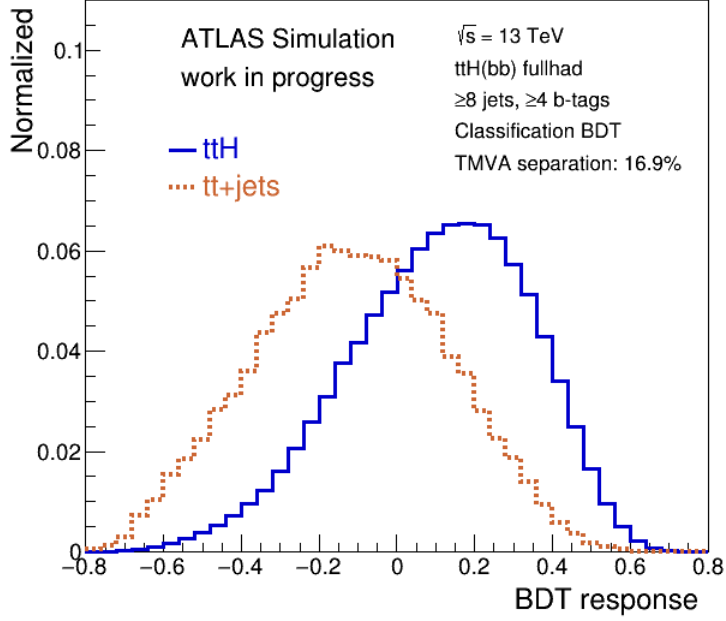


Figure 3.9.: Distribution of the classification BDT output for fully hadronic  $t\bar{t}H$  signal and  $t\bar{t}+\text{jets}$  background in events with at least eight jets and at least six  $b$ -tagged jets.

mass splittings are considered. This is exhaustively investigated for the case of proton–proton collisions at center-of-mass energy of  $\sqrt{s} = 14$  TeV. After having defined a set of working assumptions concerning the mass hierarchy and the allowed range of  $\lambda''_{33i}$ , the sensitivity of the stop decay branching ratios to  $\lambda''_{33i}$  is assessed, first analytically by means of the NWA approximation showing that the variation of  $\lambda''_{33i}$  over several orders of magnitude triggers the dominance of very different final states, then numerically relying on automated matrix element calculations.

Using for the latter a bottom-bottom approach in the phenomenological MSSM, the full mass spectrum have been generated together with the couplings and two benchmark points taking into account all possible constraints ranging from the measured Higgs mass to the experimental low energy constraints are identified. For these two benchmark points, the cross sections for the relevant final states differing by the number of heavy and light flavored quarks ( $2b2j$ ,  $4b2j$ ,  $6b2j$ ,  $1t5b2j$  and  $2t4b2j$ ), are estimated as a function of  $\lambda''_{33i}$  and the stop/chargino mass splitting, confirming numerically what is seen analytically with the NWA approximation. Finally, the phenomenology of the RPV stop production and decays is reach in experimental signatures, and *the smaller the values of  $\lambda''_{33i}$  the larger the quark mutliplicity of the dominant final states.*

After this phenemonological analysis of how different signatures arise as a



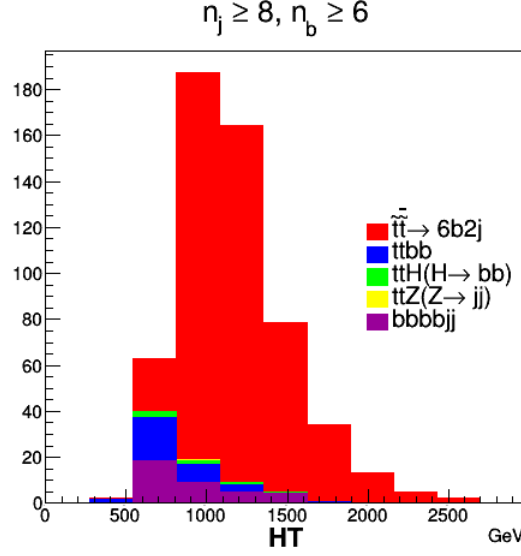


Figure 3.10.:  $H_T$  distribution for events with at least 8 jets at least 6  $b$ -tagged jets. The top signal from the  $6b2j$  final state (red full histogram) is stacked on top of the SM background composed by  $t\bar{t}b\bar{b}$  (blue full histogram),  $t\bar{t}H(H \rightarrow b\bar{b})$  (green full histogram),  $t\bar{t}Z(Z \rightarrow jj)$  (yellow full histogram),  $b\bar{b}b\bar{b} + X$  (purple full histogram). All histograms are normalized for an integrated luminosity of  $100 \text{ fb}^{-1}$  of  $pp$  collisions at  $\sqrt{s} = 14 \text{ TeV}$ .

function of  $\lambda''_{33i}$  and sparticle masses, together with Hoang Dai Nghia Nguyen Master 2 student in spring 2016, we investigated how the  $6b2j$  signal could be searched for in  $100 \text{ fb}^{-1}$  of  $p-p$  collisions at  $\sqrt{s} = 14 \text{ TeV}$ . From Benchmark 1, as defined in Tables 3.2 and 3.3, having set  $m_{\tilde{t}} = 600 \text{ GeV}$ ,  $m_{\chi^+} = 500 \text{ GeV}$  and  $\lambda''_{33i} = 10^{-3}$ , we simulated stop pair production and the relevant background processes ( $t\bar{t}H$ ,  $t\bar{t}b\bar{b}$ ,  $t\bar{t}Z(\rightarrow jj)$ ,  $b\bar{b}b\bar{b} + X$ ) with MADGRAPH5\_AMC@NLO v2.1.2 and CTEQ6L1 PDF, subsequently hadronised/parton showered in PYTHIA 8, with a customised version of DELPHES 3 [305] used for detector simulation. The result of selecting events with at least eight energetic jets,  $p_T \geq 25 \text{ GeV}$ , five of which having  $p_T \geq 55 \text{ GeV}$  to simulate a realistic multijet trigger, within inner detector acceptance ( $|\eta| < 2.5$ ), and at least six  $b$ -tagged jets, is shown in Figure 3.10 where the distribution of  $H_T$ , defined as the sum of the transeverse energy of all jets, is shown for simulated signal stacked on top of the simulated SM background. In this most sensitise region the  $S/B$  could be as large as around 6 for  $\lambda''_{33i}$  such that branching ratio of stop pairs into  $6b2j$  saturates, even though such an extreme case is most likely excluded by present searches of similar final states.

At the end, an exciting possibility still lies ahead, that a light part of the MSSM spectrum, a key issue for the naturalness of SUSY, may be stashed in the present

and future LHC data, and can be searched for using the experimental techniques presented in this document.

# Bibliography

- [1] T. W. B. Kibble. “The Standard Model of Particle Physics”. In: 2014. arXiv: [1412.4094](https://arxiv.org/abs/1412.4094) [physics.hist-ph]. URL: <https://inspirehep.net/record/1334156/files/arXiv:1412.4094.pdf> (cit. on p. 20).
- [2] S. L. Glashow. “Partial symmetries of weak interactions”. In: *Nucl. Phys.* 22 (1961), p. 579 (cit. on p. 20).
- [3] S. Weinberg. “A model of leptons”. In: *Phys. Rev. Lett.* 19 (1967), pp. 1264–1266 (cit. on p. 20).
- [4] A. Salam. “Weak and electromagnetic interactions”. In: *Proc. of the 8th Nobel Symposium* (1969), p. 367 (cit. on p. 20).
- [5] Werner Heisenberg. “Die Struktur der Atomkerne. (German) [Structure of atomic nuclei]”. German. In: *Z. Physik* 77.1 (1932) (cit. on p. 20).
- [6] M. Gell-Mann and Y. Ne’eman. *The Eightfold Way*. W A. New York: Benjamin, 1964 (cit. on p. 20).
- [7] C.-N. Yang and R. L. Mills. “Conservation of isotopic spin and isotopic gauge invariance”. In: *Physical review* 96.1 (1954), p. 191 (cit. on p. 20).
- [8] R. P. Feynman and M. Gell-Mann. “Theory of the Fermi interaction”. In: *Physical Review* 109.1 (1958), p. 193 (cit. on p. 20).
- [9] E. C. G. Sudarshan and R. E. Marshak. In: *Proc. of Padua-Venice Conference on "Mesons and Newly Discovered Particles"* (1957), pp. V–14 (cit. on p. 20).
- [10] F. Englert and R. Brout. “Broken Symmetry and the Mass of Gauge Vector Mesons”. In: *Phys. Rev. Lett.* 13 (1964), p. 321 (cit. on pp. 20, 43, 88).
- [11] P. W. Higgs. “Broken Symmetries and the Masses of Gauge Bosons”. In: *Phys. Rev. Lett.* 13 (1964), p. 508 (cit. on pp. 20, 43, 88).
- [12] P. W. Higgs. “Broken Symmetries, Massless Particles and Gauge Fields”. In: *Phys. Lett.* 12 (1964), p. 132 (cit. on pp. 20, 43, 88).
- [13] G. S. Guralnik, C. R. Hagen, and T. B. W. Kibble. “Global Conservation Laws and Mass-less Particles”. In: *Phys. Rev. Lett.* 13 (1964), p. 585 (cit. on pp. 20, 43, 88).
- [14] O. W. Greenberg. “Spin and Unitary-Spin Independence in a Paraquark Model of Baryons and Mesons”. In: *Phys. Rev. Lett.* 13 (20 1964), pp. 598–602. DOI: [10.1103/PhysRevLett.13.598](https://doi.org/10.1103/PhysRevLett.13.598). URL: <http://link.aps.org/doi/10.1103/PhysRevLett.13.598> (cit. on p. 20).

- [15] M. Y. Han and Y. Nambu. “Three-Triplet Model with Double SU(3) Symmetry”. In: *Phys. Rev.* 139 (4B 1965), B1006–B1010. DOI: [10.1103/PhysRev.139.B1006](https://doi.org/10.1103/PhysRev.139.B1006). URL: <http://link.aps.org/doi/10.1103/PhysRev.139.B1006> (cit. on p. 20).
- [16] G. Hanson et al. “Evidence for Jet Structure in Hadron Production by  $e^+e^-$  Annihilation”. In: *Phys. Rev. Lett.* 35 (1975), pp. 1609–1612. DOI: [10.1103/PhysRevLett.35.1609](https://doi.org/10.1103/PhysRevLett.35.1609) (cit. on p. 20).
- [17] J. E. Augustin et al. “Discovery of a Narrow Resonance in  $e^+e^-$  Annihilation”. In: *Phys. Rev. Lett.* 33 (1974). [Adv. Exp. Phys.5,141(1976)], pp. 1406–1408. DOI: [10.1103/PhysRevLett.33.1406](https://doi.org/10.1103/PhysRevLett.33.1406) (cit. on p. 20).
- [18] J. J. Aubert et al. “Experimental Observation of a Heavy Particle  $J$ ”. In: *Phys. Rev. Lett.* 33 (1974), pp. 1404–1406. DOI: [10.1103/PhysRevLett.33.1404](https://doi.org/10.1103/PhysRevLett.33.1404) (cit. on p. 20).
- [19] S. W. Herb et al. “Observation of a Dimuon Resonance at 9.5-GeV in 400-GeV Proton-Nucleus Collisions”. In: *Phys. Rev. Lett.* 39 (1977), pp. 252–255. DOI: [10.1103/PhysRevLett.39.252](https://doi.org/10.1103/PhysRevLett.39.252) (cit. on p. 20).
- [20] F. Abe et al. “Observation of top quark production in  $\bar{p}p$  collisions”. In: *Phys. Rev. Lett.* 74 (1995), pp. 2626–2631. DOI: [10.1103/PhysRevLett.74.2626](https://doi.org/10.1103/PhysRevLett.74.2626). arXiv: [hep-ex/9503002](https://arxiv.org/abs/hep-ex/9503002) [hep-ex] (cit. on p. 20).
- [21] D0 Collaboration. “Observation of the top quark”. In: *Phys. Rev. Lett.* 74 (1995), pp. 2632–2637. DOI: [10.1103/PhysRevLett.74.2632](https://doi.org/10.1103/PhysRevLett.74.2632). arXiv: [hep-ex/9503003](https://arxiv.org/abs/hep-ex/9503003) [hep-ex] (cit. on pp. 20, 21).
- [22] R. Brandelik et al. “Evidence for Planar Events in  $e^+e^-$  Annihilation at High-Energies”. In: *Phys. Lett.* B86 (1979), pp. 243–249. DOI: [10.1016/0370-2693\(79\)90830-X](https://doi.org/10.1016/0370-2693(79)90830-X) (cit. on p. 20).
- [23] D. P. Barber et al. “Discovery of Three Jet Events and a Test of Quantum Chromodynamics at PETRA Energies”. In: *Phys. Rev. Lett.* 43 (1979), p. 830. DOI: [10.1103/PhysRevLett.43.830](https://doi.org/10.1103/PhysRevLett.43.830) (cit. on p. 20).
- [24] M. L. Perl et al. “Evidence for Anomalous Lepton Production in  $e^+e^-$  Annihilation”. In: *Phys. Rev. Lett.* 35 (1975), pp. 1489–1492. DOI: [10.1103/PhysRevLett.35.1489](https://doi.org/10.1103/PhysRevLett.35.1489) (cit. on p. 20).
- [25] C. L. Cowan, F. Reines, F. B. Harrison, et al. “Detection of the free neutrino: A Confirmation”. In: *Science* 124 (1956), pp. 103–104. DOI: [10.1126/science.124.3212.103](https://doi.org/10.1126/science.124.3212.103) (cit. on p. 20).
- [26] G. Danby, J. M. Gaillard, Konstantin A. Goulianos, et al. “Observation of High-Energy Neutrino Reactions and the Existence of Two Kinds of Neutrinos”. In: *Phys. Rev. Lett.* 9 (1962), pp. 36–44. DOI: [10.1103/PhysRevLett.9.36](https://doi.org/10.1103/PhysRevLett.9.36) (cit. on p. 20).

- [27] K. Kodama et al. “Observation of tau neutrino interactions”. In: *Phys. Lett. B* 504 (2001), pp. 218–224. DOI: [10.1016/S0370-2693\(01\)00307-0](https://doi.org/10.1016/S0370-2693(01)00307-0). arXiv: [hep-ex/0012035](https://arxiv.org/abs/hep-ex/0012035) [hep-ex] (cit. on p. 20).
- [28] ATLAS Collaboration. “Observation of a new particle in the search for the Standard Model Higgs boson with the ATLAS detector at the LHC”. In: *Phys. Lett. B* 716 (2012), pp. 1–29. DOI: [10.1016/j.physletb.2012.08.020](https://doi.org/10.1016/j.physletb.2012.08.020). arXiv: [1207.7214](https://arxiv.org/abs/1207.7214) [hep-ex] (cit. on pp. 20, 43).
- [29] CMS Collaboration. “Observation of a new boson at a mass of 125 GeV with the CMS experiment at the LHC”. In: *Phys. Lett. B* 716 (2012), 30. DOI: [10.1016/j.physletb.2012.08.021](https://doi.org/10.1016/j.physletb.2012.08.021). arXiv: [1207.7235v1](https://arxiv.org/abs/1207.7235v1) [hep-ex] (cit. on pp. 20, 43).
- [30] Gargamelle Neutrino Collaboration. “Search for elastic muon-neutrino electron scattering”. In: *Physics Letters B* 46 (Sept. 1973), pp. 121–124. DOI: [10.1016/0370-2693\(73\)90494-2](https://doi.org/10.1016/0370-2693(73)90494-2) (cit. on p. 20).
- [31] Gargamelle Neutrino Collaboration. “Observation of Neutrino Like Interactions Without Muon Or Electron in the Gargamelle Neutrino Experiment”. In: *Phys. Lett. B* 46 (1973), pp. 138–140. DOI: [10.1016/0370-2693\(73\)90499-1](https://doi.org/10.1016/0370-2693(73)90499-1) (cit. on p. 20).
- [32] UA1 Collaboration. “Experimental Observation of Isolated Large Transverse Energy Electrons with Associated Missing Energy at  $s^{*1/2} = 540\text{-GeV}$ ”. In: *Phys. Lett. B* 122 (1983). [611(1983)], pp. 103–116. DOI: [10.1016/0370-2693\(83\)91177-2](https://doi.org/10.1016/0370-2693(83)91177-2) (cit. on p. 20).
- [33] UA2 Collaboration. “Observation of Single Isolated Electrons of High Transverse Momentum in Events with Missing Transverse Energy at the CERN anti-p p Collider”. In: *Phys. Lett. B* 122 (1983), pp. 476–485. DOI: [10.1016/0370-2693\(83\)91605-2](https://doi.org/10.1016/0370-2693(83)91605-2) (cit. on p. 20).
- [34] UA1 Collaboration. “Experimental observation of lepton pairs of invariant mass around  $95\text{-GeV}/c^2$  at the CERN SPS collider”. In: *Phys. Lett. B* 126 (1983), pp. 398–410 (cit. on p. 20).
- [35] UA2 Collaboration. “Evidence for  $Z^0 \rightarrow e^+ e^-$  at the CERN anti-p p collider”. In: *Phys. Lett. B* 129 (1983), pp. 130–140 (cit. on p. 20).
- [36] The ALEPH, DELPHI, L3, OPAL Collaborations, the LEP Electroweak Working Group. “Electroweak Measurements in Electron-Positron Collisions at W-Boson-Pair Energies at LEP”. In: *Phys. Rept.* 532 (2013), p. 119. arXiv: [1302.3415](https://arxiv.org/abs/1302.3415) [hep-ex] (cit. on p. 20).
- [37] F. Zwicky. “On the Masses of Nebulae and of Clusters of Nebulae”. In: *Astrophys. J.* 86 (1937), pp. 217–246. DOI: [10.1086/143864](https://doi.org/10.1086/143864) (cit. on p. 20).

- [38] V. C. Rubin and W. K. Ford Jr. “Rotation of the Andromeda Nebula from a Spectroscopic Survey of Emission Regions”. In: *Astrophys. J.* 159 (1970), pp. 379–403. DOI: [10.1086/150317](https://doi.org/10.1086/150317) (cit. on p. 20).
- [39] R. Cooke, M. Pettini, R. A. Jorgenson, et al. “Precision measures of the primordial abundance of deuterium”. In: *Astrophys. J.* 781.1 (2014), p. 31. DOI: [10.1088/0004-637X/781/1/31](https://doi.org/10.1088/0004-637X/781/1/31). arXiv: [1308.3240](https://arxiv.org/abs/1308.3240) [[astro-ph.CO](#)] (cit. on p. 20).
- [40] CDF Collaboration. “Observation of Top Quark Production in  $\bar{p}p$  Collisions with the Collider Detector at Fermilab”. In: *Phys. Rev. Lett.* 74 (14 1995), pp. 2626–2631. DOI: [10.1103/PhysRevLett.74.2626](https://doi.org/10.1103/PhysRevLett.74.2626). URL: <http://link.aps.org/doi/10.1103/PhysRevLett.74.2626> (cit. on p. 21).
- [41] ALEPH Collaboration. “Observation of an excess in the search for the standard model Higgs boson at ALEPH”. In: *Phys. Lett.* B495 (2000), pp. 1–17. DOI: [10.1016/S0370-2693\(00\)01269-7](https://doi.org/10.1016/S0370-2693(00)01269-7). arXiv: [hep-ex/0011045](https://arxiv.org/abs/hep-ex/0011045) [[hep-ex](#)] (cit. on p. 21).
- [42] M. Carena et al. “Report of the Tevatron Higgs working group”. In: 2000. arXiv: [hep-ph/0010338](https://arxiv.org/abs/hep-ph/0010338) [[hep-ph](#)]. URL: [http://lss.fnal.gov/cgi-bin/find\\_paper.pl?conf-00-279](http://lss.fnal.gov/cgi-bin/find_paper.pl?conf-00-279) (cit. on p. 21).
- [43] S. Weinberg. “Implications of Dynamical Symmetry Breaking”. In: *Phys. Rev. D* 13 (1976), pp. 974–996. DOI: [10.1103/PhysRevD.13.974](https://doi.org/10.1103/PhysRevD.13.974) (cit. on p. 21).
- [44] L. Susskind. “Dynamics of Spontaneous Symmetry Breaking in the Weinberg-Salam Theory”. In: *Phys. Rev. D* 20 (1979), pp. 2619–2625. DOI: [10.1103/PhysRevD.20.2619](https://doi.org/10.1103/PhysRevD.20.2619) (cit. on p. 21).
- [45] D0 Collaboration. “Search for techniparticles in e+jets events at D0”. In: *Phys. Rev. Lett.* 98 (2007), p. 221801. DOI: [10.1103/PhysRevLett.98.221801](https://doi.org/10.1103/PhysRevLett.98.221801). arXiv: [hep-ex/0612013](https://arxiv.org/abs/hep-ex/0612013) [[hep-ex](#)] (cit. on p. 28).
- [46] K. A. Olive et al. “Review of Particle Physics”. In: *Chin. Phys.* C38 (2014), p. 090001. DOI: [10.1088/1674-1137/38/9/090001](https://doi.org/10.1088/1674-1137/38/9/090001) (cit. on pp. 28, 88, 108, 109, 122).
- [47] S. Dimopoulos and L. Susskind. “Mass Without Scalars”. In: *Nucl. Phys.* B155 (1979), pp. 237–252. DOI: [10.1016/0550-3213\(79\)90364-X](https://doi.org/10.1016/0550-3213(79)90364-X) (cit. on p. 21).
- [48] B. Holdom. “Raising the Sideways Scale”. In: *Phys. Rev. D* 24 (1981), p. 1441. DOI: [10.1103/PhysRevD.24.1441](https://doi.org/10.1103/PhysRevD.24.1441) (cit. on p. 21).
- [49] C. T. Hill. “Topcolor assisted technicolor”. In: *Phys. Lett.* B345 (1995), pp. 483–489. DOI: [10.1016/0370-2693\(94\)01660-5](https://doi.org/10.1016/0370-2693(94)01660-5). arXiv: [hep-ph/9411426](https://arxiv.org/abs/hep-ph/9411426) [[hep-ph](#)] (cit. on p. 21).

- [50] K. D. Lane and E Eichten. “Two Scale Technicolor”. In: *Phys. Lett.* B222 (1989), pp. 274–280. DOI: [10.1016/0370-2693\(89\)91265-3](#) (cit. on p. 22).
- [51] K. D. Lane. “Technihadron production and decay in low scale technicolor”. In: *Phys. Rev. D* 60 (1999), p. 075007. DOI: [10.1103/PhysRevD.60.075007](#). arXiv: [hep-ph/9903369 \[hep-ph\]](#) (cit. on p. 22).
- [52] K. Lane and S. Mrenna. “The Collider phenomenology of technihadrons in the technicolor straw man model”. In: *Phys. Rev. D* 67 (2003), p. 115011. DOI: [10.1103/PhysRevD.67.115011](#). arXiv: [hep-ph/0210299 \[hep-ph\]](#) (cit. on p. 22).
- [53] D0 Collaboration. “The Upgraded D0 detector”. In: *Nucl. Instrum. Meth.* A565 (2006), pp. 463–537. DOI: [10.1016/j.nima.2006.05.248](#). arXiv: [physics/0507191 \[physics.ins-det\]](#) (cit. on p. 22).
- [54] CDF Collaboration. “Search for color singlet technicolor particles in  $p\bar{p}$  collisions at  $\sqrt{s} = 1.8$  TeV”. In: *Phys. Rev. Lett.* 84 (2000), pp. 1110–1115. DOI: [10.1103/PhysRevLett.84.1110](#) (cit. on p. 23).
- [55] DELPHI Collaboration. “Search for technicolor with DELPHI”. In: *Eur. Phys. J.* C22 (2001), pp. 17–29. DOI: [10.1007/s100520100782](#). arXiv: [hep-ex/0110056 \[hep-ex\]](#) (cit. on p. 23).
- [56] ATLAS and CMS Collaborations. “Measurements of the Higgs boson production and decay rates and constraints on its couplings from a combined ATLAS and CMS analysis of the LHC pp collision data at  $\sqrt{s} = 7$  and 8 TeV”. In: *JHEP* 08 (2016), p. 045. DOI: [10.1007/JHEP08\(2016\)045](#). arXiv: [1606.02266 \[hep-ex\]](#) (cit. on pp. 23, 73, 128).
- [57] ATLAS Collaboration. “Search for dilepton resonances in  $pp$  collisions at  $\sqrt{s} = 7$  TeV with the ATLAS detector”. In: *Phys. Rev. Lett.* 107 (2011), p. 272002. DOI: [10.1103/PhysRevLett.107.272002](#). arXiv: [1108.1582 \[hep-ex\]](#) (cit. on p. 23).
- [58] D. B. Kaplan and H. Georgi. “SU(2) x U(1) Breaking by Vacuum Misalignment”. In: *Phys. Lett.* 136B (1984), pp. 183–186. DOI: [10.1016/0370-2693\(84\)91177-8](#) (cit. on p. 23).
- [59] D. B. Kaplan, H. Georgi, and S. Dimopoulos. “Composite Higgs Scalars”. In: *Phys. Lett.* 136B (1984), pp. 187–190. DOI: [10.1016/0370-2693\(84\)91178-X](#) (cit. on p. 23).
- [60] H. Georgi, D. B. Kaplan, and P. Galison. “Calculation of the Composite Higgs Mass”. In: *Phys. Lett.* 143B (1984), pp. 152–154. DOI: [10.1016/0370-2693\(84\)90823-2](#) (cit. on p. 23).
- [61] H. Georgi and D. B. Kaplan. “Composite Higgs and Custodial SU(2)”. In: *Phys. Lett.* 145B (1984), pp. 216–220. DOI: [10.1016/0370-2693\(84\)90341-1](#) (cit. on p. 23).



- [62] ATLAS collaboration. “Search for single production of vector-like quarks decaying into  $Wb$  in  $pp$  collisions at  $\sqrt{s} = 13$  TeV with the ATLAS detector”. In: (2016) (cit. on p. 23).
- [63] ATLAS collaboration. *ATLAS detector and physics performance: Technical Design Report, 2*. Technical Design Report ATLAS. Geneva: CERN, 1999. URL: <http://cds.cern.ch/record/391177> (cit. on pp. 23, 29).
- [64] T. Sjostrand. “High-energy physics event generation with PYTHIA 5.7 and JETSET 7.4”. In: *Comput. Phys. Commun.* 82 (1994), pp. 74–90. DOI: [10.1016/0010-4655\(94\)90132-5](https://doi.org/10.1016/0010-4655(94)90132-5) (cit. on p. 23).
- [65] J. Cammin and M. Schumacher. *The ATLAS discovery potential for the channel  $t\bar{t}H$ ,  $H$  to  $b\bar{b}$* . Tech. rep. ATL-PHYS-2003-024. revised version number 1 submitted on 2003-08-14 08:08:35. Geneva: CERN, 2003. URL: <http://cds.cern.ch/record/685523> (cit. on p. 23).
- [66] ATLAS Collaboration. “Expected Performance of the ATLAS Experiment - Detector, Trigger and Physics”. In: (2009). arXiv: [0901.0512 \[hep-ex\]](https://arxiv.org/abs/0901.0512) (cit. on pp. 25, 30, 183).
- [67] T. Sjostrand, S. Mrenna, and P. Z. Skands. “PYTHIA 6.4 Physics and Manual”. In: *JHEP* 05 (2006), p. 026. DOI: [10.1088/1126-6708/2006/05/026](https://doi.org/10.1088/1126-6708/2006/05/026). arXiv: [hep-ph/0603175 \[hep-ph\]](https://arxiv.org/abs/hep-ph/0603175) (cit. on p. 24).
- [68] ATLAS Collaboration. “Performance of  $b$ -Jet Identification in the ATLAS Experiment”. In: *JINST* 11.04 (2016), P04008. DOI: [10.1088/1748-0221/11/04/P04008](https://doi.org/10.1088/1748-0221/11/04/P04008). arXiv: [1512.01094 \[hep-ex\]](https://arxiv.org/abs/1512.01094) (cit. on pp. 25, 27, 167, 172).
- [69] D0 Collaboration. “ $b$ -Jet Identification in the D0 Experiment”. In: *Nucl. Instrum. Meth.* A620 (2010), pp. 490–517. DOI: [10.1016/j.nima.2010.03.118](https://doi.org/10.1016/j.nima.2010.03.118). arXiv: [1002.4224 \[hep-ex\]](https://arxiv.org/abs/1002.4224) (cit. on p. 26).
- [70] ATLAS Collaboration. “ $b$ -Jet Tagging Efficiency Calibration using the System8 Method”. In: (2011) (cit. on p. 31).
- [71] ATLAS Collaboration. *Measurement of the  $t\bar{t}$  production cross section in the all-hadronic channel in  $4.7\text{ fb}^{-1}$  of  $pp$  collisions at  $\sqrt{s} = 7$  TeV with the ATLAS detector*. *ATLAS-CONF-2012-031* (cit. on pp. 27, 32, 174, 182).
- [72] ATLAS Collaboration. “Search for the Standard Model Higgs boson decaying into  $b\bar{b}$  produced in association with top quarks decaying hadronically in  $pp$  collisions at  $\sqrt{s} = 8$  TeV with the ATLAS detector”. In: *JHEP* 05 (2016), p. 160. DOI: [10.1007/JHEP05\(2016\)160](https://doi.org/10.1007/JHEP05(2016)160). arXiv: [1604.03812 \[hep-ex\]](https://arxiv.org/abs/1604.03812) (cit. on pp. 27, 121, 123, 176).
- [73] S. Diglio, L. Feligioni, and G. Moulta. “Stashing the stops in multijet events at the LHC”. In: *Phys. Rev.* D96.5 (2017), p. 055032. DOI: [10.1103/PhysRevD.96.055032](https://doi.org/10.1103/PhysRevD.96.055032). arXiv: [1611.05850 \[hep-ph\]](https://arxiv.org/abs/1611.05850) (cit. on pp. 27, 88, 176).



- [74] ATLAS Collaboration. “Search for  $t\bar{t}$  production in the all-hadronic channel in ATLAS with  $\sqrt{s} = 7$  TeV data”. In: (2011) (cit. on p. 32).
- [75] ATLAS Collaboration. *Measurement of  $t\bar{t}$  production in the all-hadronic channel in  $1.02 \text{ fb}^{-1}$  of  $pp$  collisions at  $\sqrt{s} = 7$  TeV with the ATLAS detector*. ATLAS-CONF-2011-140. <https://cdsweb.cern.ch/record/1385033>. 2011 (cit. on p. 32).
- [76] M. Aliev et al. “HATHOR: hadronic top and heavy quarks cross section calculator”. In: *Comput. Phys. Commun.* 182 (2011), pp. 1034–1046. eprint: [arXiv:1007.1327 \[hep-ph\]](https://arxiv.org/abs/1007.1327) (cit. on p. 33).
- [77] A. D. Martin, W. J. Stirling, R. S. Thorne and G. Watt. “Parton distributions for the LHC”. In: *Eur. Phys. J.* C63 (2009), p. 189 (cit. on pp. 33, 40).
- [78] A. D. Martin, W. J. Stirling, R. S. Thorne, et al. “Uncertainties on  $\alpha_s$  in global PDF analyses and implications for predicted hadronic cross sections”. In: *Eur. Phys. J.* C64 (2009), pp. 653–680. DOI: [10.1140/epjc/s10052-009-1164-2](https://doi.org/10.1140/epjc/s10052-009-1164-2). arXiv: [0905.3531 \[hep-ph\]](https://arxiv.org/abs/0905.3531) (cit. on p. 33).
- [79] M. Cacciari, M. Czakon, M. L. Mangano, et al. “Top-pair production at hadron colliders with next-to-next-to-leading logarithmic soft-gluon resummation”. In: (2011). arXiv: [1111.5869 \[hep-ph\]](https://arxiv.org/abs/1111.5869) (cit. on p. 33).
- [80] M. Czakon and A. Mitov. “Top++: a program for the calculation of the top-pair cross-section at hadron colliders”. In: (2011). arXiv: [1112.5675 \[hep-ph\]](https://arxiv.org/abs/1112.5675) (cit. on p. 33).
- [81] K. Nakamura et al. *Particle Data Group*. *J. Phys.* G 37, 075021. 2010 (cit. on p. 33).
- [82] ATLAS Collaboration. “The ATLAS experiment at the CERN Large Hadron Collider”. In: *JINST* 3 (2008), S08003 (cit. on p. 33).
- [83] ATLAS Collaboration. “Measurement of the cross section for top-quark pair production in  $pp$  collisions at  $\sqrt{s} = 7$  TeV with the ATLAS detector using final states with two high-pt leptons”. In: (2012). arXiv: [1202.4892 \[hep-ex\]](https://arxiv.org/abs/1202.4892) (cit. on pp. 33, 165).
- [84] ATLAS Collaboration. *Measurement of the top quark pair production cross section in  $pp$  collisions at  $\sqrt{s} = 7$  TeV in  $\mu + \tau$  final states with ATLAS*. ATLAS-CONF-2011-119. <https://cdsweb.cern.ch/record/1376411>. 2011 (cit. on p. 33).
- [85] ATLAS Collaboration. *Measurement of the  $t\bar{t}$  production cross-section in  $pp$  collisions at  $\sqrt{s} = 7$  TeV using kinematic information of lepton+jets events*. ATLAS-CONF-2011-121. <https://cdsweb.cern.ch/record/1376411>. 2011 (cit. on p. 33).

- [86] ATLAS Collaboration. *Luminosity Determination in  $pp$  Collisions at  $\sqrt{s} = 7$  TeV using the ATLAS Detector in 2011*. ATLAS-CONF-2011-116. <https://cdsweb.cern.ch/record/1299109>. 2011 (cit. on pp. 33, 41).
- [87] ATLAS Collaboration. *ATLAS Jet Trigger in the Early  $\sqrt{s} = 7$  TeV Data*. ATLAS-CONF-2010-094. <https://cdsweb.cern.ch/record/1299109>. 2010 (cit. on pp. 33, 40).
- [88] S. Frixione and B.R. Webber. “Matching NLO QCD computations and parton shower simulations”. In: *JHEP* 0206 (2002), p. 029. arXiv: [0204244 \[hep-ex\]](https://arxiv.org/abs/0204244) (cit. on p. 34).
- [89] P. M. Nadolsky et al. “Implications of CTEQ global analysis for collider observables”. In: *Phys. Rev. D* 78 (2008), p. 013004. DOI: [10.1103/PhysRevD.78.013004](https://doi.org/10.1103/PhysRevD.78.013004). eprint: [arXiv:0802.0007 \[hep-ph\]](https://arxiv.org/abs/0802.0007) (cit. on p. 34).
- [90] Lai, H.L. and others. “New parton distributions for collider physics”. In: *Phys. Rev. D* 82 (2010), p. 074024 (cit. on pp. 34, 40).
- [91] ATLAS collaboration. “The ATLAS Experiment at the CERN Large Hadron Collider”. In: *JINST* 3 (2008), S08003 (cit. on p. 34).
- [92] S. Agostinelli et al. “GEANT4 - A Simulation Toolkit”. In: *Nucl. Instr. and Meth. A* 506 (2003), p. 250 (cit. on p. 34).
- [93] M.L. Mangano et al. “ALPGEN, a generator for hard multiparton processes in hadronic collisions”. In: *JHEP* 0307 (2003), p. 001. arXiv: [0206293 \[hep-ph\]](https://arxiv.org/abs/0206293) (cit. on pp. 34, 37).
- [94] ATLAS Collaboration. “Jet energy measurement with the ATLAS detector in proton-proton collisions at  $\sqrt{s} = 7$  TeV”. In: (2011). Submitted to European Physical Journal C. arXiv: [1112.6426v1 \[hep-ex\]](https://arxiv.org/abs/1112.6426v1) (cit. on pp. 34, 39, 41).
- [95] ATLAS Collaboration. *Measurement of the Top-Quark Mass using the Template Method in  $pp$  Collisions at  $\sqrt{s} = 7$  TeV with the ATLAS detector*. ATLAS-CONF-2011-033. <https://cdsweb.cern.ch/record/1337783>. 2011 (cit. on p. 35).
- [96] ATLAS Collaboration. *Measurement of the W-boson polarisation in top-quark decays in  $pp$  collision data at  $\sqrt{s} = 7$  TeV using the ATLAS detector*. ATLAS-CONF-2011-037. <https://cdsweb.cern.ch/record/1337787>. 2011 (cit. on p. 35).
- [97] ATLAS Collaboration. *Calibrating the b-Tag Efficiency and Mistag Rate in  $35 \text{ pb}^{-1}$  of Data with the ATLAS Detector*. ATLAS-CONF-2011-089. <https://cdsweb.cern.ch/record/1356198>. 2011 (cit. on p. 40).
- [98] B.P. Kersevan and E. Richter-Was. “The Monte Carlo event generator AcerMC version 2.0 with interfaces to PYTHIA 6.2 and HERWIG 6.5”. In: (2004). arXiv: [0405247 \[hep-ph\]](https://arxiv.org/abs/0405247) (cit. on p. 40).

- [99] ATLAS Collaboration. “Rapidity gap cross sections measured with the ATLAS detector in pp collisions at  $\sqrt{s} = 7$  TeV”. In: (2012). arXiv: [1201.2808 \[hep-ex\]](#) (cit. on p. 40).
- [100] S. Frixione, P. Nason and C. Oleari. “Matching NLO QCD computations with Parton Shower simulations: the POWHEG method”. In: *JHEP* 0711 (2007), p. 070. eprint: [arXiv:0709.2092\[hep-ph\]](#) (cit. on p. 40).
- [101] T. Sjostrand and S. Mrenna and P.Z. Skands. “PYTHIA 6.4 Physics and Manual”. In: *JHEP* 05 (2006), p. 026. eprint: [hep-ph/0603175](#) (cit. on p. 40).
- [102] NNPDF Collaboration. “Precision determination of electroweak parameters and the strange content of the proton from neutrino deep-inelastic scattering”. In: *Nucl. Phys.* B823 (2009), p. 195 (cit. on p. 40).
- [103] ATLAS collaboration. “Luminosity Determination in pp Collisions at  $\sqrt{s}=7$  TeV Using the ATLAS Detector at the LHC”. In: *European Physical Journal C - Particle and Fields* C71 (2011), p. 1630. arXiv: [1101.2185 \[hep-ex\]](#) (cit. on p. 41).
- [104] ATLAS Collaboration. *Jet energy resolution and selection efficiency relative to track jets from in-situ techniques with the ATLAS Detector using Proton-Proton Collisions at a centre-of-mass energy  $\sqrt{s} = 7$  TeV*. ATLAS-CONF-2010-054. <https://cdsweb.cern.ch/record/1281311>. 2010 (cit. on p. 41).
- [105] R. Barlow. “Asymmetric Errors”. In: (2003). Proceedings at PHYSTAT2003. arXiv: [0401042 \[physics\]](#) (cit. on p. 42).
- [106] ATLAS Collaboration. “Measurements of the Higgs boson production and decay rates and coupling strengths using  $pp$  collision data at  $\sqrt{s} = 7$  and 8 TeV in the ATLAS experiment”. In: *CERN-PH-EP-2015-125* (2015). submitted to The European Physical Journal C. arXiv: [1507.04548 \[hep-ex\]](#) (cit. on pp. 43, 73).
- [107] ATLAS Collaboration. “Study of the spin and parity of the Higgs boson in diboson decays with the ATLAS detector”. In: *Eur. Phys. J. C* 75 (2015), p. 476. DOI: [10.1140/epjc/s10052-015-3685-1](#). arXiv: [1506.05669 \[hep-ex\]](#) (cit. on p. 43).
- [108] CMS Collaboration. “Precise determination of the mass of the Higgs boson and tests of compatibility of its couplings with the standard model predictions using proton collisions at 7 and 8 TeV”. In: *Eur. Phys. J. C* 75 (2015), p. 212. DOI: [10.1140/epjc/s10052-015-3351-7](#). arXiv: [1412.8662 \[hep-ex\]](#) (cit. on p. 43).

- [109] CMS Collaboration. “Constraints on the spin-parity and anomalous HVV couplings of the Higgs boson in proton collisions at 7 and 8 TeV”. In: *Phys. Rev. D* 92.1 (2015), p. 012004. DOI: [10.1103/PhysRevD.92.012004](https://doi.org/10.1103/PhysRevD.92.012004). arXiv: [1411.3441](https://arxiv.org/abs/1411.3441) [hep-ex] (cit. on p. 43).
- [110] ATLAS Collaboration. “Constraints on the off-shell Higgs boson signal strength in the high-mass  $ZZ$  and  $WW$  final states with the ATLAS detector”. In: *Eur. Phys. J. C* 75.7 (2015), p. 335. DOI: [10.1140/epjc/s10052-015-3542-2](https://doi.org/10.1140/epjc/s10052-015-3542-2). arXiv: [1503.01060](https://arxiv.org/abs/1503.01060) [hep-ex] (cit. on p. 43).
- [111] CMS Collaboration. “Constraints on the Higgs boson width from off-shell production and decay to Z-boson pairs”. In: *Phys. Lett. B* 736 (2014), pp. 64–85. DOI: [10.1016/j.physletb.2014.06.077](https://doi.org/10.1016/j.physletb.2014.06.077). arXiv: [1405.3455](https://arxiv.org/abs/1405.3455) [hep-ex] (cit. on p. 43).
- [112] S. Dittmaier et al. “Handbook of LHC Higgs Cross Sections: 1. Inclusive Observables”. In: (2011). arXiv: [1101.0593](https://arxiv.org/abs/1101.0593) [hep-ph] (cit. on pp. 44, 45).
- [113] CMS Collaboration. “Search for the associated production of the Higgs boson with a top-quark pair”. In: *JHEP* 09 (2014). [Erratum: *JHEP* 10 (2014) 106], p. 087. DOI: [10.1007/JHEP09\(2014\)087](https://doi.org/10.1007/JHEP09(2014)087), [10.1007/JHEP10\(2014\)106](https://doi.org/10.1007/JHEP10(2014)106). arXiv: [1408.1682](https://arxiv.org/abs/1408.1682) [hep-ex] (cit. on p. 44).
- [114] ATLAS Collaboration. “Search for the associated production of the Higgs boson with a top quark pair in multilepton final states with the ATLAS detector”. In: *Phys. Lett. B* 749 (2015), pp. 519–541. DOI: [10.1016/j.physletb.2015.07.079](https://doi.org/10.1016/j.physletb.2015.07.079). arXiv: [1506.05988](https://arxiv.org/abs/1506.05988) [hep-ex] (cit. on pp. 44, 71).
- [115] ATLAS Collaboration. “Search for the Standard Model Higgs boson produced in association with top quarks and decaying into  $b\bar{b}$  in pp collisions at  $\sqrt{s} = 8$  TeV with the ATLAS detector”. In: *Eur. Phys. J. C* 75 (2015), p. 349. DOI: [10.1140/epjc/s10052-015-3543-1](https://doi.org/10.1140/epjc/s10052-015-3543-1). arXiv: [1503.05066](https://arxiv.org/abs/1503.05066) [hep-ex] (cit. on pp. 44, 46, 62, 65, 70–72).
- [116] ATLAS Collaboration. “Search for  $H \rightarrow \gamma\gamma$  produced in association with top quarks and constraints on the Yukawa coupling between the top quark and the Higgs boson using data taken at 7 TeV and 8 TeV with the ATLAS detector”. In: *Phys. Lett. B* 740 (2015). DOI: [10.1016/j.physletb.2014.11.049](https://doi.org/10.1016/j.physletb.2014.11.049). arXiv: [1409.3122](https://arxiv.org/abs/1409.3122) [hep-ph] (cit. on pp. 44, 71).
- [117] ATLAS Collaboration. “Selection of jets produced in proton-proton collisions with the ATLAS detector using 2011 data”. In: ATLAS-CONF-2012-020 (2012). URL: <http://cdsweb.cern.ch/record/1430034> (cit. on p. 45).

- [118] G. Bevilacqua, M. Czakon, M.V. Garzelli, et al. “HELAC-NLO”. In: *Comput. Phys. Commun.* 184 (2013), p. 986. DOI: [10.1016/j.cpc.2012.10.033](https://doi.org/10.1016/j.cpc.2012.10.033). arXiv: [1110.1499](https://arxiv.org/abs/1110.1499) [hep-ph] (cit. on p. 45).
- [119] P. Nason. “A new method for combining NLO QCD with shower Monte Carlo algorithms”. In: *JHEP* 11 (2004), p. 040. DOI: [10.1088/1126-6708/2004/11/040](https://doi.org/10.1088/1126-6708/2004/11/040) (cit. on p. 45).
- [120] S. Frixione, P. Nason, and C. Oleari. “Matching NLO QCD computations with Parton Shower simulations: the POWHEG method”. In: *JHEP* 11 (2007), p. 070. DOI: [10.1088/1126-6708/2007/11/070](https://doi.org/10.1088/1126-6708/2007/11/070). arXiv: [0709.2092](https://arxiv.org/abs/0709.2092) [hep-ph] (cit. on p. 45).
- [121] S. Alioli, P. Nason, C. Oleari, et al. “A general framework for implementing NLO calculations in shower Monte Carlo programs: the POWHEG BOX”. In: *JHEP* 06 (2010), p. 040. DOI: [10.1007/JHEP06\(2010\)043](https://doi.org/10.1007/JHEP06(2010)043). arXiv: [1002.2581](https://arxiv.org/abs/1002.2581) [hep-ph] (cit. on p. 45).
- [122] M.V. Garzelli, A. Kardos, C.G. Papadopoulos, et al. “Standard Model Higgs boson production in association with a top anti-top pair at NLO with parton showering”. In: *Europhys. Lett.* 96 (2011), p. 11001. DOI: [10.1209/0295-5075/96/11001](https://doi.org/10.1209/0295-5075/96/11001). arXiv: [1108.0387](https://arxiv.org/abs/1108.0387) [hep-ex] (cit. on p. 45).
- [123] H.-L. Lai et al. “New parton distributions for collider physics”. In: *Phys. Rev. D* 82 (2010), p. 074024. DOI: [10.1103/PhysRevD.82.074024](https://doi.org/10.1103/PhysRevD.82.074024). arXiv: [1007.2241](https://arxiv.org/abs/1007.2241) [hep-ph] (cit. on p. 45).
- [124] T. Sjöstrand, S. Mrenna, and P. Skands. “A Brief Introduction to PYTHIA 8.1”. In: *Comput. Phys. Commun.* 178 (2008), p. 852. DOI: [10.1016/j.cpc.2008.01.036](https://doi.org/10.1016/j.cpc.2008.01.036). arXiv: [0710.3820](https://arxiv.org/abs/0710.3820) [hep-ph] (cit. on p. 45).
- [125] P. M. Nadolsky et al. “Implications of CTEQ global analysis for collider observables”. In: *Phys. Rev. D* 78 (2008), p. 013004. DOI: [10.1103/PhysRevD.78.013004](https://doi.org/10.1103/PhysRevD.78.013004). arXiv: [0802.0007](https://arxiv.org/abs/0802.0007) [hep-ph] (cit. on p. 45).
- [126] The ATLAS Collaboration. “Summary of ATLAS PYTHIA 8 tunes”. In: ATL-PHYS-PUB-2012-003 (2012). URL: <http://cdsweb.cern.ch/record/1474107> (cit. on p. 45).
- [127] G. Corcella et al. “HERWIG 6: an event generator for hadron emission reactions with interfering gluons (including supersymmetric processes)”. In: *JHEP* 01 (2001), p. 010. DOI: [10.1088/1126-6708/2001/01/010](https://doi.org/10.1088/1126-6708/2001/01/010) (cit. on p. 45).
- [128] R. D. Ball et al. “Parton distributions with LHC data”. In: *Nucl. Phys. B* 867 (2013), p. 244. DOI: [10.1016/j.nuclphysb.2012.10.003](https://doi.org/10.1016/j.nuclphysb.2012.10.003). arXiv: [1207.1303](https://arxiv.org/abs/1207.1303) [hep-ph] (cit. on p. 46).

- [129] T. Sjöstrand, S. Mrenna, and P. Skands. “PYTHIA 6.4 Physics and Manual”. In: *JHEP* 05 (2006), p. 026. DOI: [10.1088/1126-6708/2006/05/026](https://doi.org/10.1088/1126-6708/2006/05/026). arXiv: [0603175v2](https://arxiv.org/abs/0603175v2) [hep-ph] (cit. on p. 46).
- [130] P. Z. Skands. “Tuning Monte Carlo Generators: The Perugia Tunes”. In: *Phys.Rev. D* 82 (2010), p. 074018. DOI: [10.1103/PhysRevD.82.074018](https://doi.org/10.1103/PhysRevD.82.074018). arXiv: [1005.3457](https://arxiv.org/abs/1005.3457) [hep-ph] (cit. on p. 46).
- [131] M. Cacciari et al. “Top-pair production at hadron colliders with next-to-next-to-leading logarithmic soft-gluon resummation”. In: *Phys. Lett. B* 710 (2012), p. 612. DOI: [10.1016/j.physletb.2012.03.013](https://doi.org/10.1016/j.physletb.2012.03.013). arXiv: [1111.5869](https://arxiv.org/abs/1111.5869) [hep-ph] (cit. on p. 46).
- [132] P. Barnreuther et al. “Percent Level Precision Physics at the Tevatron: First Genuine NNLO QCD Corrections to  $q\bar{q} \rightarrow t\bar{t}$ ”. In: *Phys. Rev. Lett.* 109 (2012), p. 132001. DOI: [10.1103/PhysRevLett.109.132001](https://doi.org/10.1103/PhysRevLett.109.132001). arXiv: [1204.5201](https://arxiv.org/abs/1204.5201) [hep-ph] (cit. on p. 46).
- [133] M. Czakon and A. Mitov. “NNLO corrections to top-pair production at hadron colliders: the all-fermionic scattering channels”. In: *JHEP* 12 (2012), p. 054. DOI: [10.1007/JHEP12\(2012\)054](https://doi.org/10.1007/JHEP12(2012)054). arXiv: [1207.0236](https://arxiv.org/abs/1207.0236) [hep-ph] (cit. on p. 46).
- [134] M. Czakon and A. Mitov. “NNLO corrections to top-pair production at hadron colliders: the quark-gluon reaction”. In: *JHEP* 01 (2013), p. 080. DOI: [10.1007/JHEP01\(2013\)080](https://doi.org/10.1007/JHEP01(2013)080) (cit. on p. 46).
- [135] P. Fiedler M. Czakon and A. Mitov. “The total top quark pair production cross-section at hadron colliders through  $\mathcal{O}(\alpha_S^4)$ ”. In: *Phys. Rev. Lett.* 110 (2013), p. 252004. DOI: [10.1103/PhysRevLett.110.252004](https://doi.org/10.1103/PhysRevLett.110.252004). arXiv: [1303.6254](https://arxiv.org/abs/1303.6254) [hep-ph] (cit. on pp. 46, 122).
- [136] M. Czakon and A. Mitov. “Top++: a program for the calculation of the top-pair cross-section at hadron colliders”. In: *Comput. Phys. Commun.* 185 (2014), 2930. DOI: [10.1016/j.cpc.2014.06.021](https://doi.org/10.1016/j.cpc.2014.06.021). arXiv: [1112.5675](https://arxiv.org/abs/1112.5675) [hep-ph] (cit. on p. 46).
- [137] F. Cascioli, P. Maierhöfer, N. Moretti, et al. “NLO matching for ttbb production with massive b-quarks”. In: *Phys. Lett. B* 734 (2014), p. 210. DOI: [10.1016/j.physletb.2014.05.040](https://doi.org/10.1016/j.physletb.2014.05.040). arXiv: [1309.5912](https://arxiv.org/abs/1309.5912) [hep-ph] (cit. on p. 46).
- [138] T. Gleisberg et al. “Event generation with SHERPA 1.1”. In: *JHEP* 0902 (2009), p. 007. DOI: [10.1088/1126-6708/2009/02/007](https://doi.org/10.1088/1126-6708/2009/02/007). arXiv: [0811.4622](https://arxiv.org/abs/0811.4622) [hep-ph] (cit. on p. 46).
- [139] F. Cascioli, P. Maierhöfer, and S. Pozzorini. “Scattering Amplitudes with Open Loops”. In: *Phys. Rev. Lett.* 108 (2012), p. 111601. DOI: [10.1103/PhysRevLett.108.111601](https://doi.org/10.1103/PhysRevLett.108.111601). arXiv: [1111.5206](https://arxiv.org/abs/1111.5206) [hep-ph] (cit. on p. 46).



- [140] ATLAS Collaboration. “Measurements of normalized differential cross sections for  $t\bar{t}$  production in  $pp$  collisions at  $\sqrt{s} = 7\text{ TeV}$  using the ATLAS detector”. In: *Phys. Rev. D* 90 (2014), p. 072004. DOI: <http://dx.doi.org/10.1103/PhysRevD.90.072004> (cit. on p. 47).
- [141] B. P. Kersevan and E. Richter-Was. “The Monte Carlo Event Generator AcerMC 2.0 with Interfaces to PYTHIA 6.2 and HERWIG 6.5”. In: (2004). DOI: [10.1016/j.cpc.2012.10.032](https://doi.org/10.1016/j.cpc.2012.10.032). arXiv: [hep-ph/0405247](https://arxiv.org/abs/hep-ph/0405247) [hep-ph] (cit. on p. 47).
- [142] S. Frixione, E. Laenen, P. Motylinski, et al. “Single-top production in MC@NLO”. In: *JHEP* 03 (2006), p. 092. DOI: [10.1088/1126-6708/2006/03/092](https://doi.org/10.1088/1126-6708/2006/03/092). arXiv: [0512250](https://arxiv.org/abs/0512250) [hep-ph] (cit. on p. 47).
- [143] N. Kidonakis. “Next-to-next-to-leading-order collinear and soft gluon corrections for  $t$ -channel single top quark production”. In: *Phys. Rev. D* 83 (2011), p. 091503. DOI: [10.1103/PhysRevD.83.091503](https://doi.org/10.1103/PhysRevD.83.091503). arXiv: [1103.2792](https://arxiv.org/abs/1103.2792) [hep-ph] (cit. on p. 47).
- [144] N. Kidonakis. “Next-to-next-to-leading logarithm resummation for  $s$ -channel single top quark production”. In: *Phys. Rev. D* 81 (2010), p. 054028. DOI: [10.1103/PhysRevD.81.054028](https://doi.org/10.1103/PhysRevD.81.054028). arXiv: [1001.5034](https://arxiv.org/abs/1001.5034) (cit. on p. 47).
- [145] A. D. Martin et al. “Parton distributions for the LHC”. In: *Eur. Phys. J. C* 63 (2009), p. 189. DOI: [10.1140/epjc/s10052-009-1072-5](https://doi.org/10.1140/epjc/s10052-009-1072-5). arXiv: [0901.0002](https://arxiv.org/abs/0901.0002) [hep-ph] (cit. on p. 47).
- [146] A. D. Martin et al. “Uncertainties on  $\alpha_s$  in global PDF analyses and implications for predicted hadronic cross sections”. In: *Eur. Phys. J. C* 64 (2009), p. 653. DOI: [10.1140/epjc/s10052-009-1072-5](https://doi.org/10.1140/epjc/s10052-009-1072-5). arXiv: [0905.3531](https://arxiv.org/abs/0905.3531) [hep-ph] (cit. on p. 47).
- [147] J. Alwall et al. “MadGraph/MadEvent v4: the new web generation”. In: *JHEP* 09 (2007), p. 028. DOI: [10.1088/1126-6708/2007/09/028](https://doi.org/10.1088/1126-6708/2007/09/028). arXiv: [0706.2334](https://arxiv.org/abs/0706.2334) [hep-ph] (cit. on p. 47).
- [148] J. M. Campbell and R. K. Ellis. “ $t\bar{t}W$  production and decay at NLO”. In: *JHEP* 07 (2012), p. 052. DOI: [10.1007/JHEP07\(2012\)052](https://doi.org/10.1007/JHEP07(2012)052). arXiv: [1204.5678](https://arxiv.org/abs/1204.5678) [hep-ph] (cit. on pp. 47, 65).
- [149] M. V. Garzelli, A. Kardos, C. G. Papadopoulos, et al. “ $t\bar{t}W$  and  $t\bar{t}Z$  Hadroproduction at NLO accuracy in QCD with Parton Shower and Hadronization effects”. In: *JHEP* 11 (2012), p. 056. DOI: [10.1007/JHEP11\(2012\)056](https://doi.org/10.1007/JHEP11(2012)056). arXiv: [1208.2665](https://arxiv.org/abs/1208.2665) [hep-ph] (cit. on pp. 47, 65).
- [150] J. Alwall, R. Frederix, S. Frixione, et al. “The automated computation of tree-level and next-to-leading order differential cross sections, and their matching to parton shower simulations”. In: *JHEP* 07 (2014), p. 079. DOI: [10.1007/JHEP07\(2014\)079](https://doi.org/10.1007/JHEP07(2014)079). arXiv: [1405.0301](https://arxiv.org/abs/1405.0301) [hep-ph] (cit. on pp. 47, 106).

- [151] M. Bähr et al. “Herwig++ Physics and Manual”. In: *Eur. Phys. J. C* 58 (2008), p. 639. DOI: [10.1140/epjc/s10052-008-0798-9](https://doi.org/10.1140/epjc/s10052-008-0798-9). arXiv: [0803.0883 \[hep-ph\]](https://arxiv.org/abs/0803.0883) (cit. on p. 47).
- [152] J. Bellm et al. “Herwig++ 2.7 Release Note”. In: (2013). arXiv: [1310.6877 \[hep-ph\]](https://arxiv.org/abs/1310.6877) (cit. on p. 47).
- [153] J. Butterworth, J. Forshaw, and M. Seymour. “Multiparton interactions in photoproduction at HERA”. In: *Z. Phys. C* 72 (4 1996), p. 637. DOI: [10.1007/s002880050286](https://doi.org/10.1007/s002880050286). arXiv: [9601371 \[hep-ph\]](https://arxiv.org/abs/9601371) (cit. on p. 47).
- [154] P. Golonka and Z. Wąs. “PHOTOS Monte Carlo: a precision tool for QED corrections in  $Z$  and  $W$  decays”. In: *Eur. Phys. J. C* 45 (2006), p. 97. DOI: [10.1140/epjc/s2005-02396-4](https://doi.org/10.1140/epjc/s2005-02396-4). arXiv: [0506026 \[hep-ph\]](https://arxiv.org/abs/0506026) (cit. on p. 47).
- [155] S. Jadach, J. H. Kühn, and Z. Wąs. “TAUOLA - a library of Monte Carlo programs to simulate decays of polarized  $\tau$  leptons”. In: *Comput. Phys. Commun.* 64 (1991), p. 275. DOI: [10.1016/0010-4655\(91\)90038-M](https://doi.org/10.1016/0010-4655(91)90038-M) (cit. on p. 47).
- [156] ATLAS Collaboration. “The ATLAS Simulation Infrastructure”. In: *Eur. Phys. J. C* 70 (2010), pp. 823–874. DOI: [10.1140/epjc/s10052-010-1429-9](https://doi.org/10.1140/epjc/s10052-010-1429-9). arXiv: [1005.4568 \[physics.ins-det\]](https://arxiv.org/abs/1005.4568) (cit. on p. 47).
- [157] S. Agostinelli et al. “GEANT4: A simulation toolkit”. In: *Nucl. Instrum. Meth. A* 506 (2003), p. 250. DOI: [10.1016/S0168-9002\(03\)01368-8](https://doi.org/10.1016/S0168-9002(03)01368-8) (cit. on p. 47).
- [158] The ATLAS Collaboration. “The simulation principle and performance of the ATLAS fast calorimeter simulation FastCaloSim”. In: ATL-PHYS-PUB-2010-013 (2010). URL: <http://cdsweb.cern.ch/record/1300517> (cit. on p. 47).
- [159] DØ Collaboration. “Measurement of the  $t\bar{t}$  production cross section in  $pp$  collisions at  $\sqrt{s} = 1.96$  TeV using secondary vertex  $b$ -tagging”. In: *Phys. Rev. D* 74 (2006), p. 112004. DOI: [10.1103/PhysRevD.74.112004](https://doi.org/10.1103/PhysRevD.74.112004). arXiv: [0611002 \[hep-ex\]](https://arxiv.org/abs/0611002) (cit. on pp. 48, 49).
- [160] R. Achenbach et al. “The ATLAS Level-1 Calorimeter Trigger”. In: *JINST* 3.03 (2008), P03001. DOI: [10.1088/1748-0221/3/03/P03001](https://doi.org/10.1088/1748-0221/3/03/P03001). URL: <http://stacks.iop.org/1748-0221/3/i=03/a=P03001> (cit. on p. 51).
- [161] A. Hoecker et al. “TMVA-v4 Users Guide”. In: *PoS ACAT:040* (2007). DOI: [PoSACAT:040,2007](https://doi.org/10.1088/1748-0221/3/03/P03001). arXiv: [0703039v5 \[physics\]](https://arxiv.org/abs/0703039v5) (cit. on p. 58).
- [162] G. Cowan, K. Cranmer, E. Gross, et al. “Asymptotic formulae for likelihood-based tests of new physics”. In: *Eur. Phys. J. C* 71 (2011), p. 1554. DOI: [10.1140/epjc/s10052-011-1554-0](https://doi.org/10.1140/epjc/s10052-011-1554-0). arXiv: [1007.1727 \[physics\]](https://arxiv.org/abs/1007.1727) (cit. on pp. 62, 67).



- [163] ATLAS Collaboration. “Luminosity determination in  $pp$  collisions at  $\sqrt{s} = 7$  TeV using the ATLAS detector at the LHC”. In: *Eur. Phys. J. C* 71 (2011), p. 1630. DOI: [10.1140/epjc/s10052-011-1630-5](https://doi.org/10.1140/epjc/s10052-011-1630-5). arXiv: [1101.2185 \[hep-ex\]](https://arxiv.org/abs/1101.2185) (cit. on p. 64).
- [164] ATLAS Collaboration. “Jet energy measurement with the ATLAS detector in proton-proton collisions at  $\sqrt{s} = 7$  TeV”. In: *Eur. Phys. J. C* 73.3 (2013), p. 2304. DOI: [10.1140/epjc/s10052-013-2304-2](https://doi.org/10.1140/epjc/s10052-013-2304-2). arXiv: [1112.6426 \[hep-ex\]](https://arxiv.org/abs/1112.6426) (cit. on pp. 64, 164).
- [165] ATLAS Collaboration. “Measurement of the mistag rate of  $b$ -tagging algorithms with  $5 \text{ fb}^{-1}$  of data collected by the ATLAS detector”. In: ATLAS-CONF-2012-040 (2012). URL: <http://cdsweb.cern.ch/record/1435194> (cit. on p. 65).
- [166] M. Botje et al. “The PDF4LHC Working Group Interim Recommendations”. In: (2011). arXiv: [1101.0538 \[hep-ph\]](https://arxiv.org/abs/1101.0538) (cit. on p. 66).
- [167] T. Junk. “Confidence level computation for combining searches with small statistics”. In: *Nucl. Instrum. Meth.* 434 (1999), p. 435. DOI: [10.1016/S0168-9002\(99\)00498-2](https://doi.org/10.1016/S0168-9002(99)00498-2). arXiv: [9902006 \[hep-ex\]](https://arxiv.org/abs/9902006) (cit. on p. 67).
- [168] A. L. Read. “Presentation of search results: the  $CL_s$  technique”. In: *J. Phys. G* 28 (2002), p. 2693. DOI: [10.1088/0954-3899/28/10/313](https://doi.org/10.1088/0954-3899/28/10/313) (cit. on p. 67).
- [169] W. Verkerke and D. Kirkby. “RooFit Users Manual v2.91”. In: (2008). URL: <http://roofit.sourceforge.net> (cit. on p. 67).
- [170] M. Feindt and U. Kerzel. “The NeuroBayes neural network package”. In: *Nucl. Instrum. Meth.* A559 (2006), p. 190. DOI: [10.1016/j.nima.2005.11.166](https://doi.org/10.1016/j.nima.2005.11.166) (cit. on p. 71).
- [171] LHC Higgs Cross Section Working Group. “Handbook of LHC Higgs Cross Sections: 3. Higgs Properties”. In: (2013). Ed. by S Heinemeyer, C Mariotti, G Passarino, et al. DOI: [10.5170/CERN-2013-004](https://doi.org/10.5170/CERN-2013-004). arXiv: [1307.1347 \[hep-ph\]](https://arxiv.org/abs/1307.1347) (cit. on p. 73).
- [172] LHC Higgs Cross Section Working Group. “Handbook of LHC Higgs Cross Sections: 3. Higgs Properties”. In: *CERN-2013-004* (2013). DOI: [10.5170/CERN-2013-004](https://doi.org/10.5170/CERN-2013-004). arXiv: [1307.1347 \[hep-ph\]](https://arxiv.org/abs/1307.1347) (cit. on p. 73).
- [173] ATLAS Collaboration. “Observation of a new particle in the search for the Standard Model Higgs boson with the ATLAS detector at the LHC”. In: *Phys. Lett. B* 716 (2012), pp. 1–29. DOI: [10.1016/j.physletb.2012.08.020](https://doi.org/10.1016/j.physletb.2012.08.020). arXiv: [1207.7214 \[hep-ex\]](https://arxiv.org/abs/1207.7214) (cit. on p. 88).
- [174] CMS Collaboration. “Observation of a new boson at a mass of 125 GeV with the CMS experiment at the LHC”. In: *Phys. Lett. B* 716 (2012), pp. 30–61. DOI: [10.1016/j.physletb.2012.08.021](https://doi.org/10.1016/j.physletb.2012.08.021). arXiv: [1207.7235 \[hep-ex\]](https://arxiv.org/abs/1207.7235) (cit. on p. 88).

- [175] ATLAS and CMS Collaboration. “Combined Measurement of the Higgs Boson Mass in  $pp$  Collisions at  $\sqrt{s} = 7$  and 8 TeV with the ATLAS and CMS Experiments”. In: *Phys. Rev. Lett.* 114 (2015), p. 191803. DOI: [10.1103/PhysRevLett.114.191803](#). arXiv: [1503.07589 \[hep-ex\]](#) (cit. on p. 88).
- [176] LHCb Collaboration. “Test of lepton universality using  $B^+ \rightarrow K^+ \ell^+ \ell^-$  decays”. In: *Phys. Rev. Lett.* 113 (2014), p. 151601. DOI: [10.1103/PhysRevLett.113.151601](#). arXiv: [1406.6482 \[hep-ex\]](#) (cit. on p. 88).
- [177] LHCb Collaboration. “Angular analysis of the  $B^0 \rightarrow K^{*0} \mu^+ \mu^-$  decay using  $3 \text{ fb}^{-1}$  of integrated luminosity”. In: *JHEP* 02 (2016), p. 104. DOI: [10.1007/JHEP02\(2016\)104](#). arXiv: [1512.04442 \[hep-ex\]](#) (cit. on p. 88).
- [178] S. Descotes-Genon, L. Hofer, J. Matias, et al. “Global analysis of  $b \rightarrow s \ell \ell$  anomalies”. In: *JHEP* 06 (2016), p. 092. DOI: [10.1007/JHEP06\(2016\)092](#). arXiv: [1510.04239 \[hep-ph\]](#) (cit. on p. 88).
- [179] F. F. Deppisch, P. S. Bhupal Dev, and A. Pilaftsis. “Neutrinos and Collider Physics”. In: *New J. Phys.* 17.7 (2015), p. 075019. DOI: [10.1088/1367-2630/17/7/075019](#). arXiv: [1502.06541 \[hep-ph\]](#) (cit. on p. 88).
- [180] Y. A. Golfand and E. P. Likhtman. “Extension of the Algebra of Poincare Group Generators and Violation of p Invariance”. In: *JETP Lett.* 13 (1971). [*Pisma Zh. Eksp. Teor. Fiz.* 13,452(1971)], pp. 323–326 (cit. on p. 88).
- [181] P. Ramond. “Dual Theory for Free Fermions”. In: *Phys. Rev. D* 3 (1971), pp. 2415–2418. DOI: [10.1103/PhysRevD.3.2415](#) (cit. on p. 88).
- [182] A. Neveu and J. H. Schwarz. “Quark Model of Dual Pions”. In: *Phys. Rev. D* 4 (1971), pp. 1109–1111. DOI: [10.1103/PhysRevD.4.1109](#) (cit. on p. 88).
- [183] J.-L. Gervais and B. Sakita. “Functional integral approach to dual resonance theory”. In: *Phys. Rev. D* 4 (1971), pp. 2291–2308. DOI: [10.1103/PhysRevD.4.2291](#) (cit. on p. 88).
- [184] D. V. Volkov and V. P. Akulov. “Is the Neutrino a Goldstone Particle?” In: *Phys. Lett. B* 46 (1973), pp. 109–110. DOI: [10.1016/0370-2693\(73\)90490-5](#) (cit. on p. 88).
- [185] J. Wess and B. Zumino. “A Lagrangian Model Invariant Under Supergauge Transformations”. In: *Phys. Lett. B* 49 (1974), p. 52. DOI: [10.1016/0370-2693\(74\)90578-4](#) (cit. on p. 88).
- [186] P. Fayet. “Supergauge Invariant Extension of the Higgs Mechanism and a Model for the electron and Its Neutrino”. In: *Nucl. Phys. B* 90 (1975), pp. 104–124. DOI: [10.1016/0550-3213\(75\)90636-7](#) (cit. on p. 89).
- [187] A. Salam and J. A. Strathdee. “Supersymmetry and Fermion Number Conservation”. In: *Nucl. Phys. B* 87 (1975), pp. 85–92. DOI: [10.1016/0550-3213\(75\)90253-9](#) (cit. on p. 89).

- [188] J. A. Evans and Y. Kats. “LHC Coverage of RPV MSSM with Light Stops”. In: *JHEP* 04 (2013), p. 028. DOI: [10.1007/JHEP04\(2013\)028](https://doi.org/10.1007/JHEP04(2013)028). arXiv: [1209.0764](https://arxiv.org/abs/1209.0764) [hep-ph] (cit. on p. 89).
- [189] C. Csaki, E. Kuflik, O. Slone, et al. “Models of Dynamical R-Parity Violation”. In: *JHEP* 06 (2015), p. 045. DOI: [10.1007/JHEP06\(2015\)045](https://doi.org/10.1007/JHEP06(2015)045). arXiv: [1502.03096](https://arxiv.org/abs/1502.03096) [hep-ph] (cit. on pp. 89, 92).
- [190] R. N. Mohapatra. “Supersymmetry and R-parity: an Overview”. In: *Phys. Scripta* 90 (2015), p. 088004. DOI: [10.1088/0031-8949/90/8/088004](https://doi.org/10.1088/0031-8949/90/8/088004). arXiv: [1503.06478](https://arxiv.org/abs/1503.06478) [hep-ph] (cit. on pp. 89, 92).
- [191] A. E. Nelson and N. Seiberg. “R symmetry breaking versus supersymmetry breaking”. In: *Nucl. Phys. B* 416 (1994), pp. 46–62. DOI: [10.1016/0550-3213\(94\)90577-0](https://doi.org/10.1016/0550-3213(94)90577-0). arXiv: [hep-ph/9309299](https://arxiv.org/abs/hep-ph/9309299) [hep-ph] (cit. on p. 89).
- [192] L. E. Ibanez and G. G. Ross. “Discrete gauge symmetries and the origin of baryon and lepton number conservation in supersymmetric versions of the standard model”. In: *Nucl. Phys. B* 368 (1992), pp. 3–37. DOI: [10.1016/0550-3213\(92\)90195-H](https://doi.org/10.1016/0550-3213(92)90195-H) (cit. on p. 89).
- [193] ATLAS Collaboration. *Search for supersymmetry with two same-sign leptons or three leptons using 13.2 fb<sup>1</sup> of  $\sqrt{s} = 13$  TeV pp collision data collected by the ATLAS detector*. ATLAS-CONF-2016-037. Geneva, 2016. URL: <http://cds.cern.ch/record/2205745> (cit. on pp. 89, 92).
- [194] ATLAS Collaboration. “Search for a heavy narrow resonance decaying to  $e\mu$ ,  $e\tau$ , or  $\mu\tau$  with the ATLAS detector in  $\sqrt{s} = 7$  TeV pp collisions at the LHC”. In: *Phys. Lett. B* 723 (2013), pp. 15–32. DOI: [10.1016/j.physletb.2013.04.035](https://doi.org/10.1016/j.physletb.2013.04.035). arXiv: [1212.1272](https://arxiv.org/abs/1212.1272) (cit. on pp. 89, 92).
- [195] ATLAS Collaboration. *Search for supersymmetry in events with four or more leptons in  $\sqrt{s} = 13$  TeV pp collisions using 13.3 fb<sup>1</sup> of ATLAS data*. ATLAS-CONF-2016-075. Geneva, 2016. URL: <http://cds.cern.ch/record/2206245> (cit. on pp. 89, 92).
- [196] ATLAS Collaboration. *Search for massive supersymmetric particles in multi-jet final states produced in pp collisions at  $\sqrt{s} = 13$  TeV using the ATLAS detector at the LHC*. ATLAS-CONF-2016-057. Geneva, 2016. URL: <http://cds.cern.ch/record/2206149> (cit. on pp. 89, 92).
- [197] ATLAS Collaboration. *Search for new physics in a lepton plus high jet multiplicity final state with the ATLAS experiment using  $\sqrt{s} = 13$  TeV proton-proton collision data*. Geneva, 2016. URL: <https://cds.cern.ch/record/2211457> (cit. on pp. 89, 92, 124).

- [198] ATLAS Collaboration. “A search for top squarks with R-parity-violating decays to all-hadronic final states with the ATLAS detector in  $\sqrt{s} = 8$  TeV proton-proton collisions”. In: (2016). arXiv: [1601.07453 \[hep-ex\]](#) (cit. on pp. 89, 92, 119).
- [199] ATLAS Collaboration. *A search for R-parity violating decays of the top squark in four jet final states with the ATLAS detector at  $\sqrt{s} = 13$  TeV*. ATLAS-CONF-2016-022. Geneva, 2016. URL: <http://cds.cern.ch/record/2152392> (cit. on pp. 89, 92, 119, 121).
- [200] ATLAS Collaboration. “Search for top squarks in *R*-parity-violating supersymmetry using three or more leptons and *b*-tagged jets”. In: *Phys. Rev. Lett.* 111.22 (2013), p. 221801. DOI: [10.1103/PhysRevLett.111.221801](#). arXiv: [1306.6643 \[hep-ex\]](#) (cit. on pp. 89, 92).
- [201] CMS Collaboration. “Search for new physics in events with same-sign dileptons and jets in pp collisions at  $\sqrt{s} = 8$  TeV”. In: *JHEP* 01 (2014). [Erratum: *JHEP*01,014(2015)], p. 163. DOI: [10.1007/JHEP01\(2015\)014](#), [10.1007/JHEP01\(2014\)163](#). arXiv: [1311.6736](#) (cit. on pp. 89, 92).
- [202] CMS Collaboration. “Search for RPV supersymmetry with three or more leptons and *b*-tags”. In: (2012). CMS-PAS-SUS-12-027 (cit. on pp. 89, 92).
- [203] CMS Collaboration. “Searches for light- and heavy-flavour three-jet resonances in pp collisions at  $\sqrt{s} = 8$  TeV”. In: *Phys. Lett. B* 730 (2014), pp. 193–214. DOI: [10.1016/j.physletb.2014.01.049](#). arXiv: [1311.1799 \[hep-ex\]](#) (cit. on pp. 89, 92).
- [204] CMS Collaboration. “Search for RPV SUSY in the four-lepton final state”. In: (2013). CMS-PAS-SUS-13-010 (cit. on pp. 89, 92).
- [205] CMS Collaboration. “Searches for R-parity-violating supersymmetry in pp collisions at  $\sqrt{s}=8$  TeV in final states with 0-4 leptons”. In: *Submitted to: Phys. Rev. D* (2016). arXiv: [1606.08076 \[hep-ex\]](#) (cit. on pp. 89, 92, 123, 124).
- [206] CMS Collaboration. *Search for R-parity-violating SUSY in final states with zero or one lepton and large multiplicity of jets and b-tagged jets*. CMS-PAS-SUS-16-013. Geneva, 2016. URL: <https://cds.cern.ch/record/2205147> (cit. on pp. 89, 92).
- [207] CMS Collaboration. *Search for R-parity violating supersymmetry with displaced vertices*. CMS-PAS-SUS-14-020. Geneva, 2016. URL: <https://cds.cern.ch/record/2160356> (cit. on pp. 89, 92).
- [208] CMS Collaboration. “Search for pair-produced resonances decaying to jet pairs in proton–proton collisions at  $\sqrt{s}=8$  TeV”. In: *Phys. Lett. B* 747 (2015), pp. 98–119. DOI: [10.1016/j.physletb.2015.04.045](#). arXiv: [1412.7706 \[hep-ex\]](#) (cit. on pp. 89, 92, 119, 121).

- [209] R. Barbier et al. “R-parity violating supersymmetry”. In: *Phys. Rept.* 420 (2005), pp. 1–202. DOI: [10.1016/j.physrep.2005.08.006](https://doi.org/10.1016/j.physrep.2005.08.006). arXiv: [hep-ph/0406039](https://arxiv.org/abs/hep-ph/0406039) [hep-ph] (cit. on pp. 89, 90, 98, 99).
- [210] J. A. Evans. “A Swarm of Bs”. In: *JHEP* 1408 (2014), p. 073. DOI: [10.1007/JHEP08\(2014\)073](https://doi.org/10.1007/JHEP08(2014)073). arXiv: [1402.4481](https://arxiv.org/abs/1402.4481) [hep-ph] (cit. on pp. 89, 92, 93, 95, 97, 123).
- [211] Z. Liu and B. Tweedie. “The Fate of Long-Lived Superparticles with Hadronic Decays after LHC Run 1”. In: *JHEP* 06 (2015), p. 042. DOI: [10.1007/JHEP06\(2015\)042](https://doi.org/10.1007/JHEP06(2015)042). arXiv: [1503.05923](https://arxiv.org/abs/1503.05923) [hep-ph] (cit. on pp. 89, 101).
- [212] C. Csaki, E. Kuflik, S. Lombardo, et al. “Phenomenology of a Long-Lived LSP with R-Parity Violation”. In: *JHEP* 08 (2015), p. 016. DOI: [10.1007/JHEP08\(2015\)016](https://doi.org/10.1007/JHEP08(2015)016). arXiv: [1505.00784](https://arxiv.org/abs/1505.00784) [hep-ph] (cit. on pp. 89, 101).
- [213] A. Monteux. “New signatures and limits on R-parity violation from resonant squark production”. In: *JHEP* 03 (2016), p. 216. DOI: [10.1007/JHEP03\(2016\)216](https://doi.org/10.1007/JHEP03(2016)216). arXiv: [1601.03737](https://arxiv.org/abs/1601.03737) [hep-ph] (cit. on pp. 89, 96, 101).
- [214] G. D’Ambrosio, G. F. Giudice, G. Isidori, et al. “Minimal flavor violation: An Effective field theory approach”. In: *Nucl. Phys.* B645 (2002), pp. 155–187. DOI: [10.1016/S0550-3213\(02\)00836-2](https://doi.org/10.1016/S0550-3213(02)00836-2). arXiv: [hep-ph/0207036](https://arxiv.org/abs/hep-ph/0207036) [hep-ph] (cit. on p. 92).
- [215] CMS Collaboration. *Search for direct top squark pair production in the fully hadronic final state in proton-proton collisions at  $\sqrt{s} = 13$  TeV corresponding to an integrated luminosity of 12.9/fb*. CMS-PAS-SUS-16-029. Geneva, 2016. URL: <https://cds.cern.ch/record/2205176> (cit. on p. 92).
- [216] CMS Collaboration. *Search for direct top squark pair production in the single lepton final state at  $\sqrt{s} = 13$  TeV*. CMS-PAS-SUS-16-028. Geneva, 2016. URL: <https://cds.cern.ch/record/2205271> (cit. on p. 92).
- [217] ATLAS Collaboration. *Search for top squarks in final states with one isolated lepton, jets, and missing transverse momentum in  $\sqrt{s} = 13$  TeV pp collisions with the ATLAS detector*. ATLAS-CONF-2016-050. Geneva, 2016. URL: <https://cds.cern.ch/record/2206132> (cit. on p. 92).
- [218] ATLAS Collaboration. *Search for the Supersymmetric Partner of the Top Quark in the Jets+Emiss Final State at  $\sqrt{s} = 13$  TeV*. ATLAS-CONF-2016-077. Geneva, 2016. URL: <https://cds.cern.ch/record/2206250> (cit. on p. 92).
- [219] E. Nikolidakis and C. Smith. “Minimal Flavor Violation, Seesaw, and R-parity”. In: *Phys. Rev. D* 77 (2008), p. 015021. DOI: [10.1103/PhysRevD.77.015021](https://doi.org/10.1103/PhysRevD.77.015021). arXiv: [0710.3129](https://arxiv.org/abs/0710.3129) [hep-ph] (cit. on p. 94).

- [220] C. Csaki, Y. Grossman, and B. Heidenreich. “MFV SUSY: A Natural Theory for R-Parity Violation”. In: *Phys. Rev. D* 85 (2012), p. 095009. DOI: [10.1103/PhysRevD.85.095009](https://doi.org/10.1103/PhysRevD.85.095009). arXiv: [1111.1239](https://arxiv.org/abs/1111.1239) [hep-ph] (cit. on p. 94).
- [221] Y. Mambrini and G. Moultaka. “Infrared quasifixed point structure in extended Yukawa sectors and application to R parity violation”. In: *Phys. Rev. D* 65 (2002), p. 115011. DOI: [10.1103/PhysRevD.65.115011](https://doi.org/10.1103/PhysRevD.65.115011). arXiv: [hep-ph/0112353](https://arxiv.org/abs/hep-ph/0112353) [hep-ph] (cit. on p. 94).
- [222] Y. Mambrini and G. Moultaka. “Comment on ‘Infrared fixed point structure in minimal supersymmetric standard model with baryon and lepton number violation’”. In: *Phys. Rev. D* 65 (2002), p. 058901. DOI: [10.1103/PhysRevD.65.058901](https://doi.org/10.1103/PhysRevD.65.058901). arXiv: [hep-ph/0103270](https://arxiv.org/abs/hep-ph/0103270) [hep-ph] (cit. on p. 94).
- [223] N. Chamoun, H. K. Dreiner, F. Staub, et al. “Resurrecting light stops after the 125 GeV Higgs in the baryon number violating CMSSM”. In: *JHEP* 08 (2014), p. 142. DOI: [10.1007/JHEP08\(2014\)142](https://doi.org/10.1007/JHEP08(2014)142). arXiv: [1407.2248](https://arxiv.org/abs/1407.2248) [hep-ph] (cit. on pp. 94, 99, 107).
- [224] M. Papucci, J. T. Ruderman, and A. Weiler. “Natural SUSY Endures”. In: *JHEP* 09 (2012), p. 035. DOI: [10.1007/JHEP09\(2012\)035](https://doi.org/10.1007/JHEP09(2012)035). arXiv: [1110.6926](https://arxiv.org/abs/1110.6926) [hep-ph] (cit. on p. 95).
- [225] S. Lola, P. Osland, and A. R. Raklev. “Radiative gravitino decays from R-parity violation”. In: *Phys. Lett. B* 656 (2007), pp. 83–90. DOI: [10.1016/j.physletb.2007.09.048](https://doi.org/10.1016/j.physletb.2007.09.048). arXiv: [0707.2510](https://arxiv.org/abs/0707.2510) [hep-ph] (cit. on p. 95).
- [226] F. Takayama and M. Yamaguchi. “Gravitino dark matter without R-parity”. In: *Phys. Lett. B* 485 (2000), pp. 388–392. DOI: [10.1016/S0370-2693\(00\)00726-7](https://doi.org/10.1016/S0370-2693(00)00726-7). arXiv: [hep-ph/0005214](https://arxiv.org/abs/hep-ph/0005214) [hep-ph] (cit. on p. 95).
- [227] G. Moreau and M. Chemtob. “R-parity violation and the cosmological gravitino problem”. In: *Phys. Rev. D* 65 (2002), p. 024033. DOI: [10.1103/PhysRevD.65.024033](https://doi.org/10.1103/PhysRevD.65.024033). arXiv: [hep-ph/0107286](https://arxiv.org/abs/hep-ph/0107286) [hep-ph] (cit. on p. 95).
- [228] W. Beenakker, M. Kramer, T. Plehn, et al. “Stop production at hadron colliders”. In: *Nucl. Phys. B* 515 (1998), pp. 3–14. DOI: [10.1016/S0550-3213\(98\)00014-5](https://doi.org/10.1016/S0550-3213(98)00014-5). arXiv: [hep-ph/9710451](https://arxiv.org/abs/hep-ph/9710451) [hep-ph] (cit. on p. 96).
- [229] W. Beenakker, S. Brensing, M. Kramer, et al. “Supersymmetric top and bottom squark production at hadron colliders”. In: *JHEP* 08 (2010), p. 098. DOI: [10.1007/JHEP08\(2010\)098](https://doi.org/10.1007/JHEP08(2010)098). arXiv: [1006.4771](https://arxiv.org/abs/1006.4771) [hep-ph] (cit. on p. 96).
- [230] W. Beenakker, S. Brensing, M. n Kramer, et al. “Squark and Gluino Hadroproduction”. In: *Int. J. Mod. Phys. A* 26 (2011), pp. 2637–2664. DOI: [10.1142/S0217751X11053560](https://doi.org/10.1142/S0217751X11053560). arXiv: [1105.1110](https://arxiv.org/abs/1105.1110) [hep-ph] (cit. on p. 96).



- [231] G. Durieux and C. Smith. “The same-sign top signature of R-parity violation”. In: *JHEP* 10 (2013), p. 068. DOI: [10.1007/JHEP10\(2013\)068](https://doi.org/10.1007/JHEP10(2013)068). arXiv: [1307.1355](https://arxiv.org/abs/1307.1355) [hep-ph] (cit. on p. 96).
- [232] ATLAS Collaboration. “Search for new phenomena in final states with an energetic jet and large missing transverse momentum in pp collisions at  $\sqrt{s}=8$  TeV with the ATLAS detector”. In: *Eur. Phys. J. C* 75.7 (2015). [Erratum: *Eur. Phys. J. C* 75, no. 9, 408 (2015)], p. 299. DOI: [10.1140/epjc/s10052-015-3517-3](https://doi.org/10.1140/epjc/s10052-015-3517-3), [10.1140/epjc/s10052-015-3639-7](https://doi.org/10.1140/epjc/s10052-015-3639-7). arXiv: [1502.01518](https://arxiv.org/abs/1502.01518) [hep-ex] (cit. on p. 100).
- [233] K. Choi, K Hwang, and J. S. Lee. “Constraints on R-parity and B violating couplings in gauge mediated supersymmetry breaking models”. In: *Phys. Lett. B* 428 (1998), pp. 129–135. DOI: [10.1016/S0370-2693\(98\)00371-2](https://doi.org/10.1016/S0370-2693(98)00371-2). arXiv: [hep-ph/9802323](https://arxiv.org/abs/hep-ph/9802323) [hep-ph] (cit. on p. 100).
- [234] ATLAS Collaboration. “Search for massive, long-lived particles using multitrack displaced vertices or displaced lepton pairs in pp collisions at  $\sqrt{s} = 8$  TeV with the ATLAS detector”. In: *Phys. Rev. D* 92.7 (2015), p. 072004. DOI: [10.1103/PhysRevD.92.072004](https://doi.org/10.1103/PhysRevD.92.072004). arXiv: [1504.05162](https://arxiv.org/abs/1504.05162) [hep-ex] (cit. on p. 101).
- [235] V. Khachatryan et al. “Search for Long-Lived Neutral Particles Decaying to Quark-Antiquark Pairs in Proton-Proton Collisions at  $\sqrt{s} = 8$  TeV”. In: *Phys. Rev. D* 91.1 (2015), p. 012007. DOI: [10.1103/PhysRevD.91.012007](https://doi.org/10.1103/PhysRevD.91.012007). arXiv: [1411.6530](https://arxiv.org/abs/1411.6530) [hep-ex] (cit. on p. 101).
- [236] B. De Wit and J. Smith. *Field Theory in Particle Physics Volume 1*. Amsterdam, Netherlands: North-Holland, 1986 (cit. on p. 101).
- [237] D. Berdine, N. Kauer, and D. Rainwater. “Breakdown of the Narrow Width Approximation for New Physics”. In: *Phys. Rev. Lett.* 99 (2007), p. 111601. DOI: [10.1103/PhysRevLett.99.111601](https://doi.org/10.1103/PhysRevLett.99.111601). arXiv: [hep-ph/0703058](https://arxiv.org/abs/hep-ph/0703058) [hep-ph] (cit. on pp. 101, 118).
- [238] N. Kauer. “Narrow-width approximation limitations”. In: *Phys. Lett. B* 649 (2007), pp. 413–416. DOI: [10.1016/j.physletb.2007.04.036](https://doi.org/10.1016/j.physletb.2007.04.036). arXiv: [hep-ph/0703077](https://arxiv.org/abs/hep-ph/0703077) [hep-ph] (cit. on pp. 101, 118).
- [239] N. Kauer. “A Threshold-improved narrow-width approximation for BSM physics”. In: *JHEP* 04 (2008), p. 055. DOI: [10.1088/1126-6708/2008/04/055](https://doi.org/10.1088/1126-6708/2008/04/055). arXiv: [0708.1161](https://arxiv.org/abs/0708.1161) [hep-ph] (cit. on pp. 101, 118).
- [240] C. F. Uhlemann and N. Kauer. “Narrow-width approximation accuracy”. In: *Nucl. Phys. B* 814 (2009), pp. 195–211. DOI: [10.1016/j.nuclphysb.2009.01.022](https://doi.org/10.1016/j.nuclphysb.2009.01.022). arXiv: [0807.4112](https://arxiv.org/abs/0807.4112) [hep-ph] (cit. on pp. 101, 118).

- [241] F. Staub, T. Ohl, W. Porod, et al. “A Tool Box for Implementing Supersymmetric Models”. In: *Comput. Phys. Commun.* 183 (2012), pp. 2165–2206. DOI: [10.1016/j.cpc.2012.04.013](https://doi.org/10.1016/j.cpc.2012.04.013). arXiv: [1109.5147](https://arxiv.org/abs/1109.5147) [hep-ph] (cit. on p. 106).
- [242] F. Staub. “SARAH 4 : A tool for (not only SUSY) model builders”. In: *Comput. Phys. Commun.* 185 (2014), pp. 1773–1790. DOI: [10.1016/j.cpc.2014.02.018](https://doi.org/10.1016/j.cpc.2014.02.018). arXiv: [1309.7223](https://arxiv.org/abs/1309.7223) [hep-ph] (cit. on p. 106).
- [243] Wolfram Research. *Mathematica 11.0*. Champaign, Illinois, 2010 (cit. on p. 106).
- [244] W. Porod and F. Staub. “SPHeno 3.1: Extensions including flavour, CP-phases and models beyond the MSSM”. In: *Comput. Phys. Commun.* 183 (2012), pp. 2458–2469. DOI: [10.1016/j.cpc.2012.05.021](https://doi.org/10.1016/j.cpc.2012.05.021). arXiv: [1104.1573](https://arxiv.org/abs/1104.1573) [hep-ph] (cit. on pp. 106, 108, 109).
- [245] P. Bechtle, O. Brein, S. Heinemeyer, et al. “HiggsBounds: Confronting Arbitrary Higgs Sectors with Exclusion Bounds from LEP and the Tevatron”. In: *Comput. Phys. Commun.* 181 (2010), pp. 138–167. DOI: [10.1016/j.cpc.2009.09.003](https://doi.org/10.1016/j.cpc.2009.09.003). arXiv: [0811.4169](https://arxiv.org/abs/0811.4169) [hep-ph] (cit. on p. 107).
- [246] P. Bechtle, O. Brein, S. Heinemeyer, et al. “Recent Developments in Higgs-Bounds and a Preview of HiggsSignals”. In: *PoS CHARGED2012* (2012), p. 024. arXiv: [1301.2345](https://arxiv.org/abs/1301.2345) [hep-ph] (cit. on p. 107).
- [247] P. Bechtle, S. Heinemeyer, O. Stål, et al. “*HiggsSignals*: Confronting arbitrary Higgs sectors with measurements at the Tevatron and the LHC”. In: *Eur. Phys. J. C* 74.2 (2014), p. 2711. DOI: [10.1140/epjc/s10052-013-2711-4](https://doi.org/10.1140/epjc/s10052-013-2711-4). arXiv: [1305.1933](https://arxiv.org/abs/1305.1933) [hep-ph] (cit. on p. 107).
- [248] LHCb Collaboration. “First Evidence for the Decay  $B_s^0 \rightarrow \mu^+ \mu^-$ ”. In: *Phys. Rev. Lett.* 110.2 (2013), p. 021801. DOI: [10.1103/PhysRevLett.110.021801](https://doi.org/10.1103/PhysRevLett.110.021801). arXiv: [1211.2674](https://arxiv.org/abs/1211.2674) [hep-ex] (cit. on pp. 107, 111).
- [249] LHCb Collaboration. “Measurement of the  $B_s^0 \rightarrow \mu^+ \mu^-$  branching fraction and search for  $B^0 \rightarrow \mu^+ \mu^-$  decays at the LHCb experiment”. In: *Phys. Rev. Lett.* 111 (2013), p. 101805. DOI: [10.1103/PhysRevLett.111.101805](https://doi.org/10.1103/PhysRevLett.111.101805). arXiv: [1307.5024](https://arxiv.org/abs/1307.5024) [hep-ex] (cit. on pp. 107, 111).
- [250] CMS Collaboration. “Measurement of the B(s) to  $\mu^+ \mu^-$  branching fraction and search for  $B^0$  to  $\mu^+ \mu^-$  with the CMS Experiment”. In: *Phys. Rev. Lett.* 111 (2013), p. 101804. DOI: [10.1103/PhysRevLett.111.101804](https://doi.org/10.1103/PhysRevLett.111.101804). arXiv: [1307.5025](https://arxiv.org/abs/1307.5025) [hep-ex] (cit. on pp. 107, 111).
- [251] H. K. Dreiner, K. Nickel, and F. Staub. “On the two-loop corrections to the Higgs mass in trilinear R-parity violation”. In: *Phys. Lett. B* 742 (2015), pp. 261–265. DOI: [10.1016/j.physletb.2015.01.047](https://doi.org/10.1016/j.physletb.2015.01.047). arXiv: [1411.3731](https://arxiv.org/abs/1411.3731) [hep-ph] (cit. on p. 107).



- [252] J. P. Miller, E. de Rafael, B. L. Roberts, et al. “Muon (g-2): Experiment and Theory”. In: *Ann. Rev. Nucl. Part. Sci.* 62 (2012), pp. 237–264. DOI: [10.1146/annurev-nucl-031312-120340](https://doi.org/10.1146/annurev-nucl-031312-120340) (cit. on p. 108).
- [253] T. Ibrahim and P. Nath. “CP violation and the muon anomaly in N=1 supergravity”. In: *Phys. Rev. D* 61 (2000), p. 095008. DOI: [10.1103/PhysRevD.61.095008](https://doi.org/10.1103/PhysRevD.61.095008). arXiv: [hep-ph/9907555](https://arxiv.org/abs/hep-ph/9907555) [hep-ph] (cit. on p. 108).
- [254] D. Stockinger. “The Muon Magnetic Moment and Supersymmetry”. In: *J. Phys. G* 34 (2007), R45–R92. DOI: [10.1088/0954-3899/34/2/R01](https://doi.org/10.1088/0954-3899/34/2/R01). arXiv: [hep-ph/0609168](https://arxiv.org/abs/hep-ph/0609168) [hep-ph] (cit. on p. 108).
- [255] G.-C. Cho and K. Hagiwara. “Supersymmetry versus precision experiments revisited”. In: *Nucl. Phys. B* 574 (2000), pp. 623–674. DOI: [10.1016/S0550-3213\(00\)00027-4](https://doi.org/10.1016/S0550-3213(00)00027-4). arXiv: [hep-ph/9912260](https://arxiv.org/abs/hep-ph/9912260) [hep-ph] (cit. on p. 109).
- [256] S. Bertolini, F. Borzumati, A. Masiero, et al. “Effects of supergravity induced electroweak breaking on rare  $B$  decays and mixings”. In: *Nucl. Phys. B* 353 (1991), pp. 591–649. DOI: [10.1016/0550-3213\(91\)90320-W](https://doi.org/10.1016/0550-3213(91)90320-W) (cit. on p. 110).
- [257] M. Misiak et al. “Updated NNLO QCD predictions for the weak radiative  $B$ -meson decays”. In: *Phys. Rev. Lett.* 114.22 (2015), p. 221801. DOI: [10.1103/PhysRevLett.114.221801](https://doi.org/10.1103/PhysRevLett.114.221801). arXiv: [1503.01789](https://arxiv.org/abs/1503.01789) [hep-ph] (cit. on p. 111).
- [258] HFAG Collaboration. “Averages of  $b$ -hadron,  $c$ -hadron, and  $\tau$ -lepton properties as of summer 2014”. In: (2014). arXiv: [1412.7515](https://arxiv.org/abs/1412.7515) [hep-ex] (cit. on p. 111).
- [259] H. K. Dreiner, K. Nickel, and F. Staub. “ $B_{s,d}^0$  and  $BX_s$  in the R-parity violating MSSM”. In: *Phys. Rev. D* 88.11 (2013), p. 115001. DOI: [10.1103/PhysRevD.88.115001](https://doi.org/10.1103/PhysRevD.88.115001). arXiv: [1309.1735](https://arxiv.org/abs/1309.1735) [hep-ph] (cit. on p. 111).
- [260] CMS and LHCb Collaborations. “Observation of the rare  $B_s^0 \rightarrow \mu^+ \mu^-$  decay from the combined analysis of CMS and LHCb data”. In: *Nature* 522 (2015), pp. 68–72. DOI: [10.1038/nature14474](https://doi.org/10.1038/nature14474). arXiv: [1411.4413](https://arxiv.org/abs/1411.4413) [hep-ex] (cit. on p. 111).
- [261] C. Bobeth, M. Gorbahn, T. Hermann, et al. “ $B_{s,d} \rightarrow l^+ l^-$  in the Standard Model with Reduced Theoretical Uncertainty”. In: *Phys. Rev. Lett.* 112 (2014), p. 101801. DOI: [10.1103/PhysRevLett.112.101801](https://doi.org/10.1103/PhysRevLett.112.101801). arXiv: [1311.0903](https://arxiv.org/abs/1311.0903) [hep-ph] (cit. on p. 111).
- [262] C. Borschensky, M. Krämer, A. Kulesza, et al. “Squark and gluino production cross sections in pp collisions at  $\sqrt{s} = 13, 14, 33$  and 100 TeV”. In: *Eur. Phys. J. C* 74.12 (2014), p. 3174. DOI: [10.1140/epjc/s10052-014-3174-y](https://doi.org/10.1140/epjc/s10052-014-3174-y). arXiv: [1407.5066](https://arxiv.org/abs/1407.5066) [hep-ph] (cit. on pp. 113, 114).

- [263] G. L. Kane and J. P. Leveille. “Experimental Constraints on Gluino Masses and Supersymmetric Theories”. In: *Phys. Lett. B* 112 (1982), pp. 227–232. DOI: [10.1016/0370-2693\(82\)90968-6](https://doi.org/10.1016/0370-2693(82)90968-6) (cit. on p. 113).
- [264] P. R. Harrison and C. H. Llewellyn Smith. “Hadroproduction of Supersymmetric Particles”. In: *Nucl. Phys. B* 213 (1983). [Erratum: *Nucl. Phys. B* 223, 542 (1983)], p. 223. DOI: [10.1016/0550-3213\(83\)90510-2](https://doi.org/10.1016/0550-3213(83)90510-2), [10.1016/0550-3213\(83\)90070-6](https://doi.org/10.1016/0550-3213(83)90070-6) (cit. on p. 113).
- [265] S. Dawson, E. Eichten, and C. Quigg. “Search for Supersymmetric Particles in Hadron - Hadron Collisions”. In: *Phys. Rev. D* 31 (1985), p. 1581. DOI: [10.1103/PhysRevD.31.1581](https://doi.org/10.1103/PhysRevD.31.1581) (cit. on p. 113).
- [266] M. Bonvini, S. Marzani, J. Rojo, et al. “Parton distributions with threshold resummation”. In: *JHEP* 09 (2015), p. 191. DOI: [10.1007/JHEP09\(2015\)191](https://doi.org/10.1007/JHEP09(2015)191). arXiv: [1507.01006 \[hep-ph\]](https://arxiv.org/abs/1507.01006) (cit. on p. 113).
- [267] J. Rojo. “Progress in the NNPDF global analysis and the impact of the legacy HERA combination”. In: *PoS EPS-HEP2015* (2015), p. 506. arXiv: [1508.07731 \[hep-ph\]](https://arxiv.org/abs/1508.07731) (cit. on p. 116).
- [268] J. Pumplin, D. R. Stump, J. Huston, et al. “New generation of parton distributions with uncertainties from global QCD analysis”. In: *JHEP* 07 (2002), p. 012. DOI: [10.1088/1126-6708/2002/07/012](https://doi.org/10.1088/1126-6708/2002/07/012). arXiv: [hep-ph/0201195 \[hep-ph\]](https://arxiv.org/abs/hep-ph/0201195) (cit. on p. 116).
- [269] A. Heister et al. “Search for supersymmetric particles with R parity violating decays in  $e^+e^-$  collisions at  $\sqrt{s}$  up to 209-GeV”. In: *Eur. Phys. J. C* 31 (2003), pp. 1–16. DOI: [10.1140/epjc/s2003-01311-5](https://doi.org/10.1140/epjc/s2003-01311-5). arXiv: [hep-ex/0210014 \[hep-ex\]](https://arxiv.org/abs/hep-ex/0210014) (cit. on p. 121).
- [270] ATLAS Collaboration. “Search for Pair Production of Strongly Interacting Particles Decaying to Pairs of Jets in  $p\bar{p}$  Collisions at  $\sqrt{s} = 1.96\text{TeV}$ ”. In: *Phys. Rev. Lett.* 111.3 (2013), p. 031802. DOI: [10.1103/PhysRevLett.111.031802](https://doi.org/10.1103/PhysRevLett.111.031802). arXiv: [1303.2699 \[hep-ex\]](https://arxiv.org/abs/1303.2699) (cit. on p. 121).
- [271] Y. Bai, A. Katz, and B. Tweedie. “Pulling Out All the Stops: Searching for RPV SUSY with Stop-Jets”. In: *JHEP* 01 (2014), p. 040. DOI: [10.1007/JHEP01\(2014\)040](https://doi.org/10.1007/JHEP01(2014)040). arXiv: [1309.6631 \[hep-ph\]](https://arxiv.org/abs/1309.6631) (cit. on p. 121).
- [272] ATLAS Collaboration. *A search for R-parity violating scalar top decays in all-hadronic final states with the ATLAS detector in  $\sqrt{s} = 8\text{ TeV}$   $pp$  collisions*. ATLAS-CONF-2015-026. 2015 (cit. on p. 121).
- [273] S. Sapeta. “QCD and Jets at Hadron Colliders”. In: *Prog. Part. Nucl. Phys.* 89 (2016), pp. 1–55. DOI: [10.1016/j.ppnp.2016.02.002](https://doi.org/10.1016/j.ppnp.2016.02.002). arXiv: [1511.09336 \[hep-ph\]](https://arxiv.org/abs/1511.09336) (cit. on p. 121).
- [274] ATLAS Collaboration. *Expected performance of the ATLAS b-tagging algorithms in Run-2*. ATL-PHYS-PUB-2015-022. Geneva, 2015. URL: <https://cds.cern.ch/record/2037697> (cit. on p. 121).

- [275] “Identification of b-quark jets with the CMS experiment”. In: *J. Instrum.* 8.arXiv:1211.4462. CMS-BTV-12-001. CERN-PH-EP-2012-262 (2012). Comments: Submitted to the Journal of Instrumentation, P04013. 67 p. URL: <https://cds.cern.ch/record/1494669> (cit. on p. 121).
- [276] ATLAS Collaboration. “Identification of high transverse momentum top quarks in  $pp$  collisions at  $\sqrt{s} = 8$  TeV with the ATLAS detector”. In: (2015) (cit. on p. 122).
- [277] K. Hamaguchi, S. P. Liew, and M. Stoll. “How to decontaminate overlapping fat jets”. In: *Phys. Rev. D* 92.1 (2015), p. 015012. DOI: [10.1103/PhysRevD.92.015012](https://doi.org/10.1103/PhysRevD.92.015012). arXiv: [1505.02930 \[hep-ph\]](https://arxiv.org/abs/1505.02930) (cit. on p. 122).
- [278] ATLAS Collaboration. “Search for strong gravity in multijet final states produced in  $pp$  collisions at  $\sqrt{s} = 13$  TeV using the ATLAS detector at the LHC”. In: *JHEP* 03 (2016), p. 026. DOI: [10.1007/JHEP03\(2016\)026](https://doi.org/10.1007/JHEP03(2016)026). arXiv: [1512.02586 \[hep-ex\]](https://arxiv.org/abs/1512.02586) (cit. on p. 122).
- [279] G. Bevilacqua, M. Czakon, C. G. Papadopoulos, et al. “Assault on the NLO Wishlist:  $pp \rightarrow t \text{ anti-}t b \text{ anti-}b$ ”. In: *JHEP* 09 (2009), p. 109. DOI: [10.1088/1126-6708/2009/09/109](https://doi.org/10.1088/1126-6708/2009/09/109). arXiv: [0907.4723 \[hep-ph\]](https://arxiv.org/abs/0907.4723) (cit. on p. 122).
- [280] F. Maltoni, D. Pagani, and I. Tsinikos. “Associated production of a top-quark pair with vector bosons at NLO in QCD: impact on  $t\bar{t}H$  searches at the LHC”. In: (2015). arXiv: [1507.05640 \[hep-ph\]](https://arxiv.org/abs/1507.05640) (cit. on p. 122).
- [281] J. M. Campbell and R. K. Ellis. “ $t\bar{t}W^{+-}$  production and decay at NLO”. In: *JHEP* 07 (2012), p. 052. DOI: [10.1007/JHEP07\(2012\)052](https://doi.org/10.1007/JHEP07(2012)052). arXiv: [1204.5678 \[hep-ph\]](https://arxiv.org/abs/1204.5678) (cit. on p. 122).
- [282] A. Kulesza, L. Motyka, T. Stebel, et al. “Soft gluon resummation for associated  $t\bar{t}H$  production at the LHC”. In: (2015). arXiv: [1509.02780 \[hep-ph\]](https://arxiv.org/abs/1509.02780) (cit. on p. 122).
- [283] A. Buckley, J. Ferrando, S. Lloyd, et al. “LHAPDF6: parton density access in the LHC precision era”. In: *Eur. Phys. J. C* 75 (2015), p. 132. DOI: [10.1140/epjc/s10052-015-3318-8](https://doi.org/10.1140/epjc/s10052-015-3318-8). arXiv: [1412.7420 \[hep-ph\]](https://arxiv.org/abs/1412.7420) (cit. on p. 123).
- [284] ATLAS Collaboration. *Measurement of the Higgs boson coupling properties in the  $H \rightarrow ZZ^* \rightarrow 4\ell$  decay channel at  $\sqrt{s} = 13$  TeV with the ATLAS detector*. Tech. rep. ATLAS-CONF-2017-043. Geneva: CERN, 2017. URL: <https://cds.cern.ch/record/2273849> (cit. on p. 126).
- [285] ATLAS Collaboration. *Measurements of Higgs boson properties in the diphoton decay channel with  $36.1 \text{ fb}^{-1}$   $pp$  collision data at the center-of-mass energy of 13 TeV with the ATLAS detector*. Tech. rep. ATLAS-CONF-2017-045. Geneva: CERN, 2017. URL: <http://cds.cern.ch/record/2273852> (cit. on p. 126).

- [286] ATLAS Collaboration. *Combined measurements of Higgs boson production and decay in the  $H \rightarrow ZZ \rightarrow 4\ell$  and  $H \rightarrow \gamma\gamma$  channels using  $\sqrt{s} = 13$  TeV pp collision data collected with the ATLAS experiment*. Tech. rep. ATLAS-CONF-2017-047. Geneva: CERN, 2017. URL: <http://cds.cern.ch/record/2273854> (cit. on p. 126).
- [287] CMS Collaboration. “Observation of the SM scalar boson decaying to a pair of  $\tau$  leptons with the CMS experiment at the LHC”. In: (2017) (cit. on p. 126).
- [288] CMS Collaboration. “Measurements of properties of the Higgs boson in the diphoton decay channel with the full 2016 data set”. In: (2017) (cit. on p. 126).
- [289] CMS Collaboration. “Measurement of differential fiducial cross sections for Higgs boson production in the diphoton decay channel in pp collisions at  $\sqrt{s} = 13$  TeV”. In: (2017) (cit. on p. 126).
- [290] CMS Collaboration. “Measurements of properties of the Higgs boson decaying into four leptons in pp collisions at  $\sqrt{s} = 13$  TeV”. In: (2017) (cit. on p. 126).
- [291] G. F. Giudice. “Naturally Speaking: The Naturalness Criterion and Physics at the LHC”. In: (2008). DOI: [10.1142/9789812779762\\_0010](https://doi.org/10.1142/9789812779762_0010). arXiv: [0801.2562](https://arxiv.org/abs/0801.2562) [hep-ph] (cit. on p. 126).
- [292] D. de Florian et al. “Handbook of LHC Higgs Cross Sections: 4. Deciphering the Nature of the Higgs Sector”. In: (2016). DOI: [10.23731/CYRM-2017-002](https://doi.org/10.23731/CYRM-2017-002). arXiv: [1610.07922](https://arxiv.org/abs/1610.07922) [hep-ph] (cit. on p. 127).
- [293] S. Di Vita, C. Grojean, G. Panico, et al. “A global view on the Higgs self-coupling”. In: *JHEP* 09 (2017), p. 069. DOI: [10.1007/JHEP09\(2017\)069](https://doi.org/10.1007/JHEP09(2017)069). arXiv: [1704.01953](https://arxiv.org/abs/1704.01953) [hep-ph] (cit. on p. 128).
- [294] F. Bezrukov and M. Shaposhnikov. “Why should we care about the top quark Yukawa coupling?” In: *J. Exp. Theor. Phys.* 120 (2015). [*Zh. Eksp. Teor. Fiz.* 147,389(2015)], pp. 335–343. DOI: [10.1134/S1063776115030152](https://doi.org/10.1134/S1063776115030152). arXiv: [1411.1923](https://arxiv.org/abs/1411.1923) [hep-ph] (cit. on p. 128).
- [295] ATLAS collaboration. “Search for the Standard Model Higgs boson produced in association with top quarks and decaying into a  $b\bar{b}$  in  $p-p$  collisions at  $\sqrt{s} = 13$  TeV with the ATLAS detector”. In: (2017) (cit. on p. 129).
- [296] CMS collaboration. *Search for  $t\bar{t}H$  production in the  $H \rightarrow b\bar{b}$  decay channel with 2016 pp collision data at  $\sqrt{s} = 13$  TeV*. Tech. rep. CMS-PAS-HIG-16-038. Geneva: CERN, 2016. URL: <https://cds.cern.ch/record/2231510> (cit. on p. 129).

- [297] ATLAS collaboration. “Evidence for the associated production of the Higgs boson and a top quark pair with the ATLAS detector”. In: (2017) (cit. on p. 129).
- [298] CMS Collaboration. “Search for Higgs boson production in association with top quarks in multilepton final states at  $\sqrt{s} = 13$  TeV”. In: (2017) (cit. on p. 129).
- [299] CMS Collaboration. “Search for the associated production of a Higgs boson with a top quark pair in final states with a  $\tau$  lepton at  $\sqrt{s} = 13$  TeV”. In: (2017) (cit. on p. 129).
- [300] ATLAS collaboration. “Measurements of Higgs boson properties in the diphoton decay channel with 36.1 fb<sup>1</sup>  $pp$  collision data at the center-of-mass energy of 13 TeV with the ATLAS detector”. In: (2017) (cit. on p. 129).
- [301] CMS Collaboration. *Measurements of properties of the Higgs boson in the diphoton decay channel with the full 2016 data set*. Tech. rep. CMS-PAS-HIG-16-040. Geneva: CERN, 2017. URL: <https://cds.cern.ch/record/2264515> (cit. on p. 129).
- [302] M. Shochet, L. Tompkins, V. Cavaliere, et al. *Fast TrackKer (FTK) Technical Design Report*. Tech. rep. CERN-LHCC-2013-007. ATLAS-TDR-021. ATLAS Fast Tracker Technical Design Report. 2013. URL: <https://cds.cern.ch/record/1552953> (cit. on p. 129).
- [303] R. Gupta and J. Alison. *b-tagging efficiency for b-jet triggers*. Tech. rep. ATL-COM-DAQ-2017-062. Geneva: CERN, 2017. URL: <https://cds.cern.ch/record/2271945> (cit. on p. 130).
- [304] J. Berger, J. Hubisz, and M. Perelstein. “A Fermionic Top Partner: Naturalness and the LHC”. In: *JHEP* 07 (2012), p. 016. DOI: [10.1007/JHEP07\(2012\)016](https://doi.org/10.1007/JHEP07(2012)016). arXiv: [1205.0013](https://arxiv.org/abs/1205.0013) [hep-ph] (cit. on p. 130).
- [305] J. de Favereau, C. Delaere, P. Demin, et al. “DELPHES 3, A modular framework for fast simulation of a generic collider experiment”. In: *JHEP* 02 (2014), p. 057. DOI: [10.1007/JHEP02\(2014\)057](https://doi.org/10.1007/JHEP02(2014)057). arXiv: [1307.6346](https://arxiv.org/abs/1307.6346) [hep-ex] (cit. on p. 132).
- [306] ATLAS Collaboration. “The ATLAS Experiment at the CERN Large Hadron Collider”. In: *JINST* 3 (2008), S08003. DOI: [10.1088/1748-0221/3/08/S08003](https://doi.org/10.1088/1748-0221/3/08/S08003) (cit. on p. 164).
- [307] ATLAS Collaboration. “Performance of the ATLAS Trigger System in 2010”. In: *Eur. Phys. J. C* 72 (2012), p. 1849. DOI: [10.1140/epjc/s10052-011-1849-1](https://doi.org/10.1140/epjc/s10052-011-1849-1). arXiv: [1110.1530](https://arxiv.org/abs/1110.1530) [hep-ex] (cit. on p. 164).
- [308] M. Cacciari, G. P. Salam, and G. Soyez. “The anti- $k_t$  jet clustering algorithm”. In: *JHEP* 04 (2008), p. 063. DOI: [10.1088/1126-6708/2008/04/063](https://doi.org/10.1088/1126-6708/2008/04/063). arXiv: [0802.1189](https://arxiv.org/abs/0802.1189) [hep-ph] (cit. on p. 164).

- [309] M. Cacciari and G. P. Salam. “Dispelling the  $N^3$  myth for the  $k_t$  jet-finder”. In: *Phys. Lett. B* 641 (2006), p. 57. DOI: [10.1016/j.physletb.2006.08.037](https://doi.org/10.1016/j.physletb.2006.08.037). arXiv: [0512210](https://arxiv.org/abs/0512210) [hep-ph] (cit. on p. 164).
- [310] M. Cacciari, G. P. Salam, and G. Soyez. “FastJet User Manual”. In: *Eur. Phys. J. C* 72 (2012), p. 1896. DOI: [10.1140/epjc/s10052-012-1896-2](https://doi.org/10.1140/epjc/s10052-012-1896-2). arXiv: [1111.6097](https://arxiv.org/abs/1111.6097) [hep-ph]. URL: <http://fastjet.fr/> (cit. on p. 164).
- [311] C. Cojocaru et al. “Hadronic calibration of the ATLAS liquid argon end-cap calorimeter in the pseudorapidity region  $1.6 < |\eta| < 1.8$  in beam tests”. In: *Nucl. Instrum. Meth.* 531 (2004), p. 481. DOI: [10.1016/j.nima.2004.05.133](https://doi.org/10.1016/j.nima.2004.05.133). arXiv: [0407009](https://arxiv.org/abs/0407009) [physics] (cit. on p. 164).
- [312] T. Barillari et al. “Local hadronic calibration”. In: ATL-LARG-PUB-2009-001 (2009). URL: <http://cdsweb.cern.ch/record/1112035> (cit. on p. 164).
- [313] ATLAS Collaboration. “Performance of pile-up mitigation techniques for jets in  $pp$  collisions at  $\sqrt{s} = 8$  TeV using the ATLAS detector”. In: *Eur. Phys. J. C* 76.11 (2016), p. 581. DOI: [10.1140/epjc/s10052-016-4395-z](https://doi.org/10.1140/epjc/s10052-016-4395-z). arXiv: [1510.03823](https://arxiv.org/abs/1510.03823) [hep-ex] (cit. on p. 165).
- [314] ATLAS Collaboration. “Electron performance measurements with the ATLAS detector using the 2010 LHC proton-proton collision data”. In: *Eur. Phys. J. C* 72 (2012), p. 1909. DOI: [10.1140/epjc/s10052-012-1909-1](https://doi.org/10.1140/epjc/s10052-012-1909-1). arXiv: [1110.3174](https://arxiv.org/abs/1110.3174) [hep-ex] (cit. on p. 165).
- [315] ATLAS collaboration. “Performance of Missing Transverse Momentum Reconstruction in Proton-Proton Collisions at 7 TeV with ATLAS”. In: *Eur.Phys.J.* C72 (2012), p. 1844 (cit. on p. 166).
- [316] ATLAS Collaboration. “Commissioning of the ATLAS high-performance b-tagging algorithms in the 7 TeV collision data”. In: *ATLAS-CONF-2011-102* (2011). URL: <http://cdsweb.cern.ch/record/1369219> (cit. on p. 166).
- [317] ATLAS Collaboration. “Search for the Standard Model Higgs boson produced by vector-boson fusion and decaying to bottom quarks in  $\sqrt{s} = 8$  TeV  $pp$  collisions with the ATLAS detector”. In: *JHEP* 11 (2016), p. 112. DOI: [10.1007/JHEP11\(2016\)112](https://doi.org/10.1007/JHEP11(2016)112). arXiv: [1606.02181](https://arxiv.org/abs/1606.02181) [hep-ex] (cit. on p. 167).
- [318] ATLAS Collaboration. “Search for single production of a vector-like quark via a heavy gluon in the  $4b$  final state with the ATLAS detector in  $pp$  collisions at  $\sqrt{s} = 8$  TeV”. In: *Phys. Lett. B* 758 (2016), pp. 249–268. DOI: [10.1016/j.physletb.2016.04.061](https://doi.org/10.1016/j.physletb.2016.04.061). arXiv: [1602.06034](https://arxiv.org/abs/1602.06034) [hep-ex] (cit. on p. 167).



- [319] M. Campanelli, D. Gerbaudo, F. Rubbo, et al. *Jet Trigger Performance Plots from 2011 and 2012 Data*. Tech. rep. ATL-COM-DAQ-2012-210. Geneva: CERN, 2012. URL: <https://cds.cern.ch/record/1498621> (cit. on p. 167).
- [320] S. Rajagoapalan. “The Performance of the ATLAS Trigger System in the LHC Proton-Proton Collisions”. In: *Phys. Procedia* 37 (2012), pp. 1781–1790. DOI: [10.1016/j.phpro.2012.02.503](https://doi.org/10.1016/j.phpro.2012.02.503) (cit. on p. 168).
- [321] ATLAS Collaboration. “Performance of the ATLAS Trigger System in 2010”. In: *Eur. Phys. J. C* 72 (2012), p. 1849. DOI: [10.1140/epjc/s10052-011-1849-1](https://doi.org/10.1140/epjc/s10052-011-1849-1). arXiv: [1110.1530](https://arxiv.org/abs/1110.1530) [hep-ex] (cit. on p. 168).
- [322] D. Emeliyanov. “A fast vertex fitter for ATLAS level 2 trigger”. In: *PoS ACAT* (2007), p. 058 (cit. on p. 168).
- [323] ATLAS Collaboration. *Performance of the ATLAS Muon Trigger in p-p collisions at  $\sqrt{s} = 7$  TeV*. Tech. rep. ATLAS-CONF-2010-095. Geneva: CERN, 2010. URL: <http://cds.cern.ch/record/1299573> (cit. on p. 169).
- [324] A. Corso-Radu, H. Hadavand, Y. Ilchenko, et al. “Data Quality Monitoring Framework for the ATLAS experiment: Performance achieved with colliding beams at the LHC”. In: *Journal of Physics: Conference Series* 331.2 (2011), p. 022027. URL: <http://stacks.iop.org/1742-6596/331/i=2/a=022027> (cit. on p. 170).
- [325] C. Bertella. “Probing top quark and Higgs boson production in multi-jet events at the LHC with the ATLAS detector”. Theses. Aix-Marseille Université, Sept. 2013. URL: <https://tel.archives-ouvertes.fr/tel-00968336> (cit. on pp. 170, 174).
- [326] ATLAS Collaboration. “Measurement of the inclusive and dijet cross-sections of  $b$ -jets in  $pp$  collisions at  $\sqrt{s} = 7$  TeV with the ATLAS detector”. In: *Eur. Phys. J. C* 71 (2011), p. 1846. DOI: [10.1140/epjc/s10052-011-1846-4](https://doi.org/10.1140/epjc/s10052-011-1846-4). arXiv: [1109.6833](https://arxiv.org/abs/1109.6833) [hep-ex] (cit. on p. 172).
- [327] D. Madaffari. “Search for the decay  $H \rightarrow b\bar{b}$  of the standard model Higgs boson produced in association with hadronically decaying top quarks in  $pp$  collisions at 8 TeV with the ATLAS detector at the LHC”. Theses. Aix-Marseille Université, Oct. 2015. URL: <https://hal.archives-ouvertes.fr/tel-01326964> (cit. on p. 175).
- [328] A. Djouadi, J.-L. Kneur, and G. Moultaka. “SuSpect: A Fortran code for the supersymmetric and Higgs particle spectrum in the MSSM”. In: *Comput. Phys. Commun.* 176 (2007), pp. 426–455 (cit. on p. 180).
- [329] A. Djouadi, J.-L. Kneur, G. Moultaka, et al. *SuSpect: A Fortran code for the supersymmetric and Higgs particle spectrum in the MSSM*. Les Houches 2011: Physics at TeV Colliders New Physics Working Group Report, G. Brooijmans. arXiv: [1203.1488](https://arxiv.org/abs/1203.1488) [hep-ph] (cit. on p. 180).

- [330] U. Ellwanger and C. Hugonie. “NMSPEC: A Fortran code for the sparticle and Higgs masses in the NMSSM with GUT scale boundary conditions”. In: *Comput. Phys. Commun.* 177 (2007), pp. 399–407 (cit. on p. 180).
- [331] U. Ellwanger and C. Hugonie. “NMHDECAY 2.0: An Updated program for sparticle masses, Higgs masses, couplings and decay widths in the NMSSM”. In: *Comput. Phys. Commun.* 175 (2006), pp. 290–303 (cit. on p. 180).
- [332] U. Ellwanger and C. Hugonie. “Higgs bosons near 125 GeV in the NMSSM with constraints at the GUT scale”. In: *Adv. High Energy Phys.* 2012 (2012), p. 625389 (cit. on p. 180).
- [333] A. Arhrib, R. Benbrik, M. Chabab, G. Moultaka, L. Rahili. “Higgs boson decay into 2 photons in the type II seesaw model”. In: *JHEP* 2012 (136) (cit. on p. 180).
- [334] A. Benhenni, J.-L. Kneur, G. Moultaka, S. Bailly. “Revisiting no-scale supergravity inspired scenarios: updated theoretical and phenomenological constraints”. In: *Phys. Rev. D* 84 (2011), p. 075015 (cit. on p. 180).
- [335] M. Frigerio, J. Serra, A. Varagnolo. “Composite GUTs: models and expectations at the LHC”. In: *JHEP* 1106 (2011), p. 029 (cit. on p. 180).
- [336] M. Frigerio, A. Pomarol, F. Riva, A. Urbano. “Composite Scalar Dark Matter”. In: *JHEP* 1207 (2011), p. 015 (cit. on p. 180).
- [337] C. Degrande, N. Greiner and K. Wolfgang, Olivier Mattelaer, Harrison Mebane, et al. “Effective Field Theory: A Modern Approach to Anomalous Couplings”. In: *Annals Phys.* 335 (2013), pp. 21–32. DOI: [10.1016/j.aop.2013.04.016](https://doi.org/10.1016/j.aop.2013.04.016). arXiv: [1205.4231](https://arxiv.org/abs/1205.4231) [hep-ph] (cit. on p. 181).
- [338] B. Dumont, S. Fichet and G. von Gersdorff. “A Bayesian view of the Higgs sector with higher dimensional operators”. In: *JHEP* 07 (2013), p. 065. DOI: [10.1007/JHEP07\(2013\)065](https://doi.org/10.1007/JHEP07(2013)065). arXiv: [1304.3369](https://arxiv.org/abs/1304.3369) [hep-ph] (cit. on p. 181).



# ANNEXES

## A. The ATLAS detector

The ATLAS detector [306] consists of an inner tracking detector surrounded by a thin superconducting solenoid magnet providing a 2 T axial magnetic field, electromagnetic and hadron calorimeters, and a muon spectrometer incorporating three large superconducting toroid magnets. The inner detector (ID) comprises the high-granularity silicon pixel detector and the silicon microstrip tracker covering the pseudorapidity<sup>g</sup> range  $|\eta| < 2.5$ , and the straw-tube transition radiation tracker covering  $|\eta| < 2.0$ . The electromagnetic calorimeter covers  $|\eta| < 3.2$  and consists of a barrel and two endcap high-granularity lead/liquid-argon (LAr) calorimeters. An additional thin LAr presampler covers  $|\eta| < 1.8$ . Hadron calorimetry is provided by a steel/scintillator-tile calorimeter, which covers the region  $|\eta| < 1.7$ , and two copper/LAr hadron endcap calorimeters. To complete the pseudorapidity coverage, copper/LAr and tungsten/LAr forward calorimeters cover up to  $|\eta| = 4.9$ . Muon tracking chambers precisely measure the deflection of muons in the magnetic field generated by superconducting air-core toroids in the region  $|\eta| < 2.7$ . During the LHC Run 1 period, a three-level trigger system selected events for offline analysis [307]. The hardware-based Level-1 trigger is used to reduce the event rate from the 40 MHz bunch crossing rate to a maximum of 75 kHz, while the two software-based high level triggers (HLT), Level-2 and Event Filter (EF), were used to reduce the event rate to about 400 Hz.

### A.1. Jets

Jets are reconstructed with the anti- $k_t$  algorithm [308, 309, 310], with a radius parameter  $R = 0.4$  in the  $(\eta, \phi)$  plane. They are built from calibrated topological clusters of energy deposits in the calorimeters [306]. Prior to jet finding, a local cluster calibration scheme [311, 312] is applied to correct the topological cluster energies for the effects of non-compensating calorimeter response, dead material, and out-of-cluster leakage. After energy calibration based on in-situ measurements [164], jets are required to have a certain transverse momentum  $p_T$  and  $|\eta|$  coverage, which are usually analysis dependent. During jet

---

<sup>g</sup>ATLAS uses a right-handed coordinate system with its origin at the nominal interaction point (IP) in the centre of the detector and the  $z$ -axis coinciding with the axis of the beam pipe. The  $x$ -axis points from the IP to the centre of the LHC ring, and the  $y$ -axis points upward. Cylindrical coordinates  $(r, \phi)$  are used in the transverse plane,  $\phi$  being the azimuthal angle around the beam pipe. The pseudorapidity is defined in terms of the polar angle  $\theta$  as  $\eta = -\ln \tan(\theta/2)$ . Transverse momentum and energy are defined as  $p_T = p \sin \theta$  and  $E_T = E \sin \theta$  respectively.

reconstruction, no distinction is made between identified electrons and jet energy deposits. To avoid counting electrons as jets, any jet within a cone of size  $\Delta R = \sqrt{(\Delta\phi)^2 + (\Delta\eta)^2} = 0.2$  around a reconstructed electron is discarded. After this, electrons within a  $\Delta R = 0.4$  of a remaining jet are removed. To avoid selecting jets from additional  $pp$  interactions in the same event (pile-up), starting from 2012 ATLAS put in place a pile-up rejection algorithm, the jet vertex fraction (JVF), defined as the ratio of the scalar sum of the  $p_T$  of tracks matched to the jet and originating from the primary vertex to that of all tracks matched to the jet. A loose criterion,  $JVF \geq 0.5$ , was then applied to jets with  $p_T < 50$  GeV and  $|\eta| < 2.4$  [313].

## A.2. Leptons and missing transverse momentum

Leptons and missing transverse energy ( $E_T^{\text{miss}}$ ) are defined according to the following criteria:

- Electron candidates [314] are reconstructed from energy deposits (clusters) in the electromagnetic calorimeter that are associated to reconstructed tracks in the inner detector. They are required to have  $p_T > 25$  GeV and  $|\eta_{\text{cluster}}| < 2.47$  (where  $|\eta_{\text{cluster}}|$  is the pseudorapidity of the calorimeter cluster associated with the electron candidate). Candidates in the calorimetry transition region  $1.37 < |\eta_{\text{cluster}}| < 1.52$  are excluded. Electron candidates are also required to be isolated. In the 7 TeV analysis, the calorimeter transverse energy not associated to the electron deposited in a cone in  $\eta - \phi$  space of radius  $\Delta R = \sqrt{(\Delta\phi)^2 + (\Delta\eta)^2} = 0.2$  around the electron direction is required to be less than 3.5 GeV. For the 8 TeV analysis an  $\eta$ -dependent, 90% efficient isolation cut, based on the sum of transverse energy of cells around the direction of each candidate is made for a cone of radius  $\Delta R = 0.2$ . This energy sum excludes cells associated with the electron cluster and is corrected for leakage from the electron cluster itself. A further 90% efficient isolation cut is made on the track transverse momentum ( $p_T$ ) sum around the electron in a cone of radius  $\Delta R = 0.3$ , moreover the longitudinal impact parameter of the electron track with respect to the selected event primary vertex,  $z_0$ , is required to be less than 2 mm.
- Muons are reconstructed by combining the measurements of the tracks detected in the muon spectrometer with those of the associated tracks in the inner detector [83]. The final candidates are refitted using the complete track information from both detector systems, and required to satisfy  $p_T > 20$  GeV (25 GeV) for 7 (8) TeV analysis and  $|\eta| < 2.5$ . Additionally, muons are required to be separated by  $\Delta R > 0.4$  from any selected jet (see below). Furthermore, muons are required to satisfy a track-based isolation, for 2011 analysis this consisted on requiring the sum of the transverse

momenta of the inner detector tracks in a cone of  $\Delta R = 0.3$  around the muon candidate is less than 2.5 GeV and the transverse energy in a cone with  $\Delta R = 0.2$  around the muon is less than 4 GeV. For the 8 TeV data the track-based isolation is  $p_T$ -dependent, having good performance under high pileup conditions or in boosted configurations where the muon is close to a jet: the scalar sum of the track  $p_T$  in a cone of variable radius  $\Delta R < 10 \text{ GeV}/p_T^\mu$  around the muon (excluding the muon track itself) must be less than 5% of the muon  $p_T$ . Muons are required to have a hit pattern in the inner detector consistent with a well-reconstructed track. Analogously to the electrons, the muon track longitudinal impact parameter with respect to the primary vertex,  $z_0$ , is required to be less than 2 mm.

- The magnitude of the missing transverse momentum,  $E_T^{\text{miss}}$ , is calculated from calorimeter topological clusters which are reconstructed and calibrated at the EM scale with an additional, object-dependent calibration applied to individual clusters that are associated to higher level objects such as electrons or jets [315].

### A.3. Identification of $b$ -jets

The identification of jets originating from  $b$ -quarks is performed using a discriminant built from the combination of the three  $b$ -tagging algorithms JetFitter, IP3D and SV1 [316]. The JetFitter secondary-vertex-based tagging algorithm exploits the topology of  $b$ - and  $c$ -hadron weak decays inside the jet. A Kalman filter is used to find a common line on which the primary vertex and the  $b$ - and  $c$ -hadron decay vertices lie, as well as the vertex positions on this line, giving an approximate flight path for the  $b$ -hadron. With this approach, the  $b$ - and  $c$ -hadron vertices are not necessarily merged, even when only a single track is attached to each of them. The discrimination between  $b$ -,  $c$ - and light-jets is based on a likelihood variable using the masses, momenta, flight-length significances and the track multiplicities of the reconstructed vertices as inputs. To further increase the flavour discrimination power, a second  $b$ -tagger (IP3D) that does not attempt to directly reconstruct decay vertices is run. Instead, this tagger uses the transverse and the longitudinal impact parameter significances of each track within the jet to determine a likelihood that the jet originates from a  $b$ -quark. To further increase the discrimination power, the SV1 tagging algorithm takes advantage of three vertex properties: the invariant mass of all tracks associated to the vertex, the ratio of the sum of the energies of the tracks associated to the vertex to the sum of the energies of all tracks in the jet and the number of two-track vertices. The JetFitter, IP3D and SV1 variables are then combined using a likelihood ratio technique to deliver the final MV1-tagging discrimination weight used to make tagging decisions. For this analysis we tune the cut on the MV1 weight to accept  $b$ -jets with approximately 60% efficiency according to simulated  $t\bar{t}$  events. This

corresponds to a light jet rejection factor of about 700 and a charm-jet rejection factor of 8, as determined for jets with  $p_T > 25$  GeV and  $|\eta| < 2.5$  in simulated  $t\bar{t}$  events [68].

#### A.4. $b$ -tagging at trigger level in Run 1

$B$ -jet triggers are used to efficiently collect physics processes where  $b$ -jets are produced with no leptons or large amount of missing energy, which could be otherwise used at trigger level. Adding  $b$ -tagging requirements to trigger such events, instead of just using plain multi-jet triggers, allows to relax the requirement on the online jet  $p_T$  threshold necessary to limit the large rate associated to multi-jet production (see Figure A.I). This is instrumental for signal processes such Higgs boson production by vector-boson fusion and decaying to a pair of bottom quarks [317], the single production of a vector-like quark via a heavy gluon in the  $4b$  final state [318] or the fully hadronic  $t\bar{t}H (H \rightarrow b\bar{b})$ , where hard requirements on jet  $p_T$  would result in a non-negligible loss in efficiency because of the slow  $p_T$  dependency of the trigger turn-on curve [319].

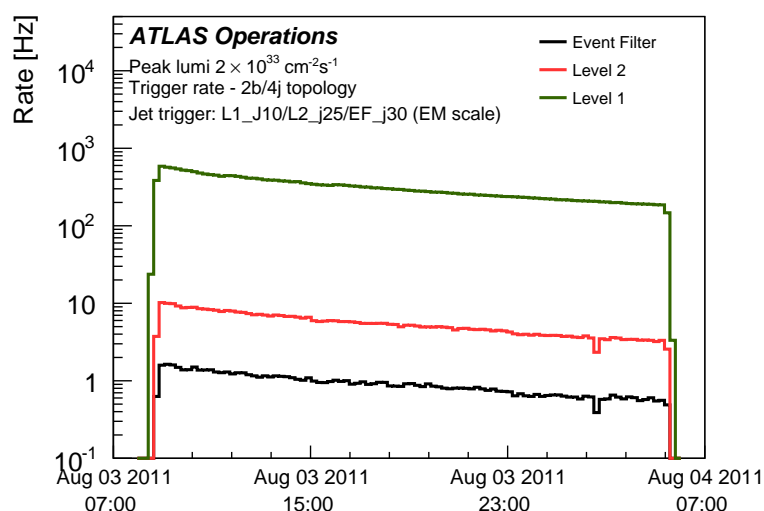


Figure A.I.: Trigger rate for 2b/4j topology. LVL1, LVL2 and EF rate of a  $b$ -jet trigger requiring at least four jets in the event and at least two  $b$ -tagged jet. The jet thresholds correspond to 10, 25 and 30 GeV at LVL1, LVL2 and EF with energies measured at the electromagnetic scale. The  $b$ -jet requirement is applied at LVL2 and EF is tuned to give 70% efficiency on a  $b$ -tagged jet sample using top MC simulation.

ATLAS has full  $b$ -tagging capability starting from HLT where fast reconstruction algorithms are used to refine the trigger selection and it uses as input LVL1

trigger towers. The LVL1 hardware based trigger system clusters trigger towers, i.e. analog sum of calorimeter cells in  $\Delta\eta \times \Delta\phi = 0.2 \times 0.2$  in the central region ( $|\eta| < 3.2$ ), in a  $4 \times 4$ ,  $6 \times 6$  and  $8 \times 8$  regions [320]. The type, position and energy threshold of the cluster of trigger towers define the jet Region of Interest (RoI) which is sent to LVL2, completely software based, which runs on processor farms and that access data from all ATLAS sub-detectors, including the Inner Detector: this is the first place where information to be able to run  $b$ -tagging are available in the entire event reconstruction chain. The information of the energy deposit in the calorimeter cells within the RoIs are used by the LVL2 jet-cone algorithm with a radius of  $R = 0.4$ . During Run 1 a so-called LVL1.5 algorithm was able to process full calorimeter information accessing the full  $0.2 \times 0.2$  jet clusters.

At LVL2 fast tracking is provided by a modular framework, L2Star, which combines different track reconstruction strategies such as *IdScan*, a three steps histogramming technique, and a combinatorial technique, *SiTrack* [321]. Within the LVL2 a fast vertex fitter is used to reconstruct primary vertices on an event by event basis [322]. Offline-like pattern recognition and fitting algorithms are used at EF optimized for fast execution time.

In details, during Run 1,  $b$ -jet triggers both at LVL2 and at EF used a combination of two likelihood based algorithms, exploiting the impact parameter significance distribution (IP3D) and the secondary vertex properties (SV1). These algorithms were combined resulting in a high performance tagger: *xComb*. Different working points with different efficiency and rejection were used during 2012 data taking campaign are shown in Table A.I. In Figure A.II it is shown the agreement between single jet triggered data, where  $b$ -tagging is run without taking decision, and dijet PYTHIA MC events for the xComb  $b$ -tagging output at LVL2 and EF.

Working point	$b$ -tagging efficiency (%)	Light jet rejection LVL2	Light jet rejection L2+EF
loose	60	16	51
medium	50	40	145
tight	40	60	350

Table A.I.: ATLAS  $b$ -tagging working points used for online xComb  $b$ -tagging algorithm. These performance are evaluated on a sample of Monte Carlo  $t\bar{t}$  events.

The presence of muons reconstructed within the jets ( $\mu$ -jets) can be used to identify semi-leptonically decaying  $b$ -mesons:  $B(b \rightarrow \mu\nu X) \approx 11\%$  of the time, and the sequential semi-leptonic decay ( $B(b \rightarrow c \rightarrow \mu\nu X)$  is also  $\approx 10\%$ ). Muons are reconstructed starting from LVL1 using the Resistive Plate Chambers (RPC) in the central region  $|\eta| < 1.05$  and Thin Gap Chambers (TGC) in the endcap

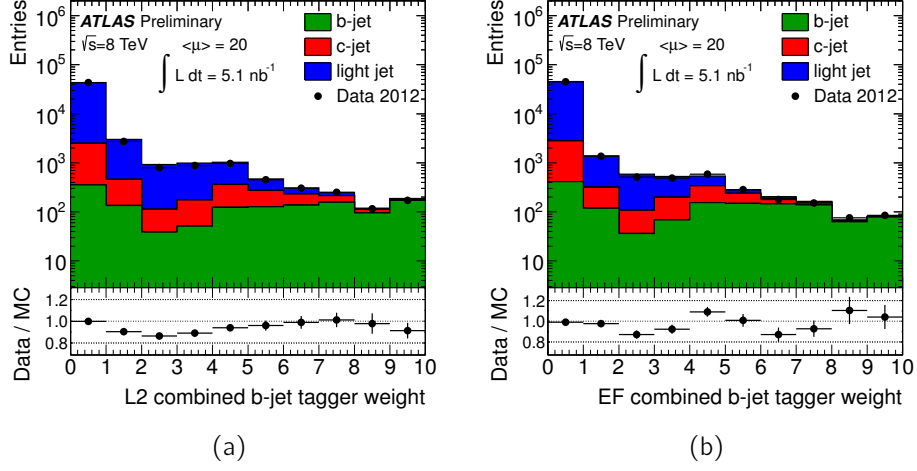


Figure A.11.: Left hand side: Jet weight distribution for the tagger based on the combination of the impact parameter significance and the secondary vertex likelihood-based taggers, calculated from prescaled Level 2 tracks in Level 2 jets with  $p_T > 50$  GeV and  $|\eta| < 2.5$ . Only statistical errors are shown. Right hand side: Same for Event Filter jets with  $p_T > 55$  GeV and  $|\eta| < 2.5$ .

regions  $1.05 < |\eta| < 2.4$  from hits in one of the muon systems and the subsequent search for adjacent hits in the nearby stations. Parametrized *roads* are used to define the  $\eta$  and  $\phi$  coordinate and the  $p_T$  of the muon candidate. At LVL1  $\mu$ -jet triggers start from a logical *AND* of a LVL1 jet and a LVL1 muon objects with different  $p_T$  thresholds. At LVL2 a fast algorithm confirms the LVL1 muon candidates and makes a more precise muon momentum measurement using the Monitored Drift Tubes (MDT) information [323]. A fast track combination algorithm matches tracks found in the Muon Spectrometer with tracks found in the Inner Detector. At this point a geometrical matching between the muon and the jet ( $\Delta R(\text{jet}, \mu) < 0.4$ ) is used both at LVL2 and at EF in order to finalize the  $\mu$ -jet trigger object. In the 2012 the matching between the muon and jet were performed also in the  $z$ -direction  $\Delta z(\text{jet}, \mu) < 2$  mm. Those trigger items are usually highly prescaled, in Run 1 these item received 1 Hz out of the EF, and different thresholds were used in order to populate uniformly the  $p_T$  spectrum, necessary for using these trigger for the calibration of track-based  $b$ -tagging algorithms.

## Monitoring $b$ -jet trigger data quality

The trigger system is monitored within the ATLAS Data Quality Monitoring (DQM): during data-taking the behaviour of a series of critical quantities are checked against reference runs. The DQM Framework, accessible via the DQM Display (DQMD) [324], assigns a DQ Flag based on the result of automatic checks. For  $b$ -jet triggers the relevant quantities which are monitored online in Run 1 were [325]:

- track and vertex related variables, such as the number of tracks per RoI, the track parameters and the primary vertex along the  $z$  direction;
- variables used by  $b$ -tagging algorithms, such as the track transverse and the longitudinal impact parameters;
- $b$ -tagging weights used for event selection, i.e. xComb.

Once the DQ Flags are assigned, these are validated by the offline DQMF, which runs on the *express stream*, which represents 10% of the data, and which is reconstructed with a maximum delay of 36 hours after collection at Tier-0. For this, a particular class of trigger is used, where the  $b$ -tagging algorithms run without taking decision. During Run 1, the trigger chains used for the monitoring were single jet triggers requiring LVL1 jet trigger object with  $p_T \geq 15$  GeV,  $p_T \geq 50$  GeV at LVL2 and  $p_T \geq 55$  GeV at EF, with or without the requirement of the jet to be matched to a muon ( $\mu$ -jet). An offline selection is added as a requirement for the  $\mu$ -jet trigger based monitoring to further enhance the heavy flavor content, i.e.:

- events have to pass a  $\mu$ -jet trigger;
- offline jets must have  $p_T \geq 15$  GeV and  $|\eta| \geq 2.5$ ;
- offline jets match to an offline muon within an angle  $\Delta R < 0.4$ ;
- basic quality cuts are applied to the muons;
- $p_T^{relh}$  has to be larger than 2 GeV.

Figure A.III represents the XComb distributions for different monitoring trigger configuration as they appear in the DQMD.

---

<sup>h</sup> $p_T^{rel}$  represents the relative transverse momentum of the muon with respect to the vector formed by the sum of the muon and the jet directions. This quantity presents a harder distribution for  $b$ -quark initiated jets compared to  $c$ - and light-jets.

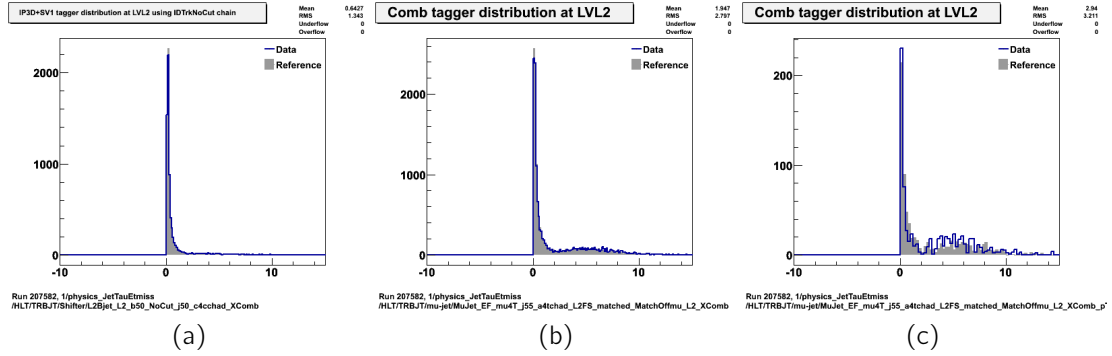


Figure A.III.: Histograms taken from the web display of Tier-0 offline monitoring of the XComb tagger weight. Left: for all the events passing the LVL2 trigger criteria for single jet triggers and for all the events passing the  $\mu$ -jet trigger offline selection, without (Center) and with (Right)  $p_T^{rel} \geq 2$  GeV requirement.

## B. Supervisory Experience

### Master 1 Internships

Damien Minenna, 2014: *R-Parity violating Supersymmetric signal in final states with multi quark at the LHC*

Damien, master student at the université de Montpellier, performed his M1 internship in the framework of the PESBLADe collaboration. During his stage he worked with Gilbert Moulta, Sara Diglio and myself on the characterisation of SUSY RPV phase space. The stage focused on the implementation of a MATHEMATICA based software which allow to convert sparticle physical masses to SUSY scale-free parameters, inputs for the SPHENO SUSY spectrum calculator. Damien completed successfully his master, he is actually enrolled in a PhD program on plasma physics with a thesis co-funded by Thalès and Cnes at the Aix-Marseille Université.

### Master 2 Internships

Sahar Aoun, 2008: *Search for a light Higgs Boson in the  $t\bar{t}H(\rightarrow b\bar{b})$  channel with the ATLAS detector*



Master student at P3TMA<sup>i</sup>, Sahar, during her stage, performed a study aimed at the amelioration of the expected sensitivity of the  $t\bar{t}H(H \rightarrow b\bar{b})$  process in the semileptonic final state using the analysis framework realized for the CSC note. The algorithm she implemented consisted on a combined fit of the measured energy of the reconstructed hadronic jets, using the value of the reconstructed mass of the top-quark and Higgs boson candidates as a constraint. This technique allows to vary the energy of the jets within the experimental resolution to accommodate for the  $t\bar{t}H$  production hypothesis. The idea behind is that  $t\bar{t}H$ -like events can be identified in data by the value of the fit quality estimator. After the stage, Sahar continued to work as PhD student with the CPPM-ATLAS group, working on the properties of the pixel cluster charge, comparing cosmic ray data and simulation, and finally on the measurement of the  $b$ -jet production cross section with 2010 ATLAS data using muons in jets [326]. Sahar is actually Associate Professor at the Université Saint-Joseph de Beirut.

**Nancy Tannoury, 2009:** *Estimation of QCD contamination in ATLAS top quark pairs production cross section measurement using Matrix Method*

Nancy, master student at P3TMA, during her M2 stage, worked on the implementation of the *Matrix Method* for the estimation of the multi-jet background in the framework of the  $t\bar{t}$  production cross section measurement in the electron plus jets channel. This background arises from jets faking the signature of an isolated electron. The Matrix Method allows to evaluate the multi-jet background from data with almost no inputs from MC simulations. Thanks to the large sample of fully simulated multijet events where it was possible to estimate the rate to which a jet fake the electron signature, we could perform this exercise and test ATLAS capability before the actual data were available. My collaboration with Nancy continued during her PhD, with the CPPM-ATLAS group, when we worked on the assessment of  $b$ -tagging efficiency using system 8 [68]. After her PhD she continued to work within the ATLAS-CPPM group for one year with a mixed research-teaching position, she then left for a post-doc position with the Bonn group, always associated to ATLAS, working on fully hadronic  $t\bar{t}H(H \rightarrow b\bar{b})$  searches. She has now a permanent position with PMB-ALCEN<sup>j</sup>, specializing on the medical use of cyclotrons facilities.

**Dragos-Bogdan Carabet, 2012:** *Top quark mass measurement in the fully hadronic final state in  $p - p$  collisions at  $\sqrt{s} = 7$  TeV with the ATLAS detector*

Dragos-Bogdan, master student at P3TMA, performed a study on the measure of the mass of the top quark using events where two top quarks are produced and

<sup>i</sup><https://physique-sciences.univ-amu.fr/master2-physique/P3TMA>

<sup>j</sup><http://www.pmb-alcen.com>

then decay fully hadronically. During his internship Dragos-Bogdan developed a top quark mass measurement technique using template mass distributions derived from Monte-Carlo simulations. He then applied the method to the data recorded by ATLAS in 2011. Dragos analysis was an extension of an already public results, which was using MC derived templates but a less discriminating mass reconstruction algorithm to perform the final fit to data.

**Yanyun Duan, 2016:** *Trigger studies for fully hadronic  $t\bar{t}H(\rightarrow b\bar{b})$  searches in  $p-p$  collisions at  $\sqrt{s} = 13$  TeV with the ATLAS detector*

Yanyun, master student at P3TMA, performed her M2 stage on the estimation of the trigger efficiency for fully hadronic  $t\bar{t}H(H \rightarrow b\bar{b})$ . Yanyun used simulated  $t\bar{t}H(\rightarrow b\bar{b})$  events, produced with MadGraph5 and interfaced with Pythia for the showering of extra partons together with the full 2015 dataset of  $p-p$  collisions recorded at  $\sqrt{s} = 13$  TeV. After applying standard event selection and evaluating the signal efficiency, Yanyun estimated the best trigger strategies by compiling relevant quantities such as signal over background in each of the regions used by the full hadronic  $t\bar{t}H$  analyses.

**Nghia Nguyen Hoang Dai, 2016:** *Search for new physics in fully hadronic final states with the ATLAS detector at the LHC*

During his stage Nghia, master student at P3TMA, analyzed pair produced stop signal and standard model background events generated with MADGRAPH interfaced with (DELPHES) for the detector simulation and object reconstruction, in order to asses ATLAS sensitivity these RPV processes. Nghia implemented a full chain analysis, including an emulation of the  $b$ -tagging algorithms, not present in DELPHES, a la  $TRF_{MC}$ , as explained in Section 2.3.3. He then developed a trigger strategy and an event selection which identifies a region with maximal signal over background ratio. After the completion of his internship, Nghia was successfully admitted into the PhD program of the Ecole Doctorale Physique et Sciences de la Matière and since October 2016, he is pursuing his PhD within the ATLAS-CPPM group.

## Tesi di Laurea

**Giovanni Bertolini, 2017:** *Multivariate strategy for signal versus background discrimination in the analysis for the search for  $t\bar{t}H(H \rightarrow b\bar{b})$  fully hadronic final state with the ATLAS detector at  $\sqrt{s} = 13$  TeV.*

Giovanni, a master student from the Physics Department of the University of

Perugia, worked on the development of multivariate techniques to reconstruct the fully hadronic  $t\bar{t}H$  system with the ATLAS detector. This study uses simulated MC events signal fully hadronic  $t\bar{t}H$  events. First Giovanni isolated a set of events where all the partons from the hard interactions are reconstructed, by picking up those events where he could associate reconstructed jets to all hard scatter partons. In this sample he exploited the knowledge on the provenience of each reconstructed jets, to identify a set of variables that, by using the correlation among objects coming from the top-quark, anti-top-quark and Higgs boson decay, can actually be used to resolve the combinatorics and associate back jets to partons. Finally, Giovanni implemented a multi variate analysis based on Boosted Decision Tree to discriminate  $t\bar{t}H$  signal and  $t\bar{t} + \text{jets}$  background in fully hadronic events. Giovanni defended his Laurea diploma in September 2017, his work granted him a scholarship from the Ecole Doctorale Physique et Sciences de la Matière and the possibility to continue his work as a PhD student with the ATLAS group at CPPM.

## PhD Theses

**Claudia Bertella:** 2011-2013 *Probing top quark and Higgs production in multi-jet events at the LHC with the ATLAS detector*

Together with Mossadek Talby I co-directed Claudia's PhD thesis [325] on the fully hadronic top pairs cross section at  $\sqrt{s} = 7$  TeV [71]. Claudia was the main contributor to the analysis, from the development and the maintenance of the analysis software, to the estimation of the multijets background, to the signal extraction and the final fit. Part of her thesis work was devoted to the implementation of profile likelihood techniques to reduce the uncertainties on the fully hadronic top cross section measurement. At the end of her thesis she initiated a feasibility study for the fully hadronic  $t\bar{t}H$  production at 7 TeV. During her thesis, Claudia worked extensively within ATLAS  $b$ -jet trigger working group. Claudia developed the online and offline monitoring infrastructure for this class of triggers and she was part of the data quality assessment team, during the 2012 LHC data-taking period, for all the active  $b$ -jet items. In summer 2014 she joined as a Post-doc the ATLAS Mainz group to work on the Vector Boson Fusion (VBF)  $qqH \rightarrow qqH(\rightarrow WW)$  analysis. Claudia is now post-doc with the Beijing IHEP group aiming at bringing to completion the VBF analysis, which she is responsible within ATLAS, and working on the ITk upgrade.

**Daniele Madaffari:** 2012-2015 *Search for the Higgs boson produced in association with top quark pairs in the fully hadronic final state with the ATLAS detector using  $20 \text{ fb}^{-1}$  of proton-proton collisions at  $\sqrt{s} = 8$  TeV.*

Together with Mossadek Talby I co-directed the PhD thesis of Daniele Madafari [327]. During his first year as a PhD, Daniele worked on the estimation of the difference of the multi-jet trigger efficiency in data and Monte Carlo simulated events. This difference was estimated as a Scale Factor to apply to MC events and applied to the fully hadronic  $t\bar{t}H$  analysis. Daniele has been the main contributor to the analysis, his main work has been the development the data driven estimation of the multi-jet production. He has been responsible for developing and maintaining the analysis code which was completely customized for the analysis, he has followed the analysis from start to end, developed most of the original software, interfacing the implementation of the systematic uncertainties and the final code producing the inputs to the likelihood fit.

**Nghia Nguyen Hoang Dai:** 2016-current *"Search for the Higgs boson produced in association with top quark pairs in the fully hadronic final state with the ATLAS detector at  $\sqrt{s} = 13$  TeV."*

Nghia has started his PhD under the direction Mossadek Talby and myself in October 2106. In his first year he has worked on his qualification task with the ATLAS  $b$ -jet trigger group. He worked on the development a software tool which is able to emulate the trigger chains currently running online to check offline on simulated events the behaviour of the trigger decision. Nghia updated the  $b$ -jet part of the ATLAS online monitoring tool, used by the shifters to check the quality of the data taking. This includes the latest  $b$ -tagging algorithms deployed online with the latest trigger configuration. Nghia is now working on the fully hadronic  $t\bar{t}H$  Run 2 analysis, he is currently implementing a data driven background estimation for the multi-jet background based on the Run 1 analysis.

**Giovanni Bartolini:** 2017-current *"Search for new physics in multi-jets events with the ATLAS detector at  $\sqrt{s} = 13$  TeV."*

Giovanni started his PhD at the beginning of October 2017 under the direction Mossadek Talby and myself. He is now working on porting the techniques he developed during his Master internships to the new analysis framework. He just started his qualification task on the calibration of the online  $b$ -tagging algorithms, adapting the analysis framework and downstream analysis codes used for the offline  $b$ -tagging calibration to include all the relevant information, such as the online jets and tracks. After this step he will proceed to the calibration of  $b$ -jet trigger algorithms using  $t\bar{t}$  events.

## Post-Doctoral positions

Sara Diglio: 2014-2015

Sara Diglio started her Post-Doc with the PESBLADe project in January 2014. She worked in close collaboration with G. Moulaka (L2C-IFAC) and myself on the characterization of R-Parity Violating SUSY models. The work consisted on generating the trilinear RpV SUSY model using SARAH software and to calculate SUSY spectra for the relevant models using SPHENO and finally by using MADGRAPH Monte Carlo event generator to simulate signal events produced in  $p - p$  collisions. The main findings of this work has been to fully unfold the link between RpV stop production phenomenology and the strength of the RpV couplings. This work has been published to PRD [73]. In April 2015 Sara Diglio moved to the Subatech laboratory<sup>k</sup>, in Nantes, where she is currently holding a post-doc position with the Xenon1T group.

Daniele Madaffari: 2015-2016

After his thesis Daniele Madaffari was hired with a mixed research and teaching position by the Aix-Marseille Université. This contract allowed him to bring his thesis work to publication [72] by contributing to the internal ATLAS review until April 2016. He is currently holding a post-doc position with the ATLAS group in Valencia, mainly working on the ATLAS ITk upgrade.

Romain Kukla: 2016-present

In October 2016 Romain Kukla was hired to work with the PESBLADe project. He is currently involved with the set up of the software framework for the fully hadronic  $t\bar{t}H$  analysis which. This analysis, once extended to higher  $b$ -tagged jet multiplicities, will be used to probe the presence of RPV signal for intermediate values of  $\lambda''_{33i}$  (see Figure 3.3). Romain als worked on integrating into the ATLAS simulation software the  $\lambda''_{33i}$  dependent RPV models developed during our previous phenomenological work [73] and which will be used for the simulation of stop pair production at  $\sqrt{s} = 13$  TeV.

## C. Scientific Animation and Outreach

---

<sup>k</sup><http://www-subatech.in2p3.fr/fr/>

## Frontiers of Fundamental Physics 14

I acted as Local Organizer Committee member for the 14th annual international symposium Frontiers of Fundamental Physics (FFP14)<sup>1</sup> which was held in Marseille between the 15<sup>th</sup> and the 18<sup>th</sup> July 2014, at the Faculty of Sciences of Aix Marseille-Université (AMU). The FFP Symposium began in India in 1997 and it became itinerant in 2004, through Europe, Canada and Australia. It covers topics in fundamental physics with the objective of enabling physicists working in related areas to meet on a single platform and exchange ideas. In addition to highlighting the progress in these areas, educational aspects are also discussed. FFP14 developed around seven main themes:

- Astroparticle Physics
- Cosmology
- High Energy Physics
- Quantum Gravity
- Mathematical Physics
- Physics Education
- Epistemology and Philosophy

Together with Jean-Loic Kneur (UM2), I was in charge of organising the High Energy Physics conference of the symposium, approximatively 30 speakers chosen among experts in the field of BSM phenomenology, LHC physics, dynamics of electroweak symmetry breaking, quark and lepton flavor physics, neutrino physics, lattice QCD, heavy ion physics and dark matter physics.

## TOP-LHC France Workshop

Since 2015 I am part of the organization of the TOP-LHC France workshops. These workshops aim at gathering the French community working on top-quark physics and fostering collaborations between experimentalists and phenomenologists.

While the first editions were mostly oriented to discussing precision measurements in the top-quark sector, a large fraction of the discussions is shifting now to the search for BSM physics in top-quark-like events: top Yukawa coupling ( $t\bar{t}H$ ) measurements, resonant and non-resonant anomalous top production, new physics produced in association with top quark, top quark partners in SUSY (top squark production) and composite models (vector like quarks).

---

<sup>1</sup><http://ffp14.cpt.univ-mrs.fr/>

Typically, the workshop unfolds over two days, a normal attendance is of about 40 physicists. The 2017 edition of the workshop was held at CPPM<sup>m</sup>, partially supported by the Labex OCEVU to the level of 4000 euros. This allowed us to cover the organizational expenses in particular to reimburse the travel expenses of participants involved with the PESBLADe project. This grant allowed us to invite to the 2107 edition of TOP-LHC France Angelo Monteux, from Rutgers university, a leading expert on RPV stop phenomenology. Angelo Monteux remained in area for about two weeks, he visited the laboratories involved with the PESBLADe collaboration, CPPM and L2C-LUPM, where, other than participating to fruitful discussions on SUSY RPV model building, he also presented his work during general laboratory-wide seminars.

## Physics ATLAS France Workshop

From 2009 to 2010 I represented the CPPM-ATLAS group as a member of the Physique ATLAS France (PAF). This organism coordinates the activities of all French laboratories (IN2P3 and CEA) part of the ATLAS collaboration. The PAF mandate is manifold and it is in charge of the following tasks:

- Organization of a yearly physics workshop, where all ATLAS French members meet to exchange ideas and foster cooperation on different matters.
- Coordination of ATLAS PhD theses proposed within the French laboratories to avoid duplications.
- Coordinating the effort in terms of data analysis within the French grid cloud and optimize ATLAS usage of the Lyon IN2P3 Centre de Calcul.

I participated to the organization of several Physique Atlas France workshops:

- EVIAN, 19-21 October 2009.
- Les Balcons du lac d'Annecy, 18-20 October 2010.
- La Londe les Maures, 3-5 October 2011 (acted as local organizer).

## CPPM weekly seminar organization

Since October 2016 I am one of the two physicists responsible for the organization of the weekly CPPM seminars. These seminars are mostly given by external speakers who are invited to CPPM to illustrate recent experimental results in high energy physics, astro-particle physics and cosmology, relevant for the research carried out at CPPM. We are also in charge for the yearly CPPM PhD student seminars, where CPPM students show the progress of their thesis work.

---

<sup>m</sup><https://indico.in2p3.fr/event/14083/>



## Teaching Experience

Ecole Centrale de Marseille, “Introduction à la physique des particules et astroparticules”, Option Générale, academic year 2009/2010. The class consisted of a total of 24 hours for around 25 students. The class also includes one computer lab session, and a guided visit to CPPM.

## General public talks

2013, “The discovery of the Higgs boson”, seminar aimed at a general audience at the Marseille’s Istituto Italiano di Cultura of the Italian Consulate.

## Cern Master Classes

2011, responsible for CERN master classes at CPPM <sup>n</sup>. From 2012 on part of the team in charge for receiving high school students at CPPM, lecturing them and tutoring them in the exercise section, all part of the Cern Master Class program.

## D. Responsibilities

### Coordinator of the OCEVU Particle Physics working group

Since 2014 I have been acting as coordinator of the Labex OCEVU Particle Physics Working Group, one of the three scientific working groups within OCEVU. This responsibility is shared between one experimentalist and theorist from the particle physics community, which counts around 50 among CNRS researchers, university professors, postdoc and students. This role consists mainly on overlooking the yearly call for project process, providing a link between the principal investigators and the decisional body, the executive committee. As part of the decisional process for the funding of the different projects, the coordinators have the role of helping the PIs to respect the OCEVU guidelines, with a particular regard to the collaborative aspects of the projects, a matricial aspect of OCEVU, which strongly value the implementation of synergies between the three particle physics laboratories (Centre de Physique Théorique, Centre de Physique des Particules de Marseille and Laboratoire Univers et Particule de Montpellier). Coordinators are responsible for the organization for the yearly OCEVU particle physics meeting which happens just before the OCEVU call for proposal. All working group coordinators have the duty to report yearly to the OCEVU steering committee, presided by Saul Perlmutter, which is composed by OCEVU institutional partners and which is in charge of evaluating the implementation of the Labex OCEVU scientific guidelines.

---

<sup>n</sup><http://physicsmasterclasses.org/>



## Principal Investigator of the PESBLADe project

The PESBLADe project (Probing the nature of Electroweak Symmetry Breaking at the LHC with the ATLAS Detector) is a collaboration between particle physicists experimentalists from the ATLAS-CPPM and theorists from LUPM-L2C funded by the labex OCEVU. The project started by scratch with a first series of meetings devoted to identifying the competence of the different actors from the two laboratories. The IFAC-UM2 theory group has a longstanding expertise in the phenomenology of minimal [328, 329] and extended [330, 331] SUSY models, as well as Higgs physics [332, 333, 334]. It also acquired in recent years further expertise in composite Higgs models and their implications on BSM collider phenomenology and particle dark matter [335, 336]. More generally, the group possesses as well quite a complementary expertise in astro-particle and early universe physics, relevant in particular to BSM and dark matter issues. These discussions put the basis of a collaborative project we submitted to the Labex OCEVU, which once successfully selected and funded gave us the possibility to hire Sara Diglio, a post-doc with a strong background on working with phenomenology, and an operating budget which cover traveling expenses either from Marseille and Montpellier and from Marseille and CERN for the members of the project, budget that has been renewed each year after review by the OCEVU scientific committee.

After a first round of studies where we investigated different BSM signatures that could be tested in experimental final states where the CPPM-ATLAS group has strong interest, we concentrated on a scenario based on R-parity violating SUSY. Starting from final states with multi-jets and multi- $b$ -jets, a final state congruent to the one of the fully hadronic  $t\bar{t}H$  analysis, we looked at a whole class of signature that eventually also contribute to other  $t\bar{t}H$  final state such as the semi-leptonic  $t\bar{t}H(H \rightarrow b\bar{b})$ .

From 2014 the PESBLADe project developed further, under its umbrella several branches were initiated. I act as Principal Investigator of the project though I do not contribute to all its activities, which are summarized below:

### A. SuperSYmmetric (SUSY) models with R-parity violation

This part has been discussed widely in Chapter 3. Recently Nguyen Hoan Dai Nghia, a former P3MA master student and now PhD student within the ATLAS group, joined the effort by performing a study of ATLAS sensitivity for Run 2 for one particular benchmark point used for the phenomenology work using fast simulation for his master internship under my supervision. Romain Kukla (post-doc OCEVU from October 2016) is now working with Nghia on putting in place the analysis framework which will allow us to search for RPV stop production.

### B. New physics beyond the SM in multi-boson final states

Multi-boson final states can be used as a probe for new physics either by precisely testing any deviation from the SM using model-independent Effective Field Theory approaches [337, 338] or by searching for specific signatures of BSM models. In the latter case, any extension of the SM should be able to account for the fact that the discovered 125 GeV scalar object behaves very much like a SM Higgs, and in the same time for the only true deviation from SM to date, namely neutrino masses.

This branch of the PESVLADe project aims at the search double charged Higgs decaying into same-sign  $W$  bosons using the Run 2 data recorded by the ATLAS detector. This is the subject of the PhD thesis of Venugopal Ellajosyula (PhD student OCEVU, 2014-2017) co-directed by Cristinel Diaconu (CPPM) and Gilbert Moulata (LUPM). The data analysis is about to be published and a phenomenology paper is in the pipeline.

### C. Study of the R-parity conserving SUSY

The R-parity conserving SUSY is one of the most motivated theories beyond the Standard Model. During the LHC 8 TeV Run1, many searches were dedicated to this model. Among those, the search for chargino and neutralino ( $\chi^{1\pm}, \chi^{20}$ ) pair production in final states with one lepton, two b-jets consistent with a Higgs boson and missing transverse energy, which have negative outcome resulting in excluding  $\chi^{1\pm}, \chi^{20}$  masses up to 250 GeV for a massless neutralino ( $\chi^{10}$ ) at 95 % CL.

This is the subject of the PhD thesis of Rima El Kousseifi (PhD student OCEVU, 2015-2018) co-directed by Steve Muanza (CPPM) and Jean-Loic Kneur (L2C). Rima participated to the reactualization of the analysis using Run 2 data, which is about to be published by ATLAS. The collaboration with L2C also includes the development of Suspect3<sup>o</sup>, a software which calculates SUSY mass spectra and couplings.

## Editor of the Run 1 ATLAS fully hadronic $t\bar{t}H(H \rightarrow b\bar{b})$ analysis

From 2014 onwards, I have been acting as coordinator of the ATLAS working group responsible for the fully hadronic  $t\bar{t}H(H \rightarrow b\bar{b})$  analysis. In Run 1 this responsibility was shared between two ATLAS physicists and included the editorial work which lead to the Run 1 publication. This coordination activity has meant ensuring the link between the analysis group and the Higgs working group management, organizing weekly meetings to supervise the group activities. By the end of Run 1 the group was composed of 20 physicists from about ten different

---

<sup>o</sup><http://www.coulomb.univ-montp2.fr/perso/jean-loic.kneur/Suspect/>

institutions. In Run 2, while the activities around this analysis are being reorganized, I am acting as contact person for the analysis.

## **France-Stanford Collaborative Research Projects funds**

While involved in the fully hadronic  $t\bar{t}$  analysis I submitted a demand to the 2011 France-Stanford Collaborative Research Projects Call For Proposals<sup>P</sup>. The project “Search for new physics in top quark events with the ATLAS detector” was funded with \$14,000, amount which covered travel expenses for travel from SLAC to CERN and from Marseille to SLAC. Together with a CPPM student, Claudia Bertella, and a postdoc at SLAC, Ignacio Aracena, we wrote the analysis software at the core of all our Run 1 data analysis activities. The first analysis performed, the top quark pair production measurement at  $\sqrt{s} = 7$  TeV [71], would be presented by Ignacio Aracena at the 2012 Rencontres de Moriond winter conference.

## **Convener of the ATLAS $b$ -jet trigger slice group**

The ATLAS  $b$ -jet trigger group is responsible for the implementation of all the trigger items which uses online  $b$ -tagging, for monitoring these during data taking, for the assessment of the collected data quality and finally, for the estimation of the trigger performance. The group is also responsible for calibration triggers, which trigger the presence of muons inside hadronic jets, used for the estimation of the  $b$ -tagging performance for both online and offline algorithms. I have been convener of the  $b$ -jet trigger group from March 2012 to March 2014. My convenership mandate, shared with another ATLAS physicist, included the responsibility of the 2012 data taking campaign, and setting up the preparation to Run 2, this included the integration of the online and offline software which resulted in the possibility of running the offline multi-variate  $b$ -tagging algorithm within the online framework. I have also been responsible for the online  $b$ -tagging monitoring, responsibility that I continue to ensure during the current Run 2, I am also acting as one of the people in charge of the validation of the trigger releases.

## **Editor of ATLAS $t\bar{t}H(H \rightarrow b\bar{b})$ sensitivity study for the CSC book**

In 2007 the ATLAS collaboration organized an effort to reassess the sensitivity to SM measures and BSM searches fundamental for the imminent LHC physics program. This global effort organized the ATLAS community around data analysis which would use status of the art MC event generators and detector simulations

---

<sup>P</sup><http://francestanford.stanford.edu>

for this exercise. During the two years that would follow I worked on estimating the sensitivity to the  $t\bar{t}H(H \rightarrow b\bar{b})$  channel for  $30 \text{ fb}^{-1}$  of proton-proton collisions at center-of-mass energy of 14 TeV, at the time the baseline scenario for Run 1. For this I lead, together with another ATLAS member, a group of about ten physicists among permanent researchers, post-docs and students from several institutions (CPPM, Glasgow, RHUL, Genova) until the publication of the analysis finally was released in the so called *CSC book* [66].